

# Portable and Versatile Cold Atom Experiments

Philip Ireland



University of  
St Andrews

This thesis is submitted in partial fulfilment for the degree of

Doctor of Philosophy (PhD)

at the University of St Andrews

November 2018

# Abstract

This thesis describes the progress achieved towards two goals. One is the construction of a compact magneto-optical trap (MOT) apparatus, used both as a standalone undergraduate laboratory experiment and as part of a public engagement demonstration of cold atom physics. The setup, which utilises a dichroic atomic vapour laser lock (DAVLL) system plus homemade sideband generation electronics, is capable of trapping and cooling up to  $8 \times 10^7$   $^{85}\text{Rb}$  atoms in a standard six-beam laser cooling scheme.

The second goal is the loading of an ultracold ensemble of  $^{87}\text{Rb}$  atoms into novel optical trap geometries using a phase-only liquid crystal spatial light modulator (LC SLM) for applications to atomtronics and quantum simulation. Details of a double vacuum chamber apparatus, designed to produce the first Bose-Einstein condensates (BECs) at St Andrews, are provided. The setup incorporates a hybrid trap evaporative cooling scheme towards quantum degeneracy and reliably produces BECs of  $1.9 \times 10^5$   $^{87}\text{Rb}$  atoms. Two computational techniques, developed during the course of this project, are presented with the aim of creating flexible, smooth holographic optical traps. The first method illuminates a single SLM with overlapped, co-propagating light beams of different wavelengths to create a composite optical pattern for atom manipulation. The second uses conjugate gradient minimisation to create exceptionally high fidelity light patterns in both amplitude and phase for light in the output plane. These techniques, combined with the implementation of a light sheet into the experimental setup, are used to trap atoms in both a ring profile and in a set of narrow waveguides connected with a tunnelling barrier.

## **Candidate's declaration**

I, Philip Ireland, do hereby certify that this thesis, submitted for the degree of PhD, which is approximately 32,000 words in length, has been written by me, and that it is the record of work carried out by me, or principally by myself in collaboration with others as acknowledged, and that it has not been submitted in any previous application for any degree.

I was admitted as a research student at the University of St Andrews in August 2014.

I received funding from an organisation or institution and have acknowledged the funder(s) in the full text of my thesis.

Date

Signature of candidate

## **Supervisor's declaration**

I hereby certify that the candidate has fulfilled the conditions of the Resolution and Regulations appropriate for the degree of PhD in the University of St Andrews and that the candidate is qualified to submit this thesis in application for that degree.

Date

Signature of supervisor

## **Permission for publication**

In submitting this thesis to the University of St Andrews we understand that we are giving permission for it to be made available for use in accordance with the regulations of the University Library for the time being in force, subject to any copyright vested in the work not being affected thereby. We also understand, unless exempt by an award of an embargo as requested below, that the title and the abstract will be published, and that a copy of the work may be made and supplied to any bona fide library or research worker, that this thesis will be electronically accessible for personal or research use and that the library has the right to migrate this thesis into new electronic forms as required to ensure continued access to the thesis.

I, Philip Ireland, confirm that my thesis does not contain any third-party material that requires copyright clearance.

The following is an agreed request by candidate and supervisor regarding the publication of this thesis:

**Printed copy**

No embargo on print copy.

**Electronic copy**

No embargo on electronic copy.

Date

Signature of candidate

Date

Signature of supervisor

## **Underpinning Research Data or Digital Outputs**

### **Candidate's declaration**

I, Philip Ireland, understand that by declaring that I have original research data or digital outputs, I should make every effort in meeting the University's and research funders' requirements on the deposit and sharing of research data or research digital outputs.

Date

Signature of candidate

### **Permission for publication of underpinning research data or digital outputs**

We understand that for any original research data or digital outputs which are deposited, we are giving permission for them to be made available for use in accordance with the requirements of the University and research funders, for the time being in force.

We also understand that the title and the description will be published, and that the underpinning research data or digital outputs will be electronically accessible for use in accordance with the license specified at the point of deposit, unless exempt by award of an embargo as requested below.

The following is an agreed request by candidate and supervisor regarding the publication of underpinning research data or digital outputs:

No embargo on underpinning research data or digital outputs.

Date

Signature of candidate

Date

Signature of supervisor

# Acknowledgements

There are a great deal of people that deserve mention for their support, guidance and friendship during my time as a PhD student at the University of St Andrews. Many of them know, as well as myself, that I have not always fully believed in my own ability to reach this point, and without the advice and encouragement from these people I would have found this a far lonelier project.

My initial thanks must go to my supervisor, Dr Donatella Cassetari, who has been a tremendous mentor and source of support during this time. As an undergraduate student at St Andrews, it was through your Atomic and Quantum Physics lecture courses that brought about my in towards experimental atomic physics and allowed me to work on both MPhys and PhD projects under your guidance. Your door was always open for queries and discussions of any nature, and I feel very grateful to have such an accommodating supervisor over these years.

A special mention must go to Dr Graham Bruce, who was a post-doc in our group during my MPhys project and for the first two years of this PhD. During that time, you were a constant source of teaching, clarification and guidance, bringing an exceptional level of understanding and a capacity for clear explanation of difficult and unfamiliar concepts within lab 105. Even after your new job took you to the distant land of lab 107, you remained available for discussions on this project and other topics (the most prominent of which, I'm sure, was football).

A significant amount of time working on the main experimental setup was shared with Dr David Bowman, a fellow PhD student who graduated himself earlier this year. Working on this project over the years did, at times, present a number of challenges and annoyances that threatened to significantly delay the progress we were striving towards. During these periods I was extremely glad to have your company, both for discussions on how to proceed with the experiment and for the general camaraderie we built up. You are an excellent researcher and a good friend.

These three members of our close-knit group have provided tremendous amounts of knowledge, support and friendship over the course of this project. However, I have also had the pleasure of working with many others, either through MPhys or summer projects offered by the group or through the taught courses with the other CM-CDT PhD students. A special thanks must also go to the staff of both the university workshop and the electronics department - I am grateful for their contributions to various aspects of both the portable MOT and the double vacuum chamber apparatus. The camera control, imaging analysis and data acquisition Matlab codes were provided by Dr Elmar Haller of the University of Strathclyde, while we collaborated extensively with Dr Paul Griffin of the University of Strathclyde during the portable MOT outreach events. The fibre laser for the optical evaporation was loaned to us by Professor Kishan Dholakia.

I am extremely thankful for my family, who constantly provide an abundance of love, support, encouragement and belief ever since I first moved to St Andrews in 2009. Finally, to my fiancée Hannah, who knows me better than anyone and who has seen how much I have struggled at times over the last three years. Thank you for your love and belief in me, for your support and care, for travelling up to St Andrews to visit each weekend over the last few months, and for reminding me over the years there is more to life than this project.

# List of Publications and Presentations

## Journal Publications:

- D. Bowman, P. Ireland, G. D. Bruce, and D. Cassettari, “Multi-wavelength holography with a single spatial light modulator for ultracold atom experiments”, *Optics Express*, vol. 23, p. 8365, 2015.
- D. Bowman, T. L. Harte, V. Chardonnet, C. D. Groot, S. J. Denny, G. L. Goc, M. Anderson, P. Ireland, D. Cassettari, and G. D. Bruce, “High-fidelity phase and amplitude control of phase-only computer generated holograms using conjugate gradient minimisation”, *Optics Express*, vol. 25, p. 11692, 2017.

## Poster Presentations:

- P. Ireland, D. Bowman, L. A. Lee, G. D. Bruce, and D. Cassettari, “Towards BEC in Flexible Optical Traps”, CM-CDT Summer School, Macdonald Aviemore Resort, Aviemore, UK, 2014.
- P. Ireland, D. Bowman, L. A. Lee, G. D. Bruce, and D. Cassettari, “Towards BEC in Flexible Optical Traps”, École Prédoctorale de Physique des Houches, Les Houches, France, 2014.
- P. Ireland, D. Bowman, G. D. Bruce, J. McGilligan, I. Kresic, B. Robertson, P. F. Griffin, and D. Cassettari, “A Portable Magneto-Optical Trap for Public Engagement Events”, International Conference on Quantum, Atomic, Molecular and Plasma Physics, University of Sussex, Brighton, UK, 2015.
- P. Ireland, D. Bowman, G. D. Bruce, P. F. Griffin, and D. Cassettari, “Portable and Flexible Cold Atom Experiments”, 24th Young Atom Opticians Conference, University of Strathclyde, Glasgow, UK, 2018.
- P. Ireland, D. Bowman, G. D. Bruce, P. F. Griffin, and D. Cassettari, “Portable and Flexible Cold Atom Experiments”, 26th International Conference on Atomic Physics, Palau de Congressos de Barcelona, Barcelona, Spain, 2018.

## Funding

This work was supported by the EPSRC (grant number EP/L015110/1).

This work was supported by the University of St Andrews (School of Physics & Astronomy).

# Contents

<b>1</b>	<b>Introduction</b>	<b>1</b>
1.1	Bose-Einstein Condensation . . . . .	1
1.2	Techniques for the Trapping and Manipulation of Ultracold Atoms . . . . .	3
1.3	Compact Cold Atom Systems . . . . .	9
1.4	Thesis Outline . . . . .	12
<b>2</b>	<b>Construction of a Compact, Portable MOT for Outreach and Teaching</b>	<b>13</b>
2.1	Motivation . . . . .	13
2.2	Vacuum Chamber Design and Build . . . . .	13
2.3	Laser System . . . . .	15
2.4	Dichroic Atomic Vapour Laser Locking . . . . .	18
2.5	Sidebands Generation . . . . .	22
2.6	Optical Setup . . . . .	24
2.7	Measurements . . . . .	26
2.7.1	Measuring the Atom Number in the MOT . . . . .	27
2.7.2	Obtaining an Estimate of the Pressure at the MOT Position . . . . .	28
2.8	Outreach Demonstrations . . . . .	29
2.9	Future Work Planned . . . . .	30
<b>3</b>	<b>Construction of a Double Vacuum Chamber Apparatus for Production of <math>^{87}\text{Rb}</math> Bose-Einstein Condensates</b>	<b>33</b>
3.1	Introduction . . . . .	33
3.2	The Double Vacuum Chamber Apparatus . . . . .	35
3.2.1	Glass Cell, Differential Pumping Tube, Octagon Chamber . . . . .	35
3.2.2	Obtaining Ultra High Vacuum Conditions . . . . .	38
3.2.3	Full Apparatus . . . . .	40
3.3	3D and 2D Laser Cooling of Rubidium . . . . .	41
3.3.1	Laser System . . . . .	42
3.3.2	Saturated Absorption Spectroscopy and Locking the Lasers . . . . .	44
3.3.3	Detuning the Cooling Lasers . . . . .	45
3.3.4	Increasing the Laser Cooling Power . . . . .	46

3.3.5	Push Beam . . . . .	48
3.3.6	Full 3D and 2D Laser Cooling Setup . . . . .	48
3.4	Magnetic Field Generation . . . . .	49
3.4.1	3D MOT Magnetic Field . . . . .	50
3.4.2	2D MOT Magnetic Field . . . . .	52
3.4.3	Shim Coils . . . . .	53
3.4.4	Water Cooling . . . . .	54
3.5	MOT Optimisation . . . . .	55
3.6	Optical Pumping . . . . .	58
3.7	Imaging . . . . .	60
3.8	Evaporative Cooling . . . . .	64
3.8.1	Hybrid Trap Design . . . . .	64
3.8.2	Radio-frequency Evaporation in the Magnetic Trap . . . . .	66
3.8.3	Optical Evaporation in a Focused ODT . . . . .	69
3.9	Bose-Einstein Condensation . . . . .	74
3.10	Full Experimental Sequence Procedure . . . . .	76
3.11	Summary . . . . .	78
<b>4</b>	<b>Cold Atoms in Holographic Optical Traps using a Phase-only Spatial Light Modulator</b> . . . . .	<b>80</b>
4.1	Introduction . . . . .	80
4.2	Phase-only Liquid Crystal SLMs . . . . .	80
4.3	Phase Pattern Generation Techniques . . . . .	82
4.3.1	Iterative Fourier Transform Algorithms . . . . .	83
4.3.2	Mixed Region Amplitude Freedom Algorithm . . . . .	86
4.3.3	Conjugate Gradient Minimisation . . . . .	88
4.3.4	Initialising the Algorithm . . . . .	95
4.3.5	Feedback-enhanced Aberration Correction . . . . .	97
4.4	Multi-wavelength and Phase and Amplitude Control Investigations . . . . .	98
4.4.1	Multi-wavelength Holography Results . . . . .	98
4.4.2	Phase and Amplitude Control Results . . . . .	102
4.5	SLM Experimental Implementation . . . . .	109
4.5.1	Setting Up the Vertical Trapping Path . . . . .	110
4.5.2	Setting Up the SLM Alignment . . . . .	113
4.6	Cold Atoms in Holographic Traps . . . . .	115
4.7	Light Sheet Setup . . . . .	117
4.8	Additional Trap Configurations . . . . .	122
4.9	Summary . . . . .	125
<b>5</b>	<b>Conclusions</b> . . . . .	<b>127</b>
5.1	Summary . . . . .	127

5.2 Future Plans . . . . .	129
----------------------------	-----

# List of Figures

1.1	Comparison of Different Techniques for the Trapping and Manipulation of Ultracold Atoms . . . . .	8
1.2	Examples of Different Methods for Miniaturising Cold Atom Setups . . . . .	11
2.1	Compact Vacuum Chamber Setup . . . . .	15
2.2	$^{85}\text{Rb}$ D2 Line . . . . .	16
2.3	$^{85}\text{Rb}$ Saturated Absorption Spectroscopy . . . . .	17
2.4	DAVLL Spectroscopy Setup . . . . .	19
2.5	DAVLL Error Signal Generation . . . . .	20
2.6	Simplified Circuit Diagram for DAVLL . . . . .	21
2.7	Simplified Schematic for Homemade Sidebands Generation . . . . .	23
2.8	Observation of Sidebands using a Fabry-Perot Interferometer . . . . .	24
2.9	Optics Breadboard Layout for the portable MOT . . . . .	25
2.10	Vacuum Chamber Breadboard Layout for the portable MOT . . . . .	26
2.11	Example Image of the MOT using DAVLL and Sideband Techniques . . . . .	28
2.12	Photos taken during the International Year of Light Launch Event in 2015 . . . . .	29
2.13	Photos taken during Dundee Science Festival 2015 . . . . .	30
2.14	Comparison of the Grating Chip MOT versus the Standard Six-beam MOT . . . . .	31
2.15	Proposed Compact MOT Setup incorporating the Grating Chip . . . . .	31
3.1	Glass Cell with Differential Pumping Tube Models . . . . .	36
3.2	Model of the Main Experiment Chamber (Octagon) connected to the Glass Cell . . . . .	38
3.3	Model of the Full Double Vacuum Chamber Apparatus . . . . .	39
3.4	Bakeout Graph . . . . .	40
3.5	Full Apparatus and Schematic with 2D Optics in Place . . . . .	41
3.6	$^{87}\text{Rb}$ D2 Line . . . . .	42
3.7	Block Diagram of the Optics Table Layout . . . . .	44
3.8	$^{87}\text{Rb}$ Saturated Absorption Spectroscopy Results . . . . .	45
3.9	Comparison of Master Laser Absorption Spectrum with Slave Laser Absorption Spectrum . . . . .	47
3.10	Diagram showing the Full 2D and 3D Laser Cooling Setup . . . . .	49

3.11	Model of our Magnetic Coil Holders . . . . .	51
3.12	Cutaway Image of the Octagon with Recessed Viewports . . . . .	52
3.13	Model of the 2D MOT Coil Holders . . . . .	53
3.14	2D MOT Setup with Coils in Place . . . . .	53
3.15	Temperature Response of the 3D Coils under Water Cooling . . . . .	55
3.16	MOT Optimisation data . . . . .	56
3.17	Further 3D MOT Optimisation data . . . . .	57
3.18	Optical Pumping Schematic . . . . .	59
3.19	Example Plot highlighting the Optical Pumping Effect . . . . .	60
3.20	Absorption Imaging Example . . . . .	62
3.21	Horizontal Imaging Optical Setup . . . . .	63
3.22	Vertical Imaging Optical Setup . . . . .	64
3.23	Hybrid Trap Evaporative Cooling Design . . . . .	65
3.24	Magnetic Trap Lifetime Measurement . . . . .	66
3.25	Radio Frequency Evaporation Schematic . . . . .	67
3.26	PSD plot for the Radio Evaporation Sequence . . . . .	69
3.27	AC Stark Shift effect . . . . .	70
3.28	Horizontal ODT Optical Setup . . . . .	71
3.29	ODT Lifetime Measurement . . . . .	72
3.30	Full PSD plot for both RF Evaporation and Optical Evaporation . . . . .	73
3.31	Absorption Image Surface Plots and Associated Fits for BEC Formation . . . . .	75
3.32	Schematic of a Full Experimental Sequence Procedure . . . . .	77
3.33	Schematic for Data Acquisition and Analysis . . . . .	78
4.1	LC SLM Operation . . . . .	81
4.2	Fourier Transform Relationship Diagram . . . . .	82
4.3	Block Diagram for the IFTA Procedure . . . . .	85
4.4	Regions of Interest for MRAF Algorithm . . . . .	87
4.5	Comparison of GS and MRAF Algorithms . . . . .	88
4.6	Steepest Descent Diagram . . . . .	90
4.7	Conjugate Gradient Diagram . . . . .	91
4.8	Block Diagram for Conjugate Gradient Minimisation . . . . .	93
4.9	Cost Function Importance Example . . . . .	94
4.10	Construction of the Guess Phase . . . . .	96
4.11	Example of Padding the Input Plane . . . . .	97
4.12	Multi-wavelength Holography Principle . . . . .	100
4.13	Gallery of Multi-wavelength Light Patterns . . . . .	101
4.14	Cost Function Choice Analysis . . . . .	104
4.15	Output Plane Intensity and Phase Results for Different Cost Functions . . . . .	106
4.16	High Fidelity Phase and Amplitude Light Profiles using CG Minimisation . . . . .	108
4.17	Experimental Verification of High Fidelity Light Profiles . . . . .	109

4.18	Vertical Trapping Path Optical Setup . . . . .	111
4.19	Vertical Trapping Path Alignment Images . . . . .	113
4.20	SLM Double Spot Pattern Results . . . . .	115
4.21	Gallery of Cold Atoms Trapped in Various 1D Optical Potentials with the SLM . . . . .	116
4.22	Light Sheet Thickness Analysis . . . . .	118
4.23	Full Optical Path Setup for the 1064nm Light . . . . .	119
4.24	Light Sheet Alignment Images . . . . .	120
4.25	Alignment of the Light Sheet with the SLM . . . . .	122
4.26	Absorption Images of Atoms Trapped in Ring and Cross Patterns . . . . .	124
4.27	Example of Phase Manipulation of Light in the Output Plane . . . . .	125

# List of Tables

3.1	Available Laser Power at the Output of each Optical Fibre. . . . .	50
3.2	Table showing the Optimised MOT Parameters. . . . .	58
3.3	Table showing approximate Atom Number, Temperature and PSD at various experimental stages. . . . .	75
4.1	Table summarising the Cost Function investigation results. . . . .	105
4.2	Table summarising Error Values and Optimisation Parameters for a selection of High Fidelity Light Patterns. . . . .	107

# Chapter 1

## Introduction

### 1.1 Bose-Einstein Condensation

A Bose-Einstein Condensate (BEC) is a state of matter that exhibits quantum phenomena on a macroscopic scale, observed when particles with integer spin (bosons) accumulate in the lowest quantum mechanical energy state, at which point they begin to behave as a collective ensemble. Ever since the initial groundbreaking experimental realisation of a BEC in 1995 achieved using rubidium [1], and closely followed by sodium [2], lithium [3] and hydrogen [4], progress in the field of so-called ultracold atoms has developed rapidly, continually pushing the boundaries on the degree of flexibility and control one can exert in such experiments. BEC formation is not just limited to cold atomic gases, either - it has also been observed in exciton polaritons [5], quasi-equilibrium magnons [6] and photons [7]. Despite the prediction of such a quantum-statistical phase transition being made as early as 1925 [8, 9, 10, 11], it took many decades for the now well-established experimental techniques of laser cooling and evaporative cooling of alkali atoms to be realised. However, it took only one year to move from the first observations of evaporative cooling in alkalis to BEC formation. Nowadays, BECs are routinely created in labs around the world. In this section, a brief guide to BEC production is provided, but a more comprehensive review can be found in [12].

As the temperature  $T$  of an ensemble of non-interacting, indistinguishable particles decreases, the average number of particles occupying a certain energy level will be dictated by the fundamental nature of the particles themselves - Bose-Einstein statistics for bosonic atoms and Fermi-Dirac statistics for fermions. For the case of bosons, the Bose-Einstein distribution function that describes the average number of particles  $n$  having energy  $\epsilon$  is:

$$n(\epsilon) = \frac{1}{e^{\beta(\epsilon-\mu)} - 1} \quad (1.1)$$

where  $\mu$  is the chemical potential of the system and  $\beta = 1/k_B T$ . Bosons are gregarious particles capable of multiple occupation of the same quantum state, and so as the tem-

perature approaches absolute zero, the particles condense into the lowest energy state and undergo a phase transition into the quantum degenerate BEC. The BEC is based on the indistinguishability and wave nature of the particles involved, and in a simplified picture, quantum degenerate effects begin to occur when the thermal de Broglie wavelength  $\lambda_{dB}$ , defined as:

$$\lambda_{dB} = \left( \frac{2\pi\hbar^2}{mk_B T} \right)^{\frac{1}{2}} \quad (1.2)$$

of the individual particles (of mass  $m$ ) becomes comparable to the interatomic separation. At this point, the indistinguishability of the particles becomes important and a coherent cloud of atoms begins to form when the temperature of the gas has been reduced and additionally the density has been increased. Condensation occurs when the phase space density  $n\lambda_{dB}^3 \geq 2.612$ , where  $n$  is the peak number density.

Realising a suitably cold and dense atomic cloud requires some care - high densities are desired but due to interactions being present in reality, inelastic two- and three-body collisions can negatively impact the route to BEC. If the density of the cloud must be lessened to avoid these so-called ‘bad collisions’ then correspondingly the temperature of the ensemble is usually required to be in the sub-microkelvin range. The pathway to BEC then necessarily describes the route to achieving such low temperatures and high densities in a dilute atomic vapour. The cornerstone of the majority of BEC experiments is the magneto-optical trap (MOT), first realised in 1987 [13] as a technique to confine and cool neutral sodium atoms via radiation pressure (a more in-depth description of the laser cooling and trapping process can be found in [14]). Nowadays, the MOT is recognised as one of the most effective methods of cooling neutral atoms, with the combined optical and magnetic fields able to create clouds of cold atoms below the 1mK temperature range.

However, the laser cooling process that takes place at the centre of the MOT has a fundamental practical limit, imposed by inelastic, light-induced collisions that lead to atom loss, as well as absorption from scattered laser light that lessens the density achievable due to the outward pressure. As such, despite providing an increase in the phase space density of about six orders of magnitude, the atoms are neither cold nor dense enough to condense. In 1990, evaporative cooling of alkali atoms was suggested as the answer to increase the phase space density further as it removes the density-limiting interactions with light. Taking place in a purely conservative potential, the cloud is compressed to achieve high densities and elastic collision rates for rethermalisation, while the hottest proportion of the atoms are expelled from the trap. This selective removal can be done in numerous ways - in 1994, rf-induced evaporation of alkali atoms in a magnetic trap was demonstrated [15, 16], and just a year later came the observations of BEC. The signature of the BEC was detected by the presence of a bimodal momentum distribution via absorption imaging: a narrow peak centred at zero velocity superimposed on the broad, non-condensed thermal fraction of the cloud.

In the time since, the field has grown rapidly; not just with the extraordinary array of experiments performed using quantum degenerate gases, but also exploring more versatile

and flexible approaches to BEC production. Despite the limitations of typical MOTs, there has been recent progress in achieving quantum degeneracy using laser cooling alone, either using the favourable narrow transition linewidth of strontium [17] or by greatly reducing the amount of light-induced atomic losses [18]. Evaporative cooling performed in a conservative optical trap has been demonstrated [19] - optical evaporation can offer the advantages of spin-state independent trapping and potentially tighter confinement than some magnetic traps. However, sufficiently deep optical traps in which to capture laser cooled atoms often requires unreasonably high laser powers, and so hybrid trap designs that benefit from the advantages of each while eliminating their individual weaknesses can be employed [20].

A fast and reliable BEC production is the first step for performing a huge array of fascinating experiments outlined briefly below. In some of the earliest experiments, Bose condensed atoms were made to interfere and were shown to have long-range coherence in an interferometry setup [21]. Ultracold atoms also provide a highly controlled environment for quantum simulation, such as observation of the quantum phase transition from a superfluid to a Mott insulator [22]. Additionally, the study of the collective excitations of certain quantum gases has allowed measurements of the speed of sound [23], and the creation of vortices [24, 25] within BECs to further understand superfluidity.

Such experiments demonstrating the quantum nature of the BEC, as well as the high degree of control and precision that can be achieved, means that there is an ever-increasing emphasis on experiments displaying increased flexibility and versatility in view of applications to quantum instruments and sensors. The work in this thesis has concentrated on two main areas: one is the construction of a compact cold atoms apparatus for pedagogical and public engagement purposes, with a view of demonstrating some of the underlying physics in an accessible manner. The other focus is on investigations of trap geometry in a cold atoms experiment with applications to quantum simulation and atomtronics in mind. For this reason, what follows is a review of possible methods available for the trapping and manipulation of ultracold atoms, as well as some of the recent developments achieved for the purposes of miniaturising atom-based measurement systems.

## 1.2 Techniques for the Trapping and Manipulation of Ultracold Atoms

The ability to dynamically manipulate, for example, the atom number, temperature, interaction strength or trap geometry in an ultracold atoms experiment whilst being able to monitor the behaviour of the atoms is the subject of much current research. Much emphasis is placed on designing versatile and flexible setups that provide a highly sensitive and controllable testing ground with future applications in mind.

The trapping of cold atoms is achieved using either laser light or magnetic fields (or a combination), taking place inside a high vacuum to ensure isolation from sources of

heating. Both cases rely on the lowering of the atomic ground state in the presence of either a magnetic or optical potential - magnetic trapping requires a strong magnetic moment (atoms with an unpaired electron) while optical trapping is possible due to the AC Stark shift for far-detuned light.

Magnetic trapping is achieved by utilising the interaction of the atom's magnetic moment with an externally applied magnetic field. Trapping of atoms in this way is however dependent on the  $m_F$  state of the atom, resulting in atoms either being high-field seekers or low-field seekers in their efforts to minimise their energy. For low-field seeking atoms, the minimum is located at the magnetic field zero created at the midpoint between a pair of coils constructed in the anti-Helmholtz setup. In order to mitigate the Majorana loss mechanism at the trap centre (where spin-flips to a high-field seeking state can occur for the coldest proportion of atoms due to the degeneracy of the  $m_F$  states at zero field), flexible magnetic trap geometries include time-averaged magnetic fields [26], Ioffe-Pritchard traps [27, 28] or plugged quadrupole traps [2]. Time-averaged orbiting potential (TOP) traps add a changing bias field to shift the location of the field zero at a faster rate than the atoms can respond. Further geometries are possible by applying RF radiation to a conventional TOP trap and producing a time-averaged adiabatic potential (TAAP) trap; geometries include double-well potentials [29] and ring traps [30, 31], as well as the trapping and rotation of a BEC in such a potential [32]. Restrictions regarding the size and placement of coils of wire or permanent magnets to create the magnetic field can be circumvented with so-called atom chips (reviewed in [33]). The atom chip allows the trapping, cooling and manipulation of cold atom experiments within a miniaturised, integrated setup. First realised at the turn of the century [34, 35, 36], with the first BECs on atom chips following shortly after [37, 38], the setup allows for different magnetic field geometries through differing wire configurations on the surface of a substrate.

The striking level of control that can be exerted on cold atoms is further enhanced when using optical trapping, due to the wide variety of techniques capable of manipulating laser light. Optical lattices, created by the interference between two or more counter-propagating laser beams, are periodic potentials in one, two, or three dimensions in which the lattice depth and dimension [39, 22] can be varied in order to engineer different environments in the field of quantum simulation. More complex lattice geometries have been realised, such as a checkerboard pattern [40] or honeycomb structure [41].

Such a repeating, periodic lattice structure provides a flexible and controllable environment for experiments on quantum simulation. Bosonic atoms confined in a Hubbard regime optical lattice [42, 22] are an excellent tool for the probing of quantum phase transitions - that is, a phase transition governed purely by the quantum fluctuations present in a system at absolute zero temperature. The most prominent and well-known quantum phase transition is that between a superfluid and a Mott insulator - ultracold bosonic atoms in an optical lattice undergo such a transition when the relative strength between the kinetic energy and interaction energy is varied across a critical point. Atoms in the Mott insulator phase lose any long-range coherence or phase between different lattice sites that they had

in the superfluid phase, opening up an avenue towards further quantum control.

The use of cold atoms as an engineering tool for quantum simulation is not only limited to bosons, either - fermions, despite the Pauli exclusion principle prohibiting multiple occupation of any quantum mechanical state, can still be cooled to a degenerate fermi gas (DFG) with the states instead filled sequentially upward from the ground state. Such a condensed system of fermionic atoms is also a convenient exploration tool for quantum many-body physics within an optical lattice structure [43, 44, 45]. The quantum simulations performed in this way rely on the macroscopic properties of the condensed atoms such as coherence. The ability to address individual atoms or lattice sites, however, is key in the realm of quantum computation and information - the individual atoms act as qubits in a highly controlled quantum information system. For many years, there existed a significant disconnect between the two approaches, until the demonstration of the so-called quantum gas microscope in 2009. The device, based on exceptionally high resolution and sensitivity, bridges the gap by individually detecting atoms of a macroscopic ensemble within the lattice sites of an optical lattice. The quantum gas microscope has been utilised for both bosonic [46, 47, 48, 49, 50, 51] and, roughly six years later, for fermionic atoms [52, 53, 54, 55, 56] and provides an excellent testing ground for both gaining insight into many-body quantum systems and as a simulation for complicated condensed matter systems.

An alternative to creating a standing wave structure is to use an acousto-optic deflector (AOD) to create a rapidly-scanning laser beam that then ‘paints’ a time-averaged optical dipole potential that the atoms experience (Figure 1.1a). This method has been shown to create BECs in a variety of geometries, including toroids, ring lattices and square lattices [57] (Figure 1.1(b)-(e)), as well as smooth, larger radius ring traps [58]. Use of an AOD can lift the self-imposed limits of magnetic trapping and create fully arbitrary and dynamic optical potentials. An AOD operates by creating a periodically changing refractive index in an optically transparent material, created by a propagating sound wave from one end to the other. The resulting refractive index modulation causes an incident laser beam to diffract, with fine control of the frequency of the sound wave able to alter the angle of diffraction of the diffracted orders and providing a scanning laser output. The response time of the AOD is fast (about  $1\mu s$ ) [57], faster than the radial trapping frequency of the time-averaged optical potential (about 1kHz). The optical potentials are painted on top of a light sheet that provides confinement perpendicular to the axis of the focused laser beam. Dynamic manipulation of the atoms is also possible using this method, with a toroidal condensate being transformed into a ring lattice and back again. Applications of this method to atomtronics have been realised in [59], where the rapidly-scanning laser beam is used to create a pair of Josephson junctions for the cold atom analogue of the superconducting quantum interference device (SQUID). However, a limiting factor regarding this technique is there is an upper bound on the complexity of the optical pattern to be generated - very intricate patterns mean that the laser beam may not be able to scan the entire pattern before the atoms detect a local change in the potential.

Spatial modulation of an input light field is another method of manipulating laser light

that results in many trapping potentials. Amplitude modulation can be achieved using a digital micromirror device (DMD) [60], which consists of a large array of tiny, individually configurable micromirrors that can each be configured to either reflect or block the light at their location. As such, the amplitude of an input light field can be modified using a precise setup to create a target light profile which can then be projected onto the atoms (Figure 1.1f). A typical DMD contains up to millions of these individually addressable mirrors with a pitch of about  $10.8\mu\text{m}$ , with fast refresh rates on the order of 20kHz [61]. Some of the patterns demonstrated with the DMD include the trapping of BECs in both discrete and continuous ring patterns (Figure 1.1g), as well as a checkerboard pattern [61, 62].

Amplitude modulation is necessarily a lossy and inefficient process as unused light is redirected away from the atoms. Spatial phase modulation of the input light field is an alternative method that can improve the efficiency. Most commonly, the phase modulation routine creates specific light profiles at the position of the atoms via diffraction and as such usually requires some computational modelling to figure out the best phase mask that will best reproduce the target optical potential. A device that can achieve this phase modulation is a spatial light modulator (SLM) (Figure 1.1i) operating in phase-only modulation. Amplitude modulation is also possible [63] (Figure 1.1j), in which case the SLM acts similar to the DMD and adjusts the intensity of an incoming light field. A typical SLM consists of an array of liquid crystal (LC) pixels that are birefringent - varying the orientation of the LC pixels modifies the refractive index and thus the amount of phase retardation imparted to the part of the light beam passing through a given pixel. Changing the orientation is achieved by applying a voltage to the pixel electrode at the back of the device using computer control. The result is a variable phase mask that can be applied to an incident laser beam.

SLM devices tend to suffer from slow refresh rates compared to AOD or DMD devices - faster models (based on ferroelectric liquid crystal materials) are capable of refresh rates in the kHz regime, but this comes at the cost of restricting oneself to binary phase modulation. Nematic liquid crystal devices only offer refresh rates around 10-100 Hz, but offer significantly more levels of phase modulation. Nematic LC devices, having the slower refresh rates, mean that dynamic manipulation of cold atoms is difficult for such low refresh rates - although there has been more progress recently for developing nematic LC SLMs with response times between 3-6ms (see e.g. Meadowlark). However, the ferroelectric version has been shown to be capable of dynamic manipulation of a BEC at rates of up to 1kHz [64] (Figure 1.1k). Additionally, various proposals exist for utilising an SLM to generate suitable optical traps for cold atom experiments, including microtrap arrays for single atoms [65, 66], an optical ferris wheel with MHz-frequency rotation [67], smooth ring traps for superfluidity studies [68], power-law traps for more efficient evaporative cooling [69] and the use of feedback to correct for aberrations in the generated optical traps [70].

The SLM therefore has the potential to play a pivotal role moving forward for the production and manipulation of ultracold atoms. As an example, a proposal towards the goal of ultracold atomic gas analogues of electronic circuits, or “atomtronics”, is the

creation of a ring trap for investigations of superfluidity using a single phase-only SLM [68]. The ring in this case is holographically generated and contains two bright spots of high intensity to perform the “stirring” action of inducing a rotation. Dynamically changing the phase pattern on the SLM such that the two spots rotate around the ring is proposed to induce superflow in the atoms - once achieved, the bright spots can be gradually eliminated, leaving a uniform ring. Such experiments could provide great progress in the realisation of the atomic-gas analogue of the DC superconducting quantum interference device (SQUID). A further example is a proposal for using the SLM as an alternative, efficient evaporation scheme towards quantum degeneracy [69]. Instead of performing the usual optical evaporation sequence in a focused optical dipole trap, which suffers from reduced trap frequencies during the evaporation sequence and therefore limiting the density, evaporation could be performed in a power-law trap of order 2 designed such that the elastic collision rate is kept constant, followed by adiabatically and reversibly reducing the trap order to 0.5 to cross the BEC transition point [71]. Another proposal of interest is a planned solid state system simulation of the topological Kondo effect with Majorana fermions. Topological quantum computing is a much sought after goal within condensed matter physics - by taking advantage of the topological nature of a system, topological qubits could provide more robustness against decoherence arising from interactions with the external environment. One such topological qubit is the Majorana-Coulomb box: a solid state system consisting of a central superconducting island with one-dimensional wires connected in a star-geometry, with Majorana fermions located at the ends of the wires. However, experimental realisation of such a complex solid state system has not been achieved to date. Recently, however, an analogous system which results in the same class of Hamiltonian has been proposed in [72] - using ultracold atoms that are confined to one-dimensional guides and with a junction or tunnelling barrier in the centre. Such a system is more immediately achievable compared to the experimental construction of the Majorana-Coulomb box itself, and therefore could provide a great deal of insight into the physics of the topological Kondo effect and, subsequently, for future progress towards topological quantum computing.

In conclusion, the SLM already shows promise as a device that is capable of generating arbitrary, smooth optical potentials for ultracold atomic experiments. As such, further developments regarding the level of control and versatility that can be exerted on the atoms through the use of an SLM is particularly appealing.

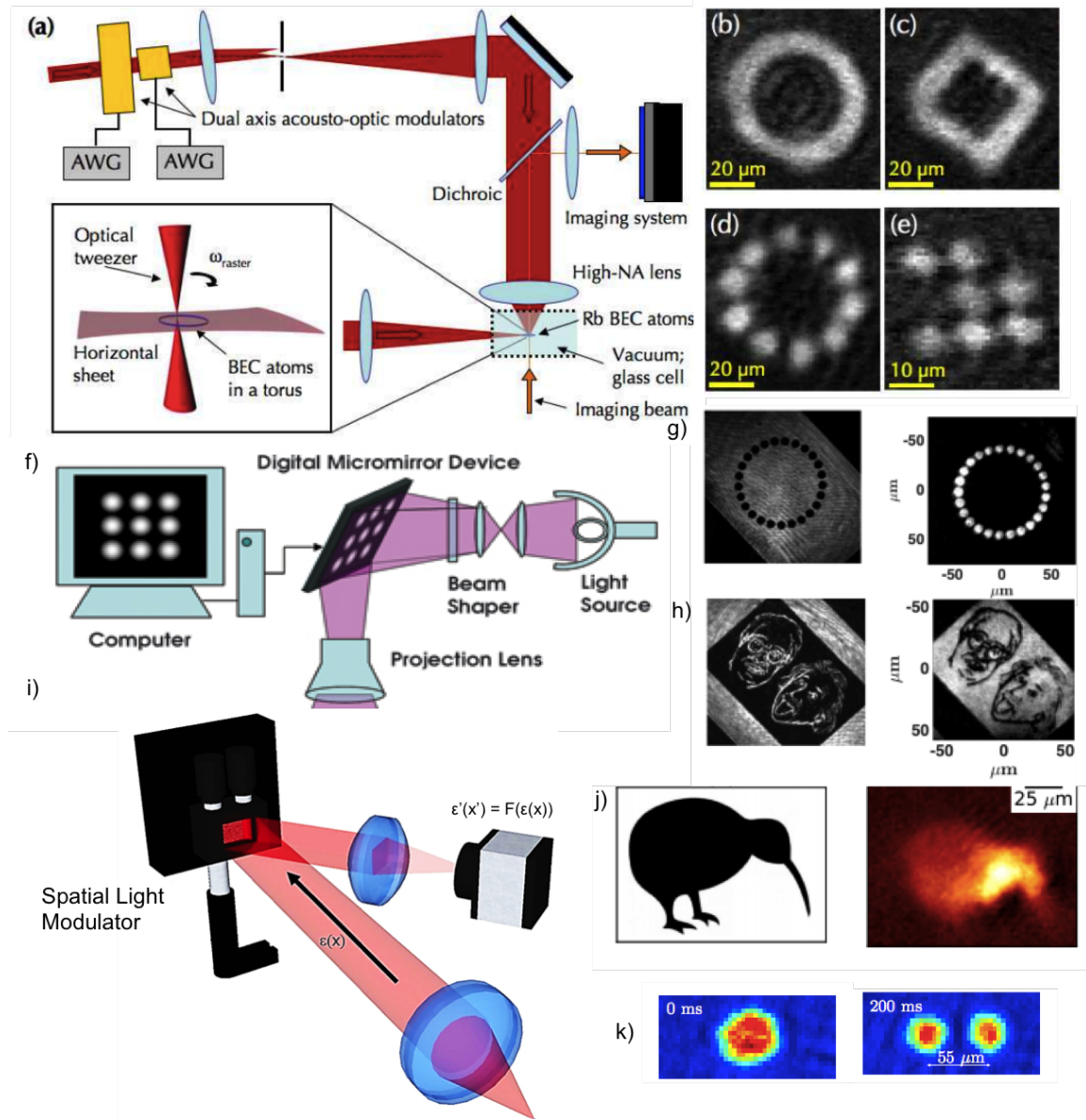


Figure 1.1: a) Experimental setup for a scanning laser beam created using an AOD; b)-e) Absorption images of atoms trapped using the painted potential of a torus, diamond, ring of ten spots, and a  $3 \times 3$  lattice with defects, respectively. Figures from [57]; f) A DMD operates by projecting an image of a desired trapping potential onto the atoms; g)-h) Projected light pattern (left) and atomic density (right) for ring lattice and artistic impressions of Bose and Einstein respectively [61]; i) An SLM modulates either the amplitude or phase of an incoming beam; j) Target profile (left) and atomic density (right) for a kiwi bird trapping potential using amplitude modulation of an SLM [63]; k) Splitting of a BEC using phase modulation of a ferroelectric SLM [64].

## 1.3 Compact Cold Atom Systems

Due to their complexity, it is hard to imagine the first groundbreaking experiments that used cold atoms as a tool for investigations of fundamental physics being turned into commercially available devices to be used by non-specialists. However, within the cold atoms community, there is an increasing emphasis on translating the major lab-based experiments on cold atoms into practical devices for sensing and metrology. The apparatus used for the production and manipulation of ultracold atoms therefore benefits from the miniaturisation and compactness that allows this to be possible, with emphasis on simplifying and reducing the size of cold atom setups. This has a major benefit not just for the real-world applications mentioned above, but also from a pedagogical viewpoint - being able to showcase the underlying principles of cold atom physics in an accessible way is useful for both undergraduate teaching and public engagement.

Currently, atom interferometers and atomic clocks are beginning to be available as integrated packages to be used either for industrial ground-based applications, but also as future instruments for precision measurements performed in space [73, 74]. One downside of earth-based cold atoms experiments is that gravity limits the maximum time-of-flight (TOF) of the clouds; knowing that the sensitivity of a sensor based on an atom interferometer increases with the square of the time the atoms spend in the interferometer [75], then the appeal of microgravity experiments is clear. Examples of experiments simulating the zero-g conditions of space are the creation of magneto-optically cooled atoms in microgravity using the drop tower in Bremen [76], the first BECs prepared in microgravity [77, 78], as well as plans for dual-species atom interferometers [79, 80] in such conditions.

Typical lab-based cold atoms experiments are often large and bulky (Figure 1.2a). The previously mentioned atom chip is an example of a compact technology that is capable of trapping and detecting ultracold atoms within an integrated package (Figure 1.2b). Atom chips allow for a fully integrated cold atoms experiment to be established in a portable package for applications such as clocks and magnetometers. Additionally, the realisation of the BEC using the atom chip opens up the realm of quantum behaviour in such setups. However, use of an atom chip is just one step towards fully integrated, cold atom technology - miniaturisation of the surrounding apparatus, including the vacuum system, pumps, and laser optics, is essential, and much emphasis is on manufacturing completely scaled-down systems [81].

The necessary laser cooling stage of a cold atoms experiment is one area in which miniaturisation would benefit - being able to produce a cloud of laser cooled atoms without the somewhat bulky six-beam laser setup (Figure 1.2c) would be very beneficial. In this regard, there has been a great deal of advances that offer this. One of these, a pyramidal MOT, produces the necessary cooling beams from a pyramidal reflector [82, 83, 84] and offers the advantage of creating a cooling volume from just a single circularly-polarised input laser beam, significantly simplifying the total optics and alignment needed (Figure 1.2d). Pyramidal reflectors have been integrated into the atom chip [84, 86]; however, the

number of atoms captured and cooled is less than  $7 \times 10^3$ , which is much too low a number to continue towards quantum degenerate effects. Additionally, in such setups the atom cloud is hard to access as it is trapped below the chip surface. A tetrahedral geometry can help to alleviate the negative features of the pyramidal MOT [87].

An alternative technique to produce an optical molasses from just a single input beam is through the use of diffraction gratings. Such a microfabricated chip has a diffraction pattern etched onto the surface and forms a cooling volume from the overlap of the initial input beam with the diffracted orders (Figure 1.2e). Usually referred to as the grating MOT or GMOT [88, 89, 90, 91, 92], as many as  $6 \times 10^7$  atoms can be captured and cooled using the balanced radiation pressure between the input beam and the diffracted orders generated from the grating surface. Such an integrated and compact setup offers a wide range of applications for quantum sensing and metrology due to its drastically reduced spatial scale and alignment requirements compared to a six-beam MOT.

Another aspect of laser cooling that often contributes to a larger scale apparatus is that the alkali atoms necessarily require two laser frequencies for the cooling and repumping processes to address the two hyperfine ground states (which have a large separation of multiple GHz). The use of a second laser to pump atoms back into the cooling cycle is commonplace in many labs, but for a more compact setup the additional alignment, optics and electronics tends to add to the overall bulk and expense of the apparatus. As such, techniques to modify the laser output such that both the cooling and repumper roles can be accomplished using just a single laser are very appealing. Fortunately, the amount of laser power needed to perform the repumping role is usually very low (at least for atoms such as Rb and Cs), often only a small percentage of the total laser cooling power. An alternative then is to induce sidebands on the single cooling laser at the frequency needed for repumping, either through direct modulation of the laser current in a laser diode [93, 94] or using an external modulator [95, 96] for direct imprinting of frequency sidebands, producing a cloud of cold atoms in a compact and inexpensive manner.

Other methods of stabilising the laser frequency to an atomic transition could prove valuable when performing cold atoms experiments outside of a controlled lab environment. The standard saturated absorption spectroscopy lock is a relatively simple and popular method in many labs, but other techniques may prove more advantageous outside the lab. Other laser locking techniques include the dichroic atomic vapour laser lock (DAVLL) [97, 98, 99], frequency modulation spectroscopy [100] or modulation transfer spectroscopy [101, 102, 103]. A more unique method is harnessing the speckle pattern originating from the numerous scattering and interference effects from light propagating in a disordered medium [104]. Capable of stabilizing an external cavity diode laser to provide a narrow linewidth output below 1MHz, this technique also has the advantage of not relying on the atomic spectroscopy itself for locking, as well as the capability to lock at any desired wavelength.

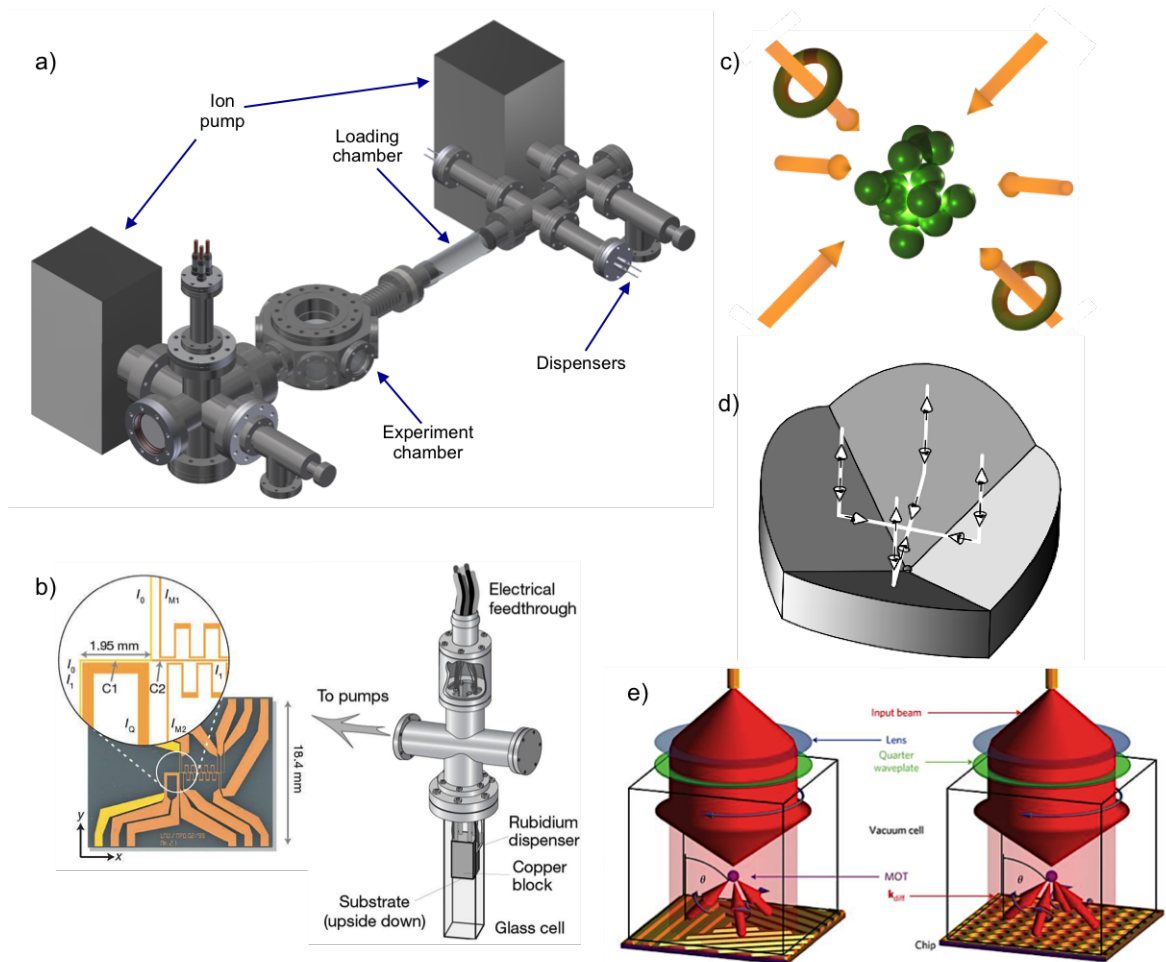


Figure 1.2: a) Model of a full-scale double vacuum chamber cold atoms experiment, including loading and experiment chambers, pumps and dispensers; b) Atom chips offer the trapping and cooling of an atomic ensemble in a significantly more compact setup [38]; c) The standard six-beam MOT is often bulky and covers a large spatial area; d) The pyramidal MOT is an example of a compact laser cooling scheme which forms an optical molasses from a single input beam [85]; e) A more recent example of compact laser cooling is the grating chip MOT or GMOT [88].

With the recent emphasis on quantum technologies it is only natural to create exposure to both undergraduate students and the general public about the physics that underpins such experiments. The ability to take a transportable apparatus outside of the lab and display it at outreach events acts as an introduction to the physics for a new generation to potentially generate interest, as well as exemplifying the exciting principles that leads

to the creation of a cloud of atoms with a temperature that is a fraction of a degree above absolute zero. Additionally, a cold atoms experiment that is available to undergraduate students in the teaching lab helps to reinforce the quantum physics ideas that are a large part of many lecture programs. Such a practical experience consisting of aligning laser beams, searching for spectroscopy signals and acquiring some quantifiable data about the MOT is again good exposure to have at any stage of an undergraduate degree and gives a valuable insight into what experimental cold atoms physics is like.

## 1.4 Thesis Outline

The remainder of this thesis is outlined as follows. Chapter 2 details the design and construction of a compact, robust cold atoms apparatus for teaching and outreach. With much demand placed on creating portable cold atom sensing devices, this project was constructed to enable the demonstration of some of the underlying principles of the MOT in an accessible learning environment for students and the general public alike. The vacuum chamber construction and bakeout was done collaboratively with Andrew Morgan, an MPhys student who worked on the portable MOT as part of his project. The outreach demonstrations were done in collaboration with Dr Paul Griffin of the University of Strathclyde. Setup and optimisation of the MOT as a teaching lab experiment, including the DAVLL setup and integration of the sidebands electronics, was primarily work carried out by myself.

Chapter 3 describes our experimental work in creating the first BECs seen at St Andrews using a double vacuum chamber design. This work was carried out in collaboration with Dr David Bowman and Dr Graham Bruce. My own contribution primarily focused on the integration of the computer control of the experiment with Labview, improvement of the MOT, radio-frequency evaporation and optical trap transfer stages, and optimisation of the phase-space density of the atomic cloud near the BEC transition temperature.

Chapter 4 contains two parts - the first half describes the methods by which phase-only SLMs are used to produce holographic optical potentials suitable for cold atom trapping, while the second half describes the experimental results of loading cold atoms into a variety of flexible geometries with applications to quantum simulation and atomtronics in mind. For the multi-wavelength holography work, my contribution involved optimisation of the Matlab codes for individual wavelengths of light, including work improving a feedback mechanism that aims to improve the experimental light outputs. For the high fidelity phase and amplitude light profiles based on conjugate gradient minimisation, my focus was on the choice of cost function and how it can be appropriately modified to include the phase of the light. Experimentally, the trapping of cold atoms using holographic optical traps in combination with the light sheet was achieved primarily by myself.

Chapter 5 summaries the main results and looks to the near-future steps that are planned for both the compact MOT setup and the main holographic trap experiment.

## Chapter 2

# Construction of a Compact, Portable MOT for Outreach and Teaching

### 2.1 Motivation

With such an emphasis on miniaturising atomic metrology and sensing setups, fully integrated devices are naturally incentivised. With this view in mind, we have designed and built a compact, portable MOT apparatus with the intention of demonstrating cold atom trapping at various outreach events and as part of an undergraduate laboratory experiment. While the setup we have built is not fully integrated, it serves as a simple, affordable and easy to transport apparatus that has been used both for public engagement and as part of the school's teaching program. The main experimental components fit onto two individual breadboards measuring roughly  $45 \times 45$  cm, with the vacuum chamber being one of the most compact setups possible that can be constructed out of commercially available components. One advantage of the fact that this setup is not fully integrated into a readily-deployable device is that, from a pedagogical viewpoint, the lack of integration offers more benefits to both the general public and to students in that they are more able to visualise the underlying physical principles of the operation of the MOT.

In this chapter, we report on the details towards building this compact, portable MOT, the public engagement events we attended demonstrating this apparatus, and the future ideas that are planned to be implemented.

### 2.2 Vacuum Chamber Design and Build

Efficient laser cooling of an atomic gas requires complete isolation from any possible sources of heating that would counteract the cooling process. For this reason, the portable MOT

requires a high vacuum chamber to be built, which reduces collisions with background gases that would lower the MOT lifetime. Our vacuum system is designed around a Pyrex glass cell, measuring  $70 \times 22 \times 22$  mm (with 3mm wall thickness) to allow for good optical access whilst still resulting in a compact apparatus. The glass cell is connected via a conflat (CF40) flange, with M6 screw holes, to the remainder of the vacuum chamber apparatus (Figure 2.1), which is based around a stainless steel cube of side length 7cm. Each face of the cube has a CF compatible vacuum flange, onto which the remaining components are attached, consisting of two rubidium dispensing getters, a Gamma Vacuums 3S-DI ion pump and a valve connection that is used when performing the bakeout procedure and is closed shut otherwise. The rubidium dispensers (SAES) are located below the joining “tee” structure in this setup - when a current is passed through the electrical feedthroughs located outside and underneath the vacuum chamber, gaseous rubidium is released into the vacuum to be captured by the MOT. Once the bakeout procedure has reduced the pressure substantially, the ion pump is turned on and remains on, which maintains the vacuum in the chamber (usually at around  $10^{-7}$ mbar).

To achieve the necessary low pressure in our vacuum system, the following steps were taken:

- cleaning the main components involved,
- building the chamber,
- connecting the turbo pump and performing a bakeout,
- degassing the dispensers,
- initialising the ion pump,
- reducing the temperature, disconnecting the turbo pump and shutting off the closing valve to maintain the vacuum.

All components used in the setup are first cleaned with isopropanol to avoid any contamination, after which the vacuum chamber system is put together. The turbo pump is connected via the valve shown in Figure 2.1, and is used as the initial pumping-out mechanism. This pumping out procedure is performed at high temperatures to ensure substances are released from the walls of the interior of the chamber. To achieve the high temperatures necessary in the bakeout procedure, the entire apparatus in Figure 2.1 is wrapped in resistive tape heaters and covered in tin foil to keep the heat in. Variacs were used to slowly increase the temperature of the apparatus, ensuring roughly uniform heat distribution, until the temperature reached approximately  $200^\circ\text{C}$  (monitored using thermocouples placed at various point of the apparatus). As the chamber was kept at this temperature the turbo pump pumped out the chamber - this process lasted about 12 full days, and the pressure was monitored using an ion gauge. During the bakeout procedure, the rubidium

dispensers were turned on at a current of roughly 3A in order to degas the dispensers into the chamber during the bakeout.

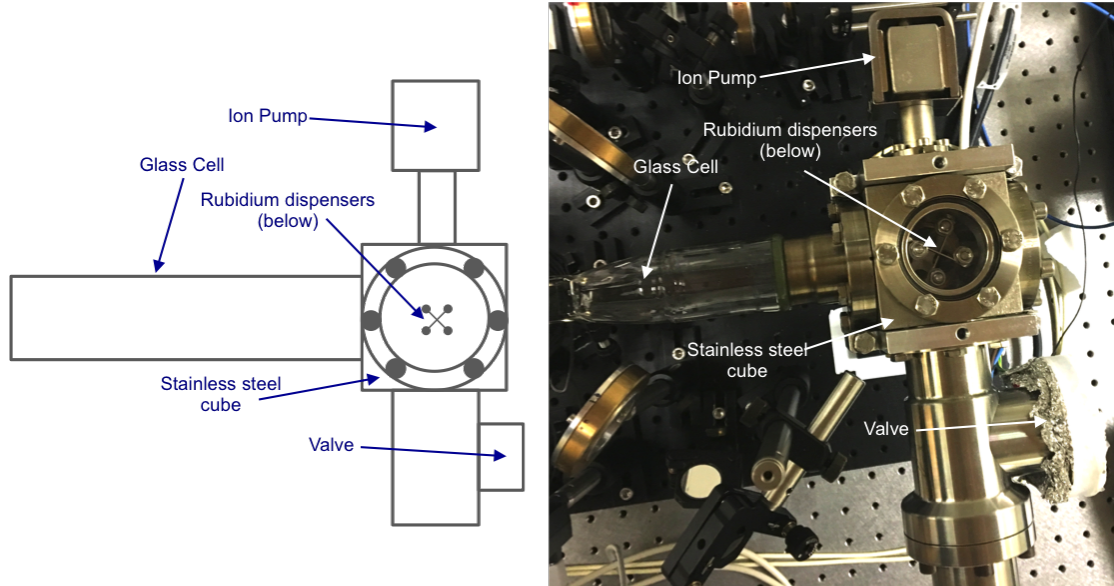


Figure 2.1: Top-down drawing and photograph of the compact vacuum chamber used for the portable MOT experiment. The rubidium dispensers are located at the bottom of the apparatus and they are visible through the viewport placed at the top. The photograph taken here of the chamber is after the various optics for the MOT are in place.

After the pressure was measured to drop to around  $5 \times 10^{-8}$  mbar, the temperature was slowly reduced over the next couple of days to bring the chamber back down to room temperature, after which the foil and resistive tape heaters are removed. After the valve is closed to seal the vacuum, the turbo pump is turned off and removed and the ion pump remains on from this point to maintain the vacuum. The Gamma Vacuums ion pump chosen for the portable MOT has a controller with a display that can be used to monitor the pressure to ensure the chamber is not flooded with rubidium.

## 2.3 Laser System

The portable MOT is designed for the trapping and cooling of  $^{85}\text{Rb}$ . Laser cooling is performed by cycling atoms on a specific transition, which for  $^{85}\text{Rb}$  is the D2 line depicted in Figure 2.2; specifically, the cooling process cycles atoms between the  $F=3$  hyperfine ground state and the  $F'=4$  hyperfine excited state of the D2 line.

The D2 line has a transition wavelength at 780nm, meaning semiconductor laser diodes are readily available as a device for laser cooling. Unfortunately, the linewidth of such a

laser if used on its own far exceeds the natural linewidth of the  $^{85}\text{Rb}$  D2 line (which is roughly  $2\pi \times 6.1$  MHz) - this broad linewidth would result in other, unwanted excitations being stimulated. We therefore use an external cavity diode laser (ECDL), capable of producing laser light with a linewidth of less than 1MHz, which is much more suitable for this application. A piezo-electric transducer is also placed at one end of the cavity - applying a voltage to the piezo element causes an extension which changes the cavity length and therefore the output laser frequency. Rapidly scanning the cavity length, and therefore the output laser frequency, is essential for the spectroscopy processes described later.

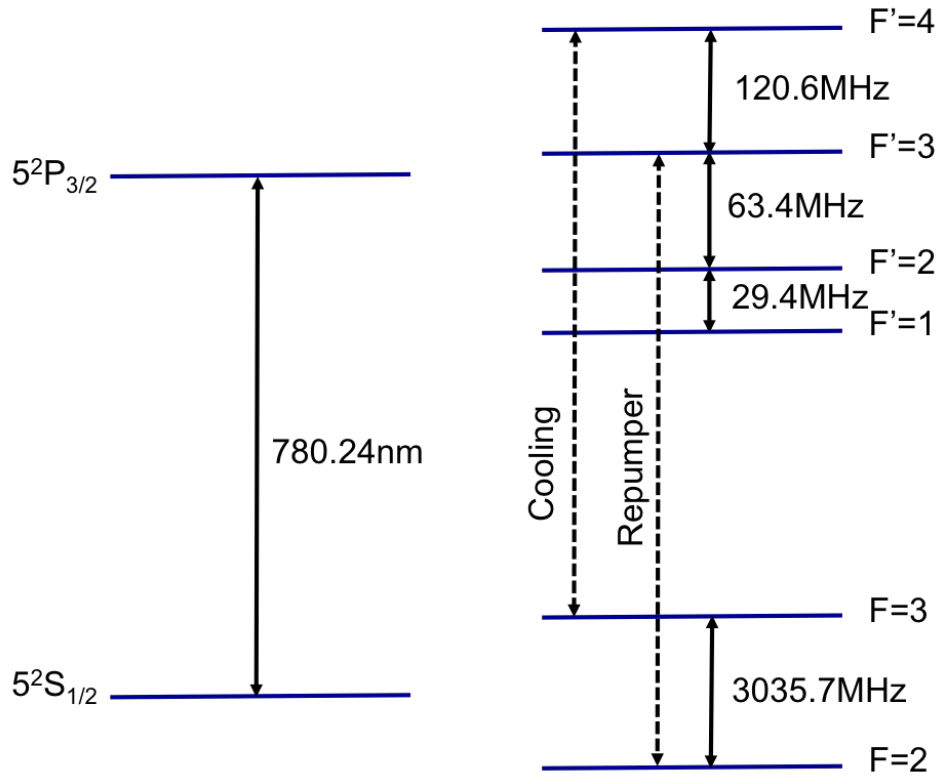


Figure 2.2:  $^{85}\text{Rb}$  D2 Line, showing the cooling and repumper transitions and the approximate hyperfine spacings.

The laser mount itself is a TUI DL100 mount previously used as part of the school's undergraduate laboratory program. The laser diode is a Thorlabs LD 785 diode, capable of producing up to 45mW of optical power. An optical isolator placed at the output of the laser prevents optical feedback back into the laser diode.

The hyperfine transitions of the D2 line are probed using saturated absorption spec-

troscopy. Frequency stabilisation of the laser is necessary in order to keep the laser resonant with the cooling transition, which therefore requires locking the laser frequency to a specific hyperfine transition. Saturated absorption spectroscopy is used as part of the locking process for the portable MOT in order to identify the individual hyperfine transitions. A simple absorption spectroscopy signal, with just a single probe beam shone through an atomic vapour in a glass cell and using the piezo to create a rapid scan of the output laser frequency, shows an extremely broad Doppler absorption profile due to the thermal motion of the atoms causing absorption of the probe beam to occur over a wide range of frequencies. The saturated absorption spectroscopy technique improves on this by using a second, weak probe beam of the same frequency and counter-propagating to a strong pump beam. The strong pump beam saturates the transition for the set of atoms it interacts with. The secondary probe beam, travelling in the opposite direction, will interact with the same set of atoms only if their velocity vectors are orthogonal to the beam propagation i.e. those atoms in which no Doppler effect is present. Since the transitions have been saturated by the strong pump beam, there will therefore be less absorption recorded at the transition frequencies, which correspondingly show up as narrow peaks appearing on top of the underlying Doppler broadened spectrum (Figure 2.3).

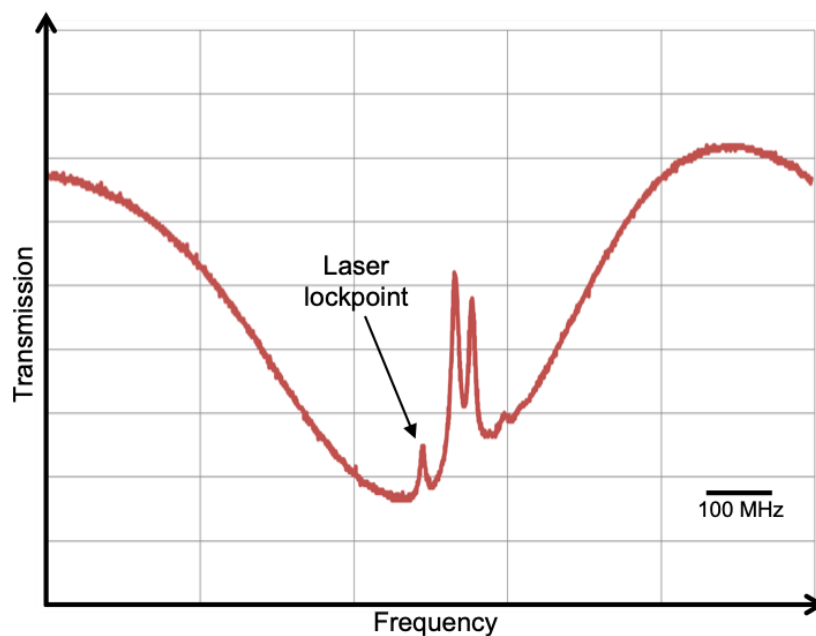


Figure 2.3: Saturated absorption spectrum of the  $^{85}\text{Rb}$  cooling transition, indicating the transition lockpoint used in the experiment. The absorption spectrum shows both the real hyperfine transitions and also the crossover transitions.

Two different types of narrow transmission peaks can be seen on the trace of Figure 2.3. The first type is that of the real hyperfine transition, such as the leftmost peak in Figure 2.3. This peak corresponds to the transition between the  $F=3$  hyperfine ground state and the  $F'=4$  hyperfine excited state in Figure 2.2, and it is this peak that is used as our reference point when we wish to lock our laser frequency (see section 2.4). In this case, both the strong pump beam and weaker probe beam are resonant with this particular transition and address atoms whose motion is perpendicular to the laser beam propagation. The second type of peak is what is known as a crossover transition, which for example corresponds to the (larger) peak just to the right of the lockpoint in Figure 2.3. A crossover transition is not a real hyperfine transition of the atom, but rather occurs when the laser frequency ends up exactly halfway between two real transitions. For example, for the aforementioned crossover peak, it is a result of the laser frequency lying halfway between the  $F=3$  to  $F'=4$  transition and the  $F=3$  to  $F'=3$  transition. When this happens, there exists a velocity class for which the pump beam is resonant with one of the transitions, and the probe beam is resonant with the other. Since the ground state population is depleted because of the pump beam saturation, a reduction in the absorption of the light is still detected even though it is not indicative of a real hyperfine transition. Additionally, since this scenario affects two atomic velocity classes, the ground state population is even more depleted compared to a real hyperfine transition, which is why crossover transitions typically have greater transmission compared to the real transitions.

In the majority of lab environments, when wanting to lock the laser to a specific transition, the signal (such as that seen in Figure 2.3) can be differentiated to obtain an error signal that can then be used to lock the laser. The error signal obtained in this way, however, typically has a rather small recapture range (tens of MHz), which gives adequate stability in a controlled lab environment but may struggle if the portable MOT is being used for outreach where more significant perturbations may be present. For this reason, we have chosen to set up an alternative method of locking the laser that is more robust and stable in an external environment.

## 2.4 Dichroic Atomic Vapour Laser Locking

To produce a more stable laser lock, we use the Dichroic Atomic Vapour Laser Lock (DAVLL) system [97]. The optical setup for the dichroic atomic vapour laser lock is shown in Figure 2.4. It works by utilising the Zeeman shift of the atomic sub-levels when a glass cell with rubidium vapour is placed in a weak (about 100G) longitudinal magnetic field - the resulting magnetic field lifts the degeneracy of the Zeeman sub-levels.

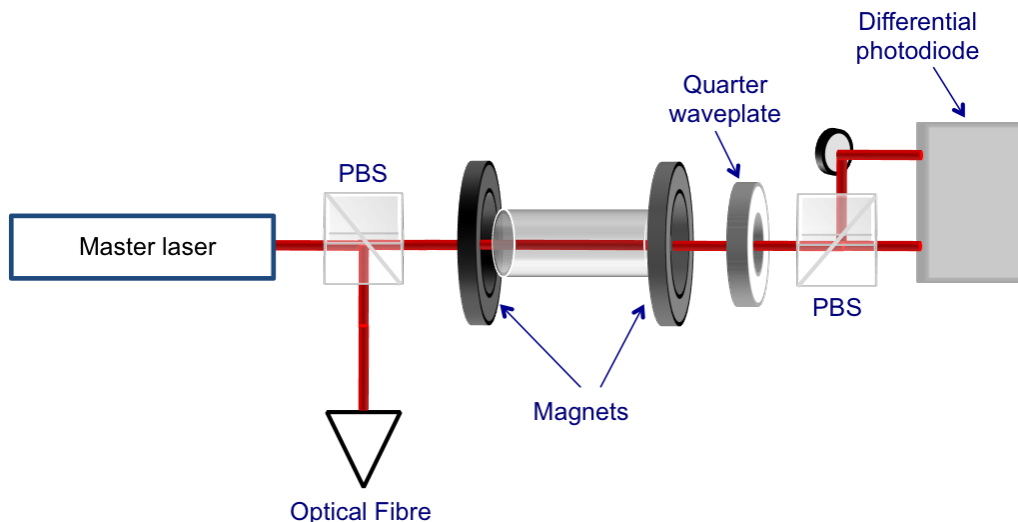


Figure 2.4: Setup used for the DAVLL mechanism. A small amount of power is split off for the spectroscopy. The glass cell containing rubidium vapour is placed in a longitudinal magnetic field, which we create using two permanent ring-shaped magnets. The differential photodiode subtracts one signal from the other and outputs this to the scope.

Linearly polarised light, which can be thought of as consisting of an equal superposition of right and left circularly polarised light, is then incident on the cell. Selection rules govern that the right and left circularly polarised light stimulate different transitions, with  $\sigma^+$  light stimulating a transition that results in an  $m_F$  change of +1, while  $\sigma^-$  light stimulates a transition that results in an  $m_F$  change of -1. This means that the usual Doppler-broadened absorption spectrum recorded with a photodiode will shift to higher and lower central frequencies for right and left circularly polarised light respectively compared to the Doppler-broadened absorption spectrum seen without any magnetic field present.

To accomplish this, we use two ring-shaped permanent magnets placed either side of the glass cell. This results in a longitudinal magnetic field measured to be  $\sim 120\text{G}$ . Pure linear polarisation is achieved using a PBS, and the individual circular polarisations are separated by using a quarter waveplate and PBS placed after the glass cell. A differential photodiode is then used to subtract one signal from the other which generates the antisymmetric error signal. The absorption profiles taken using our DAVLL setup are shown in Figure 2.5. Each port of the differential photodiode can be blocked in order to obtain the absorption profile corresponding to one circular polarisation and then the other; when both ports are unblocked, the difference signal is obtained.

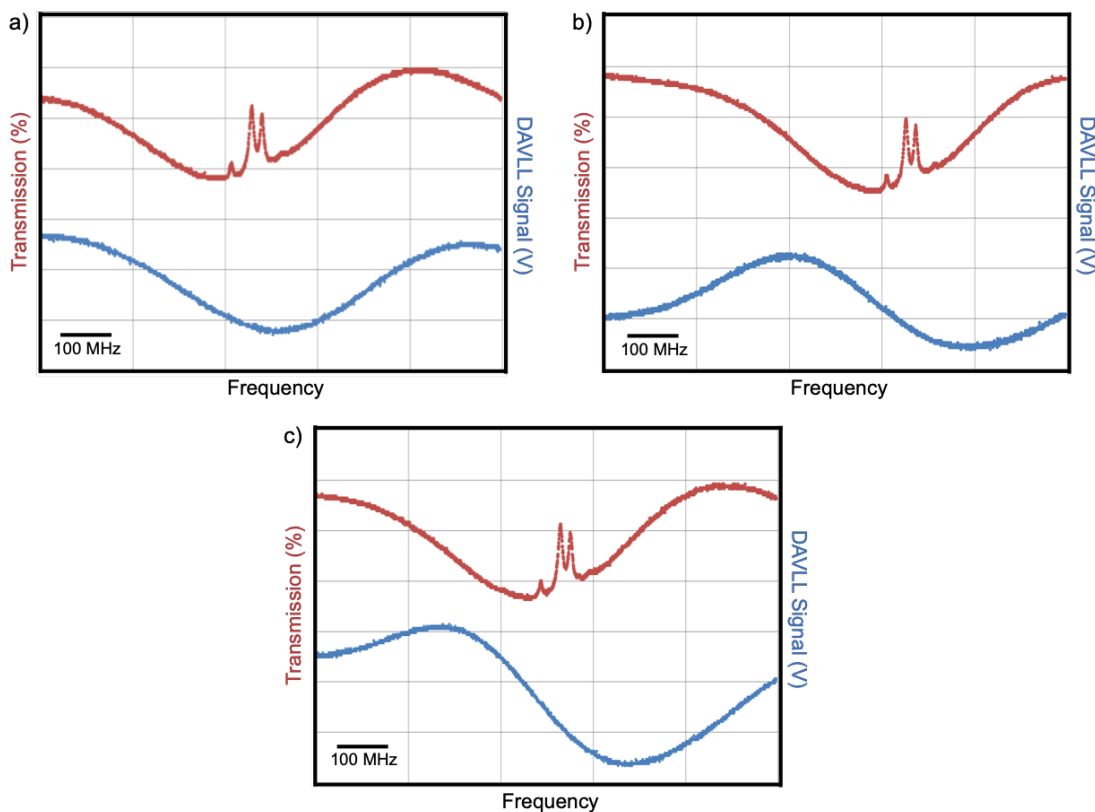


Figure 2.5: Plots showing the origin of the DAVLL signal for the  $^{85}\text{Rb}$   $F=3 \rightarrow F'$  transitions (red trace in each plot is the saturated absorption spectrum for the aforementioned transition). The absorption profiles for the DAVLL signals are the blue traces, showing the absorption profile in the presence of a weak longitudinal magnetic field for (a)  $\sigma^+$  light, (b)  $\sigma^-$  light and (c) the resulting error signal obtained from subtraction of the two profiles. The absorption profile in (b) has the inversion built into the differential photodiode, which is why the signal is inverted. The error signal in (c) has a zero crossing at the position of the cooling transition.

The current supplied to the laser diode, the temperature of the diode and the ramp generator for the piezo element all have separate panels that are powered off a main rack which is part of the TUI DL100 laser system (Toptica DL100 Supply Rack DC 110). The rack has additional spaces which allows additional panels to be added and powered as well, which is what we make use of when it comes to locking the laser with the error signal obtained from the differential photodiode. Our panel is designed to take the differential photodiode signal as an input, as well as the voltage ramp that is output from the ramp generator panel. An error signal is created which can be monitored on the scope and used

as a lockpoint at the corresponding peak on the saturated absorption spectrum. The user can also apply either an electronic offset to the error signal (giving freedom to tune the laser lockpoint) or increase the gain value to amplify the slope if required. The resulting voltage output is then fed into the piezo in the laser cavity which, when locked using the lock switch on the panel, keeps the laser stabilised to the desired frequency.

A sketch of the simplified DAVLL circuit we have built to lock the laser is shown in Figure 2.6. Instead of a standard proportional-integral-derivative (PID) regulator circuit, we simply set up a proportional error correction circuit to account for slow drifts of the laser frequency. In this way, the various op-amps in the circuit are used to modify the original error signal arising from the differential photodiode with either an electronic offset, a variable gain, an inversion factor, or some combination. The final op-amp is used as the lock-switch to send the voltage feedback into the piezo if locking is required.

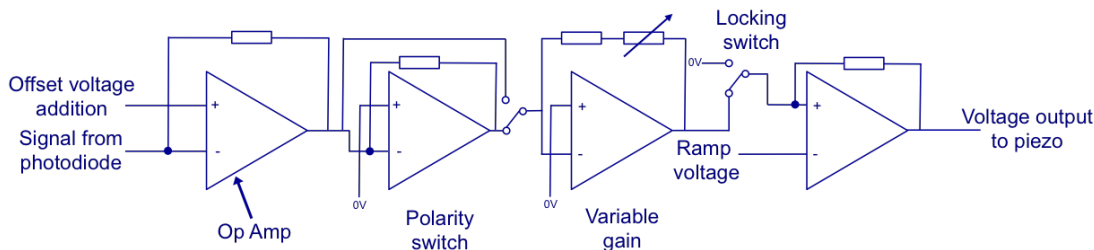


Figure 2.6: Simplified circuit diagram describing the proportional procedure of the locking circuit electronics designed for the portable MOT.

Due to the broad recapture range (hundreds of MHz) afforded by the antisymmetric error signal generated this way, this lock mechanism rarely loses lock [97]. However, we encountered a potential problem with our setup when looking to stabilise the MOT after applying the sidebands generation (more details in section 2.5) - the temperature stabilisation setup for the Toptica DL100 does not use a thermistor but instead an AD590 integrated circuit temperature transducer. We discovered that the microwave radiation causes a false temperature reading to be detected (if the diode laser is stabilised to e.g. 21°C before the microwave radiation is turned on, turning on the sidebands would cause the reading to drop to around 18°C, and therefore cause the circuit to work very hard to try to correct for this, even though the actual temperature had not changed). For this reason, due to these significant temperature changes constantly affecting the output laser frequency, we had to work without the temperature stabilisation feedback for the laser diode. Despite this, the DAVLL lock was still capable of stabilising the laser frequency sufficiently for data to be taken for teaching lab purposes, but without the long-term locking that should be possible with a properly stabilised temperature. In the future, we plan to replace the AD590 circuitry with a thermistor, which we have tested to ensure no adverse effect on the temperature reading is seen when the microwave electronics are turned on.

## 2.5 Sidebands Generation

To simplify the total optical setup further and remove the need for a second laser to act as the repumper for the cooling cycle, we employ homemade sideband generation electronics to couple with the existing laser spectrum, thereby providing a small fraction of power at the repumper transition. The advantage of employing sideband generation is removing the need to set up and align a second laser onto the existing setup as the sidebands can be generated at a frequency of 3GHz (which is roughly the ground state splitting of the D2 level of  $^{85}\text{Rb}$ , see Figure 2.2).

To generate the sidebands, we use an electronic circuit to provide a voltage input to a voltage controlled oscillator (VCO, MiniCircuits ZX95-3050C-S+) - variation of the input tuning voltage is used to alter the oscillation frequency over a range of 2856-3050 MHz. The amplitude of the microwave frequency signal at the output of the VCO is quite small, so we use an amplifier (MiniCircuits ZRL-3500+) to amplify the signal (to give a total power of +22dBm). Finally, we use a bias-tee (MiniCircuits ZFBT-352-FT+) to combine the generated microwave signal with the DC component of the laser (see Figure 2.7). Applying the modulation signal to the DC laser current results in sidebands forming in the following way.

The current modulation causes a modulation of the refractive index of the laser medium, hence a phase in the output field which is also modulated:

$$Ae^{i\omega_1 t + i\alpha \sin(\omega_2 t)}. \quad (2.1)$$

In the above equation,  $\omega_1$  is the laser output frequency (chosen to be the cooling transition seen before) and  $\omega_2$  is the generated microwave frequency. Since the amplitude  $\alpha$  is small, then the above exponential can be Taylor-expanded (only up to the first-order terms) to give:

$$Ae^{i\omega_1 t} (1 + i\alpha \sin(\omega_2 t)). \quad (2.2)$$

The sine function can then be expressed as the following:

$$Ae^{i\omega_1 t} \left(1 + \frac{\alpha}{2} (e^{i\omega_2 t} - e^{-i\omega_2 t})\right) \quad (2.3)$$

$$= A(e^{i\omega_1 t} + \frac{\alpha}{2} (e^{i(\omega_1 + \omega_2)t} - e^{i(\omega_1 - \omega_2)t})). \quad (2.4)$$

The above can be interpreted as the original laser signal at frequency  $\omega_1$ , plus the creation of two small-amplitude sidebands at frequencies  $\omega_1 + \omega_2$  and  $\omega_1 - \omega_2$ . A simplified diagram of the electronics setup for our sideband generation is shown in Figure 2.7.

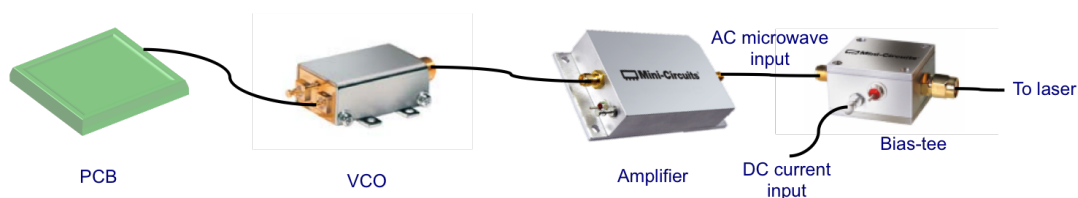


Figure 2.7: Simplified setup used for the sidebands generation in the portable MOT experiment. The PCB is a homemade circuit providing a tuning voltage to the input of the VCO. The output of the bias-tee is connected to the laser input.

To test for the presence of sidebands, we use a Fabry-Perot interferometer to perform high-resolution analysis of the laser output. To set up the Fabry-Perot interferometer, we split off a small fraction of power using a flip-mirror mount and direct the light into the Fabry-Perot. After optimising the alignment into the Fabry-Perot without the sidebands and observing the strong peaks at the free spectral range (FSR) separation, we turned the sidebands on and observed the presence of first-order sideband generation, as well as some smaller second-order sideband generation as well (see Figure 2.8). The amplitude of the sidebands seen in Figure 2.8 means we estimate that roughly 15% of the total optical power can be generated for the repumper role in this setup, which from the 45mW initial output power results in about 6.75mW repumper power available.

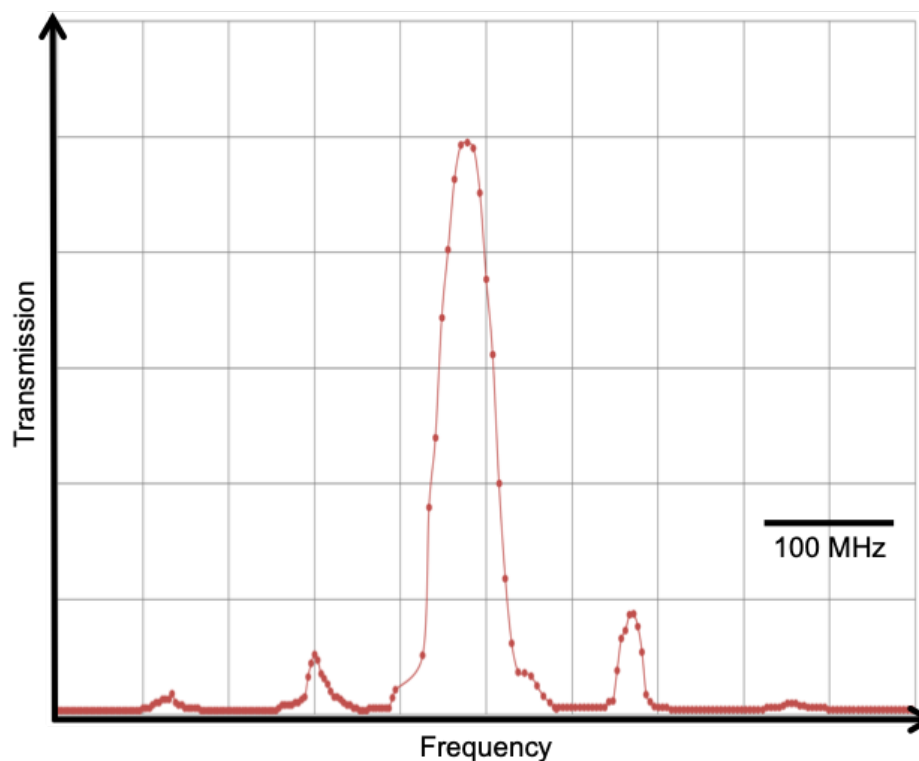


Figure 2.8: Plot showing the output from the Fabry-Perot when the sideband electronics is switched on and indicating the presence of the low amplitude sidebands appearing either side of the main carrier signal. When zooming in, the second order sideband generation can be seen.

## 2.6 Optical Setup

The total optical setup for the portable MOT is split over two breadboards - one breadboard houses the laser, saturated absorption spectroscopy setup, DAVLL spectroscopy setup, and the input to the optical fibre (plus the Fabry-Perot setup if it is needed), shown in Figure 2.9. The electronics used for the sideband generation, which connects to the laser, sits off to the side of the breadboard and can be disconnected from the laser if the setup has to be moved. To make moving the setup easier we house the microwave electronics (everything in Figure 2.7) in a stainless steel casing - connectors attached to the casing allow the electronics box to be disconnected from the laser if needed. The fibre output coupler is then placed on a second breadboard, and it is on this breadboard that the vacuum chamber is placed. Here, the beam is split into three beams of equal power and directed through the glass cell towards retro-reflecting mirrors placed on the other side (Figure 2.10).

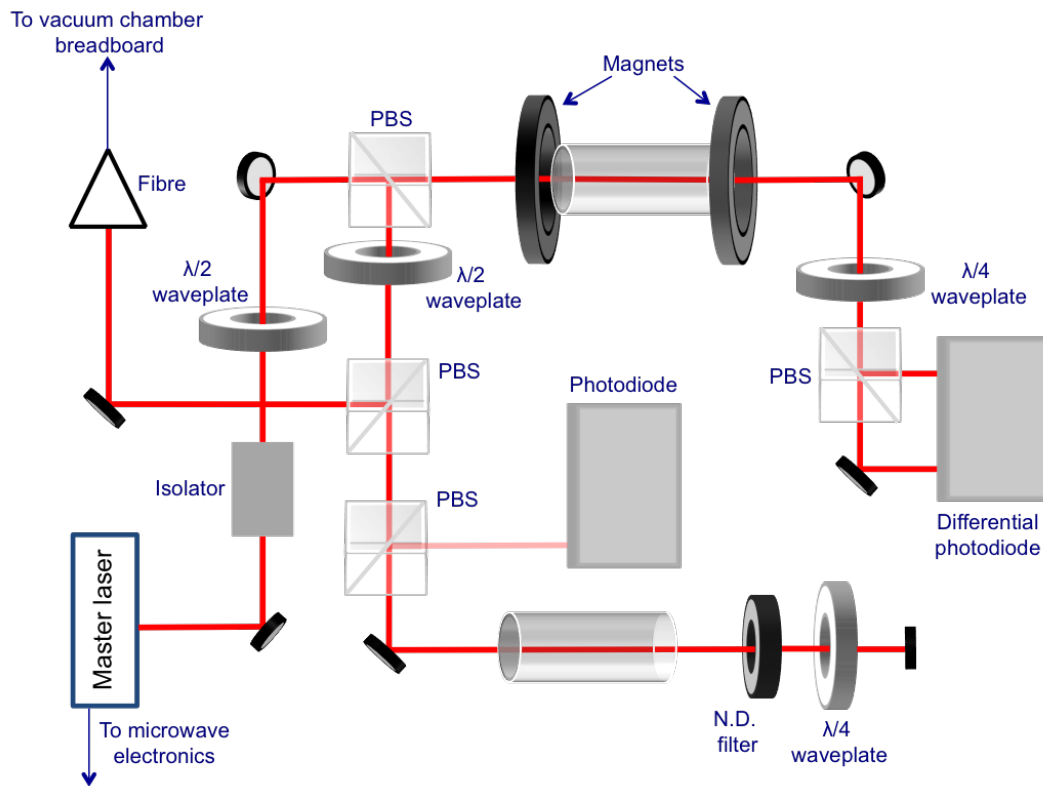


Figure 2.9: Compact setup of the optics breadboard used in the portable MOT experiment. The optics breadboard houses the laser system and both spectroscopy techniques. Most of the optical power is directed into the optical fibre that transports the light to the vacuum chamber breadboard; a small amount is reserved for each of the spectroscopy paths.

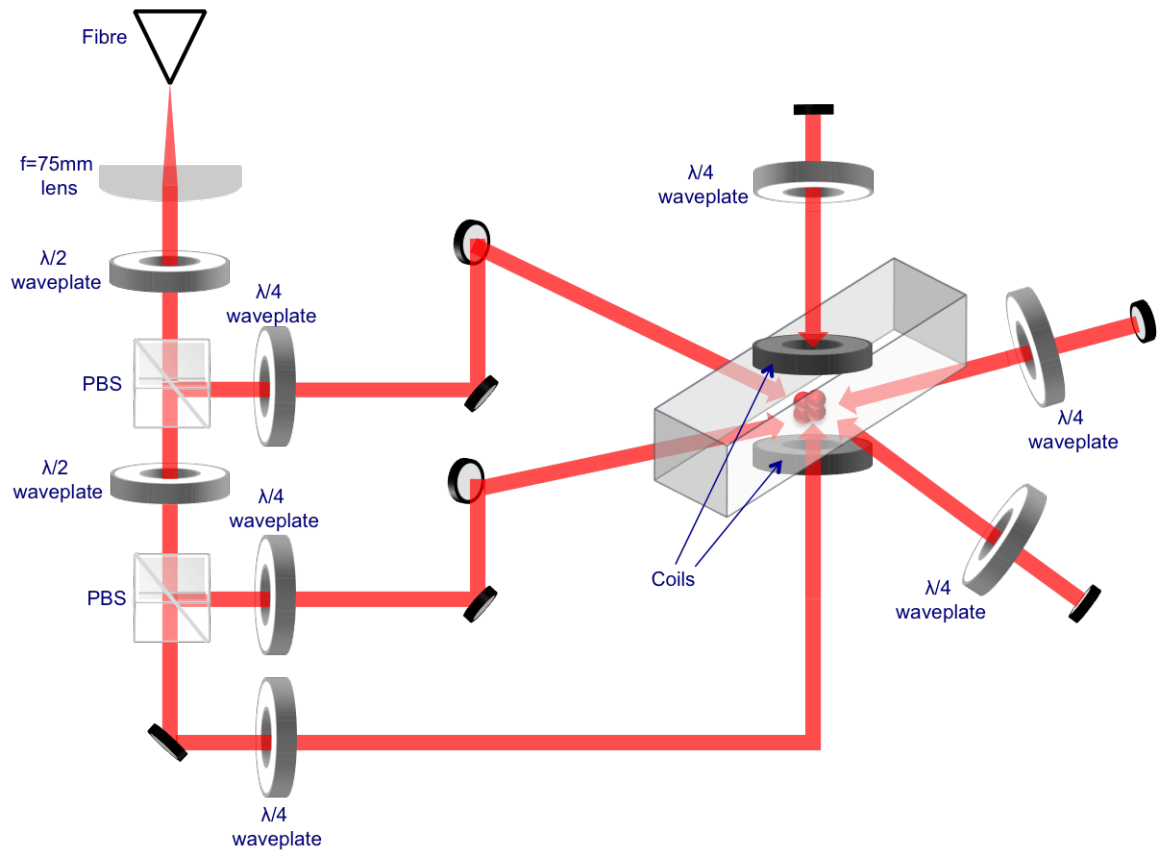


Figure 2.10: Optical setup of the vacuum chamber breadboard used in the portable MOT experiment. Only the glass cell of the vacuum chamber is shown for clarity. The six-beam MOT is created using retro-reflections of the three input beams. Around 21mW of power is measured at the output of the optical fibre.

Our magnetic field gradient for the MOT is generated using two pairs of current-carrying coils in the anti-Helmholtz configuration - the coils have 45 turns each, have a radius of 3cm and have a separation of 5cm when placed above and below the glass cell (see Figure 2.10). The resulting magnetic field gradient is roughly  $4.21\text{Gcm}^{-1}\text{A}^{-1}$  - we run 4.5A through the coils to generate a field gradient of roughly  $19\text{Gcm}^{-1}$  for the experiment.

## 2.7 Measurements

With the viewpoint that the portable MOT setup is suitable for use as an undergraduate teaching lab experiment, below we list a couple of simple measurements that a student can undertake in the timeframe of a couple of afternoons (the standard format of our 4th year

teaching lab experiments). Some future ideas regarding further planned experiments are mentioned in the final section.

### 2.7.1 Measuring the Atom Number in the MOT

When the portable MOT is used as an undergraduate teaching lab experiment, one of the first measurements that can be made by the students is an estimation of the total number of atoms in the MOT after some experience of aligning the various beams. This allows the student to characterize the MOT and can be used as an optimisation metric when changing the various parameters available.

An estimation of the MOT number can be established by setting up a lens and photodiode combination to record the fluorescence emitted by the MOT. To take into account scattered laser beams or any ambient light being picked up the photodiode during the recording, a reading of the photodiode level with the coils switched off can be made and this subtracted from the signal obtained when the coils are on. The formula used for calculating the atom number from the photodiode reading is:

$$N = \frac{4\pi}{0.96^\kappa \Omega} \frac{P}{h\nu R} \quad (2.5)$$

where  $\Omega$  is the solid angle subtended by the collecting lens,  $\kappa$  is the number of uncoated glass surfaces between the MOT and photodiode (the transmission of one of these is 0.96),  $P$  is the detected optical power (equal to the photodiode voltage reading divided by the responsivity),  $h\nu$  is the energy of a single photon and  $R$  is the photon scattering rate, given by:

$$R = \frac{\Gamma}{2} \frac{\frac{I}{I_{sat}}}{1 + \frac{I}{I_{sat}} + 4\frac{\delta^2}{\Gamma^2}} \quad (2.6)$$

with  $\Gamma$  being the natural linewidth of the transition,  $I$  the total intensity of the MOT beams,  $I_{sat}$  the saturation intensity of the transition and  $\delta$  the detuning from resonance. Unfortunately, in the current setup it is difficult to know the exact detuning of the laser from atomic resonance - an estimate could be obtained by unlocking the laser, increasing the sweep of the piezo slightly and estimating where the exact lockpoint is for the MOT to load. By making an estimate of the photodiode reading, an approximate atom number of  $8 \times 10^7$  atoms is obtained in our setup. An example image of the MOT taken with a Thorlabs CCD camera is seen in Figure 2.11.

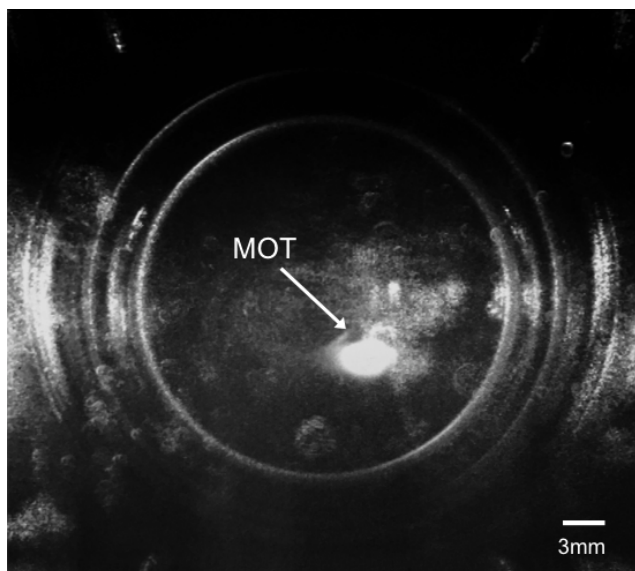


Figure 2.11: Example image of the MOT obtained using the DAVLL and sideband techniques. This MOT is the typical size for when the setup was used as part of the undergraduate teaching lab. The circular structure seen in the background is the lens that is used to focus the fluorescence light onto the photodiode.

### 2.7.2 Obtaining an Estimate of the Pressure at the MOT Position

With an emphasis on cold atoms apparatus becoming more portable, it may not always be practical to include a vacuum gauge. Therefore, alternative ways of estimating the background pressure may need to be utilised. One such method is using the lifetime of the cloud to obtain an estimate of the pressure, since the lifetime of an atomic sample is inversely proportional to the background pressure - effectively, using the MOT as a vacuum gauge. This is based on work that was previously undertaken in our group [105]. Essentially, the MOT loading curve can be obtained to acquire the  $1/e$  loading time  $\tau$ . The corresponding loss rate  $\gamma$  (give as  $1/\tau$ ) can then be converted into an estimate of the pressure  $P$  using a conversion formula obtained in [106]:

$$\frac{\gamma}{P} = 4.4 \times 10^7 \text{Torr}^{-1} \text{s}^{-1}. \quad (2.7)$$

The estimate for the pressure can then be compared to the pressure reading obtained from the ion pump - as an example, we estimate a pressure of  $3.6 \times 10^{-7} \text{Torr}$  compared to the ion pump reading of  $1.7 \times 10^{-8} \text{Torr}$ . It is not unusual for the two pressure readings to differ and can be attributed to the fact that the lowest pressures in a vacuum system are found at the position of the pump. Generally, it may be more useful or relevant to obtain a pressure estimate at the MOT region as opposed to at the location of the pump.

## 2.8 Outreach Demonstrations

Some photos taken of the portable MOT at the International Year of Light (IYL) Launch event in February 2015 are seen in Figure 2.12. At this early stage of our own portable MOT development, with work on it having only begun in late 2014, we had just managed to set up the DAVLL mechanism for locking the master laser. As such, the portable MOT demonstration was a collaboration with the University of Strathclyde, who provided their own vacuum chamber for the exhibit. Also provided were a secondary repumper laser (since the sidebands had not been set up yet) and finally a microfabricated grating chip that was used as a compact way of realising an optical molasses as an alternative to the six-beam MOT. More details on the grating chip technology and our own plans for it can be found in the next section.

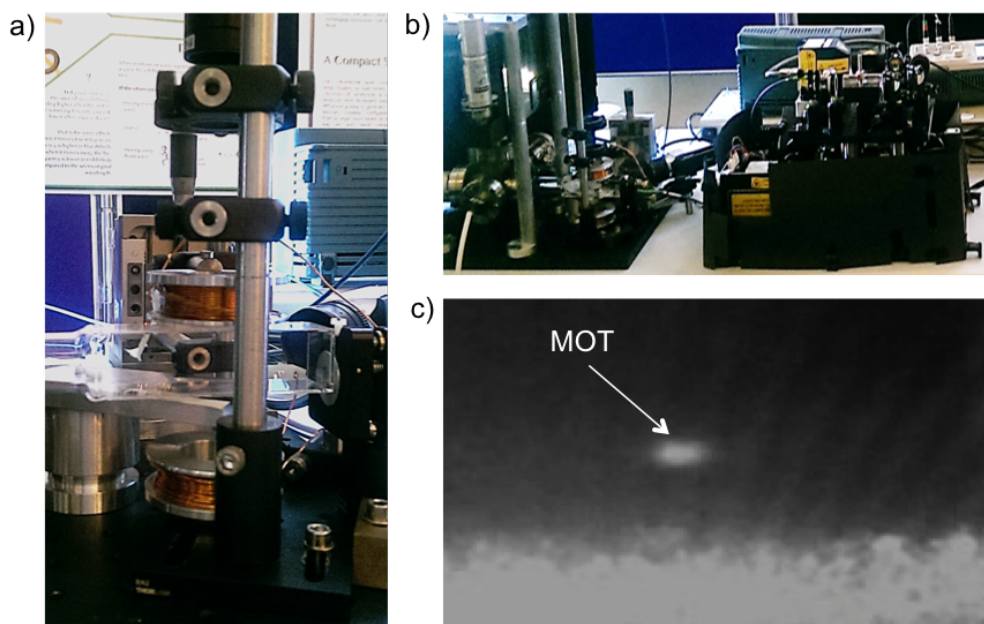


Figure 2.12: Photos taken of the portable MOT setup in Edinburgh during the IYL event launch in February 2015. a) Photo of the vacuum chamber (glass cell), coils and grating chip setup as provided by the University of Strathclyde; b) Photo of the full experimental setup, with vacuum chamber on the left breadboard and laser system on the right. In this case, the repumper laser is mounted above our master laser setup on its own breadboard; c) Example image of a MOT generated at the event and displayed on a monitor.

The second outreach event that we demonstrated the portable MOT was Dundee Science Festival in November 2015. Some photos taken at this event are shown in Figure 2.13. Again, a collaboration with the University of Strathclyde was had as we had not yet

started work on our own vacuum chamber.

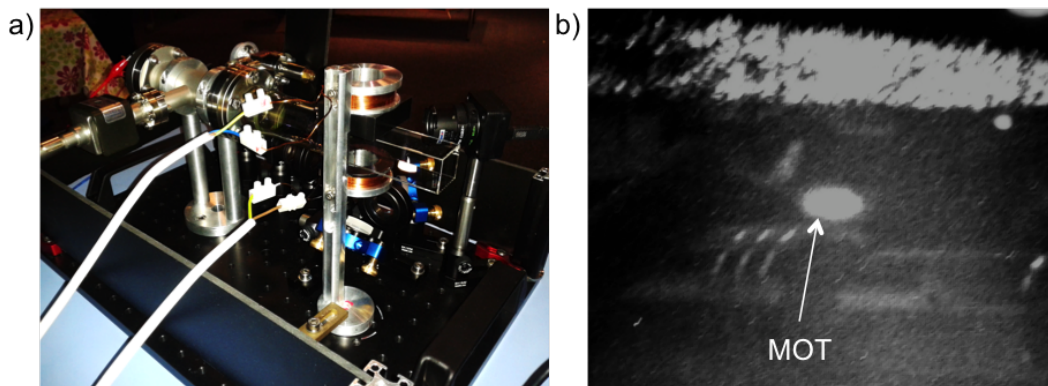


Figure 2.13: Photos taken at Dundee Science Festival in November 2015. The vacuum chamber, which our own design is based on, is shown. An image of the MOT generated at this event is shown alongside.

## 2.9 Future Work Planned

The use of the DAVLL and sideband techniques to create a compact, robust cold atoms apparatus has been demonstrated and used most recently in the undergraduate teaching laboratory. However, one further addition that is planned to be implemented is that of a micro-fabricated diffraction grating chip [88] as mentioned in the previous section. The chip is an alternative method of producing an optical molasses, with the significant advantage of being much more compact compared to the standard six-beam setup in the current apparatus. The ability to create an optical molasses using just a single, circularly-polarised input beam is very advantageous due to the compact design and ease of alignment compared to the six-beam setup. A grating chip placed below the glass cell will diffract into various orders, and the cooling volume of the optical molasses is created at the intersection of the initial input beam with the diffracted orders (Figure 2.14).

The proposed optical setup which incorporates the grating chip technology is shown in Figure 2.15. The grating chip MOT significantly reduces the total optical components needed for the vacuum chamber breadboard as a single input beam can be collimated from the output from an optical fibre, passed through a quarter waveplate and directed through the glass cell with the diffraction grating typically placed just below the glass cell.

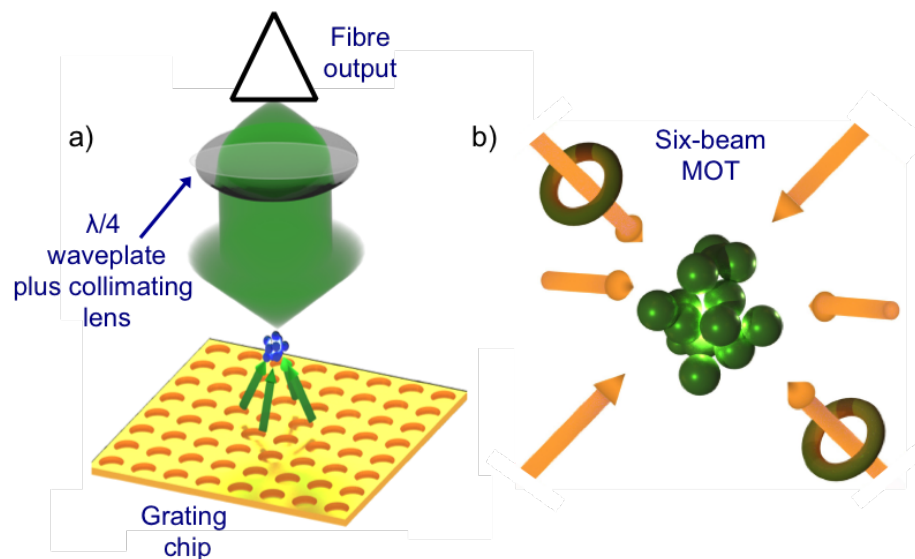


Figure 2.14: Comparison of a) the grating chip MOT and b) a standard six-beam MOT. The cooling volume for the grating chip is formed at the intersection of the input beam with the diffracted orders.

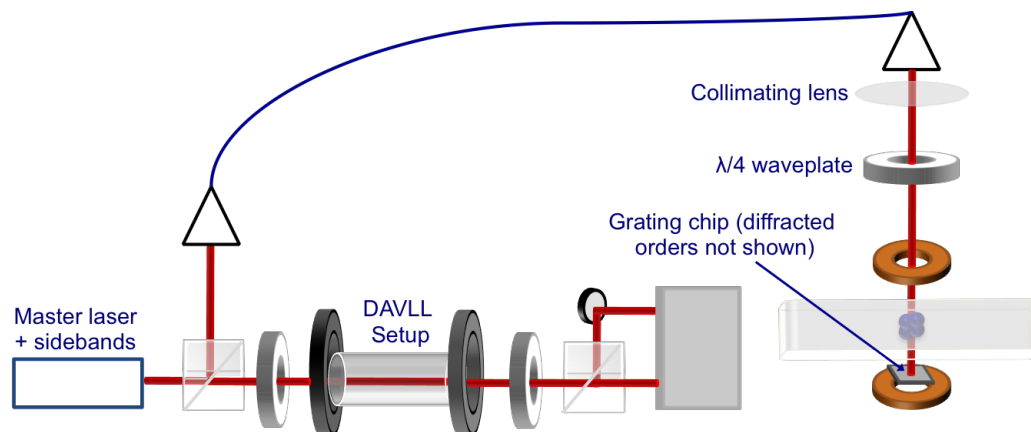


Figure 2.15: Proposed compact setup for the portable MOT experiment, incorporating DAVLL, sidebands generation and the grating chip MOT.

In addition to the implementation of the grating chip, which is a setup aimed primarily at increasing the robustness of the setup when transported compared to the six-beam MOT, a couple of further additions to the setup will be:

- setting up the proper temperature stabilisation of the laser diode by using the ther-

mistor as opposed to the current AD590 electronic circuit;

- setting up a computer program to estimate the temperature of the MOT. This would be achieved by monitoring the expansion of the cloud after the coils are switched off, from which a temperature estimate can be obtained. This would add an extra task for undergraduate students in the lab, but could also be set up as an easy-to-use interface for outreach events that would allow the general public to obtain a temperature estimate. Practically, we plan to switch off only the coils and not the laser beams so as to observe the slow diffusion of the atoms within the optical molasses, captured using a CCD camera. The temperature can then be extracted from the rate of expansion using a method similar to that outlined by Dalibard et al [107]. The advantage of this technique compared to the more standard time-of-flight expansion (where the laser beams are also switched off) is that observation of this slowly expanding cloud using the camera demonstrates intuitively how cold the atoms are, which we view as an important factor for both outreach and teaching.

## Chapter 3

# Construction of a Double Vacuum Chamber Apparatus for Production of $^{87}\text{Rb}$ Bose-Einstein Condensates

### 3.1 Introduction

This chapter details the design, construction and results of a double vacuum chamber apparatus setup to realise the first BECs formed in St Andrews. The experimental apparatus was designed to reliably produce  $^{87}\text{Rb}$  Bose-Einstein condensates and subsequently load an ultracold atomic ensemble into a holographically generated optical trap. General methods to achieve Bose-Einstein condensation are nowadays well-established (see for example [108, 109, 110]) - gaseous atoms are first slowed and hence cooled via the radiation pressure force exerted on the atoms by three pairs of mutually orthogonal, counter-propagating laser beams in a scheme known as laser cooling that takes place in a magneto-optical trap (MOT). Even after an optical molasses stage of further cooling, the atoms are neither cold nor dense enough to begin condensing, hence evaporative cooling is performed. The exact specifics of the evaporative cooling process differs between experiments, but in all cases the hottest fraction of the atoms are selectively removed from the ensemble, gradually allowing the remaining atoms to re-thermalise at lower and lower temperatures up to the onset of a bimodal momentum distribution forming.

Central to the ability to trap and cool the atoms over the course of this process is the effectiveness of the vacuum where the experiment is performed - a poor vacuum leads to the atoms colliding with either background gases or untrapped atoms, potentially ejecting them from a trap and causing them to be lost to the cooling cycle. Typically, pressures of the order of  $10^{-11}\text{mbar}$  [12] are required to provide a sufficiently long lifetime ( $>10\text{s}$ ) for atoms

held in a trap. The re-design of our original single chamber apparatus was deemed necessary due to the difficulty of maximising both the atom number  $N$  and the lifetime of the cloud  $\tau$  simultaneously within one chamber. This eventually led to a decision to construct a dual-chamber vacuum apparatus, capable of separating the loading and experimental stages of the experiment and ensuring both a large atomic flux for the MOT loading stage and a long lifetime for the stages beyond. Details of the double vacuum chamber setup are found in section 3.2.

Our atomic beam to load the 3D MOT is generated using a 2D MOT setup [111, 112, 113]. In the 2D MOT, atoms are cooled along two orthogonal axes and transferred into the experiment chamber along the third axis. This is achieved by creating a line of zero magnetic field along which the atoms are confined as they are being cooled transversally, and using a push beam to perform the transfer into the other chamber. The result is a flux of cold atoms that can then be more easily captured by the 3D MOT, having already undergone pre-cooling in the 2D chamber. Details of the laser cooling setup are described in section 3.3. Having a higher pressure loading chamber means that we can generate a significant atomic flux to obtain fast MOT loading, while ensuring that in the lower pressure science chamber the presence of background gases or untrapped atoms is minimised.

Once the 3D laser cooling has been performed in the science chamber, the beams are extinguished and the atoms are compressed in the purely conservative quadrupole magnetic trap, increasing their density and collision rate. A description of our magnetic field generation is found in section 3.4. Section 3.5 covers optimisation of our 3D MOT, while our optical pumping scheme is briefly outlined in section 3.6. The setup for absorption imaging of the atoms is described in section 3.7. A first stage of evaporative cooling (section 3.8) is performed using the well-known technique of a radio-frequency “knife” to spin-flip the hottest proportion of atoms from a trapped state to an anti-trapped state and allowing the remainder to re-thermalise via collisions. A problem arising from this method is the loss of atoms occurring near the zero point of the magnetic field - at very low magnetic field values, there is a degeneracy of the Zeeman sub-levels, meaning that some of the coldest atoms in the ensemble may spin-flip and leave the trap, which is detrimental to the goal of the experiment. To negate this, after the RF evaporation stage we adiabatically transfer the atoms from the purely magnetic trap into a focused optical dipole trap (ODT) with a slight gravity-compensating magnetic field present to help with confinement, in a scheme similar to that detailed in [20]. The high power, far-detuned ODT light is sufficiently far from resonance that the radiation pressure force is negligible and instead the gradient force dominates, causing an AC Stark shift in the atomic energy levels based on the intensity of the light present. The result for red-detuned light is a potential well capable of confining the atoms, resembling the Gaussian nature of the beam itself. Further evaporation can then be performed by reducing the power of the light, gradually reducing the trap depth and resulting in the hotter, more energetic atoms leaving the trap. After sufficient cooling with this method, the bimodal momentum distribution leading to BEC formation (section 3.9) can be detected via absorption imaging. An outline of our full experimental sequence is

provided in section 3.10, while a brief summary of the experiment performance is provided in section 3.11.

In chapter 4, the power removed from the ODT during evaporation is instead used for the SLM and light sheet paths, allowing the capture of atoms into arbitrary trap geometries. For the rest of this chapter, however, the focus will be on the details of the experimental setup and sequence that led to the formation of Bose-Einstein condensates.

## 3.2 The Double Vacuum Chamber Apparatus

### 3.2.1 Glass Cell, Differential Pumping Tube, Octagon Chamber

Our double chamber setup consists of a glass cell where 2D cooling is performed, connected via a differential pumping tube to a spherical octagon, where the pre-cooled atoms are loaded into the standard six-beam MOT. Rubidium atoms are loaded into the glass cell from dispensers and cooling is performed along two perpendicular axes. The cylindrical glass cell (LewVac GA-DE33L-40CF) was chosen due to its large optical access: a larger cooling volume leads to a greater atomic flux [112]. Our 152mm length glass cell has an optical access of roughly 110mm length (Figure 3.1a). Rather than using large, expensive rectangular optics, the 2D transversal cooling of rubidium is set up such that three sets of cooling beams could be directed both down and across the chamber, and then retroreflected back to form the counter-propagating beams. This is achieved using standard 25.4mm diameter optics, arranged in close proximity with minimal separation so as to fill the glass cell as much as possible, giving an effective cooling volume of  $\sim 75 \times 25 \times 25$  mm. No anti-reflection coating on the glass cell means there is a 17% reduction in optical power of the retroreflected beams at the position of the atoms. Additionally, to counteract the -350mm focal length lensing effect from the glass cell, we position an  $f=300$  mm cylindrical lens behind the glass cell to both collimate and increase the peak intensity of the retro-reflected beams.

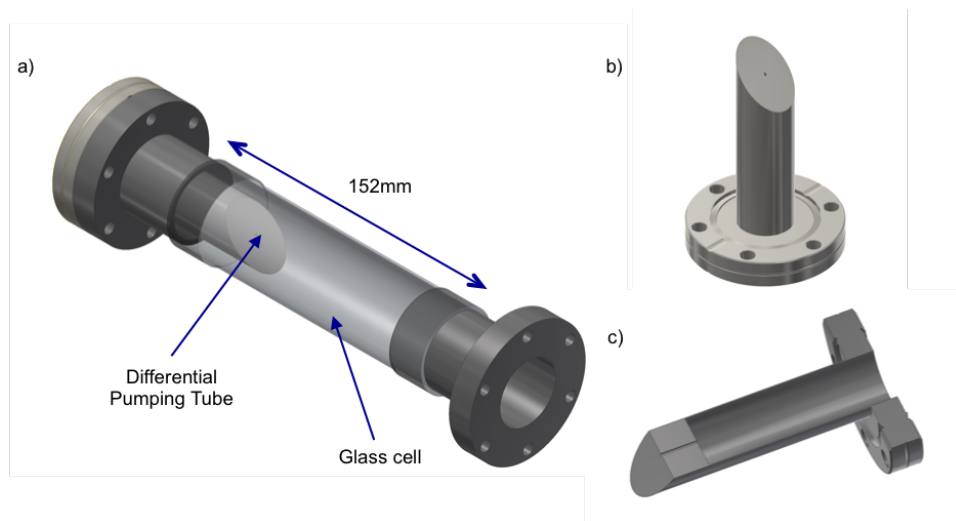


Figure 3.1: a) Model of the full glass cell with differential pumping tube in place; b) Full model and c) cutaway of the differential pumping tube.

The differential pumping tube (Figure 3.1b) is used as the connection between the glass cell (loading chamber) and the octagon (experiment chamber) - the concentrated beam of atoms are transferred through the small opening whilst maintaining a pressure differential between the two chambers due to the tube's low conductance. To achieve this, we custom-made our tube from LewVac with the aim of minimising the conductance through the tube and hence maximising the difference in pressure at either end of the tube. Knowing that gas flowing through a pipe produces a pressure differential at each end [114], the ratio of the pressure in the loading chamber  $\rho_{loading}$  to the pressure in the science chamber  $\rho_{science}$  can be approximated as:

$$\frac{\rho_{science}}{\rho_{loading}} = \frac{C}{S} \quad (3.1)$$

where  $C$  is the conductance and  $S$  is the pumping speed. The ion pump connected to our science chamber has a pumping speed of  $55\text{Ls}^{-1}$ , which we use for  $S$ , while for molecular flow the conductance of air at  $20^\circ\text{C}$  in a pipe is given by:

$$C = 12.1 \frac{d^3}{l} \text{Ls}^{-1} \quad (3.2)$$

where  $d$  is the diameter of the pipe and  $l$  is the length, both expressed in centimetres. As mentioned, to minimise the conductance we therefore require a small diameter tube with a long length. However, there is a limit to what can be built due to the divergence of the atomic beam, with typical values in the range  $10 - 45\text{mrad}$  [111, 112, 113]. We chose an upper limit of  $47\text{mrad}$  for the beam divergence to be safe, and therefore customised our

pumping tube with a 1.2mm diameter hole and a length of 12.7mm (Figure 3.1c). The approximate pressure differential between the two chambers is then  $\rho_{science} \sim 10^{-4} \rho_{loading}$ , allowing us to maintain good UHV conditions in the science chamber whilst being able to load a large 3D MOT swiftly (with a pressure of  $\sim 10^{-6}$  mbar in the loading chamber).

To perform the transfer of atoms through the differential pumping tube into the 3D MOT, we use a push beam to add a radiation pressure imbalance in the longitudinal direction. Additionally, some longitudinal cooling is performed by using the angle cut of the differential pumping tube to act as a mirror in what is known as a 2DMOT<sup>+</sup> [111] setup. A beam directed through the top of the glass cell is reflected by the 45 degree cut polished surface, providing some cooling power along the longitudinal direction. A beam directed from above can be reflected with 60% efficiency (with a small hole in the centre), and a viewport at the end of the 2D side is used for the push beam.

Our science chamber is a spherical octagon (Kimball Physics MCF600-SO200800) chamber, with six viewports around the circumference and two on top and bottom to allow for plenty of optical access. In addition, three of these viewports are recessed - the two vertical viewports are recessed to allow the current-carrying coils to be placed much closer to the atoms, meaning that the appropriate field gradients can be achieved with more reasonable current values. One of the horizontal viewports is also recessed - the recession also allows a lens with a shorter focal length to be placed close to the atoms, which is desirable as shorter focal length lenses provide higher image resolution. This in turn provides more accurate diagnosis of the atomic cloud during imaging, as well as more detailed light patterns originating from the SLM along the vertical direction.

The octagon connects to the differential pumping tube/glass cell via a bellow (Figure 3.2) which provides some give and flexibility in the support, especially when it comes to moving the entire apparatus into place. The flexibility provided allowed the chamber system to be moved transversally into place to ensure good alignment of the atomic beam through to the 3D MOT.

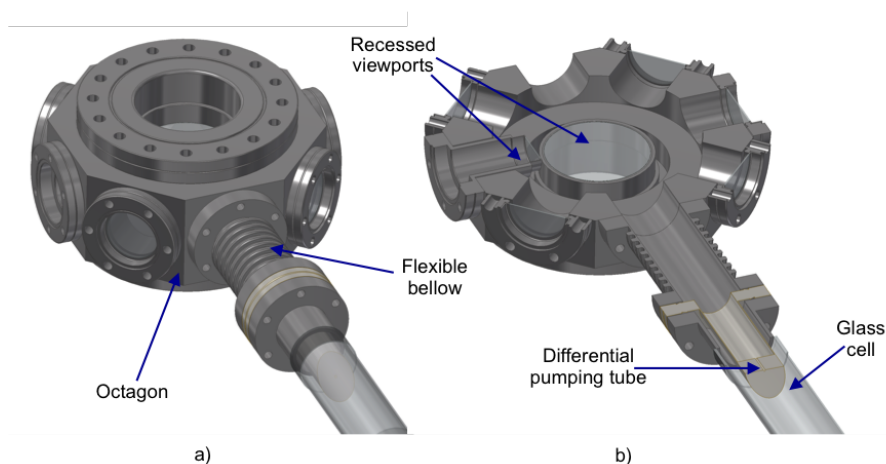


Figure 3.2: a) Full model and b) cutaway of the main experiment chamber (octagon), connected to the differential pumping tube and glass cell via the bellow.

After the double vacuum chamber system was in place, the next step was to perform a bakeout and obtain ultra high vacuum (UHV) conditions.

### 3.2.2 Obtaining Ultra High Vacuum Conditions

Obtaining quantum degeneracy of atomic gases necessarily requires direct avoidance from any sources of heating, including collisions with air molecules or from atoms that are not trapped in the MOT. This thermal isolation is managed by maintaining ultra high vacuum (UHV) conditions in the chamber where investigations are taking place. For this reason, the octagon is kept at a lower pressure compared to the glass cell - a lower pressure in the octagon prolongs the lifetime of the cloud and separates it from the higher pressure loading chamber, where a higher pressure is beneficial for increased atomic flux.

To complete the full setup of the apparatus, the 2D side of the setup is centred around two four-way stainless steel crosses (Figure 3.3). One of the flanges is connected to a  $40\text{Ls}^{-1}$  Varian VacIon Starcell Plus 40 ion pump. The ion pump maintains the vacuum conditions after the initial pumping out stage has been completed, and it remains on constantly. It works by ionising gas particles when they pass through a cathode and anode that have a high voltage between them. The ionised particles are then attracted to the cathode and stick there. A valve on the 2D side of the chamber allows a turbo pump (Pfeiffer HiPace 80) to be connected during the bakeout. The viewport on the end of the chamber is used as the push beam access.

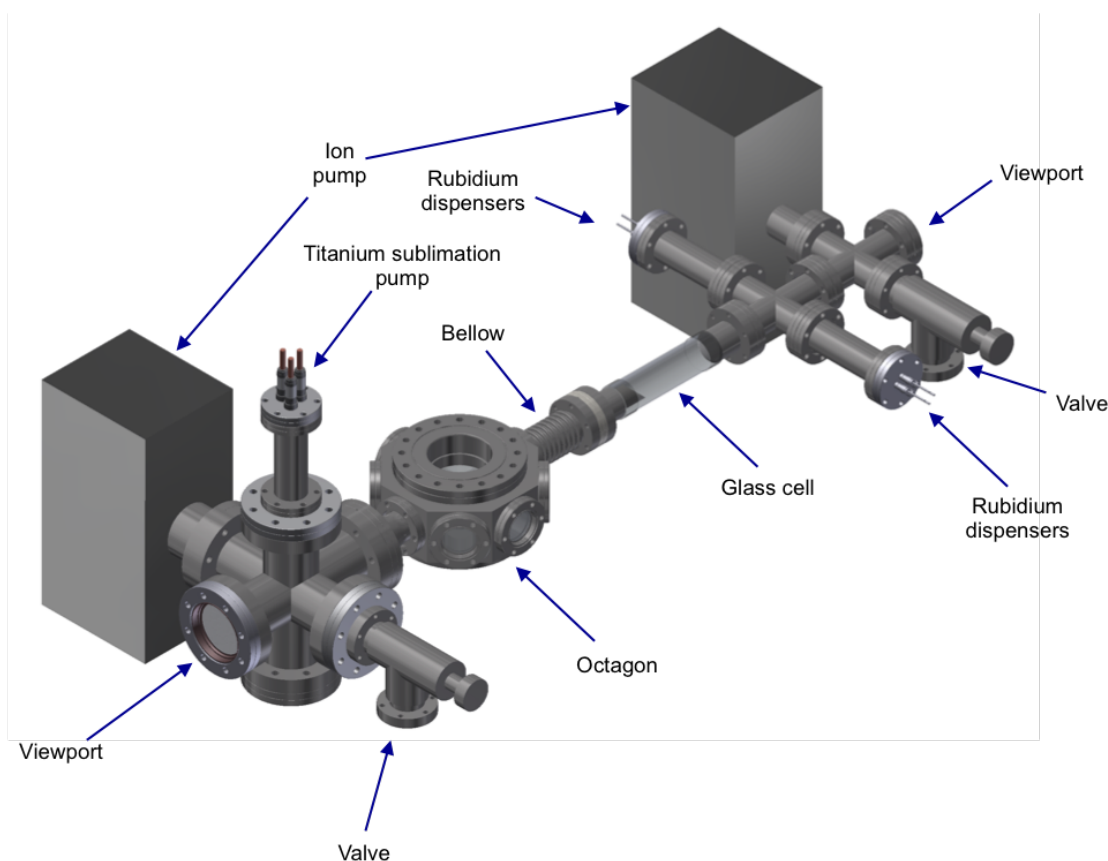


Figure 3.3: Model of the full double vacuum chamber apparatus.

The two remaining flanges on the 2D side of the apparatus are sealed with 4-pin electrical feedthroughs. Inside the vacuum chamber, each pair of feedthrough rods is connected to an alkali metal dispenser (SAES). When a current is applied, gaseous rubidium is dispensed upon heating via sublimation. A reducing agent ensures that any other chemicals produced are absorbed by the chemical compound. There exists a threshold value for the current below which hardly any atoms are released - this varies between dispensers but is usually in the range 2.5A to 3A. Driving the dispensers at a higher current provides a more immediate gain of atoms but might end up shortening the lifetime of the dispenser. As long as the current is managed sensibly and the chamber does not become flooded with rubidium, each dispenser lasts about one year before needing to switch to another. Typically we turn the dispenser on first thing in the morning to allow the rubidium level to build up, and overnight we reduce the current to around threshold.

On the 3D side of the experiment, a six-way cross is connected to a  $55\text{Ls}^{-1}$  Varian VacIon Starcell Plus 55 ion pump, a titanium sublimation pump (VG Scienta ST22), a

valve connection to connect the turbo pump to during the bakeout, and a viewport that is used as the access point for the optical pumping light.

Once the apparatus was set up, the bakeout procedure was performed. Connecting the turbo pump to the two valves in Figure 3.3 allows both chambers to be pumped out without the need to pump through the differential pumping tube. Before beginning, all components were cleaned with acetone followed by isopropanol. To set up the bakeout, we used resistive tape heaters wrapped around the apparatus and then covered the entirety in tin foil to keep the heat in - thermocouples were inserted at various points to keep track of the temperature of the different parts of the apparatus and ensure an even heat distribution. While monitoring the temperature, we increased the current through the heat tapes slowly until a temperature of roughly  $200^{\circ}\text{C}$  was established throughout the chamber. The bakeout procedure lasted roughly two weeks until a pressure of  $10^{-9}$  mbar was achieved with the ion pump current read-out connected to the octagon (Figure 3.4), while the loading chamber pressure reached  $10^{-7}$  mbar.

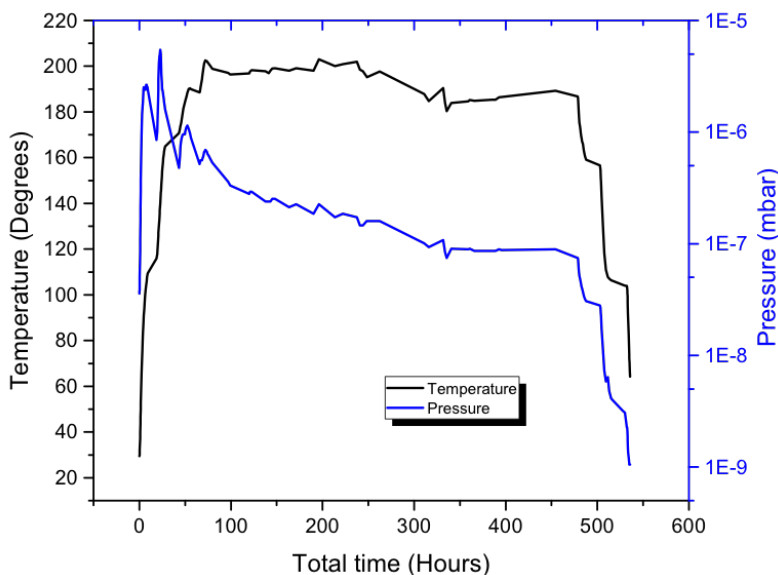


Figure 3.4: Temperature and pressure of the octagon during the bakeout procedure.

### 3.2.3 Full Apparatus

A model of the full apparatus with the 2D MOT optics in place is shown in Figure 3.5. The 2D cooling and repumper light is overlapped after exiting the optical fibres and split into six beams using a sequence of half-waveplates and PBS cubes. Three beams are directed down through the chamber and retro-reflected back using mirrors and lenses placed under the glass cell, while the other three beams are directed across the chamber, with mirrors

and lenses on the other side retroreflecting those beams back. The push beam is directed through the chamber using the viewport on the end of the chamber of the 2D side.

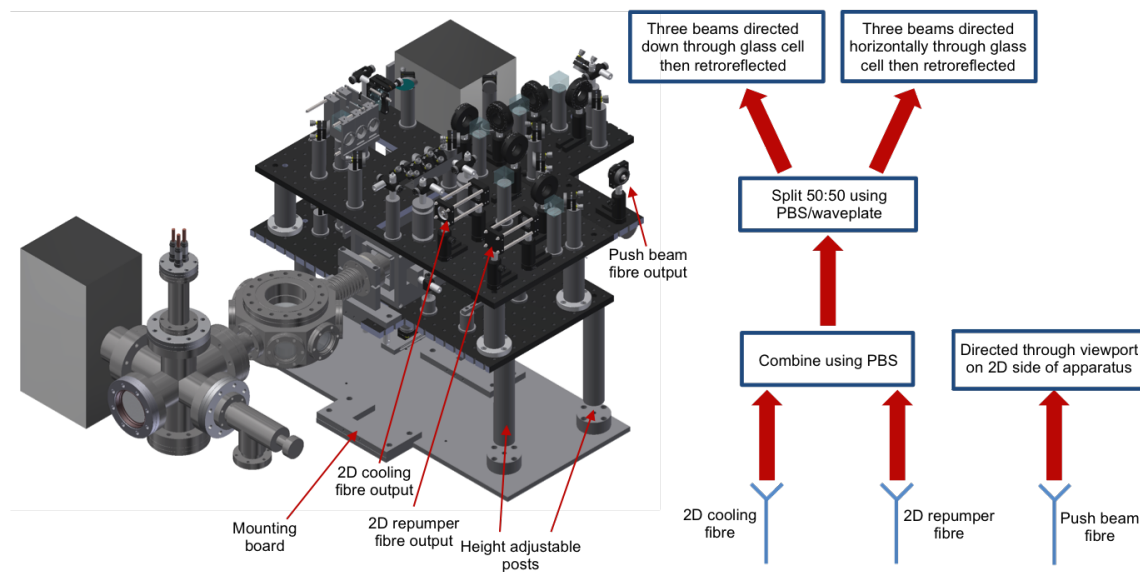


Figure 3.5: Model of the double vacuum chamber apparatus with the optical components in place for the 2D cooling, 2D repumper and push beams. The breadboards are able to be adjusted in height using the posts, and the entire configuration can be moved as one. The schematic on the right describes the optical layout of the top and middle breadboards shown in the model.

The whole 2D side of the apparatus was designed to be height-adjustable to allow good alignment of the pre-cooled atomic beam into the 3D MOT - this was achieved by placing the entire 2D side onto a mounting board. The mounting board allows the setup to be slowly slid across the optical table, while the height adjustable posts in Figure 3.5 allows the setup to be moved up or down. Finally, the flexibility of the bellow that connects the 2D side to the 3D chamber allows the exact angle of the setup to be adjusted for alignment of the atomic beam.

### 3.3 3D and 2D Laser Cooling of Rubidium

Laser cooling of  $^{87}\text{Rb}$  is performed through cycling atoms on the D2 line (Figure 3.6), between the  $F=2$  and  $F'=3$  hyperfine levels of the  $5^2\text{S}_{1/2}$  and  $5^2\text{P}_{3/2}$  energy levels respectively.

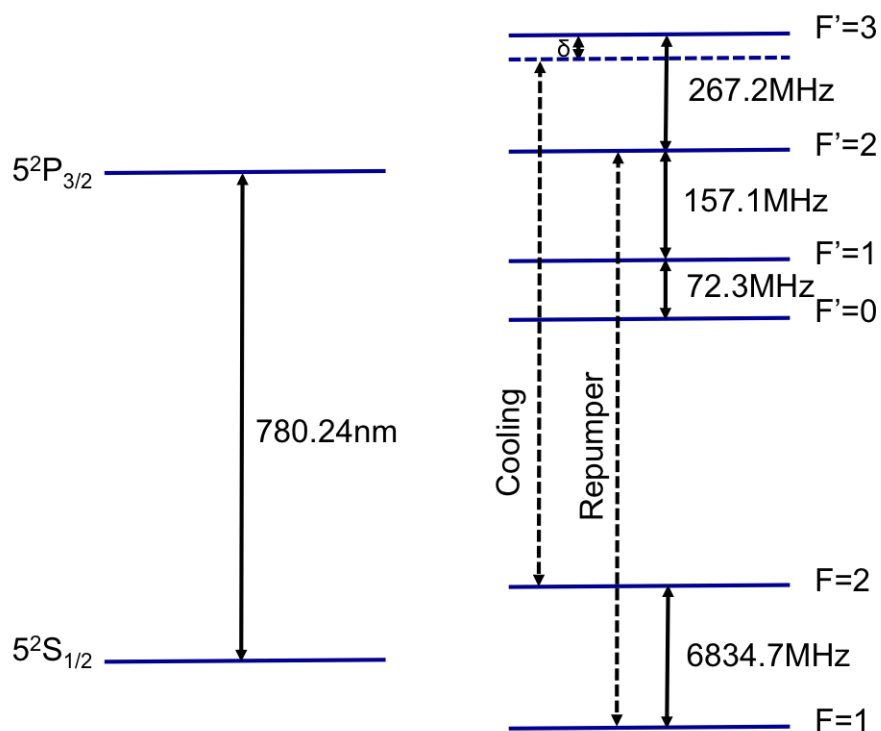


Figure 3.6: D2 Line of  $^{87}\text{Rb}$ , depicting cooling and repumper cycles used in the experiment. The detuning  $\delta$  takes different values during the experimental sequence for laser cooling, optical molasses or imaging.

Red detuning of the laser frequency from the  $F'=3$  level results in a small but non-negligible probability of atoms being excited from the  $F=2$  to the  $F'=2$  upper level - selection rules mean that emission of a photon can result in atoms decaying to the  $F=1$  ground state. An energy separation of nearly 7GHz means the cooling laser is unable to excite atoms from this lower manifold and, without further intervention, these atoms would be lost from the cooling process. To prevent this from happening, we use a second laser to excite atoms from the  $F=1$  lower manifold, after which they may return to the cooling cycle. This repumper laser typically has substantially less power compared to the cooling laser, and additionally no detuning is needed.

### 3.3.1 Laser System

Our laser system is set up on a separate bench from the one where our vacuum chamber is located. This optics table is used to manipulate the laser light to perform the various roles required in the full experimental setup, such as laser cooling, optical pumping and

imaging. A block diagram of this optical layout is shown in Figure 3.7.

Laser light is generated using two External Cavity Diode Lasers (ECDLs) - a Toptica Model DL100 mount with a Toptica LD-0785-P220-1 laser diode for the cooling light and a homemade cavity for the repumper light (Sanyo DL7140-201S). Semiconductor diode lasers are readily available at the transition wavelength for the D2 line of  $^{87}\text{Rb}$ , but typically having a larger linewidth than the natural linewidth ( $2\pi \times 6.1\text{MHz}$ ) of the  $^{87}\text{Rb}$  D2 transition, which could cause unwanted additional excitations. The external cavity drastically reduces the linewidth of the output light, creating a narrow linewidth output suitable for performing the laser cooling role. We also use piezo-electric transducers in both our ECDLs to allow us to rapidly scan the cavity length, and therefore the output light frequency, for the purposes of spectroscopy (see section 3.3.2).

The cooling laser produces around 50mW of output light and the repumper laser gives around 35mW. The output beam from the cooling laser has a slight elliptical profile; we therefore use a set of anamorphic prisms to produce a more circular output. Optical isolators placed on both the cooling and repumper beam paths prevent feedback of the light back into the laser diodes. A very small amount of power is then siphoned off from both the master and repumper outputs to be used for spectroscopy and locking the lasers.

The remaining power is then used in a double-pass acousto-optic modulator (AOM, Crystal Technologies) setup to allow for the appropriate detuning to be established. The 3D MOT AOM (model 3080-125) is used to set the detuning of the laser beams for the MOT loading, optical molasses and imaging stages; additionally, this AOM is used as a fast switch for the imaging process. The 2D MOT AOM (model 3110-120) sets the detuning of the laser beams used in the 2D MOT, plus the push beam. An optical pumping (OP) AOM (model 3200-121) shifts the frequency of the light for the optical pumping stage of the experiment, and also is used to supply the short pulse of OP light. The 3D MOT and 2D MOT AOMs are setup in a double-pass configuration to eliminate the spatial shift of the output beam whenever the frequency of the light needs to be altered. After the double-pass AOM a small amount of power from the 3D path is split off to be used for imaging. The two beams then inject a slave laser (home-made mount, Thorlabs LD785-SE400 high power laser diode), which generates the cooling power for the 3D MOT, and a tapered amplifier (TA) (Eagleyard EYP-TPA-0780-01000-3006-CMT03-0000), which generates the cooling power for the 2D MOT. The slave laser provides around 300mW of output light, while the TA produces around 550mW. The injecting power of the beam for the slave laser after the double-pass AOM is around 7mW, while for the TA the power is around 9mW. Some of the TA output light is then split off to be used for the push beam. Temperature stabilisation of all the lasers is achieved using thermistors and peltier elements, and the TA also uses a mechanical fan placed nearby to provide additional cooling.

Polarization-maintaining single mode optical fibers are then used to transfer the 3D cooling, 2D cooling, 3D repumper, 2D repumper, optical pumping, push beam and imaging light to the experiment table, giving a total of seven fibres used. Mechanical shutters are placed along each of these paths to block the light as needed.

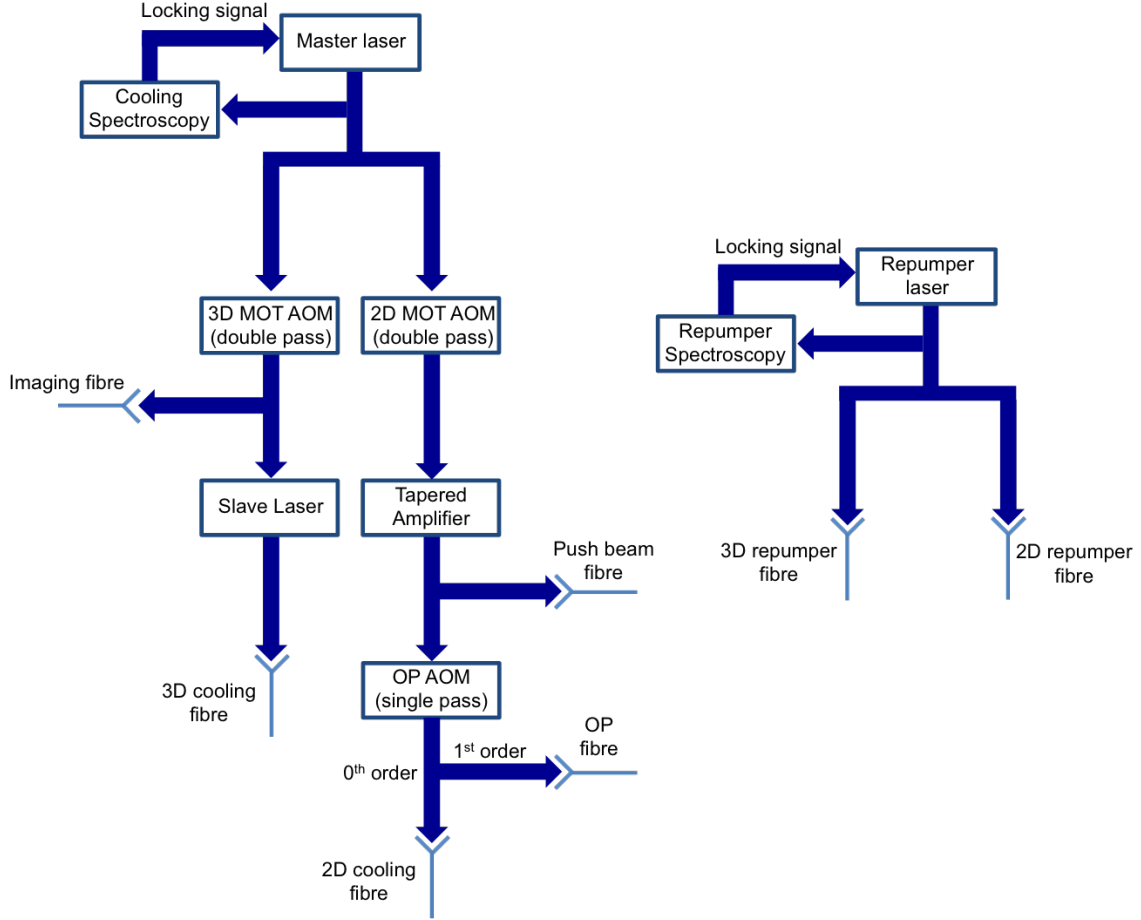


Figure 3.7: Block diagram showing the main layout of the optical setup for the experiment. Mechanical shutters omitted for clarity.

### 3.3.2 Saturated Absorption Spectroscopy and Locking the Lasers

Precise locking of the laser frequency is required to ensure efficient cooling of the atoms. This is achieved using the Doppler-free saturated absorption spectroscopy technique. The setup for the saturated absorption spectroscopy is identical to that described in section 2.3 and so will not be described again here.

An image of the saturated absorption spectroscopy of the  $^{87}\text{Rb}$  cooling and repumper profiles is shown in Figure 3.8. The error signal is obtained with a phase-sensitive detector by applying a small modulation to the laser current. This gives a differentiated signal which can then be used as a lock point as part of a proportional-integrable-derivative (PID) regulator. Reducing the amplitude of the sweep to zero allows the laser to be locked

to a specific transition, and the locking mechanism will keep the laser frequency tuned to the lock point against fluctuations in temperature or noise.

As can be seen in Figure 3.8a, we do not lock to the real  $F=2 \rightarrow F'=3$  transition on the D2 line (which would be the leftmost peak in the figure) - doing so would require applying a detuning of  $\sim 15\text{MHz}$  to the light for the MOT loading stage, and such a small detuning is hard to achieve using AOMs. Instead, we lock our cooling laser to the peak indicated in Figure 3.8a, which is the crossover transition between the  $F'=1$  and  $F'=3$  hyperfine levels from the  $F=2$  ground state. The AOMs in our setup are then capable of shifting the frequency closer to the value required by the MOT. The repumper laser is simply locked to the leftmost peak of the spectrum of Figure 3.8b, which is the real hyperfine transition corresponding to the  $F=1 \rightarrow F'=2$  levels as no detuning is applied to this laser.

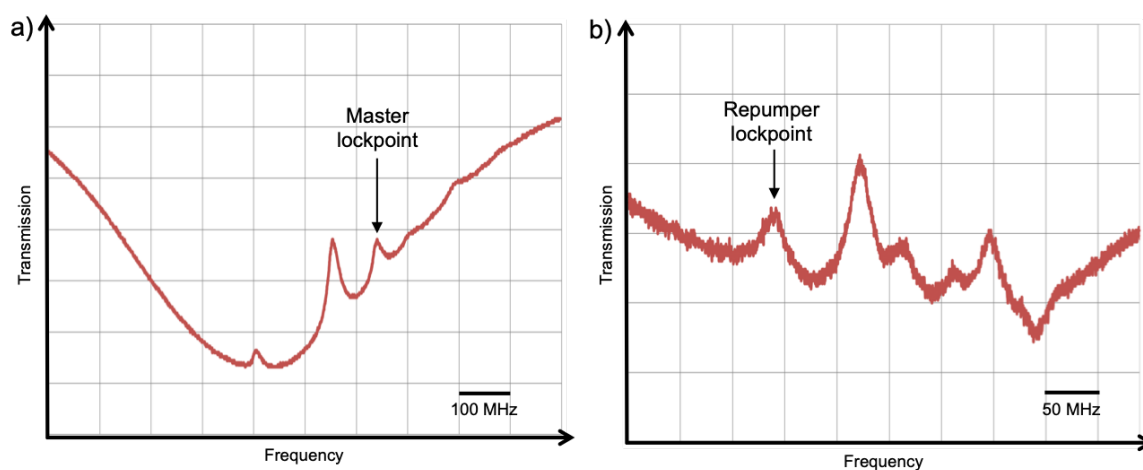


Figure 3.8: Doppler-free saturated absorption spectrum of a) the  $F=2 \rightarrow F'$  and b) the  $F=1 \rightarrow F'$  of the  $^{87}\text{Rb}$  D2 line for the cooling and repumper laser respectively. Laser lockpoints used in the experiment are indicated.

### 3.3.3 Detuning the Cooling Lasers

AOMs are capable of altering the intensity, direction and, most importantly, the frequency of an incoming laser beam via Bragg diffraction off an internally-generated sound wave which propagates through the crystal medium. The acoustic wave, consisting of alternating crests of compression and expansion corresponding to increased and decreased refractive index respectively, scatters the incoming light. When the constructive interference condition is met, the diffracted orders are shifted in frequency by an integer multiple of the sound wave frequency.

The AOM for the 3D MOT has a nominal operating frequency of  $80\text{MHz}$  with a bandwidth of  $25\text{MHz}$ . The double-pass setup mentioned before ensures there is no loss of

alignment whenever the detuning of the laser is changed. As we lock to the crossover peak located 212.15MHz from the  $F'=3$  level, we drive the AOM with a voltage such that the frequency of the generated sound wave is  $(106 - \delta/2)$  MHz, where  $\delta$  is the detuning from the  $F'=3$  level. For the MOT loading stage which uses a -20MHz detuning, this means the AOM is operated at 96MHz, while for the optical molasses stage at -60MHz detuning the AOM is operated at 76MHz. For imaging where resonant light is desired, the AOM operates at 106MHz. The changes to the detuning does slightly affect the efficiency of diffraction, but for each stage there is still sufficient power to properly inject the slave laser.

The AOM for the 2D MOT operates at 110MHz and has a bandwidth of 24MHz. Our 2D MOT beams operate at a detuning of -20MHz, resulting in the AOM operating at 96MHz. After the TA, some of the power is split off to be used for the optical pumping stage. A third AOM on this path (operated in single pass) shifts the frequency down to near the  $F'=2$  level for this purpose. The OP AOM has a centre line of 200MHz and a bandwidth of 50MHz, which is operated at 268MHz with a relatively low efficiency due to the high amount of initial power (only a small amount is needed for optical pumping).

Additionally, the AOMs have an external on/off switch that acts to stop sending the signal to the AOM, thereby eliminating the diffraction. As this would just leave the zeroth order light (which is blocked using an iris on the double pass path), we can use this switch behaviour to extinguish the light in the chamber much more quickly compared to a mechanical shutter (the shutters have a response time of  $\sim 1$ ms and a switching time to shut the power off of between 100 - 200 $\mu$ s). The AOM switch is better suited to sending short pulses of light, especially important for the optical pumping and imaging stages. For imaging, we use the 3D AOM to generate imaging pulses of 80 $\mu$ s for diagnostic absorption imaging. The optical pumping stage uses a short pulse of light to pump the atoms into the appropriate magnetically trappable sub-level, but too long of a pulse may cause unwanted heating. We use the OP AOM to provide a 500 $\mu$ s pulse for optical pumping.

### 3.3.4 Increasing the Laser Cooling Power

For the purpose of increasing the 3D cooling light power, we employ a master-slave configuration. An injecting power of 7mW is directed to the slave laser - the frequency of the slave laser light will be the correct detuning required for MOT operation because the beam injecting the slave laser comes after the double pass of the AOM, and so has already been frequency shifted. The stimulated emission that then occurs will match that of the input beam. Overlap of the output slave laser beam and input master beam is critical for this to be the case, and is achieved by checking the overlap at two positions over a considerable path length. It is important, however, to check that the slave laser is lasing at the correct frequency, and this is done by using a microscope slide on a flip-mount to split off a small amount of power after the slave output and perform optical spectroscopy in a separate Rb cell. The slave current and the beam alignment can then be adjusted until

the expected Doppler profile is obtained (Figure 3.9), ensuring the two laser modes match. Displaying the saturated absorption profile from the original master signal can be used for comparison, showing that the slave profile is missing the hyperfine transmission peaks (as we only pass once through the Rb cell) and frequency shifted (due to the frequency shift from the double pass through the AOM).

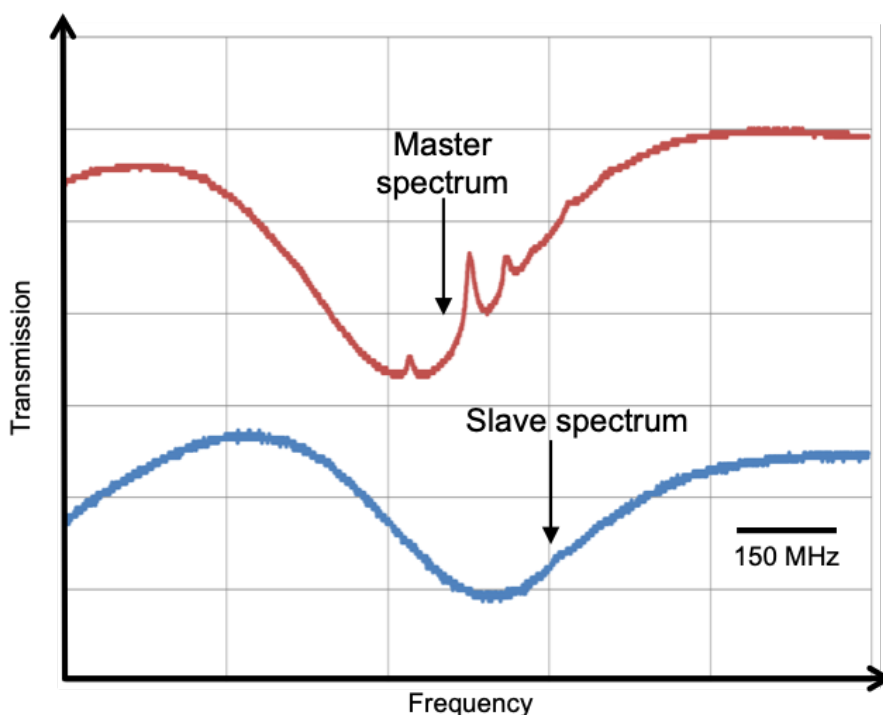


Figure 3.9: Comparison of the master laser absorption spectrum (red trace) with the slave laser spectrum (blue trace). The slave spectrum profile is missing the hyperfine peaks, and is also frequency shifted due to the double pass through the AOM.

An optical isolator once again prevents optical feedback into the slave laser diode. The total output power of the slave laser is roughly 300mW, for a current of 496mA, meaning that for the case of the 3D MOT we have roughly 240mW of 3D cooling light before entering the optical fibre. For the case of the 2D cooling light, we inject a Tapered Amplifier (TA). This gives around 550mW of output light available before entering the corresponding optical fibre. Another optical isolator prevents unwanted feedback into the amplifier.

### 3.3.5 Push Beam

A push beam is used to transfer the pre-cooled atoms from the loading chamber through the differential pumping tube into the experiment chamber, necessary because the pre-cooled atomic beam has no preferential direction of propagation. The push beam is directed through the viewport on the 2D side of the experimental apparatus of Figure 3.3, and the viewport on the 3D side is used for alignment of the push beam through the tube. The push beam is derived from the TA and directed towards a polarization-maintaining optical fibre - a shutter is placed on the path to block the light once the MOT has fully loaded. A half-waveplate and PBS combination can be used to choose the amount of power used for the push beam. After the fibre, the push beam has a  $1/e^2$  radius of 1mm, similar to that of the differential pumping tube (1.2mm).

### 3.3.6 Full 3D and 2D Laser Cooling Setup

The full optical setup for the 2D and 3D MOT stages in the double vacuum chamber is shown in Figure 3.10. The optical fibres are used to transfer the laser light to the experiment table from the optics bench. On the 2D side, the available optical power for laser cooling at the output of the optical fibre is 250mW, with the available repumper power being about 6.5mW. These two fibre outputs are combined and overlapped, and then split into six beams - three beams directed down vertically through the chamber and three directed straight across. Quarter waveplates placed before the glass cell provide the appropriate circularly polarised beams, and the beams are retroreflected off mirrors placed after the cell to give the appropriate counter-propagating beam. The push beam power available is around 2mW, and this beam is directed through the entire apparatus from one of the viewports to perform the transfer from the 2D to the 3D side.

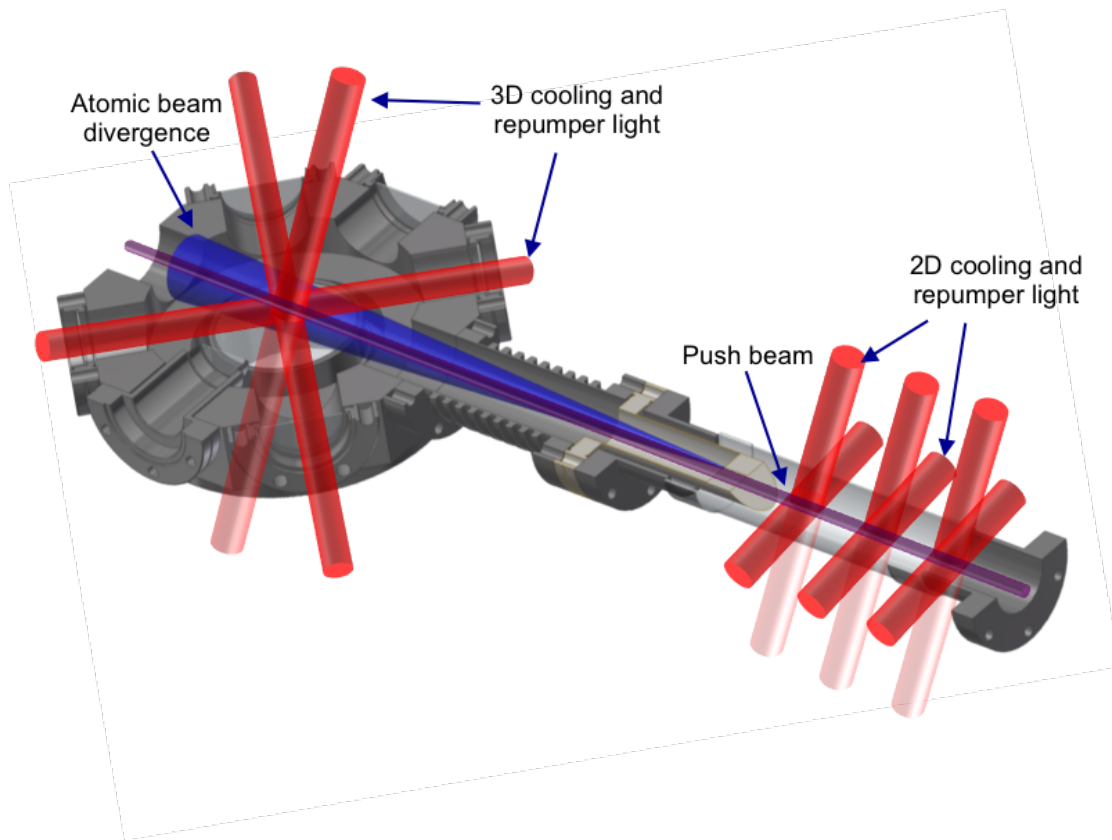


Figure 3.10: Diagram showing the layout of the 2D and 3D laser cooling setup.

On the 3D side, the available power for laser cooling is around 120mW, with about 1.6mW repumper power. Again, the cooling and repumper beams are overlapped at the fibre outputs and then split into six beams and directed through the octagon. Quarter waveplates placed just before the chamber again give the appropriate circularly polarised beams. The total available optical power after each optical fibre is summarised in Table 3.1.

### 3.4 Magnetic Field Generation

The laser cooling light alone, being only a velocity-dependent force, is incapable of holding the atoms in a given position within the beam overlap volume while the cooling is performed. In the MOT, a restoring force is provided with a set of two current-carrying coils in the anti-Helmholtz configuration, resulting in a point of zero magnetic field at the mid-point between the two coils, and providing a positional-dependence force such that when

Optical Fibre	Output Power (mW)
2D Cooling	250
2D Repumper	6.5
Push Beam	2
3D Cooling	120
3D Repumper	1.6
Optical Pumping	5
Imaging	0.5

Table 3.1: Table depicting the available laser power at the output for each of the optical fibres used.

an atom drifts away from the zero-point, it will be Zeeman-shifted into resonance with the appropriate counter-propagating laser beam, restoring it towards the trap centre.

The magnetic field  $B$  along the ( $z$ ) axis of a current-carrying coil, with  $N$  turns, is:

$$B(z) = \frac{\mu_0 INr^2}{2(z^2 + r^2)^{3/2}} \quad (3.3)$$

where  $I$  is the current through the coils and  $r$  is the coil radius. For a pair of such coils that are separated by a distance  $d$ , with current flowing in opposite directions, the magnetic field  $B$  at some point  $z$  along the axis between the coils is given by:

$$B(z) = \frac{\mu_0 NIr^2}{2} \left( \frac{1}{\left( (z - \frac{d}{2})^2 + r^2 \right)^{3/2}} - \frac{1}{\left( (z + \frac{d}{2})^2 + r^2 \right)^{3/2}} \right) \quad (3.4)$$

fulfilling the requirement that the magnetic field at the midpoint ( $z = 0$ ) is zero.

### 3.4.1 3D MOT Magnetic Field

For the 3D MOT coils, we designed our own coils holder due to the necessity of the coils needing to be water cooled. The 3D coils themselves have a total of 48 windings, achieved by winding the coil (1mm diameter wire) around the former and creating a total of 12 layers with 4 windings per layer. The radius of the coils is 24.4mm, and the separation of the coils when placed in the recessed viewports above and below the octagon is 52mm. Heat sink paste was applied first and then after each layer to ensure good thermal conductivity. After the final winding, glue was applied all around the outside of the coil to hold it in place. The second coil was wound after the first ensuring an identical number of windings.

The same set of coils are used for both the MOT and for magnetic trapping. To obtain a suitable compression before the radio frequency evaporation stage, we calculate that we

need to compress to around  $100\text{Gcm}^{-1}$ , which means running close to  $20\text{A}$  through the coils given the setup described above. A figure of the magnetic coil holders is shown in Figure 3.11. The coil holders also have a thin slit cut into the circumference to stop them from forming a closed ring, which could allow circulating currents to be generated.

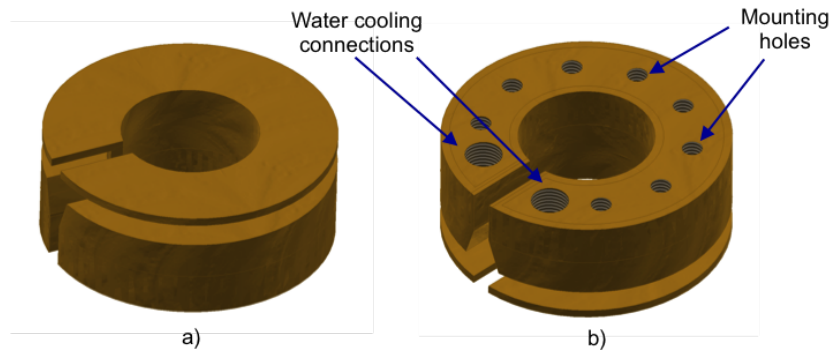


Figure 3.11: Model of our magnetic coil holders, showing mounting holes and water cooling connections.

Once the coils were mounted and tested, both with and without water cooling (see section 3.4.4), they were placed in the lower and upper recesses of the octagon, as shown in Figure 3.12. The close proximity of the coils allows a significant compression with a high magnetic field gradient to be established without large currents being passed through the coils. The power supply unit controlling the coils is connected to the computer, which allows full computer control over the magnetic field during the experimental sequence. Additionally, a relay placed in series can be used for a fast switch when turning off the coils.

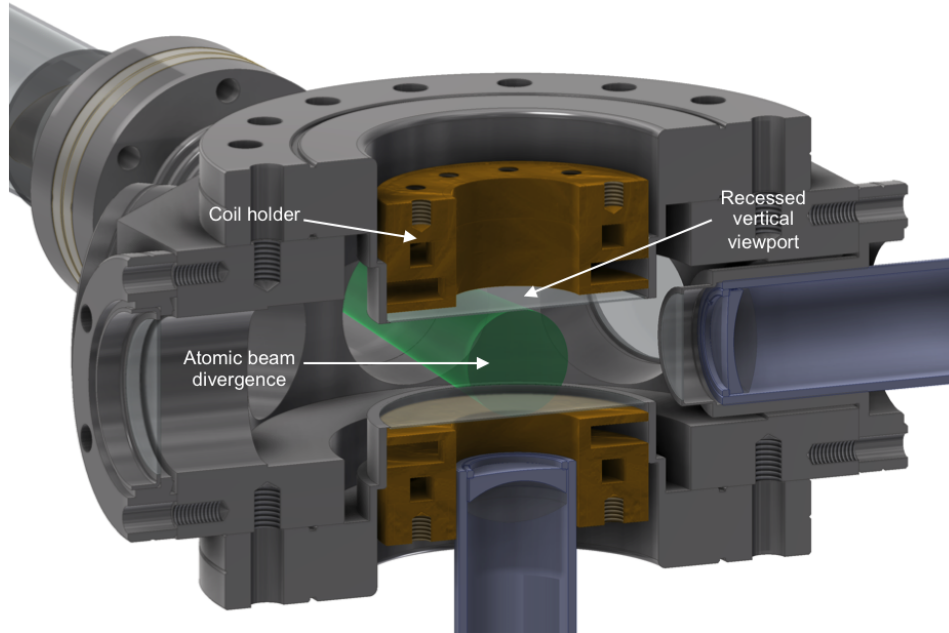


Figure 3.12: Cutaway of the main octagon chamber indicating the close proximity the coil holders can be placed to the atoms due to the recessed viewports. This also allows short focal length lenses to be placed near the atoms (along both the horizontal and vertical directions) for imaging.

### 3.4.2 2D MOT Magnetic Field

The 2D MOT magnetic field differs in that it requires a line of zero magnetic field along which the push beam can transfer the atoms. To achieve this, we design rectangular coil holders of nylon material, and wind 96 turns of 1mm diameter copper wire around the holder, which has dimensions of length 196mm and width 50mm (Figure 3.13), with a separation of 82mm. With these dimensions we can generate a magnetic field gradient of  $6\text{Gcm}^{-1}\text{A}^{-1}$ , and we supply the coils with 2.5A to give a field gradient of  $15\text{Gcm}^{-1}$ . The four sets of coils are wired in such a way that a line of zero magnetic field is produced within the glass cell. This field gradient value does not change throughout the experiment, so computer control of these coils is not necessary. Additionally, water cooling is not required for the 2D MOT coils. A diagram showing the full 2D MOT setup, with the 2D coils in place, for the glass cell is shown in Figure 3.14.

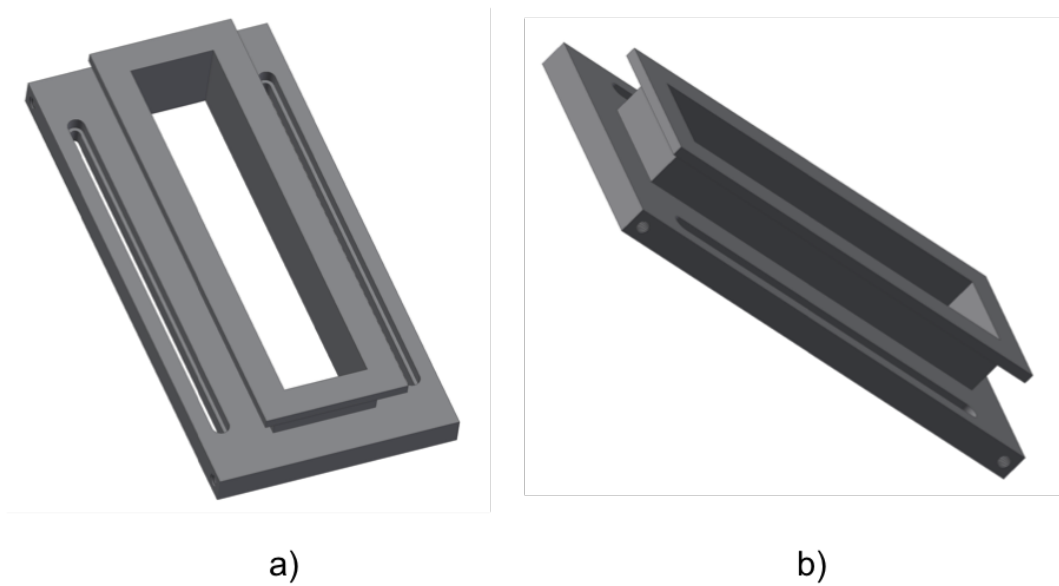


Figure 3.13: Model of the nylon coil holders designed for the 2D MOT magnetic field.

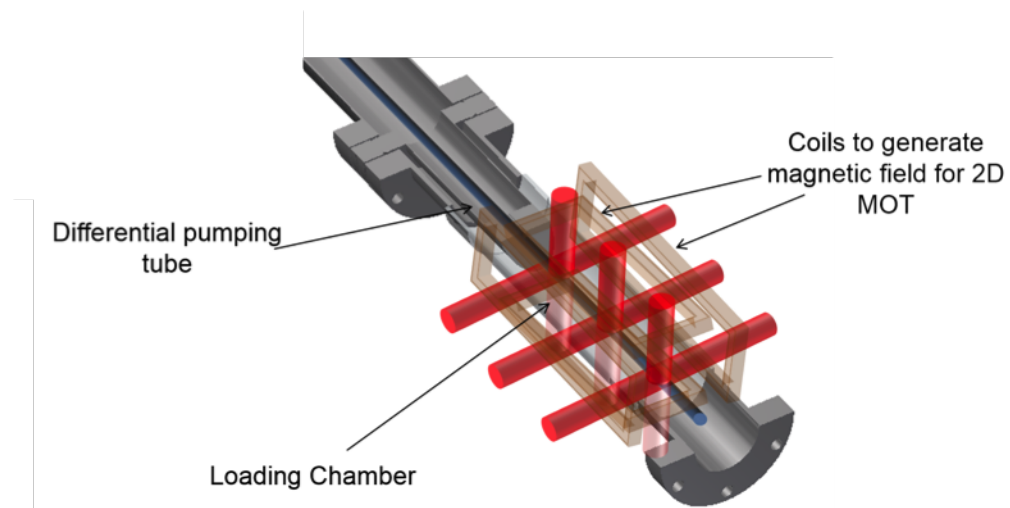


Figure 3.14: Diagram showing the full 2D MOT setup with the 2D MOT coils in place.

### 3.4.3 Shim Coils

Shim coils are used for both the experimental and loading chamber to compensate for the presence of stray magnetic fields.

For the 2D MOT, we wrapped additional coils around the existing MOT coil formers (Figure 3.13). Each shim coil had 20 turns of 0.8mm diameter wire, set up in a Helmholtz configuration, providing a compensating field of  $2.5\text{GA}^{-1}$ . These shim coils were optimised by maximising the loading rate of atoms into the 3D MOT. For the 3D MOT we use a pair of shim coils set up along each axis to ensure isotropic expansion of the cloud during the optical molasses phase - the vertical axis shim coils had 50 turns, a total diameter of 160mm and a separation of 120mm, giving a field of  $1.3\text{GA}^{-1}$ . Square shim coils were used for the other two axes, composed of 90 turns with a side length of 110mm. Separated by 180mm, they provide a compensating field of  $3\text{GA}^{-1}$ .

### 3.4.4 Water Cooling

Due to the design of our coils, a current of 20A is required to obtain a magnetic field gradient of  $100\text{Gcm}^{-1}$  during the radio-frequency evaporation stage of the experiment, and such high currents remaining on during the radio frequency evaporative stage causes a considerable amount of heating.

To counteract the heating problem, we set up water cooling through our 3D coils using the  $6\text{mm}\times 6\text{mm}$  channel and the connectors seen in Figure 3.11b. This allows water at a temperature of  $15^\circ\text{C}$  to be continually cycled through the coils for the duration of the experiment. For this application we use a chiller (Kühlmobile, Van der Heijden).

To test the water cooling response of the coils, we operated them offline before implementing them into the experimental setup. We chose a 15s on-off duty cycle to be safe - in a real experimental run, the coils operate at the maximum current of 20A for just over 10s, while for all other stages the current is either at the much lower MOT or expanded field values. To monitor the temperature response of the coils, we use thermocouples on both coils - one situated in the inner part of the coil winding (placed when the coil was initially wound) and one placed on the outside of the coil winding. The inner thermocouple of one of the coils (coil B) stopped working soon after testing began and so we only had 3 thermocouples to monitor, but the inner thermocouple of coil A should indicate the hottest part of the coil former.

A quick test of the response of the coils at the MOT gradient value ( $17\text{Gcm}^{-1}$  field gradient requiring 3.4A of current) shows that even without water cooling the temperature only increased a few degrees over the course of 10 minutes with a 15s on-off duty cycle (Figure 3.15a) - nevertheless the water cooling will still be on as the MOT is loading at this current value. Figure 3.15b shows the temperature of the coils while being operated at a current of 20A with the 15s duty cycle - even after a few cycles, there is a clear increase in temperature, showing the need for water cooling. With the water cooling on, the response of the coils is shown in Figure 3.15c - the water cooling helps to keep the coils at a nearly constant temperature over the course of 10 minutes.

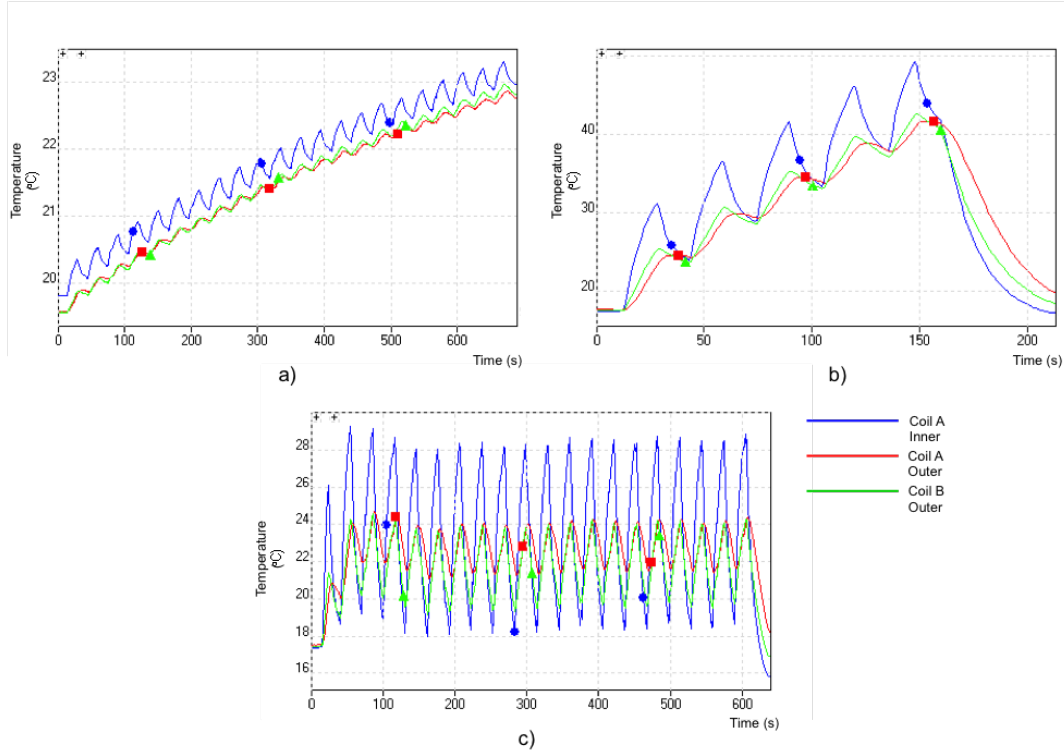


Figure 3.15: a) Temperature of coils operated at 3.4A without water cooling; b) Temperature of coils operated at 20A without water cooling; c) Temperature of coils operated at 20A with water cooling at 15°C.

### 3.5 MOT Optimisation

When loading our MOT we aim to capture in the region of  $10^9$  atoms or more to ensure we have a significant atom number before the evaporative cooling phase. There are various parameters to optimise at this stage, including the various powers and detunings of both the 2D MOT and 3D MOT, the alignment and power of the push beam and the magnetic field gradients.

To characterise the loading of the MOT, we record the fluorescence emitted by the MOT as it loads with a photodiode (Thorlabs DET100A/M) and a 60mm lens in a 2f-2f configuration, placed on one of the horizontal viewports that is not used for laser cooling. The photodiode reading can be converted to an estimate of the atom number using equation 2.5.

A plot of the atom number vs time can be drawn in real-time to quickly convert the photodiode reading into a loading curve for the MOT. Plots of the atom number vs laser

power are shown in Figure 3.16, when performing optimisation of the total atom number in the 3D MOT as a function of 2D repumper, 2D cooling, 3D repumper and 3D cooling laser power. Loading times for the data in Figure 3.16 was 10s.

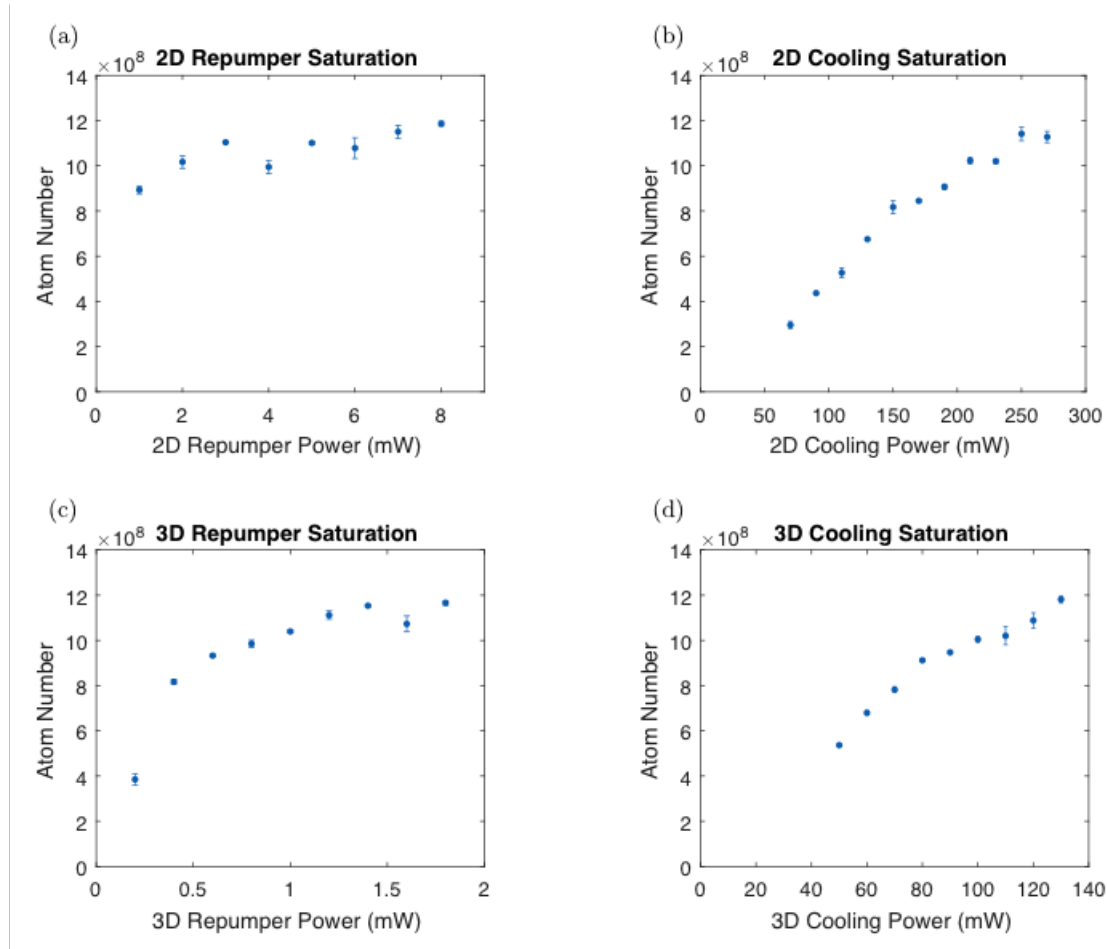


Figure 3.16: MOT optimisation data taken by recording the atom number in the 3D MOT as a function of different laser powers. More cooling power could lead to a further increase in atom number based on the data, but more repumper power would not necessarily be beneficial.

Further optimisation tests were performed by changing the magnetic field gradient and detuning of the 2D MOT, magnetic field gradient and detuning of the 3D MOT, and the push beam power (Figure 3.17). All optimisations were performed by monitoring the atom number in the 3D MOT.

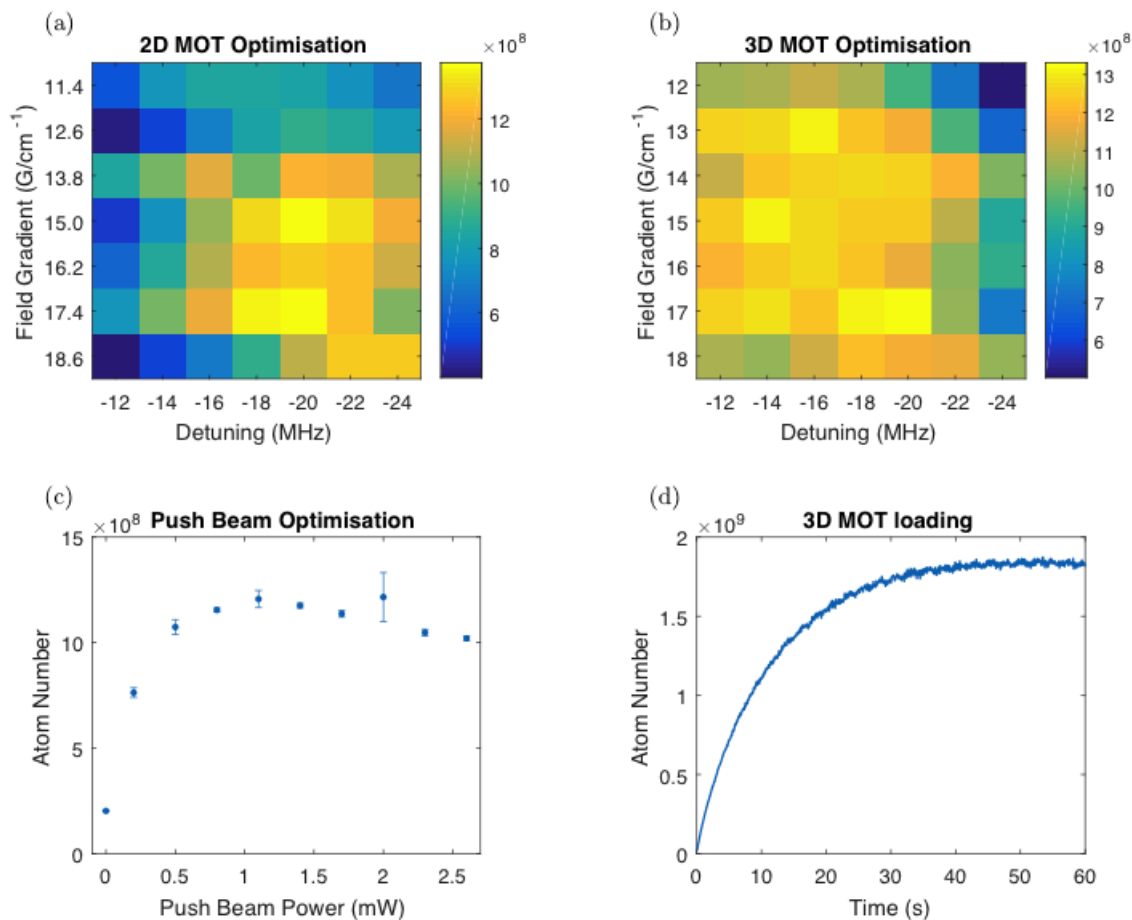


Figure 3.17: Further 3D MOT optimisation; a) 2D MOT optimisation with  $\delta_{3D} = -15\text{MHz}$  and  $3D B' = 15\text{Gcm}^{-1}$  (although the plot still shows the 3D MOT atom number and the optimisation is performed on this); b) 3D MOT optimisation with  $\delta_{2D} = -20\text{MHz}$  and  $2D B' = 15\text{Gcm}^{-1}$ ; c) Push beam power optimisation, with  $\delta_{3D} = -15\text{MHz}$ ,  $3D B' = 15\text{Gcm}^{-1}$ ,  $\delta_{2D} = -15\text{MHz}$ ,  $2D B' = 15\text{Gcm}^{-1}$ ; d) Example MOT loading curve.

The optimised parameters for both the 2D MOT and 3D MOT stage are shown in table 3.2. After the MOT fully loads, there is a short optical molasses stage, which results in colder clouds before the transfer to the magnetic trap. The sub-Doppler cooling mechanism from this process results in the following temperature dependence [116]:

$$k_B T \propto \frac{I}{|\delta|} \quad (3.5)$$

with  $T$  being the temperature of the atoms,  $I$  the intensity of the cooling beams and  $\delta$  the

detuning. Increased detuning from resonance plus lower intensity of the cooling beams will result in colder clouds, and in our experiment we ramp the detuning from the MOT value of -20MHz to the molasses value of -60MHz over 5ms. Removing the magnetic field during this process is also necessary, so we additionally ramp down the magnetic field from the MOT value of  $17\text{Gcm}^{-1}$  to 0 over the 5ms time period. The optical molasses period then lasts 10ms before the next experimental stage. After optical molasses our cloud temperature is approximately  $(50 \pm 4)\mu\text{K}$ . Optimisation of the molasses was performed by monitoring the temperature of the cloud and appropriately changing the duration and detuning values.

Parameter	2D MOT	3D MOT
Power per cooling beam (mW)	41.7	20
Total repumper power (mW)	8	1.8
Detuning (MHz)	-20	-20
B' ( $\text{Gcm}^{-1}$ )	15	17
Shim coil (along x) (G)	2	1.5
Shim coil (along y) (G)	-	1.1
Shim coil (along z) (G)	1.5	0

Table 3.2: MOT parameters. For the 2D MOT detuning, we later found that a value of -15MHz led to slightly colder temperatures of a similar atom number when transferring to the magnetic trap. Subsequent data is therefore taken with -15MHz 2D MOT detuning.

### 3.6 Optical Pumping

Once the optical molasses stage has completed, an optical pumping stage is performed on the atoms in order to ensure a significant capture into the magnetic trap in preparation for evaporative cooling. For a purely magnetic trap, the energy of the atoms  $U$  in an inhomogeneous magnetic field is:

$$U = g_F m_F \mu_B B \quad (3.6)$$

where  $g_F$  is the Lande g-factor,  $m_F$  is the magnetic sub-level,  $\mu_B$  is the Bohr magneton and  $B$  is the magnetic field. For the  $F = 2$  energy level, the Lande g-factor is  $1/2$ , and if the product  $g_F m_F$  is positive, then the atoms will be attracted to regions of lower magnetic field in order to minimise their energy, resulting in the  $m_F = +1$  and  $m_F = +2$  sub-levels being magnetically trappable. Without any optical pumping, one would only expect to trap atoms that are in the magnetically trappable  $m_F = +1$  and  $m_F = +2$  sub-levels - atoms in the  $m_F = -1$  and  $m_F = -2$  sub-levels are actually high field seekers, attracted to regions of higher magnetic field in order to lower their energy and thus will not be captured in the magnetic trap. In order to capture more atoms into the magnetic trap, the compensating

shim coils along the optical pumping axis are switched off, which returns the presence of the small background magnetic field, and a short ( $500\mu\text{s}$ ) pulse of  $\sigma^+$  light is directed onto the atoms. The small magnetic field lifts the degeneracy of the magnetic sub-levels of the  $F = 2$  state, which then allows the  $\sigma^+$  pulse to swiftly pump the atoms into the magnetically trappable  $m_F = +1$  and  $m_F = +2$  states (Figure 3.18). Spontaneous emission means the atoms can relax back to any sub-level within the selection rules criteria, but the  $\sigma^+$  light means that it can only pump atoms into a sub-level where the change in  $m_F$  is  $+1$ , and so in this way the atoms can be optically pumped to a magnetically trappable sub-level for the magnetic trap to be turned on again.

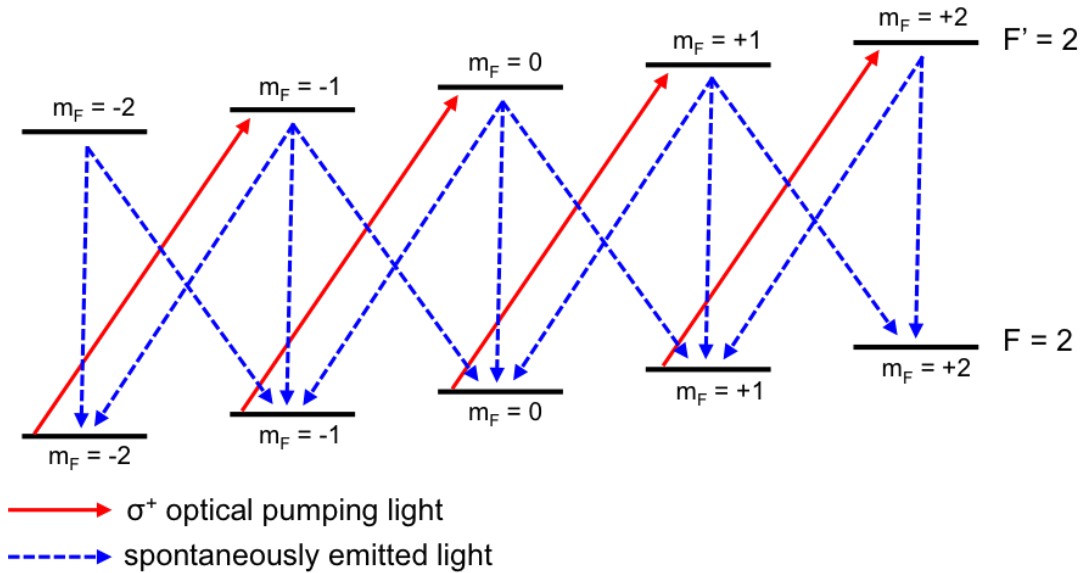


Figure 3.18: Optical pumping schematic. The selection rule governing the  $\sigma^+$  transition means only a change of  $m_F$  of  $+1$  is allowed, allowing the build up of atoms to the magnetic trappable states.

Using this method, we are able to increase the number of atoms captured into the magnetic trap by about a factor 3, as seen in the example plot of Figure 3.19. After the optical pumping pulse has completed, the AOM used to produce the short pulse is switched off and the shutter is then put down to block the light. Additionally it is important that the 3D MOT repumper is left on throughout the optical pumping to avoid sending the atoms to the  $F = 1$  ground state.

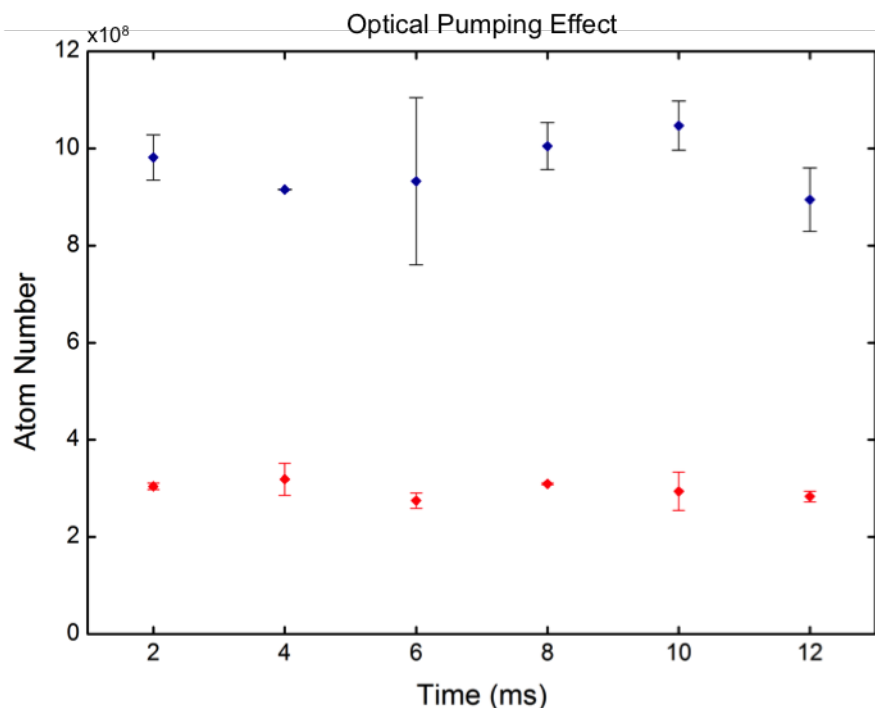


Figure 3.19: Example plot of the effect on atom number in the magnetic trap with (blue) and without (red) optical pumping. Error bars are the scatter in atom number over multiple runs. The time indicates the time-of-flight expansion before absorption imaging takes place. The optical pumping gives an increase in atom number of about a factor 3, which is close (within the error bars) to the theoretical value of 2.5.

### 3.7 Imaging

Absorption imaging is used to obtain information about the atoms for all stages once the MOT has fully loaded. A short pulse of resonant light is sent onto the atoms and recorded by a camera. Two further images of the same duration are also used in order to extract quantitative information about the atoms - another imaging pulse of the same duration to detect the imaging beam alone (i.e. with no atoms present) and an image of the background light without the imaging beam (Figure 3.20). From these images, an estimate of the atom number can be extracted. As well as atom number, the temperature of the cloud can be determined using time-of-flight measurements.

For a determination of the atom number, the Beer-Lambert law describes the intensity of a beam decaying exponentially as it passes through an atomic cloud [110]. As long as the light intensity is well below the saturation intensity of the transition, then the intensity

of the light can be described as:

$$I_{out}(x, y) = I_{in}(x, y) \exp \left( - \sigma(\omega) \int_{z_1}^{z_2} n(x, y, z) dz \right) \quad (3.7)$$

with the light propagating in the z-direction. In equation 3.7,  $\sigma(\omega)$  is the scattering cross section for absorption,  $n(x, y, z)$  is the number density of the cloud, and the integral spans the entire cloud size. For atoms that do not have a quantisation axis and with the Zeeman sub-levels degenerate, the scattering cross section is written as:

$$\sigma(\omega) = \frac{\sigma_{0(iso,eff)}}{1 + \left( \frac{2(\omega - \omega_0)}{\Gamma} \right)^2} \quad (3.8)$$

with  $\omega - \omega_0 = \delta_{Img}$  and  $\sigma_{0(iso,eff)} = 1.36 \times 10^{-13} \text{ m}^2$  [117], which is the resonant scattering cross section for isotropic light polarisation between the  $F = 2 \rightarrow F' = 3$  transition for the D2 line. The integral of equation 3.7 gives a column density:

$$\begin{aligned} n_{2D}(x, y) &= \int_{z_1}^{z_2} n(x, y, z) dz \\ &= \frac{1}{\sigma(\omega)} \ln \left( \frac{I_{in}(x, y)}{I_{out}(x, y)} \right) \\ &= \frac{1}{\sigma(\omega)} \text{OD}(x, y) \end{aligned} \quad (3.9)$$

where  $\text{OD}(x, y)$  is the optical density. The atom number  $N$  can then be obtained by summing over the pixels of the image:

$$N = \frac{1}{\sigma(\omega)} \left( \frac{d_{px}}{M} \right)^2 \sum_{ij} \text{OD}(i, j) = \frac{1}{\sigma(\omega)} \left( \frac{d_{px}}{M} \right)^2 \sum_{ij} \ln \left( \frac{I_{in}(i, j) - I_{bkg}(i, j)}{I_{out}(i, j) - I_{bkg}(i, j)} \right). \quad (3.10)$$

In equation 3.10,  $i$  and  $j$  denote the CCD camera pixel indices,  $d_{px}$  is the pixel pitch,  $M$  is the magnification of the imaging system,  $I_{out}(i, j)$  is the image of the absorption with the atoms present,  $I_{in}(i, j)$  is the image of the imaging beam without the atoms present and  $I_{bkg}(i, j)$  is the image of the background light without both the atoms and imaging light. This method assumes the optical density stays the same over each camera pixel. Images in our experimental sequence are separated by 200ms, and each pulse of imaging light lasts  $80\mu\text{s}$ . Figure 3.20 shows an example of the three images plus the resulting atomic cloud image.

The temperature of the cloud can be extracted by monitoring the width of the cloud during time of flight, which indicates the momentum distribution of the cloud. The velocity distribution of a thermal cloud along one axis is given by the standard Maxwell-Boltzmann distribution:

$$f(v_x) = \sqrt{\frac{m}{2\pi k_B T}} \exp \left( - \frac{mv_x^2}{2k_B T} \right) = \frac{1}{\sqrt{2\pi}\sigma_{v_x}} \exp \left( - \frac{v_x^2}{2\sigma_{v_x}^2} \right) \quad (3.11)$$

where  $T$  denotes the temperature of the atoms. For a ballistic expansion of the cloud, the final position of an atom is given by  $x = x_0 + v_x t$ , and the final distribution is:

$$n(x, t) = \frac{1}{\sqrt{2\pi}\sigma_x(t)} \exp\left(-\frac{x^2}{2\sigma_x(t)^2}\right) \quad (3.12)$$

and the width of the cloud,  $\sigma_x(t)$ , is:

$$\sigma_x(t) = \sqrt{\sigma_x(0)^2 + \frac{k_B T}{m} t^2} \quad (3.13)$$

A plot of the width of the cloud as a function of time allows the temperature  $T$  to be extracted.

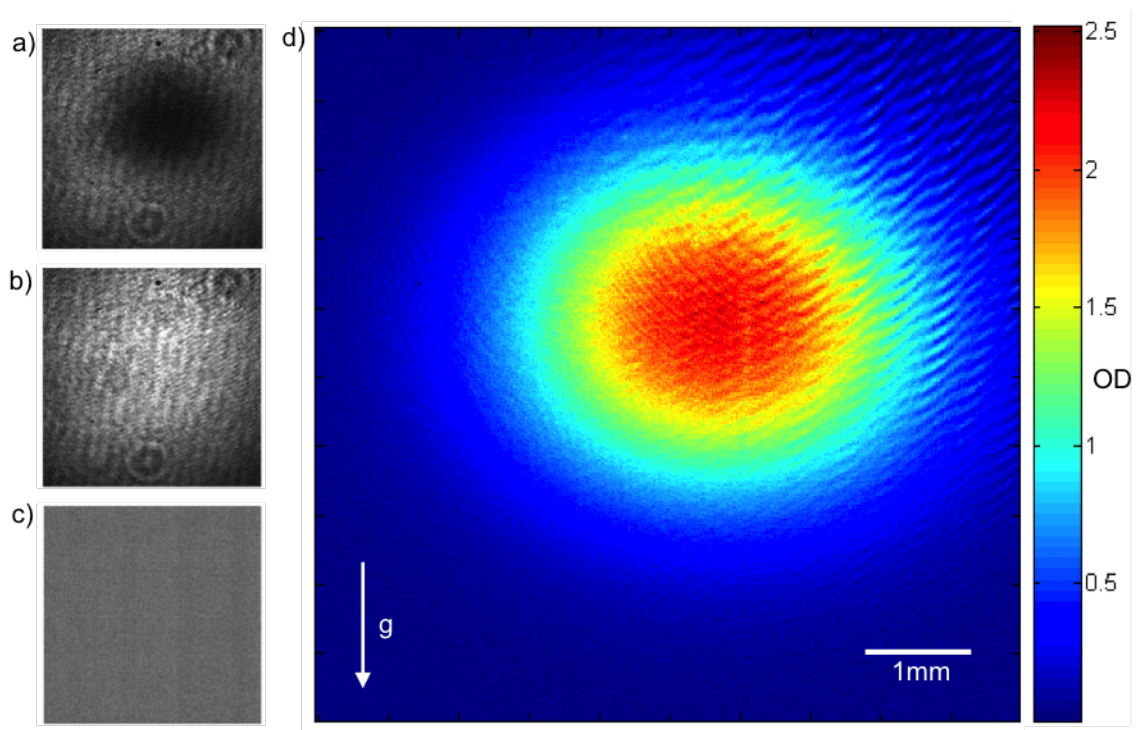


Figure 3.20: Example generation of an absorption image of an atomic cloud initially confined in the magnetic trap, taken after 10ms of time-of-flight. a) Shadow of the atomic cloud after absorption of the imaging beam; b) Imaging beam alone; c) Background light alone; d) Atomic cloud image obtained from the previous images.

To record the images we use an Andor Luca CCD Camera (1004×1002 pixels, pixel pitch 8μm), and imaging of the atomic cloud can be performed along either the horizontal

axis or the vertical axis as required. For the initial trapping of a fully loaded MOT in the magnetic trap, we use a horizontal imaging setup consisting of a 1:1 confocal telescope with two  $f=60\text{mm}$  achromatic doublet lenses. For later stages of the experiment e.g. after evaporation when magnification is required, we swap out the second  $f=60\text{mm}$  lens and replace it with a  $f=150\text{mm}$  focal length doublet to provide a 1:2.5 confocal telescope, also moving the position of the camera further back to compensate (Figure 3.21).

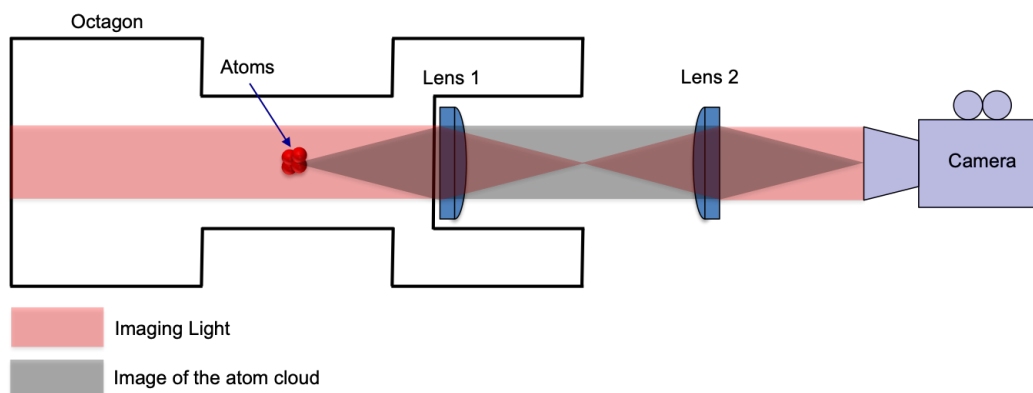


Figure 3.21: Setup used for horizontal imaging of the atomic cloud. Lens 1 has a focal length of 60mm, while lens 2 is either a 60mm focal length lens or 150mm focal length lens (if magnification is desired) - if so the camera position can be moved back.

The vertical imaging setup is slightly more complex - the lens located in the vertical recess on the bottom of the octagon has three separate beams passing through it:

- a MOT beam incident on the atoms from below, which must be collimated at the position of the atoms;
- an SLM beam incident on the atoms from below, which must be focused at the point of the atoms (more details in chapter 4);
- a vertical imaging beam from above, meaning the lens must collimate the shadow originating from the atomic cloud.

To accommodate this, we use the setup shown in Figure 3.22. Within the recess is a  $f=40\text{mm}$  focal length lens, chosen to provide the most detailed SLM patterns originating from the SLM (high N.A., small diffraction limit). A second  $f=40\text{mm}$  focal length lens, set up as a 1:1 confocal telescope with the first lens, keeps the initially collimated MOT beam unchanged, with only a slight loss of power that can be addressed. The short focal length lenses chosen mean that the first image plane in this setup forms only 160mm from where the atoms are, meaning it is almost impossible to place the camera at this point. To

address this, we use another pair of lenses to create a second image plane on the camera. By inserting a dichroic mirror (Thorlabs DMSP1000L) and a PBS between the two sets of lenses, it allows the SLM light and MOT beam to be separated from the second set of lenses, leaving just the imaging beam, which can then be magnified. To do this we use a  $f=75\text{mm}$  doublet and  $f=200\text{mm}$  singlet lens to give a magnification of 2.67.

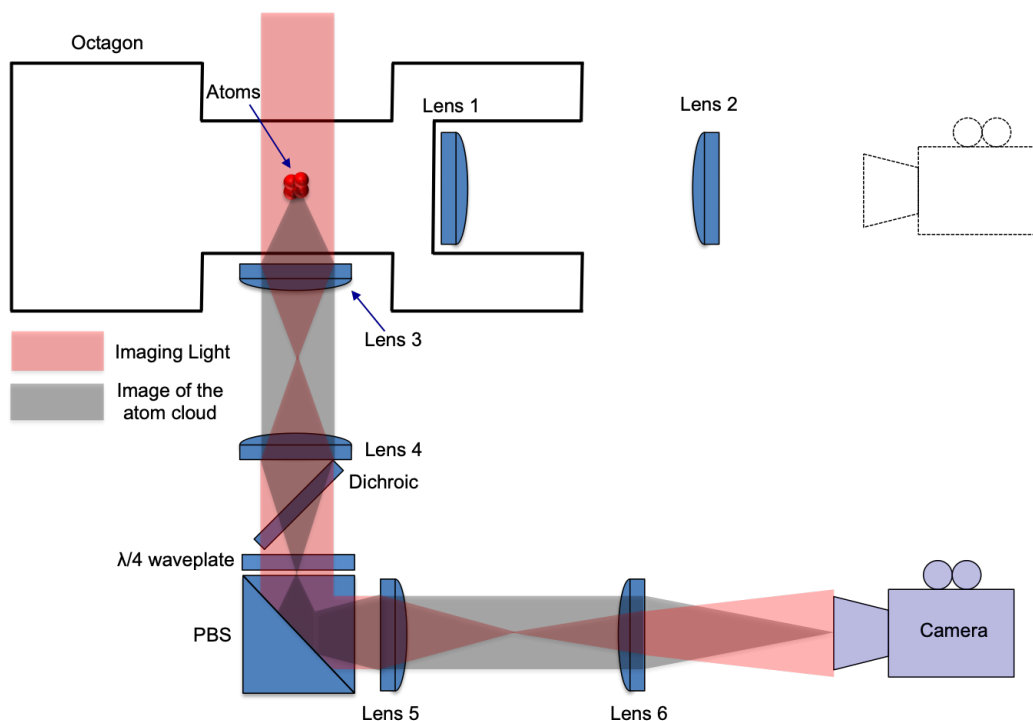


Figure 3.22: Setup used for vertical imaging of the atomic cloud. Lens 3 and lens 4 have a focal length of 40mm, lens 5 has a focal length of 75mm, and lens 6 has a focal length of 200mm. The dichroic reflects the incoming 1064nm light originating from the SLM, and transmits 780nm light (MOT beam and imaging beam). The PBS transmits the MOT beam (coming from below), while the imaging beam is reflected, allowing the magnifying telescope to be set up.

## 3.8 Evaporative Cooling

### 3.8.1 Hybrid Trap Design

Our experimental procedure for the evaporative cooling stage involves a hybrid trap - a first stage of radio-frequency (RF) evaporative cooling in a purely magnetic trap, followed by an adiabatic transfer to a high power focused optical dipole trap whereby the optical

power is slowly reduced over time. In both cases, selective removal of the hottest atoms in the ensemble allows the remaining atoms to re-thermalise at a lower temperature, resulting in a gradual increase in phase space density. The schematic of our hybrid trap design is shown in Figure 3.23, where the plot shows the potential experienced by the atoms under the effects of gravity, the magnetic trap and the optical dipole trap.

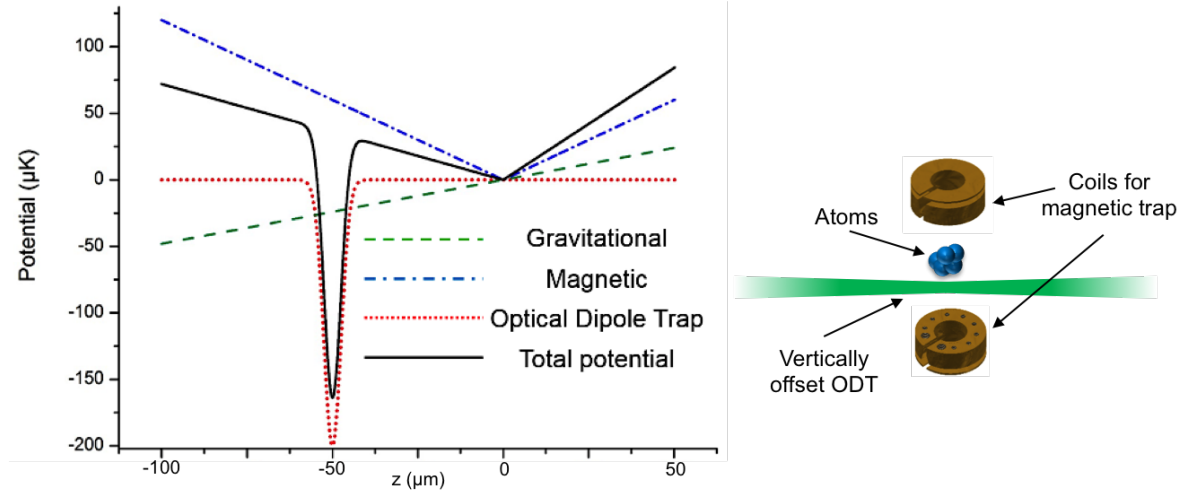


Figure 3.23: Graph showing the potential experienced by the atoms as a function of vertical ( $z$ ) position. When the magnetic field gradient is relaxed, the magnetic potential decreases until the atoms are transferred into the optical dipole potential instead. The image alongside shows the vertical offset of the ODT from the zero point of the magnetic field.

For the RF evaporation in the magnetic trap, the compression to  $100\text{Gcm}^{-1}$  provides a strong confinement as the RF knife sweeps through the atoms. After this process has completed, the atoms must be transferred to the optical dipole trap for further evaporation. To avoid potential losses arising from Majorana spin flips near the zero point of the magnetic field, the optical dipole trap is vertically offset from the centre of the magnetic trap (see Figure 3.23). To perform the transfer, the magnetic field gradient is relaxed from its compressed value down to a much shallower gradient such that the vertical component is just unable to support the atoms against gravity - the result of this is that the atoms are slowly transferred into the deep optical potential. Once the transfer has completed, evaporative cooling can continue in this combined (hybrid) potential.

Before the beginning of the evaporative cooling sequence, we load  $(1.2 \pm 0.05) \times 10^9$  atoms at a temperature of  $(244 \pm 8)\mu\text{K}$  after the compression to  $100\text{Gcm}^{-1}$ . The typical lifetime  $\tau$  of the atomic cloud in the magnetic trap is  $>60\text{s}$ ; an example lifetime measurement with  $\tau = (138 \pm 46)\text{s}$  is shown in Figure 3.24.

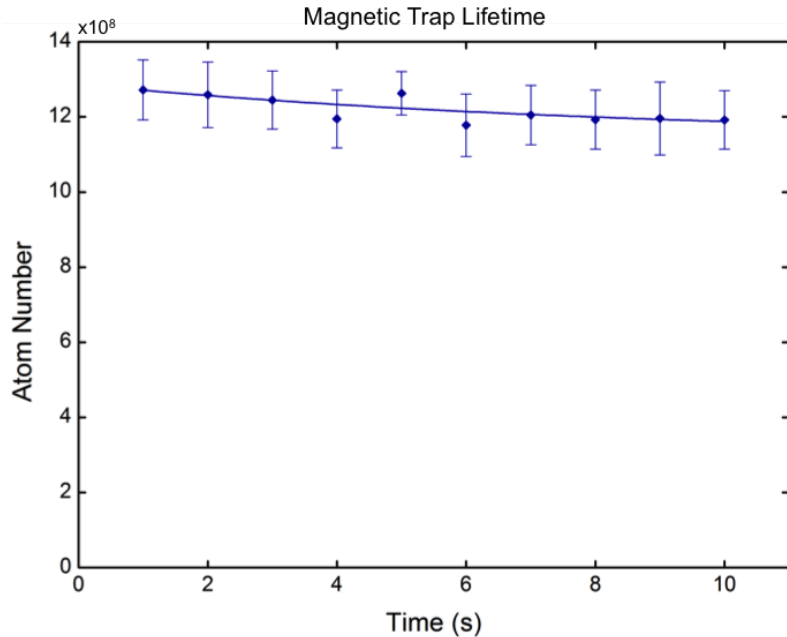


Figure 3.24: An example magnetic trap lifetime measurement. The lifetime was measured to be  $\tau = (138 \pm 46)\text{s}$  for this particular run - this lifetime is consistent with a pressure of  $10^{-11}\text{Torr}$ .

### 3.8.2 Radio-frequency Evaporation in the Magnetic Trap

In terms of our experimental procedure, the RF evaporation stage begins immediately following the compression of the atoms in the magnetic trap (to  $100\text{Gcm}^{-1}$ ). The schematic of this RF evaporation procedure is shown in Figure 3.25. In short, the hotter proportion of the atomic ensemble is transferred from a low-field seeking trapped magnetic sub-level ( $m_F = +2$ ) to a high-field seeking anti-trapped state ( $m_F = -1$  or  $m_F = -2$ ). With a large proportion of hotter atoms removed, the remaining atoms are able to re-thermalise via collisions resulting in a decrease of the temperature of the ensemble. One potential issue with this procedure is the degeneracy of the magnetic sublevels at the centre of the trap (where the magnetic field is zero; see Figure 3.25) - with no Zeeman splitting, atoms may undergo a spin-flip from a low-field seeking trapped state to a high-field seeking anti-trapped state, and since the coldest atoms will be located near the zero point, this would be a detrimental effect to happen when trying to achieve cold, dense clouds. It is for this reason that we set up our hybrid trap scheme to allow us to continue to evaporatively cool the atoms and avoid the losses through Majorana spin flips.

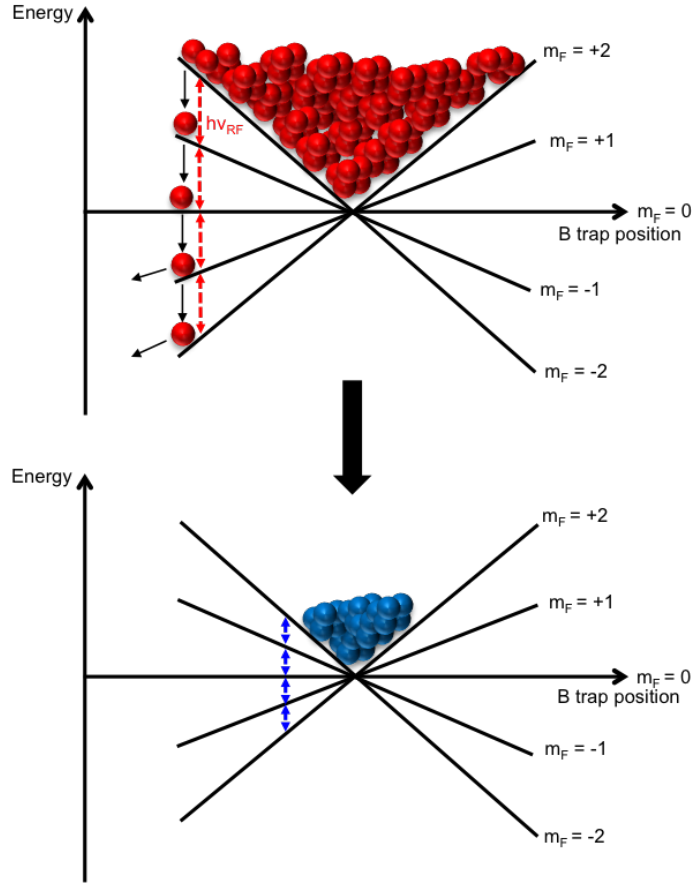


Figure 3.25: Schematic of RF evaporation in a purely magnetic trap. The more energetic atoms are flipped from a low-field seeking trapped state to a high-field seeking anti-trapped state.

To generate the RF radiation we use a setup consisting of two single loops of wire in the Helmholtz configuration, wound around the existing magnetic coils for the 3D MOT. The sweep itself is output from a TTI TG2000 function generator. The power of the RF radiation from the function generator is not enough to expel atoms from the magnetic trap and so we connected the output of the function generator to a 40dB gain RF amplifier (Mini Circuits ZHL-5W-1), which has a maximum output power of 5W. A  $50\Omega$  RF terminator is connected in series with the coils for impedance matching, while the function generator is connected to the amplifier via a combination of attenuators and a limiter (Mini Circuits VLM-33W-2W-S+), set up to ensure the input power to the amplifier does not exceed the designated maximum.

As seen in Figure 3.25, the amount of splitting of the magnetic sub-levels increases with

magnetic field strength and, subsequently, with distance from the trap centre. The function generator has a maximum RF frequency output of 20MHz, but in our case we found that almost no atoms were evaporated in the range 20→17MHz. For this reason we chose 17MHz as the starting point for our sweep. Other parameters to optimise include the amplitude of the output, end frequency point and duration of the sweep. We found that a 1V peak-to-peak signal output from the function generator did not cause significant evaporation and so we chose to work with a 2V peak-to-peak output signal. The end frequency point should be chosen such that a significantly low enough temperature is reached in order to transfer to the optical dipole trap, but not sweeping too far such that atoms start to be lost to the Majorana spin-flips. In our case, the end point of our sweep is set to be 1.4MHz. The duration of the sweep can be shortened or extended depending on the collision rate - if the collision rate is low, the sweep time can be extended to allow the atoms more time to re-thermalise via collisions. We found that a sweep duration of 10s proved sufficient for a magnetic trap with a  $100\text{Gcm}^{-1}$  field gradient - further compression could be used to lower the sweep duration but we found the increased heating imparted to the atoms to be too detrimental. Segmented ramps were also attempted but it was found that the linear ramp gave the best results.

Therefore, the full RF sweep we use is a 10 second sweep from 17MHz to 1.4MHz at a 2V peak-to-peak output amplitude. At the conclusion of the sweep, absorption images taken indicate the atom number is  $(2.4 \pm 0.5) \times 10^7$  atoms, at a temperature of  $(19.7 \pm 0.25)\mu\text{K}$ . Values for the atom number  $N$  and temperature  $T$  can be used to obtain the phase space density (PSD) for the atomic cloud, which is used as the optimisation parameter when performing the evaporation. In the purely quadrupole magnetic trap, the phase space density is written as [20]:

$$\text{PSD} = \frac{N}{32\pi} \left( \frac{\mu_B B'}{k_B T} \right)^3 \left( \frac{2\pi\hbar^2}{mk_B T} \right)^{\frac{3}{2}} \quad (3.14)$$

where  $B'$  is the axial magnetic field gradient and  $\mu_B$  is the Bohr magneton. With equation 3.14 the PSD of the atomic cloud can be calculated for various stages of the RF evaporation. At the end of the RF evaporation, a phase space density of  $(6.9 \pm 1.1) \times 10^{-4}$  is achieved using the atom number and temperature from above. A PSD plot showing the effect of the evaporation on the phase space density as the sweep progresses is shown in Figure 3.26.

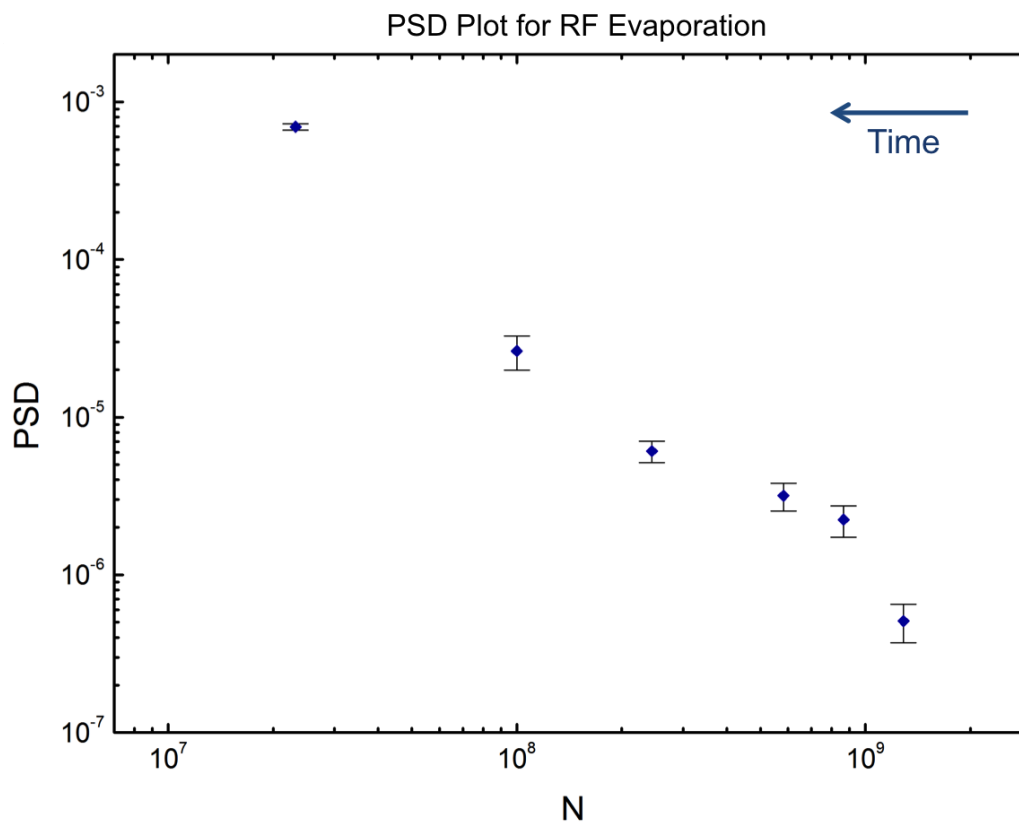


Figure 3.26: The PSD plot for the radio frequency evaporation procedure. The rightmost value is the PSD directly after compression to  $100\text{Gcm}^{-1}$  in the magnetic trap. The leftmost value is the PSD at the conclusion of the RF sweep.

### 3.8.3 Optical Evaporation in a Focused ODT

Further evaporation proceeds using a focused 1064nm optical dipole trap. Far away from atomic resonance, the scattering force prominent in the laser cooling process becomes negligible and the atoms experience a purely conservative potential in the presence of the light - a concept known as the gradient force. The potential experienced by the atoms depends on the detuning and intensity of the light. For red-detuned light, atoms will be attracted to regions of higher intensity, allowing a trap to form at the focus of a single laser beam (Figure 3.27).



Figure 3.27: a) The atomic ground state is shifted to lower energy while in the presence of far red-detuned light; b) In the case of a Gaussian laser beam, the corresponding shift for the ground state resembles a well that reflects the Gaussian nature of the trapping laser, causing the atom to sit at the lowest potential (highest intensity).

Our focused optical dipole trap is produced using a fibre laser (IPG Photonics, YLP-5-1070-LP), capable of a maximum 5W output at a wavelength of 1064nm. The beam has a  $1/e^2$  waist of 1mm; to produce a planned spot size of  $50\mu\text{m}$ , we use the following combination of lenses in our optical setup - a 150mm lens and two 60mm lens, one of which is already in place in the horizontal recessed viewport. At 100% power, which corresponds to roughly 3.5W being directed onto the atoms after taking into account reflection and transmission losses, a trap with an estimated depth of  $120\mu\text{K}$  is created. A diagram showing the beam path is displayed in Figure 3.28.

For the initial alignment we are able to make use of the overlap with the horizontal imaging beam to align the ODT beam roughly onto the centre of the imaging beam. The confinement of the ODT beam is fairly weak along the propagation axis, but initial coarse alignment could be performed by looking at absorption images of the cloud after the RF evaporation with the ODT beam on and off - coarse alignment was achieved when a slight increase in the density of the cloud could be observed when the ODT was on. Further optimisation could be performed by optimising the atom number and temperature after the transfer.

To perform the transfer, the magnetic field gradient is ramped down from  $100\text{Gcm}^{-1}$  to a designated lower value (below the MOT value of  $17\text{cm}^{-1}$ ) such that the gradient just under-compensates gravity along the vertical (so that atoms can still escape when the optical evaporation is performed). The best value for us was deemed to be  $14\text{Gcm}^{-1}$  - any higher and we found that some atoms eventually returned to the camera field of view after a long enough wait time and so they hadn't managed to escape the trap. We perform our field relaxation in a time of 1s. The optimal position of the ODT in the vertical direction was  $60\mu\text{m}$  below the zero point of the magnetic trap.

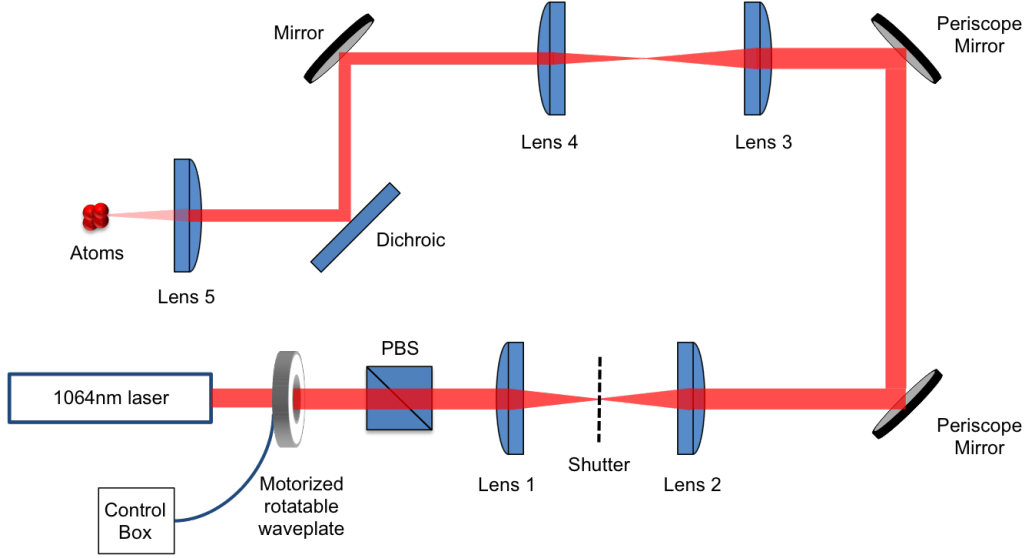


Figure 3.28: Optical setup for the horizontal ODT light. Some additional mirrors before the motorised waveplate are omitted for clarity. The lenses have the following focal lengths: Lens 1 = 100mm, Lens 2 = 100mm, Lens 3 = 150mm, Lens 4 = 60mm, Lens 5 = 60mm. Lens 1 is mounted on a translation stage.

To carry out evaporative cooling, we use a  $\lambda/2$  waveplate mounted on a motorised rotatable stage (Thorlabs PRM1Z8 and TDC-001) next to a PBS - as the waveplate is rotated the power of the optical dipole trap is reduced steadily. As seen in Figure 3.28, a 1:1 confocal telescope is placed after the PBS to allow a mechanical shutter to be placed in the focus of this telescope, allowing it to block off the light effectively. The first lens of this telescope is additionally mounted on a translation stage, which allows for the focus of the ODT to be shifted if necessary. To avoid overheating and damaging the shutter, the ODT is let through onto the atoms from the beginning of the experimental sequence - no change in atom number or temperature was observed in the early stages of the sequence when taking data and leaving the ODT on or off.

With the setup established, the optimised transfer into the ODT led to an atom number of  $(1.0 \pm 1.6) \times 10^7$  atoms at a temperature of  $(8.8 \pm 0.1) \mu\text{K}$ . The lifetime in the ODT was measured to be  $(29.5 \pm 9.4)\text{s}$ , reduced from the longer magnetic trap lifetime due to the finite optical trap depth, resulting in some free evaporation. An example lifetime plot is shown in Figure 3.29.

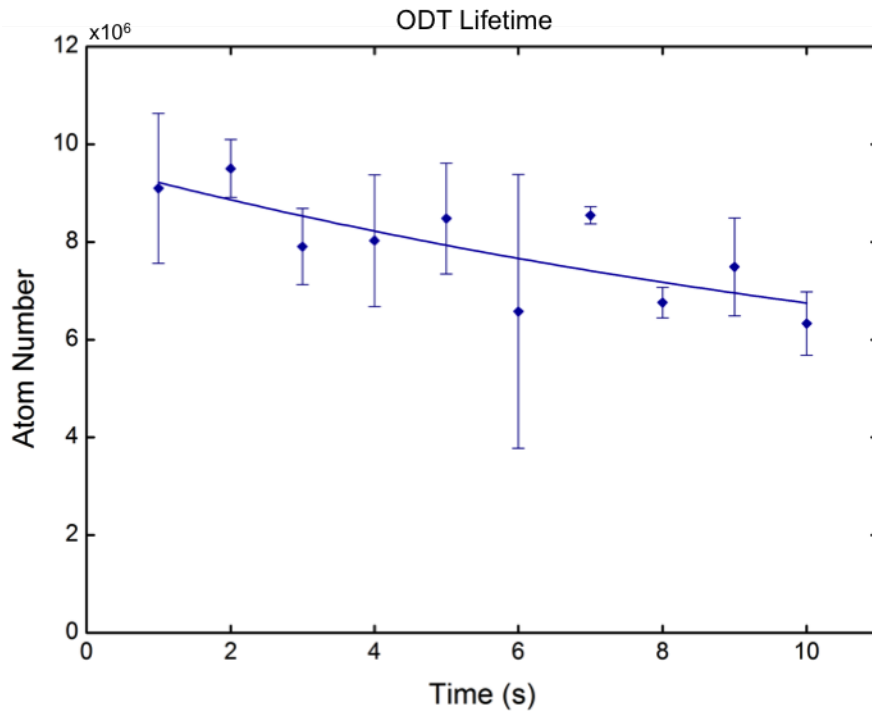


Figure 3.29: An example lifetime measurement obtained for atoms held in the ODT, measured as  $\tau = (30 \pm 9)$ s.

Performing the transfer results in an increase in the PSD, which can be calculated from the following equation:

$$\text{PSD} = N \left( \frac{\hbar}{k_B T} \right)^3 \frac{1}{\sqrt{\omega_x \omega_y \omega_z}} \quad (3.15)$$

where  $\omega_x = \frac{1}{2} \sqrt{\mu_B B' / m z_{min}}$  (under the assumption that the magnetic field dominates the confinement along the propagation of the beam, due to the relatively weak focusing of the ODT, and  $z_{min}$  is the distance below the zero point of the magnetic trap where the ODT is located),  $\omega_y = \omega_z = 2 \sqrt{U_0 / m w_0^2}$  (whereby the ODT confinement is dominant over the magnetic field along these axes) and  $U_0$  and  $w_0$  is the ODT trap depth and waist respectively.

After the transfer, evaporative cooling in the optical trap can proceed. The velocity with which the waveplate rotates is determined by the start and end points of the rotation, as well as the time taken. There is also a small period of acceleration and deceleration at the beginning and end of each ramp, but apart from those small windows the constant velocity ensures a linear rotation. The transmission and reflection response of the PBS is sinusoidal. Investigations with the optical evaporation involved different durations for the

ramps and also whether a single ramp or a double segmented ramp gave the best results. In our case, a double segmented ramp was decided upon, with an initial 100% to 30% power in 3s ramp succeeded by a 30% to X% ramp, where X is a user-defined final power, in 9s, giving a total of 12s duration optical ramp. A small amount of leakage light is present at the minimum position of the waveplate, but the power was measured to be about 10mW and no atoms were retained, allowing for full control over the evaporation process. A PSD plot of the full evaporation process combining both RF evaporation and optical evaporation is shown in Figure 3.30.

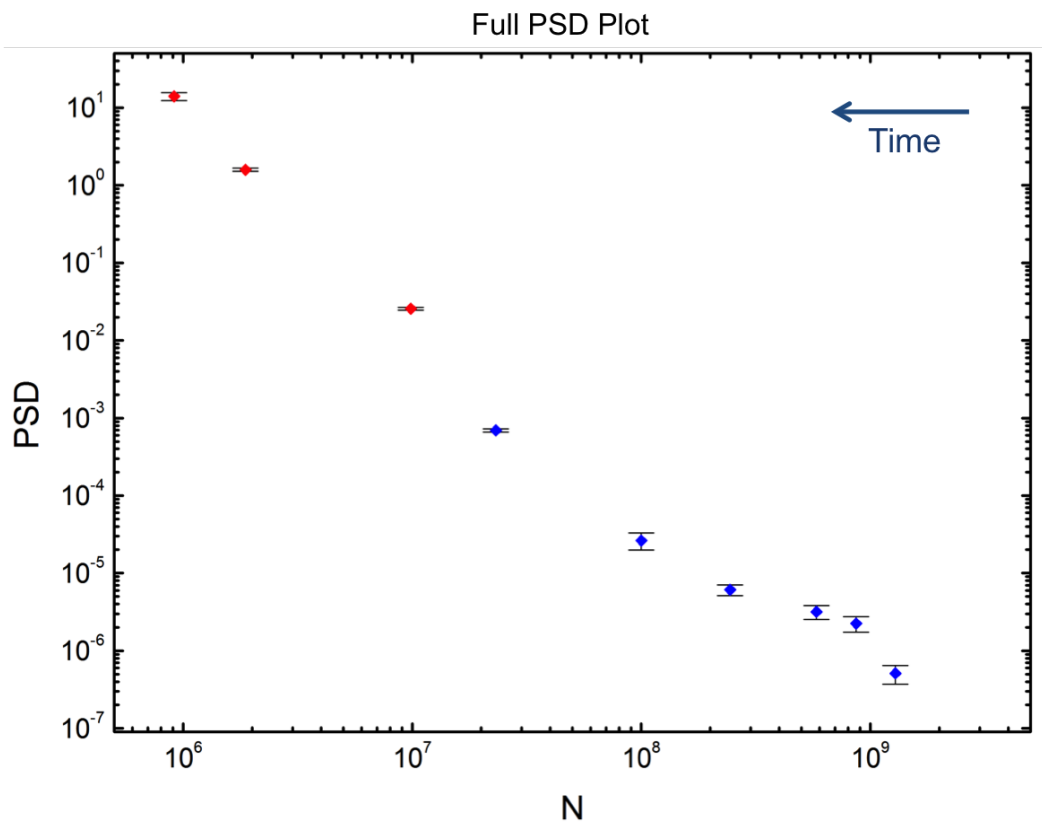


Figure 3.30: PSD plot for both RF evaporation and optical evaporation sequences. Data points in blue correspond to RF evaporation, while those in red correspond to optical evaporation in the hybrid trap.

### 3.9 Bose-Einstein Condensation

Further evaporation proceeds in the optical dipole trap until the onset of Bose-Einstein condensation can be observed. Absorption images obtained at long time-of-flight intervals reveal a bimodal distribution present in the cloud, indicating an accumulation of atoms in the lowest quantum state. For a harmonic potential, the condensed atoms take the form of an inverted parabola that is superimposed on top of the regular Gaussian distribution of atoms that have not condensed, with the fraction of atoms in this regime increasing as evaporation proceeds and the PSD increases. The presence of this central peak appearing on top of the regular thermal distribution of the atoms can be seen in Figure 3.31 below.

The density of the inverted parabola takes the form [110]:

$$n_{BEC}(x, y, z) = n_{BEC}(0, 0, 0) \left( 1 - \left( \frac{x^2}{R_x^2} + \frac{y^2}{R_y^2} + \frac{z^2}{R_z^2} \right) \right) \quad (3.16)$$

with a peak density  $n_{BEC}(0, 0, 0)$  at the centre of the trap and where the density goes to zero beyond the values of  $x = \pm R_x$ ,  $y = \pm R_y$  and  $z = \pm R_z$ . This bimodal distribution is retained and so it can be observed at the long TOF absorption images [118] seen in the Figures. As the absorption images taken provide the column density of the cloud, equation 3.16 needs to be integrated along the imaging ( $z$ ) axis:

$$\tilde{n}_{BEC}(x, y) = \tilde{n}_{BEC}(0, 0) \left( 1 - \frac{x^2}{R_x^2} - \frac{y^2}{R_y^2} \right)^{\frac{3}{2}}. \quad (3.17)$$

We approximate the non-condensed (thermal) fraction of the cloud below the critical temperature to a standard Gaussian distribution. For estimating the condensate fraction in the absorption images above, a combined fit comprising both a Gaussian fit and a Thomas-Fermi fit is performed on the cloud:

$$\begin{aligned} \tilde{n}_{total} &= \tilde{n}_{BEC}(0) \left( 1 - \frac{x^2}{R_x^2} - \frac{y^2}{R_y^2} \right)^{\frac{3}{2}} \\ &+ \tilde{n}_{Thermal}(0) \exp \left( - \left( \frac{x^2}{\sigma_x^2} + \frac{y^2}{\sigma_y^2} \right) \right). \end{aligned} \quad (3.18)$$

The overall function is integrated to give the total atom number  $N_{Tot}$ , while the integrated thermal function gives  $N_{Thermal}$ . These numbers are then used to obtain an estimate for the condensate fraction of the cloud.

The onset of Bose-Einstein condensation was observed for trap depths below  $2.88\mu\text{K}$ . The Gaussian component of the fit to the thermal cloud at this point (just as BEC onset occurs) can be used to give an estimate of the temperature of the cloud which in turn leads to an estimation of the critical temperature, which in our case comes out as  $T_C \sim 230\text{nK}$ . As can be seen from Figure 3.31, a 97% BEC is achieved at a trap depth of  $1.2\mu\text{K}$ , with an atom number of  $(1.95 \pm 0.3) \times 10^5$ .

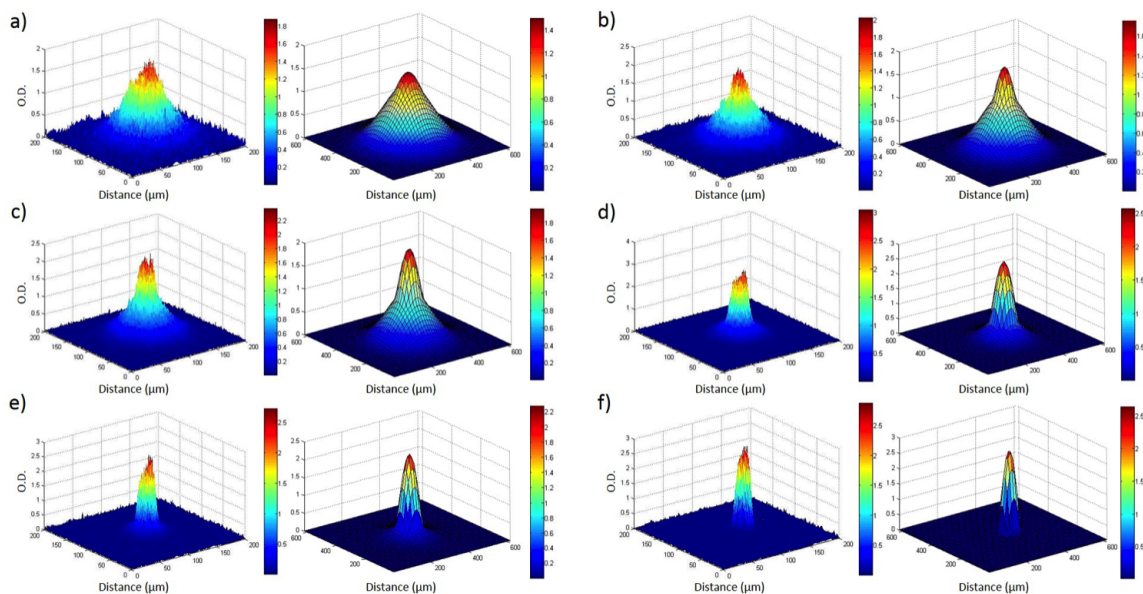


Figure 3.31: Absorption image surface plots (left) and associated fits (right) for atomic clouds at increasingly lower optical evaporation stages. Images taken with  $-4\text{MHz}$  detuning for the imaging beam and  $21\text{ms}$  TOF; a) Trap depth =  $2.88\mu\text{K}$ ,  $n_{Tot} = 1.54 \times 10^6$ ,  $n_{BEC}/n_{Tot} = 0.12$ ; b) Trap depth =  $2.76\mu\text{K}$ ,  $n_{Tot} = 1.16 \times 10^6$ ,  $n_{BEC}/n_{Tot} = 0.30$ ; c) Trap depth =  $2.40\mu\text{K}$ ,  $n_{Tot} = 1.08 \times 10^6$ ,  $n_{BEC}/n_{Tot} = 0.52$ ; d) Trap depth =  $1.80\mu\text{K}$ ,  $n_{Tot} = 6.09 \times 10^5$ ,  $n_{BEC}/n_{Tot} = 0.74$ ; e) Trap depth =  $1.44\mu\text{K}$ ,  $n_{Tot} = 3.65 \times 10^5$ ,  $n_{BEC}/n_{Tot} = 0.85$ ; f) Trap depth =  $1.20\mu\text{K}$ ,  $n_{Tot} = 1.95 \times 10^5$ ,  $n_{BEC}/n_{Tot} = 0.97$ .

A table summarising the optimised atom number, temperature and PSD for each of the main experimental stages is shown in Table 3.3.

Experiment Stage	Atom Number	Temperature ( $\mu\text{K}$ )	PSD
MOT Loading	$1.4 \times 10^9$	-	-
Optical Molasses	$1.4 \times 10^9$	50	-
Magnetic Trap Compression	$1.3 \times 10^9$	245	$5.0 \times 10^{-7}$
RF Evaporation	$2.4 \times 10^7$	19.6	$6.9 \times 10^{-4}$
ODT Transfer	$1.0 \times 10^7$	8.5	0.03
ODT Evaporation (Pure BEC)	$2.0 \times 10^5$	0.23	14.2

Table 3.3: Atom number, temperature and approximate PSD after each main experimental stage.

### 3.10 Full Experimental Sequence Procedure

The experiment is controlled and executed using the LabVIEW software program, which generates various analogue and digital signals that are then sent to the various computer-controlled parts of the experiment using two Data Acquisition (DAQ) cards (National Instruments PCI-6723 and PCI-6229).

A full experimental sequence example is shown in Figure 3.32. When this is run, the first step is that the motorised stage housing the waveplate rotates to its initial starting position (usually, maximum power available for the ODT). Once this has been set, the MOT then loads for a predetermined time (either 10 or 30 seconds) with a magnetic field gradient of  $17\text{Gcm}^{-1}$ . Once MOT loading has completed the 2D cooling, repumper and push beams are blocked using mechanical shutters (a time of about 6ms is sufficient for the shutters to close), at which point the optical molasses stage begins. The detuning of the 3D MOT beams is ramped from  $-20\text{MHz}$  to  $-60\text{MHz}$  in 5ms, while at the same time the magnetic field gradient is ramped down to zero from  $17\text{Gcm}^{-1}$ . Optical molasses lasts for 10ms. Following the optical molasses is the optical pumping stage into the appropriate magnetic sub-level, for which the 3D cooling beams and the shim coils along the optical pumping axis are switched off. A 0.5ms pulse of optical pumping light is sent using an AOM on the path to perform the optical pumping, and the 3D repumper stays on during this process until the OP shutter shuts once again (due to some small leakage through the OP AOM). Once all the 780nm laser light is switched off the OP axis shim coils are switched back on, along with the magnetic trapping coils, switched on at  $50\text{Gcm}^{-1}$  using a relay and ramped to  $100\text{Gcm}^{-1}$  in 100ms. The atoms are held at  $100\text{Gcm}^{-1}$  while the radio-frequency sweep proceeds over the next 10s, ramping from  $17\text{MHz}$  to  $1.4\text{MHz}$ . After a 300ms wait after the RF, the magnetic field gradient is expanded from  $100\text{Gcm}^{-1}$  down to  $14\text{Gcm}^{-1}$  in 1s, transferring the atoms to the full power ODT in the process. A 1s hold in the ODT allows for some free evaporation to occur before the trap depth is lowered. A two-stage ramp is then performed for the optical trap depth, from 100% to 30% in 3s, and then from 30% down to a user-specified final value in 9s with the motorised rotatable waveplate. Atoms can be held for a further 1s in the ODT for further free evaporation before the ODT is switched off using another mechanical shutter, at the same time the magnetic field gradient is switched off. A designated time-of-flight then occurs for the atoms, after which 3 pulses of imaging light are sent and the absorption images recorded by the Andor camera for analysis.

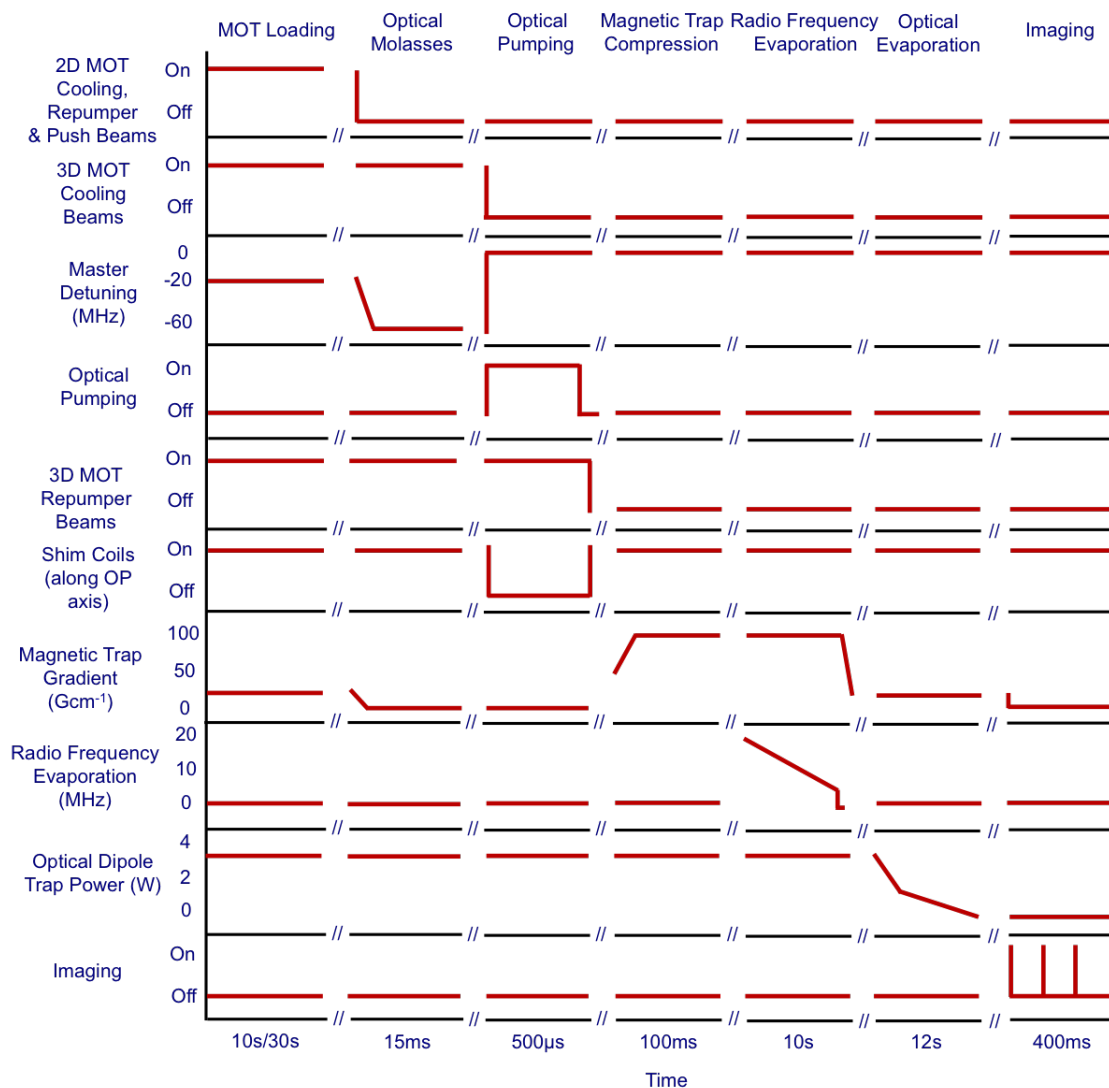


Figure 3.32: Schematic showing an example of a full experimental run. Shutters are omitted for clarity. The imaging stage pulse length is  $80\mu\text{s}$  per pulse.

The LabVIEW computer is networked to the analysis computer, where the images are analysed and data can be plotted and fitted. When an experimental sequence is initiated, a data package is sent to the analysis computer from the LabVIEW computer using the User Datagram Protocol (UDP), containing information such as the run number, variable parameters and camera settings. After the Andor camera is triggered and the three images are taken and saved at the analysis computer, fitting is automatically performed and

parameters such as atom number, cloud width, etc. are extracted from the image as the program updates. These parameters can be plotted in real time in the DatFitAna program, allowing for fast plotting of temperature fits, exponential curves, etc., as soon as an experimental run finishes. This data acquisition and analysis schematic is shown in Figure 3.33 below.

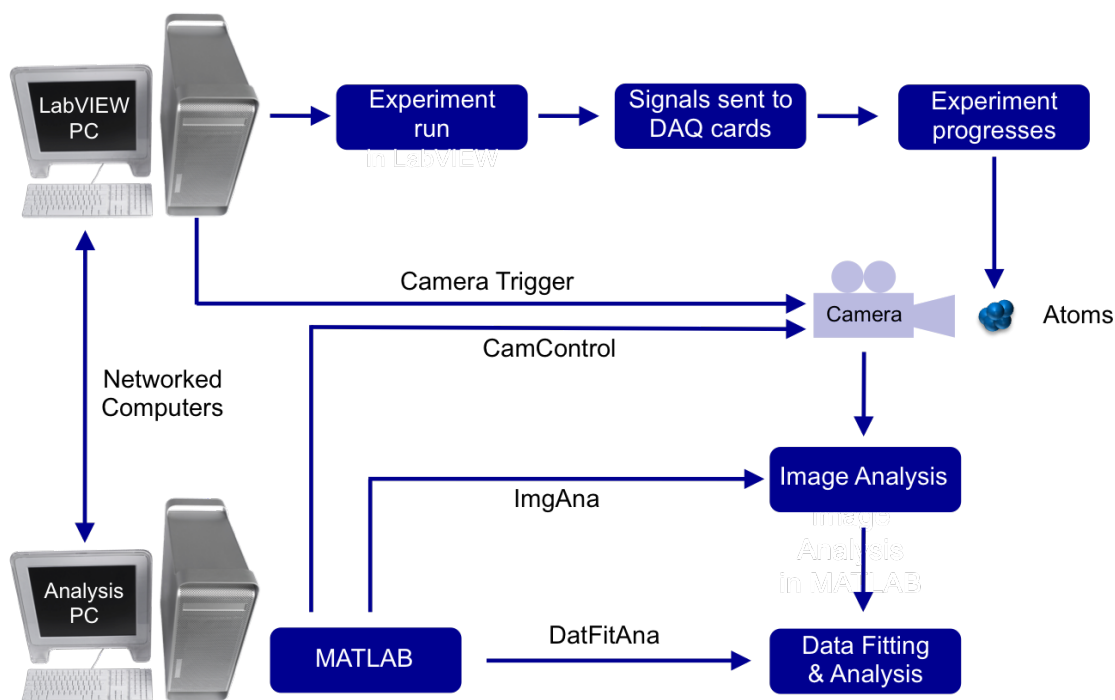


Figure 3.33: Diagram of the data acquisition and analysis setup for a typical experimental run.

### 3.11 Summary

In conclusion, we have designed and constructed a double vacuum chamber apparatus to realise the first BECs at St Andrews. This setup allows a significant atomic flux to be generated within the higher pressure 2D MOT loading chamber, while allowing a large MOT with a long lifetime to be loaded within the 3D MOT experiment chamber. MOT optimisation was performed over a large parameter space, after which the optimised fully loaded MOT is stored and compressed in a purely conservative quadrupole trap. A first stage of evaporative cooling using radio frequency evaporation is optimised by determining the phase-space density of the atoms at the conclusion of the sweep, after which the atoms are adiabatically transferred to a vertically offset, high power, far-detuned optical

---

dipole trap. Further evaporation, achieved by reducing the optical power, is successful in producing Bose-Einstein condensed atoms, with a 97% BEC obtained at an atom number of  $(1.95 \pm 0.3) \times 10^5$ .

## Chapter 4

# Cold Atoms in Holographic Optical Traps using a Phase-only Spatial Light Modulator

### 4.1 Introduction

This chapter details the work undertaken in loading cold atoms into red-detuned optical traps, generated using a single phase-only spatial light modulator (SLM). Beginning with a description of the operation of an SLM, as well as the different variations of SLM available, the focus will then turn to the different methods of phase generation techniques used in this work. Having generated a suitable phase profile, or hologram, that can be applied to the SLM, some examples of simple light patterns extending along the propagation axis of the ODT and shown to be capable of trapping cold atoms are provided. Trapping with more complicated patterns, however, requires the use of a light sheet to be set up to provide additional confinement. The addition of the light sheet in our setup allows more complex, two-dimensional geometries to be attempted, and we successfully manage to trap atoms in geometries that have applications for quantum simulation and atomtronics.

### 4.2 Phase-only Liquid Crystal SLMs

A spatial light modulator (SLM) is a diffractive optical device consisting of an array of liquid crystal (LC) pixels. The individual liquid crystal pixels are birefringent, meaning that light passing through the medium experiences a different refractive index depending on the orientation of the pixel. The SLM is therefore capable of imparting a phase modulation onto an incoming light field by varying the orientation of the liquid crystal pixels. The orientation of the pixels is manipulated using an array of electrodes connected to the pixels (Figure 4.1).

There are two main types of LC SLM based on the type of liquid crystal material. Ferroelectric liquid crystal (FLC) SLMs have the superior refresh rate (in the kHz regime) compared to the nematic liquid crystal (NLC) SLMs, which only manage refresh rates between 10-100Hz (although more recently faster nematic devices are becoming available, see for example Meadowlark). However, FLC SLMs can only manage a binary change when it comes to the phase modulation, which substantially limits the complexity of phase pattern that can be generated. NLC devices, on the other hand, can achieve between 500-1000 levels of phase modulation between 0 and  $2\pi$  (with 16-bit devices becoming more common), allowing for significantly more complex phase patterns if high refresh rates are not required. Additionally, SLM devices can operate either in transmission or reflection mode. Reflective SLMs, such as the one in Figure 4.1, have a slightly higher fill factor than the transmissive types: in transmission modulation the addressing wires must be between the pixels, rather than behind them as in reflection mode.

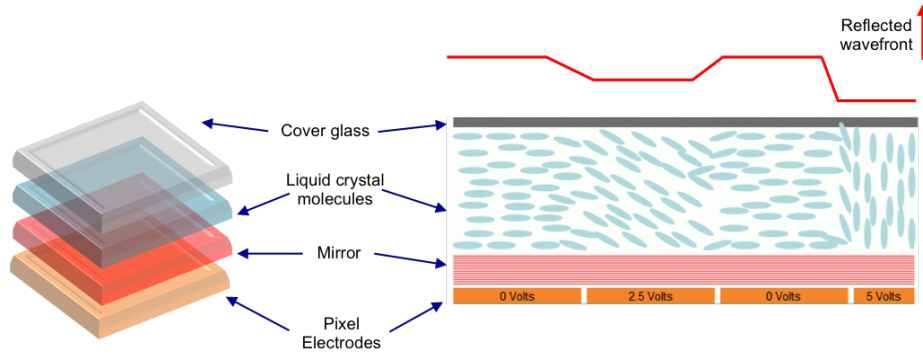


Figure 4.1: Principle of operation for an electronically addressed liquid crystal spatial light modulator. The birefringence of the liquid crystal pixels retards parts of an incoming wavefront, applying a phase modulation.

For the work undertaken in loading cold atoms into red-detuned optical traps, we use an electronically addressed reflective nematic liquid crystal SLM. This allows for more complexity when it comes to atom trap generation, at the cost of a slower refresh rate. Additionally, operating in phase-only modulation of the light field results in better light efficiencies compared to amplitude modulation or some combination of amplitude and phase modulation. The SLM model used for the trapping of cold atoms is a Boulder Nonlinear Systems (BNS) XY-series P256 phase-only SLM, while for the conjugate gradient minimisation investigations we were loaned a Meadowlark XY-series P1920 SLM (more details in section 4.4). For the BNS P256 SLM, each pixel is capable of imparting a phase shift between 0 and  $2\pi$  in steps of 256 onto an incident light field, with a total pixel array size of  $256 \times 256$  and a pixel pitch of  $24\mu\text{m}$ . When the incident light field has vertical linear polarisation the SLM provides a phase-only modulation response.

### 4.3 Phase Pattern Generation Techniques

The principle behind using an SLM to create light patterns with which to trap cold atoms is the Fourier transform relationship existing between the electric field at some defined input plane, and the output electric field in the far field after diffraction. The far field diffraction can be modelled with a Fourier transform  $\mathcal{F}$  such that:

$$\epsilon'(x') = \mathcal{F}[\epsilon(x)] \quad (4.1)$$

where  $\epsilon(x)$  is the electric field at the SLM plane (with the phase modulation applied) and  $\epsilon'(x')$  is the electric field in the far field; equivalently, the far field limit can be realised experimentally with a lens (Figure 4.2). This relationship means that a desired intensity distribution in the output plane, given by  $I = |\epsilon'(x')|^2$  using the nomenclature defined above, can be created if the corresponding hologram (or phase profile) that modifies the incoming light field can be realised.

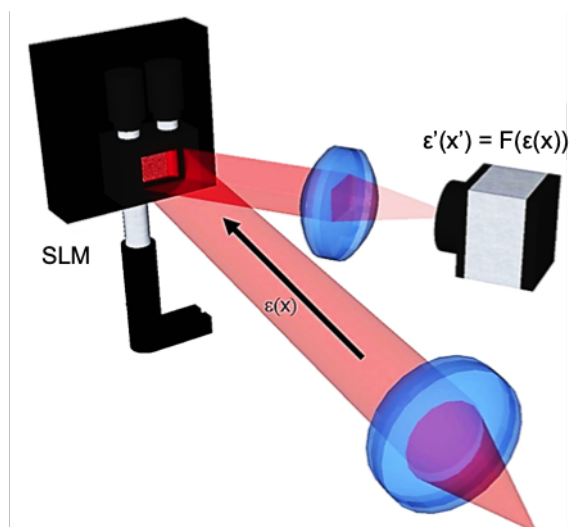


Figure 4.2: Experimental realisation of the far field diffraction limit with a lens placed after the SLM. The Fourier transform relationship allows arbitrary intensity pattern generation in the output plane. In the above diagram, the far field is imaged onto a CCD camera.

Assuming that we know the full details of the input light field (e.g. a Gaussian laser beam), the question becomes what is the necessary phase modulation to be displayed on the SLM that results in the desired intensity distribution in the output plane. However, if one wants to obtain the input plane hologram, then one needs to know the full electric field information in the output plane. Unfortunately, in most circumstances, we only know the amplitude information in both planes (the input Gaussian laser and the desired output

plane light distribution), but we do not know the phase profile in either plane. If one were to assume a uniform phase at the output plane, then the output electric field can be defined and an inverse Fourier transform can be performed to obtain the input electric field. Usually, however, this results not only in a phase modulation in the input plane, but also some amplitude modulation. The amplitude of the light at the input plane in our case is fixed (given by a Gaussian beam distribution), and so we cannot use this as a method. To overcome this, some simplifications can be made - when performing cold atom trapping, the phase of the light at the output plane does not affect the trapping profile. This “phase freedom” means that the phase at the output plane can have any value, and consequently one can improve the hologram at the input plane until the desired output amplitude is realised. However, the phase freedom does mean there is no exact analytical solution for the SLM phase - numerous solutions are possible and so the phase profile must be obtained computationally.

There are two main methods of phase retrieval discussed in this section. One is the Iterative Fourier Transform Algorithm (IFTA) approach to hologram generation - in short, iteratively Fourier transforming between and applying perturbative modulations to the input and output plane gradually improves the phase hologram and subsequently the target light profile at the output until a convergence point is reached. The most common and accurate version of IFTA is the Mixed-Region Amplitude Freedom (MRAF) algorithm, which will be discussed. However, the IFTA routine is not actually a minimisation algorithm. An example of a cost function minimisation routine is the method of using Conjugate Gradients (CG) as an approach to hologram generation, which provides a guided, efficient optimisation process through judicious choice of cost function. Both the MRAF and CG minimisation algorithms are used in this work and will be described next.

### 4.3.1 Iterative Fourier Transform Algorithms

As mentioned, the IFTA is not a minimisation technique - the operating principle is based on computationally iteratively Fourier transforming between the input and output plane, making use of the phase freedom and at each iteration forcing the amplitude to be either that of the Gaussian laser beam at the input plane or that of the target light distribution at the output plane. The phase of the light is retained at each iteration and consequently evolves as the algorithm progresses towards a solution. The first IFTAs were those developed by Gerchberg and Saxton [119] in 1972. Commonly known as the GS algorithm, it works as follows.

The first iteration determines the electric field at the input plane  $E_{in}^{(1)}$ , consisting of the (fixed) amplitude  $A_0$  (which is that of the Gaussian laser) and some initial “guess” phase profile  $\phi_0$ :

$$E_{in}^{(1)} = A_0 e^{i\phi_0}. \quad (4.2)$$

Careful choice of the initial guess phase helps the starting conditions for the IFTA to be more favourable [120]. With an input plane electric field fully defined, it is then Fast

Fourier Transformed (FFT) to model the resulting electric field  $E_{out}^{(1)}$  at the output plane:

$$E_{out}^{(1)} = \text{FFT}(E_{in}^{(1)}), \quad (4.3)$$

$$E_{out}^{(1)} = A_{out}^{(1)} e^{i\varphi^{(1)}}. \quad (4.4)$$

Now,  $A_{out}^{(1)}$  is the resulting output plane amplitude for the first iteration, with  $\varphi^{(1)}$  being the corresponding output plane phase. At this point the output plane light amplitude is unlikely to match the desired target profile, and so the phase is retained at this point in the algorithm and the amplitude is now enforced to be that of the desired target light profile  $\tau$  to give a new output electric field  $G_{out}^{(1)}$ :

$$G_{out}^{(1)} = \tau e^{i\varphi^{(1)}}. \quad (4.5)$$

Now, the inverse FFT can be performed on  $G_{out}^{(1)}$  to give an electric field at the input plane, denoted  $G_{in}^{(1)}$ :

$$G_{in}^{(1)} = \text{IFFT}(G_{out}^{(1)}), \quad (4.6)$$

$$G_{in}^{(1)} = A_{in}^{(1)} e^{i\phi^{(1)}} \quad (4.7)$$

with  $A_{in}^{(1)}$  being the resulting amplitude back at the input plane and  $\phi^{(1)}$  being the new phase profile. Now, the input plane light amplitude will not match the (fixed) Gaussian laser beam profile, and so the phase profile is again retained and the amplitude at the input plane is now enforced to be that of the Gaussian laser beam  $A_0$  once again. Once this change has been made, the resulting electric field  $E_{in}^{(2)}$  is what is to be used for the next iteration:

$$E_{in}^{(2)} = A_0 e^{i\phi^{(1)}}. \quad (4.8)$$

This completes one iteration of the algorithm and the further iterations proceed in a similar way, each time retaining the phase profile at the input or output plane and enforcing the amplitude. The algorithm progresses until either the number of iterations reaches a user-specified limit, or when a defined error metric difference between successive iterations drops below a certain value. A typical error metric is the root mean square (RMS) error between the target amplitude  $\tau$  and the predicted output amplitude  $A_{out}$  for iteration  $n$  summed over the entire output plane with  $x$  and  $y$  being the pixel indices (with  $N$  as the number of pixels):

$$\epsilon^{(n)} = \sqrt{\frac{1}{N} \sum_{x,y} \left( A_{out}^{(n)}(x,y)^2 - \tau(x,y)^2 \right)^2} \quad (4.9)$$

after which a stagnation criterion can be defined as:

$$\epsilon^{(n)} - \epsilon^{(n-1)} < 10^{-k} \quad (4.10)$$

with  $k$  being the user-defined stagnation number. After the algorithm concludes, the final phase profile  $\phi^{(n)}$  can be exported to the SLM in the experimental setup. A block diagram of the IFTA process is shown in Figure 4.3.

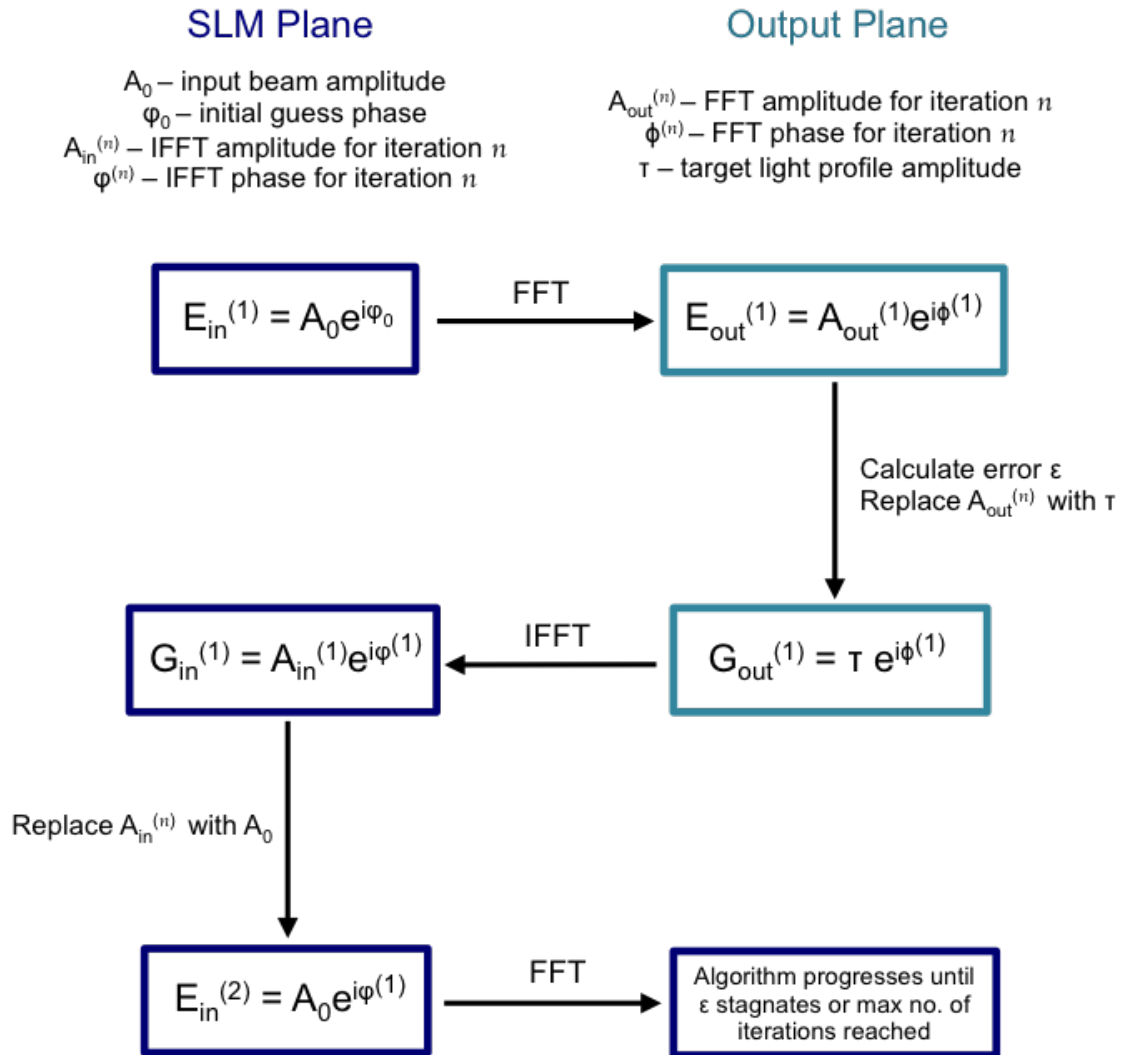


Figure 4.3: Block diagram for the IFTA procedure.

The GS version of the IFTA can work well for relatively simple discrete patterns (e.g. simple Gaussian spot patterns), but has more difficulty producing smooth and accurate continuous patterns - the predicted intensity profiles tend to suffer from some speckle which would result in a rough, uneven potential if attempting to trap cold atoms.

### 4.3.2 Mixed Region Amplitude Freedom Algorithm

An improvement on the GS algorithm was realised in 2008 by Pasienski and DeMarco [120], titled the Mixed Region Amplitude Freedom (MRAF) algorithm. As the name suggests, instead of imposing the amplitude to be constrained over the entire output plane, this algorithm allows for some amount of amplitude freedom as well as the phase freedom from the usual IFTA. The MRAF algorithm achieves this by splitting the output plane into different regions - any light that is not contributing to the target pattern can instead be placed in a region far away from the pattern location, and in this region the amplitude is allowed to be unconstrained. As expected, this does lower the light efficiency of the target pattern as part of the light is dispersed into a separate region, but it does result in greatly improved accuracy and smoothness.

The regions of the output plane that are now defined are:

- a signal region (SR) that encompasses the target pattern plus some additional zero-intensity region to separate the target light profile from any noisy light, in which the amplitude is kept constrained and the phase unconstrained,
- a measure region (MR), which is a subset of the SR and includes the high intensity parts of the target pattern, defined for the purposes of error calculations,
- a noise region (NR), which is the entire output plane that is not included in the SR and in which both the amplitude and phase is left unconstrained.

The relationship between these output plane regions can be seen in Figure 4.4. To take into account the amplitude freedom constraint in the NR, the electric field  $G_{out}^{(n)}$  from equation 4.5 before is modified to:

$$G_{out}^{(n)} = (m\tau|_{SR} + (1 - m)A_{out}^{(n)}|_{NR})e^{i\varphi^{(n)}}. \quad (4.11)$$

Instead of enforcing the amplitude to be that of the target, a fraction of the target profile is mixed in to the output amplitude, defined by the mixing parameter  $m$ . Part of the light is transferred to the NR as defined by the equation above, and now the algorithm is capable of evolving towards a smoother, more accurate intensity profile.

Additionally, careful definition of the SR means that the dispersed light can be placed sufficiently far away from where the target pattern is placed to avoid the noise light being in close proximity to the atoms when trying to trap atoms experimentally. A further course of action would be to place an iris after the SLM in the first focal plane, which can then be imaged onto the atoms - if centred on the first order of diffraction, then the iris could be used to block the NR light.

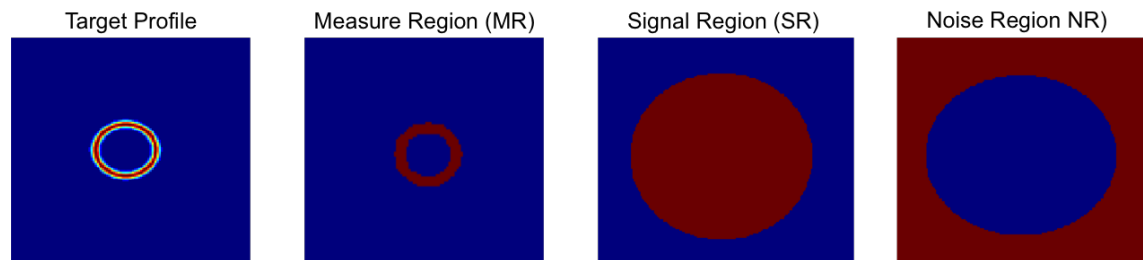


Figure 4.4: Diagram indicating the corresponding regions of the output plane (in red) when using the MRAF algorithm for a Gaussian ring target light profile. The SR is typically defined to be significantly larger than the target profile to ensure any noisy light is not placed close to what would be the trapping profile.

A comparison between the GS algorithm and the MRAF algorithm can be seen in Figure 4.5, which compares a Gaussian ring target profile with the predicted outputs for both the GS and MRAF. As can be seen, the predicted MRAF profile contains much less fragmentation at the cost of less light efficiency, with the excess light placed away from the predicted profile.

A new error metric is defined when working with the MRAF algorithm, defined within the measure region:

$$\epsilon_{\text{MR}}^{(n)} = \sqrt{\frac{1}{N_{\text{MR}}} \sum_{x,y \in \text{MR}} \left( \tilde{A}_{\text{out}}^{(n)}(x,y)^2 - \tau(x,y)^2 \right)^2} \quad (4.12)$$

where  $N_{\text{MR}}$  is the number of pixels in the measure region and  $\tilde{A}_{\text{out}}$  is the renormalised output electric field (such that the maximum intensity in the predicted output field matches the maximum intensity of the target). Both the GS and MRAF algorithms are coded in MATLAB. The MRAF codes were used for the multi-wavelength investigations, in section 4.4.1, and also for some of the initial atom traps done experimentally. Before that, a review of an alternative phase pattern generation technique based on conjugate gradient minimisation will be described.

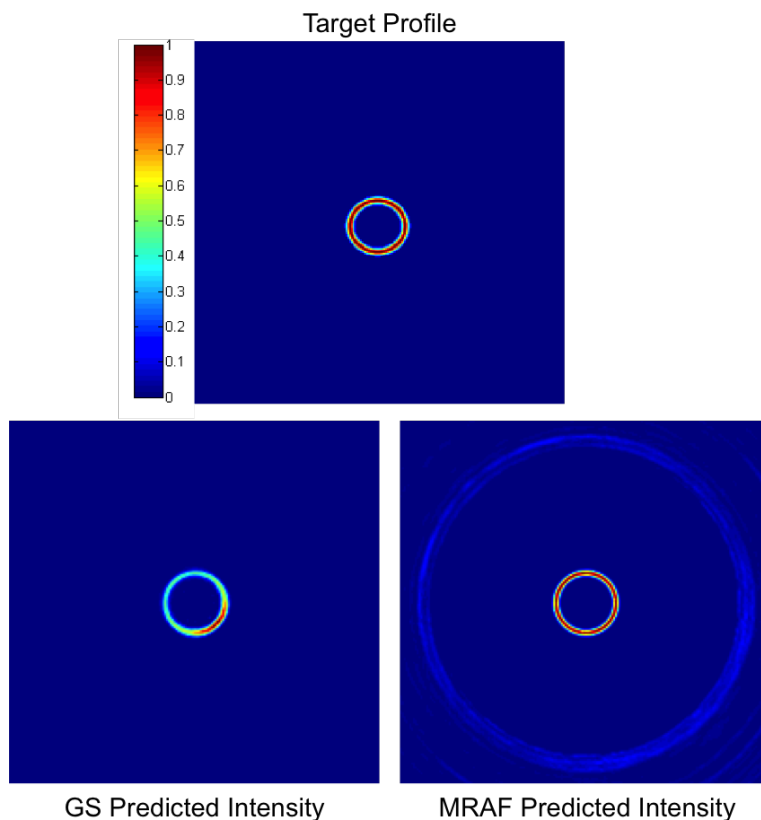


Figure 4.5: Comparison of the predicted intensity profiles for a Gaussian ring target pattern using the GS and MRAF algorithms. The GS algorithm struggles to produce a smooth, uniform output, while the MRAF algorithm produces a much smoother output at the cost of light efficiency. In the GS case the light efficiency was 99%, while for MRAF the efficiency was 15.26% obtained with a mixing parameter of  $m = 0.3$ . Error values obtained from 200 iterations were  $\epsilon_{\text{MR}}^{\text{GS}} = 12.4\%$  and  $\epsilon_{\text{MR}}^{\text{MRAF}} = 0.2\%$ . Excess light placed at the boundary of the signal region can also be seen in the MRAF output.

### 4.3.3 Conjugate Gradient Minimisation

As previously mentioned, IFTA algorithms are not actually minimisation algorithms; some examples of minimisation algorithms include direct search [121] or genetic algorithms [122]. Both algorithms benefit from a directed minimisation process, but in turn they are computationally far more demanding compared to the IFTAs, requiring a longer run time and often using more memory. Defining a specific cost function also means that the algorithm can be better guided compared to the IFTA, as more importance can be given to specific regions and the cost function appropriately tailored. The most basic and brute force min-

imisation technique is the direct search algorithm [121] - after an initial guess hologram is defined, the algorithm changes the phase value of each pixel sequentially and, after each change, computes the cost function (which might be the difference between the target output profile and the predicted profile). If the cost function is lowered, the pixel change is retained; if not, the pixel change is reversed. The algorithm then progresses towards a minimum of the cost function but as expected this expends considerable time and computing power; even more demand is placed on the computer if the pixel changes are not binary and multiple phase values are possible.

An alternative to direct search algorithms is the method of genetic algorithms. Instead of a single initial guess phase profile, a range of initial phase profiles are chosen and they are used to produce a new set of holograms via a breeding process. The new set of holograms are compared against each other using a designated cost function and the best ones are kept for future breeding processes. Genetic algorithms were the focus of a Masters student in our group in 2015 and it was found to be effective for simple patterns with a binary phase value. Larger patterns and multiple phase levels required a huge amount of computing power, with run times taking several hours and extra RAM having to be used. More information can be found in Callum MacArthur's Masters thesis [123].

Another alternative, and the focus of this subsection, is the method of conjugate gradients, originally developed in our group in 2012 [124, 125]. The conjugate gradient approach makes use of the derivative of a chosen cost function and reaches a minimum by using this gradient, rather than scan through an entire parameter space.

The simplest form of gradient minimisation approach is that of the method of steepest descent. In the steepest descent approach, we can consider a simple two-dimensional parameter space - this would equate to an SLM with just two pixels, but those two pixels could take multiple phase values. A cost function that is parabolic in shape can be defined. In order to find the minimum of the two-dimensional space, the calculation starts in some initial position. Then, from this location the direction in the parameter space of steepest descent is determined for the chosen cost function. The calculation moves in this direction until the cost function reaches the minimum. Once the minimum has been reached, the calculation then moves in the orthogonal direction to the previous direction, and continues along this path until the minimum is again reached. This new direction incidentally corresponds to the direction of steepest descent at the new position. Subsequent steps are then taken in a similar fashion until the total minimum is found. A diagram showing the steepest descent minimisation routine for a two-dimensional space is shown in Figure 4.6.

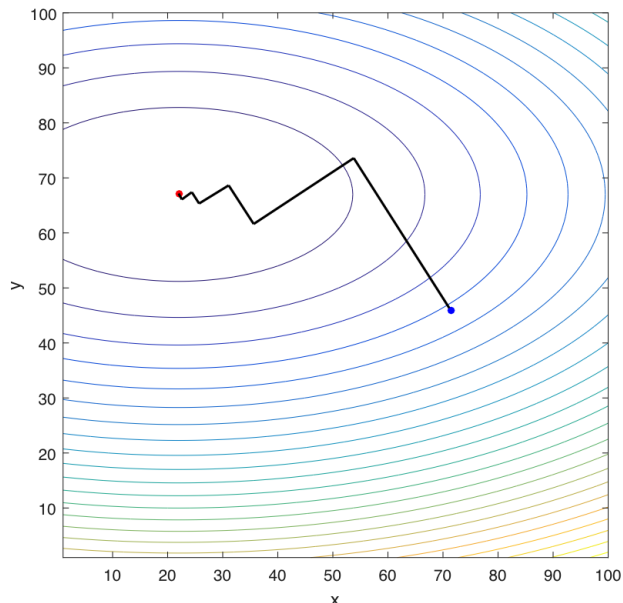


Figure 4.6: Diagram illustrating the method of steepest descent for finding the minimum of a chosen cost function for a simple two-dimensional parameter space. In the above diagram, the blue point is the starting position and the red point is the location of the minimum - the algorithm progresses along the path of steepest descent each time, but there is nothing that stops the algorithm from following a direction it has previously attempted.

Part of the problem with the method of steepest descent is that the calculation often follows a path in the same direction as previous iterations, since each step taken is in an orthogonal direction to the previous one. This could lead to an increase in calculation time if the initial starting position is poorly chosen. The method of conjugate gradient minimisation overcomes this and will be briefly described here - a more thorough description can be found in [126].

Instead of choosing the orthogonal direction being taken once a minimum is reached, the conjugate direction is instead taken, defined as:

$$\mathbf{d}_1^T \mathbf{A} \mathbf{d}_2 = 0 \quad (4.13)$$

where  $\mathbf{d}_1$  and  $\mathbf{d}_2$  are the search vectors which are conjugate to one another with respect to the matrix  $\mathbf{A}$ . Another way to view the conjugate vectors is taking orthogonal directions, but in a stretched space - two vectors that are conjugate in the space  $\mathbf{A}$  are orthogonal when the space is converted to an isotropic space  $\mathbf{A}'$ , as shown in Figure 4.7.

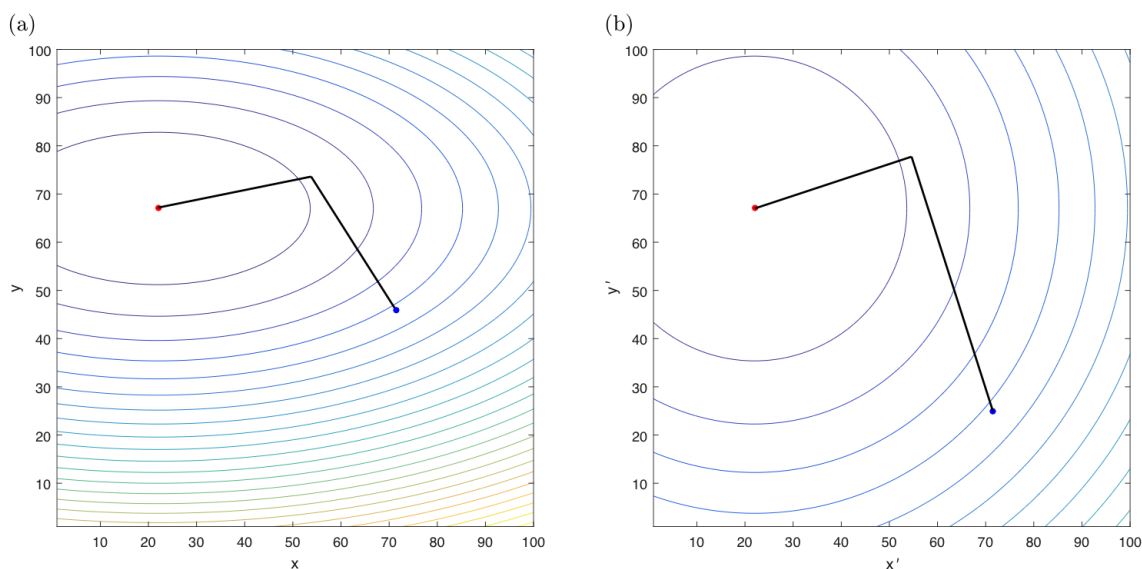


Figure 4.7: Diagram illustrating the method of conjugate gradients for finding the minimum for the same cost function and parameter space as Figure 4.6. The CG method converges in significantly fewer steps (a) compared to the method of steepest descent, while (b) shows that in a stretched parameter space  $A'$  (such that the parabola is symmetric) the two search directions become orthogonal.

To generate the search directions, conjugation of the steepest descent directions is performed using a conjugate Gram-Schmidt process, resulting in the following equation [126]:

$$\mathbf{d}_{i+1} = \mathbf{r}_{i+1} + \beta_{i+1}\mathbf{d}_i. \quad (4.14)$$

Here,  $i$  denotes the iteration step,  $\mathbf{r}_{i+1}$  is the direction of steepest descent at the location of step  $i+1$ , and  $\beta_{i+1}$  is given by:

$$\beta_{i+1} = \frac{\mathbf{r}_{i+1}^T \mathbf{r}_{i+1}}{\mathbf{r}_i^T \mathbf{r}_i}. \quad (4.15)$$

When carrying out the calculation, the computer needs only to store the previous search direction and previous steepest descent direction, resulting in a computationally efficient minimisation process. Our group has shown that highly accurate hologram calculations are possible with the conjugate gradient method [124]. For our hologram calculations, a block diagram describing the conjugate gradient method is shown in Figure 4.8. The initial input electric field is once again defined using both the (fixed) input amplitude and an educated guess phase. The Fourier transform method is once again used to model the output electric field. For the first iteration, the direction of steepest descent is calculated for the chosen

cost function (which the user defines; typically, the chosen cost function to minimise looks at the difference between the target light field and the predicted light field, but there exists a large amount of freedom to tailor the cost function in order to improve the algorithm - more details in section 4.4.2). Physically, the steepest descent corresponds to the greatest rate of change for each pixel, and the algorithm changes each pixel in this way to minimise the designated cost function. Once completed, the pixel values are set to those that give the minimum. This gives a new input plane phase profile, which sets up the next iteration of the calculation. For each subsequent iteration after Fourier transforming to the output plane, the conjugate direction is calculated for the previous search direction, and the pixel values again changed such that a minimum is obtained. At the conclusion, the pixel values are set to those values that give a minimum and the next iteration is established. The process continues in this way until the cost function change between successive iterations stagnates or the maximum number of iterations is reached. Just like for the MRAF, the final phase profile can be exported to be used experimentally.

As previously mentioned, careful choice of cost function is capable of guiding the minimisation process and greatly improving the final results. An example of this is seen in Figure 4.9, which is a figure that can be found in [125]. In Figure 4.9a), the cost function used for the algorithm for re-creating a second-order power-law trap was:

$$C_a = \sum_{x,y} \left( \tilde{\tau}^2(x,y) - \tilde{A}_{out}^2(x,y) \right)^2. \quad (4.16)$$

As can be seen, the predicted output light profile contains multiple points with large variations in intensity between neighbouring pixels. This is a result of a phase winding occurring in the output plane, and the algorithm struggles because attempting to correct for these actually would cause an increase in the cost function value, which the algorithm (with the cost function defined above) will not do. As such, it gets stuck in this minimum, but the light profile is clearly not acceptable. Fortunately, a cost function that penalises large discrepancies between neighbouring pixels can be defined:

$$C_b = \sum_{x,y} \left[ \left( \tilde{\tau}^2(x,y) - \tilde{A}_{out}^2(x,y) \right)^2 + \left[ \left( \tilde{A}_{out}^2(x,y) - \tilde{A}_{out}^2(x,y \pm 1) \right)^2 + \left( \tilde{A}_{out}^2(x,y) - \tilde{A}_{out}^2(x \pm 1,y) \right)^2 \right] \right]. \quad (4.17)$$

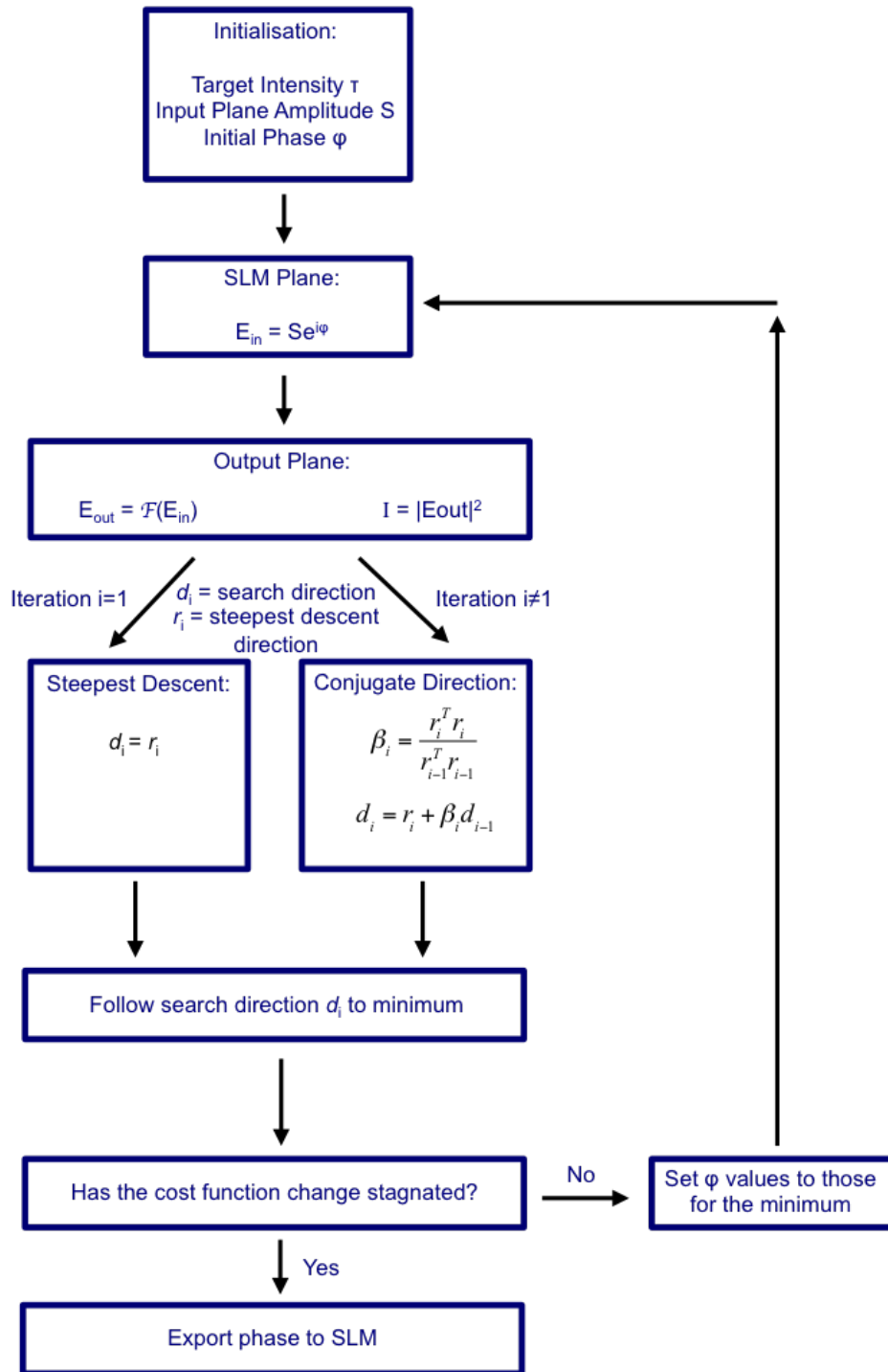


Figure 4.8: Block diagram describing the method of conjugate gradients for calculating phase holograms.

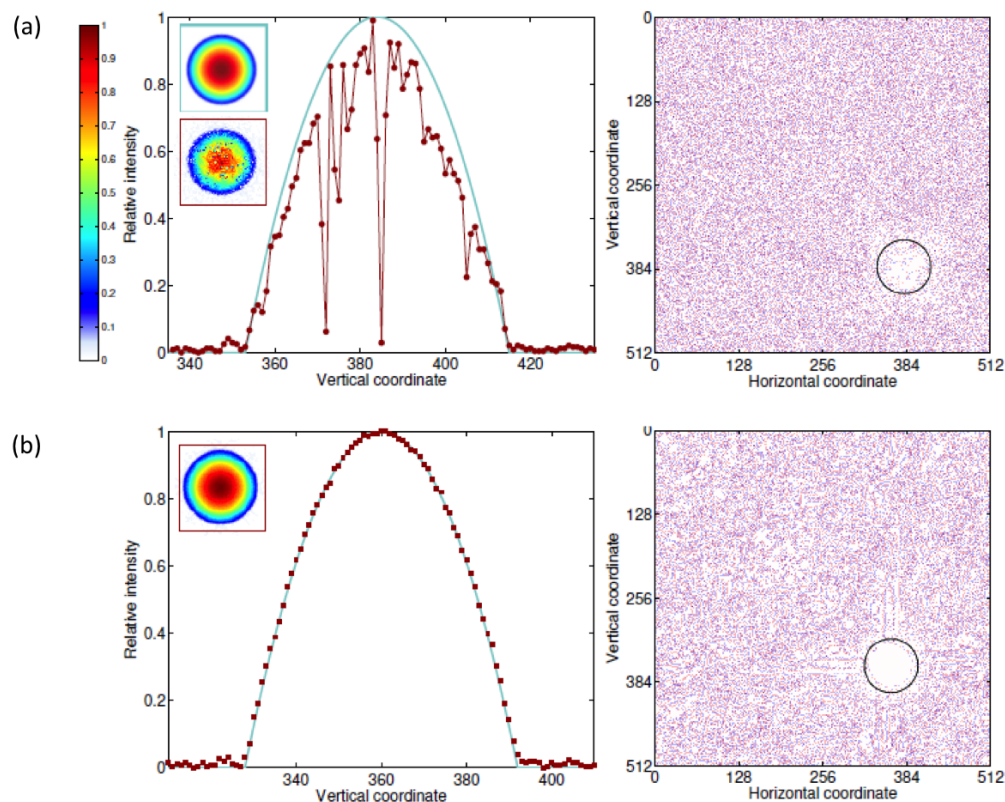


Figure 4.9: Example of cost function importance for calculation of a second-order power-law trap. The left plots shows the intensity profiles. while the right shows the location of phase windings in the output plane, with the circled area denoting the SR for the target pattern. The green inset shows the target intensity, while the red insets show the predicted intensity after 20000 iterations of CG minimisation. For cost function  $C_a$  in (a), the algorithm struggles to remove the phase windings in the region of the target profile and so the resulting output intensity contains multiple instances of large differences in intensity between neighbouring pixels. Cost function  $C_b$  greatly improves the output intensity profile in (b) by simultaneously penalising large intensity variations between neighbouring pixels, reducing the number of phase windings present. This figure is taken from [125].

Defined in this way, the cost function helps to reduce the number and improve the location of the optical vortices (Figure 4.9b) - a reduction from 232 to 130 vortices in the circled SR, and the remainder are now only present towards the edges of the circled area (where the intensity of the pattern should be zero). The cost function customisation that the CG routine provides offers an excellent level of control that is absent from the MRAF calculations.

#### 4.3.4 Initialising the Algorithm

Both the IFTA and the CG minimisation algorithm perform Fourier transforms between the SLM plane and the output plane, and therefore for the first iteration a good educated guess is required, in general, for the input electric field (although this was found to be more critical for MRAF calculations). With the amplitude of the electric field defined by the Gaussian laser beam parameters, this leaves a guess phase to be constructed to ensure a good starting point for the algorithm. The reason for this is that an arbitrary guess phase could result in speckle noise appearing in the output pattern [127, 128]. Instead, a proper guess phase leads to better convergence [120] as it can avoid the formation of optical vortices, which is detrimental to the calculation progressing.

The guess phase that is used in this work consists of three parts:

- a quadratic profile,  $K_Q$ , that acts as a Fresnel lens and as such modifies the spatial coverage of the output plane intensity after the Fourier transform, allowing it to be increased for larger patterns or reduced for smaller ones.
- a linear shift term,  $K_L$ , that acts to move the output plane intensity to a specific region of the output plane, necessary to at least place the output intensity away from the zeroth-order light in an experimental output.
- a conical phase gradient,  $K_C$ , that is able to create a hole in the output plane intensity, which can be useful for ring-shaped target patterns.

Mathematically, the above guess phase terms have the following definitions:

$$K_Q = 3R(\alpha x^2 + (1 - \alpha)y^2), \quad (4.18)$$

$$K_L = D(x \cos(\mu) + y \sin(\mu)), \quad (4.19)$$

$$K_C = B\sqrt{(x^2 + y^2)}, \quad (4.20)$$

$$K_0 = K_Q + K_L + K_C. \quad (4.21)$$

The above guess phase terms are the same that are reported in [120]. In the above equations,  $R$  is the curvature of the quadratic profile and  $\alpha$  is used to define the aspect ratio of the spreading out of the light profile. For the linear shift, the magnitude of the shift from the centre of the output plane is given by  $D$ , while the angle of the shift is given by  $\mu$ . Lastly,  $B$  is used to define the size of the hole in the centre of the profile if required. Pixel indices are given by  $x$  and  $y$ . Trial and error is typically used in an effort to try and shape the output light profile for different target patterns. An example of guess phase generation using a ring-based target profile is seen in Figure 4.10.

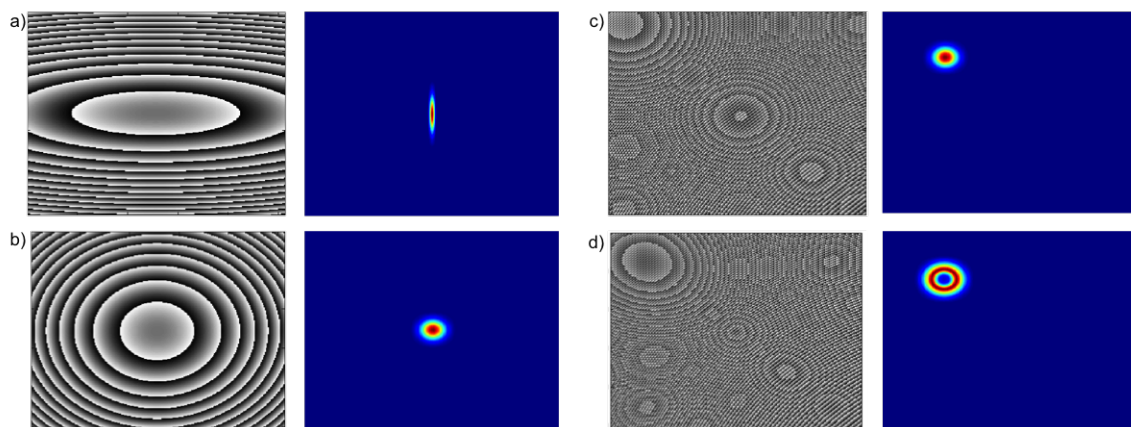


Figure 4.10: Construction of an appropriate guess phase for a Gaussian ring target profile using the  $K_0 = K_Q + K_L + K_C$  equation above, showing phase profile (left) and resulting output intensity (right). a) Only a quadratic phase gradient term  $K_Q$  produces output light in the centre of the output plane, with a poor aspect ratio ( $\alpha = 0.1$ ); b) For a Gaussian ring profile target, the aspect ratio can be changed (to 0.5 in this case) to give a more appropriate spreading; c) With an aspect ratio of 0.5, the more uniform light distribution can be shifted towards the upper quadrant of the output plane, away from the zeroth order, with  $D = 2.25$  and  $\mu = 1.25\pi$ ; d) Lastly, a hole in the centre of the distribution can provide a more beneficial starting point for the algorithm, achieved here with  $B = 45\pi$ .

Another important aspect to consider when performing the algorithms is to consider the resolution of the output plane. When using a two-dimensional Fast Fourier Transform (FFT), the input and output plane are discretised into a two-dimensional matrix such that the FFT can then be carried out. Given that the size of the SLM is  $256 \times 256$  pixels, the input plane in MATLAB is defined as a  $256 \times 256$  matrix - the mapping of the FFT then produces a  $256 \times 256$  output plane. However, this means that the output plane is not fully resolved. The best resolution experimentally is determined by the diffraction limit of the system, which is not reached if the output plane is restricted to the same size as the SLM, and so results in a loss of resolution in this case. In reality, the output plane is not restricted by the SLM size and light can be diffracted into a larger area. Increasing the size of the output plane (and, consequently, the resolution) is achieved by adding a zero-intensity region around the input amplitude - a concept known as padding. In doing this, the output plane can be fully resolved, while the input intensity is still defined only over the size of the SLM. The Nyquist theorem states that the output plane can be fully resolved by padding an  $N \times N$  hologram into a  $2N \times 2N$  matrix, with the  $N \times N$  hologram in the centre [129]. An example of this padding effect is shown in Figure 4.11. The calculation consequently deals with matrices of  $512 \times 512$  pixels for a defined SLM plane of  $256 \times 256$  pixels. At the end of the calculation, the final phase profile to be used on the SLM still

has a size of  $256 \times 256$  pixels to allow it to be used on the experimental SLM.

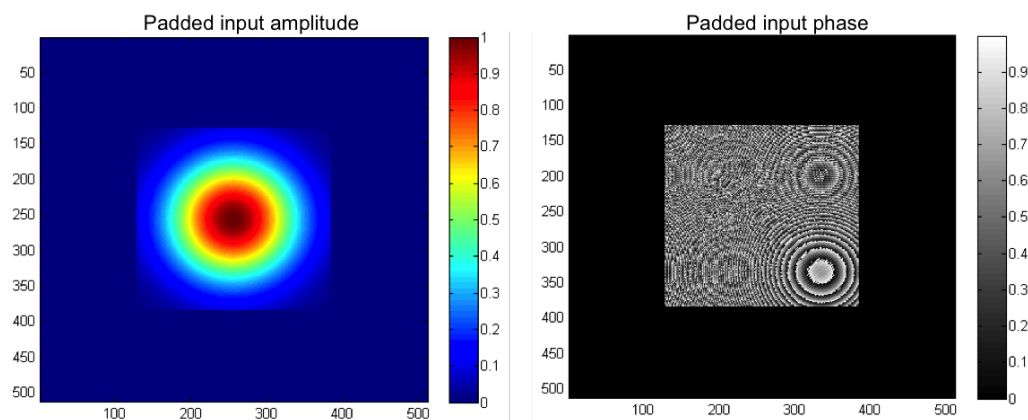


Figure 4.11: Example of padding the input plane for the hologram calculation in order to not lose resolution when performing the FFT. The original  $256 \times 256$  matrix is padded with zeroes into a  $512 \times 512$  matrix, with the input beam amplitude and phase still defined centrally over a  $256 \times 256$  size.

Padding is used in all hologram calculations to ensure no resolution is lost, and while performing the hologram calculations the guess phase parameters can be tweaked by the user until a suitable result is found.

### 4.3.5 Feedback-enhanced Aberration Correction

Very often, the generated experimental target light profiles will deviate significantly from the predicted outputs from the algorithm due to imperfect device response or optical aberrations in the system. To correct for this, one method is the use of a feedback process previously utilised by our group [70]. In short, the hologram calculation process is enclosed in a robust feedback loop that helps to reduce the discrepancy between the experimental light output and the target profile. It achieves this by running the full algorithm once, which provides the phase profile, and then loads the phase profile to the SLM. A camera obtains an image of the light profile in the focal plane after diffraction, and this experimental output is compared to the original target. This is used to then obtain a *new* target profile aimed at minimising the errors discovered in the initial target profile. As a new target profile has been defined, the phase calculation algorithm runs again and a new phase profile is obtained for the next comparison. This feedback process has been shown to reduce the RMS error between the target light profile and the experimental light profile down to the level of a few percent [70].

## 4.4 Multi-wavelength and Phase and Amplitude Control Investigations

This section will cover the main results achieved using the previously mentioned algorithms to generate light patterns for a variety of applications with cold atoms in mind. The first set of results is the use of a single SLM to generate multi-wavelength light patterns using the MRAF algorithm for cold atom experiments, while the second set of results uses the CG minimisation approach to produce exceptionally high fidelity light patterns with both amplitude and phase control of the output plane light. To recap, two different SLM models were used for the investigations - for the multi-wavelength holography with MRAF, and also for the atom trapping done later in this chapter, the SLM is a Boulder Nonlinear Systems (BNS) XY-series P256 phase-only SLM, consisting of an array of  $256 \times 256$  pixels with a pitch of  $24 \mu\text{m}$ . For the CG minimisation investigations, we used a Meadowlark XY-series P1920 phase-only SLM - this model has a much larger array of  $1920 \times 1152$  pixels with pixel pitch  $9.2 \mu\text{m}$ .

Within this group, the MRAF algorithm has previously yielded light profiles suitable for applications to cold atom trapping and as a proposal for an alternate scheme to reach BEC [68, 69, 70]. The multi-wavelength results are an extension of this work and will be discussed briefly here, but more details can be found in [130]. Similarly, the CG work presented is an extension of work originally developed by Tiffany Harte [124, 125] - more details of the CG results can be found in [131]. Apart from the aforementioned publications, further details can be found in the thesis of David Bowman [115].

### 4.4.1 Multi-wavelength Holography Results

Light of different wavelengths can be used to either trap, repel or excite atoms depending on the requirement. We have shown that a single spatial light modulator can be illuminated by co-propagating, overlapped laser beams of different wavelengths in order to create an overlapped structure in the Fourier plane. One of the main advantages of this technique is the ability to overlap multiple wavelengths of light onto a single path, useful in experimental setups with minimal optical access. We have demonstrated this technique for two and three overlapped wavelengths.

Central to this technique is the wavelength-dependency of diffraction - the size and position of the output plane features resulting from diffraction depends on the wavelength of light used, which can be seen from the distance  $d$  between the central maximum of the diffraction and the first constructive order:

$$d = 1.22 \frac{\lambda}{2\text{NA}} \quad (4.22)$$

where  $\lambda$  is the wavelength of the light and NA is the numerical aperture of the lens. Thus, longer wavelength light diffracts further and results in larger output plane features

compared to shorter wavelength light. This fact is used to design a target intensity pattern when considering more than one wavelength of incident light - the linear dependence of the diffraction means that specially tailored target patterns can be constructed, with different features then overlapping in the Fourier plane at the position of the atoms. A simple example is a target pattern consisting of two Gaussian spots, with a separation equal to the ratio of the two wavelengths of light used (780nm and 1064nm in this case) - one Gaussian spot was programmed to be 208 pixels from the centre of the output plane, meaning that the second spot was placed a distance  $1064/780 \times 208$  pixels = 283 pixels away. In the Fourier plane, the closer spot resulting from the 1064nm light is then overlapped with the further spot from the 780nm diffraction.

Experimentally, the calculated phase profiles can be loaded onto the SLM and images obtained using a  $f=150$ mm focal length lens and a Thorlabs DCU224M CCD camera with the two wavelengths of light. When the hologram is illuminated with 780nm light, the two Gaussian spots are measured at positions  $(1.34 \pm 0.01)$ mm and  $(1.93 \pm 0.01)$ mm from the zeroth-order light, with a  $1/e^2$  waist of  $(91 \pm 3)\mu\text{m}$ . When the same hologram is illuminated with the 1064nm light, the two spots are measured at positions  $(1.86 \pm 0.01)$ mm and  $(2.57 \pm 0.01)$ mm, with a  $1/e^2$  waist of  $(130 \pm 9)\mu\text{m}$ . The further Gaussian from the 780nm light and the nearer Gaussian from the 1064nm light are therefore almost overlapped in the output plane, with a  $70\mu\text{m}$  offset (Figure 4.12). The ratio of the widths of the two spots is also comparable to the ratio of the two wavelengths.

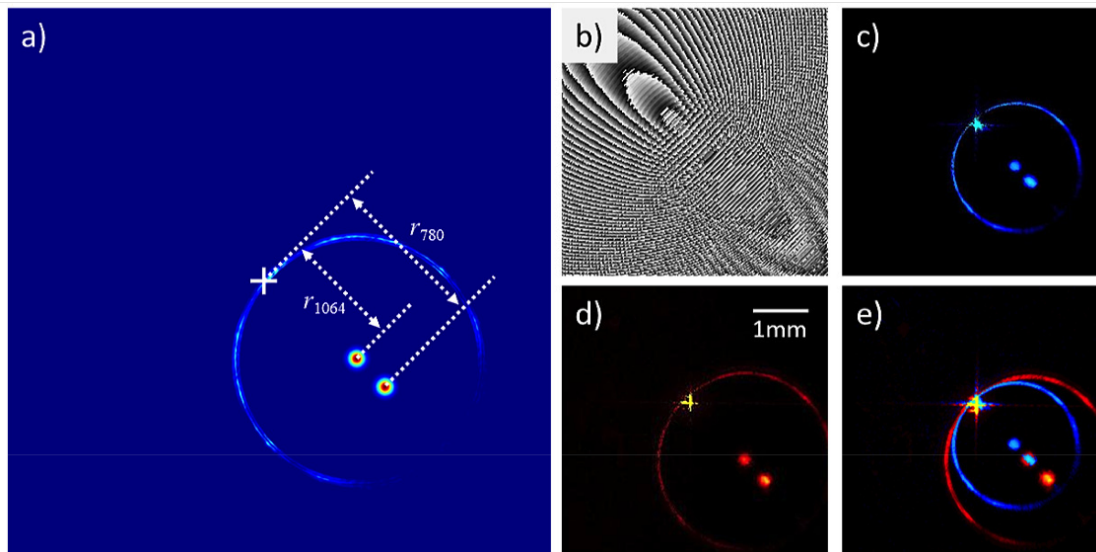


Figure 4.12: Example of multi-wavelength holography using a single phase-only SLM. The predicted pattern is shown in (a), consisting of two Gaussian spots separated by the ratio of their wavelengths (the noise light can be seen collecting at the edge of the defined SR in the predicted profile). At the end of the MRAF calculation, the corresponding phase profile shown in (b) is displayed on the SLM. Images taken of the light profile when the SLM is illuminated with just 780nm (c), just 1064nm (d) and both wavelengths (e) are displayed. Figure from [130].

To showcase the versatility of this technique, Figure 4.13 displays a few example target patterns that we have generated for potential applications in ultracold atom experiments. Figure 4.13a is an image of a red-detuned elliptical optical trap, partly superimposed with a 6th-order super-Lorentzian profile that is detuned by several tens of GHz from atomic resonance. With this partial illumination, the two phase sections of a trapped BEC would evolve at different rates, resulting in a phase slip that would lead to soliton formation [132]. Figure 4.13b is an image of a ring trap, red-detuned from atomic resonance, with a separate blue-detuned barrier to be utilised as a setup for soliton interferometry, suggested in [133]. Figure 4.13c shows two red-detuned Gaussian reservoirs, connected by a thin channel, but the channel is interrupted by individual repulsive barriers. This setup can be used for a study of conduction between two reservoirs as suggested in [134]. Lastly, Figure 4.13d shows a red-detuned trap with a slightly offset attractive dimple, which is enclosed with a repulsive blue-detuned ring to act as a barrier around the circumference of the trapping potential. This potential is related to a proposal for non-equilibrium dynamic behaviour investigations of BECs in such potentials, as suggested in [135].

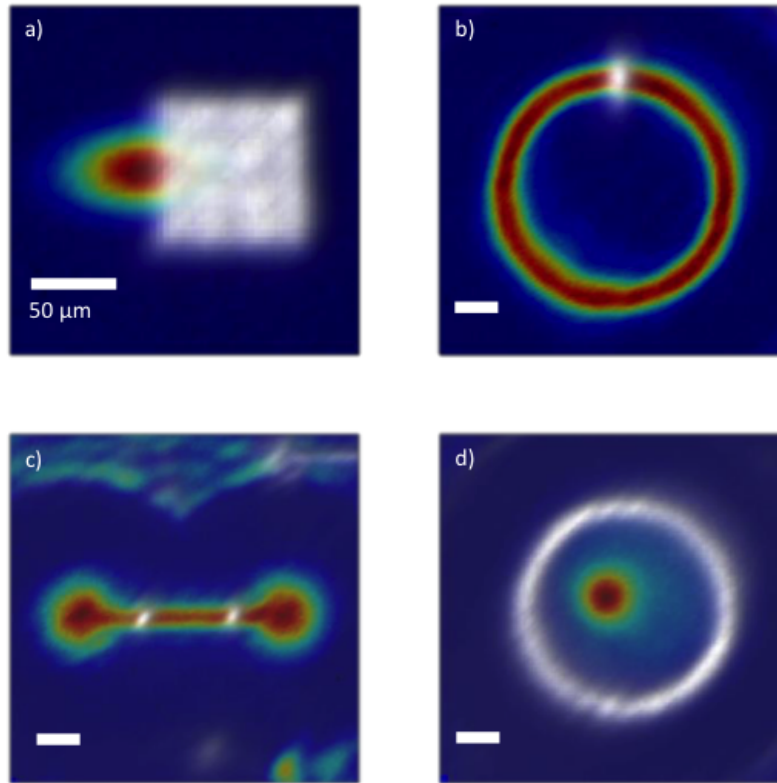


Figure 4.13: Gallery of light patterns generated using the multi-wavelength setup, with 1064nm light shown in colour and 780nm light shown in grayscale. a) Red-detuned elliptically shaped dipole trap, partially illuminated by a far-resonant super-Lorentzian for creation of a phase slip in BECs. b) Red-detuned ring trap with blue-detuned barrier. c) Red-detuned dumbbell potential interrupted by blue-detuned barriers. d) Red-detuned trap with offset attractive simple with hard walls provided by blue-detuned ring. Figure from [130].

The multi-wavelength scheme is a relatively simple method of generating overlapped structures of different wavelengths for use in cold atom experiments, with the ease of aligning additional light beams of different wavelength in a setup with little optical access a major benefit. As mentioned, further details of the experimental setup and results can be found in [130] or [115] - this subsection serves to mention these results achieved by the group without going into the full details.

### 4.4.2 Phase and Amplitude Control Results

Using the CG minimisation routine now as opposed to the MRAF algorithm, our results here show that the output light amplitude and phase can be controlled in creating high-fidelity light patterns to be used to trap cold atoms. Only a brief summary of the main results of the investigation will be mentioned here, but more details can be found in [131] or [115]. The conjugate gradient minimisation code itself was originally developed in Fortran by Tiffany Harte; now, it is written in Python 2.7 using the Theano library [136]. The Python conjugate gradient minimisation uses the Polak and Ribière method [126]. The CG codes are available online and can be found at [137].

One of the main advantages of the CG routine is the ability to guide the optimisation process, and this comes down to a good choice of cost function to minimise. We investigated how the choice of cost function affects the results of controlling the output plane amplitude and phase for a target test pattern consisting of a Gaussian line amplitude profile with a linear gradient of phase across the line. The initial conditions were kept the same for each cost function used.

In terms of the error metrics used for the investigation, the intensity RMS error is defined similar to equation 4.12 above. A relative phase error term between the target phase  $\Phi$  and the output phase  $\varphi$  is given by:

$$\epsilon_{\Phi} = \frac{\sum_{x,y} |(\Phi(x,y) - \varphi(x,y) + P(x,y))|^2}{\sum_{x,y} |\Phi(x,y)|^2} \quad (4.23)$$

where the  $P(x,y)$  term is a correction term to take into account that the phase is cyclical (ensures the correct phase difference is used if for example the target phase pixel needs to have a  $\pi$  phase value, but the output phase pixel value is something like  $3.3\pi$ , the  $P$  term ensures this difference in phase is only  $0.3\pi$  as opposed to  $2.3\pi$ .) The fidelity  $F$  is defined such that a perfect fidelity of 1 corresponds to an exact match between the target pattern and the output pattern - as such, it is defined as the complex inner product of the output and target electric fields:

$$F = \left| \sum_{x,y} \tilde{\tau}(x,y)^* \tilde{E}_{out}(x,y) \right|^2 \quad (4.24)$$

with  $\tilde{\tau}(x,y) = \sqrt{\tilde{T}(x,y)} \exp(i\Phi(x,y))$  being the target electric field. The over-tilde signifies a normalisation over a specific region of interest including regions of non-zero amplitude in the target pattern plus a sizeable area of zero intensity. The light efficiency  $\eta$  is the percentage of light contained in the region of interest compared to the total output plane. For the far field results (Figure 4.15), we define the non-uniformity error  $\epsilon_{nu}$  identical to [138] to compare with their single SLM method of controlling amplitude and phase. The

non-uniformity error is given as:

$$\epsilon_{nu} = \frac{\sum_{x,y} |M(x,y) (\tilde{I}(x,y) - I_a)|^2}{\sum_{x,y} |M(x,y) \tilde{T}(x,y)|^2} \quad (4.25)$$

where  $M(x,y)$  is a binary mask which is equal to one where the target intensity is approximately uniform ( $T(x,y) > 0.98$ ) and zero everywhere else, and  $I_a = (1/N) \sum_{x,y} M(x,y) \tilde{I}(x,y)$  is the average output intensity in the uniform region ( $N$  is the total number of pixels in the measure region). The most straightforward cost function is one that expands on the cost function in equation 4.16, which previously involved only the amplitudes of the electric fields. An extension of this to incorporate the phase term would be:

$$C_1 = \sum_{x,y} \left[ \alpha \left( \tilde{I}(x,y) - \tilde{T}(x,y) \right)^2 + \beta \left( \Phi(x,y) - \varphi(x,y) + P(x,y) \right)^2 \right]. \quad (4.26)$$

Here,  $\tilde{I}$  and  $\tilde{T}$  are the normalised output and target intensities, and  $\alpha$  and  $\beta$  are the relative weightings for the intensity and the phase parts of the cost function. As can be seen from the graphs in Figure 4.14, even with different scaling for  $\alpha$  and  $\beta$ , the fidelity stayed at an exceptionally low value over the course of the calculation, resulting in inaccurate outputs.

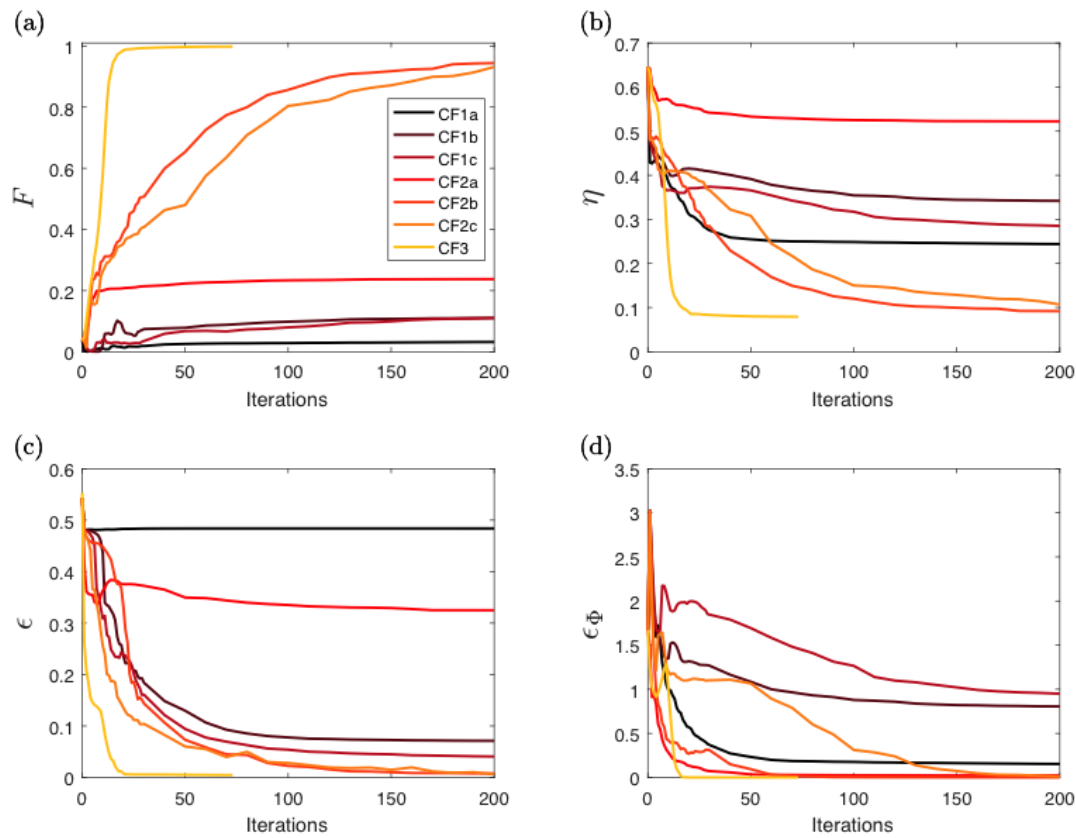


Figure 4.14: Graphs showing the effect on the error metrics for different cost functions. CF1 corresponds to  $C_1$  in equation 4.25, with CF1a having  $\alpha=1$  and  $\beta=1$ , CF1b having  $\alpha=1$  and  $\beta=0.01$  and CF1c having  $\alpha=1$  and  $\beta=0.005$ . CF2 represents  $C_2$  in equation 4.26, with CF2a having  $\alpha=0.1$  and  $\beta=1$ , CF2b having  $\alpha=1$  and  $\beta=1$  and CF2c having  $\alpha=1$  and  $\beta=0.1$ . Finally, CF3 corresponds to  $C_3$  in equation 4.27 (with  $d=0$ ).

Additionally, the phase error term placed equal weighting at regions of both high and low intensity in the signal region of the output plane, even though much less necessity should be attributed to the low intensity pixels of the pattern. To correct for this, we wish to change the cost function such that the phase term includes an intensity weighting and so will give less priority to low intensity pixel values which are not as important:

$$C_2 = \sum_{x,y} \left[ \alpha \left( \tilde{I}(x,y) - \tilde{T}(x,y) \right)^2 + \beta \tilde{T}(x,y) \left( \Phi(x,y) - \varphi(x,y) + P(x,y) \right)^2 \right]. \quad (4.27)$$

With this additional intensity-weighting of the phase term in the cost function, the results showed a general improvement, especially regarding the fidelity of the pattern - however,

the results were strongly dependent on the weighting values of  $\alpha$  and  $\beta$ .

A third alternative was to manually incorporate the fidelity term into the cost function - since the fidelity has a maximum value of 1 corresponding to a perfect match, it can then be used as a minimisation criterion within the cost function. One problem with using the fidelity was that a complex function was difficult to differentiate in Python and so instead the chosen cost function uses only the real part of the inner product:

$$C_3 = 10^d \left( 1 - \sum_{x,y} \text{Re}(|\tilde{\tau}(x,y)^* \tilde{E}_{out}(x,y)|) \right)^2, \quad (4.28)$$

$$C_3 = 10^d \left( 1 - \sum_{x,y} \sqrt{\tilde{I}(x,y)\tilde{T}(x,y)} \cos(\Phi(x,y) - \varphi(x,y)) \right)^2 \quad (4.29)$$

where the over-tilde now denotes normalisation so that the total intensity in the signal region is 1. The factor  $10^d$  was found to increase the steepness of the cost function, increasing convergence time. As can be seen from Figure 4.14, this choice of cost function substantially improves the fidelity at the cost of light efficiency  $\eta$  compared to the other cost function choices, while also converging in fewer iterations. The results for the three cost functions mentioned above, and their associated weightings, are shown in Table 4.1, while the predicted intensity and phase profiles for each of the cost functions is shown in Figure 4.15. As cost function  $C_3$  results in the lowest fidelity and error values, at a cost of slightly increased calculation time and less light efficiency, it is this cost function that we will be using for the experimental light patterns henceforth, unless otherwise specified, for our phase and amplitude calculations.

-	CF	$\alpha$	$\beta$	F	$\eta$ %	$\epsilon_\Phi$ %	$\epsilon_{MR}$ %
CF1a	$C_1$	1.0	1.0	0.030	24.4	15	48.4
CF1b	$C_1$	1.0	0.01	0.110	34.2	81	7.1
CF1c	$C_1$	1.0	0.005	0.110	28.5	95	4.1
CF2a	$C_2$	0.1	1.0	0.237	52.2	2.0	32.5
CF2b	$C_2$	1.0	1.0	0.944	9.2	0.03	0.8
CF2c	$C_2$	1.0	0.1	0.932	10.7	1.0	0.6
CF3	$C_3$	-	-	0.998	7.9	0.02	0.5

Table 4.1: Table summarising the cost function investigation results.

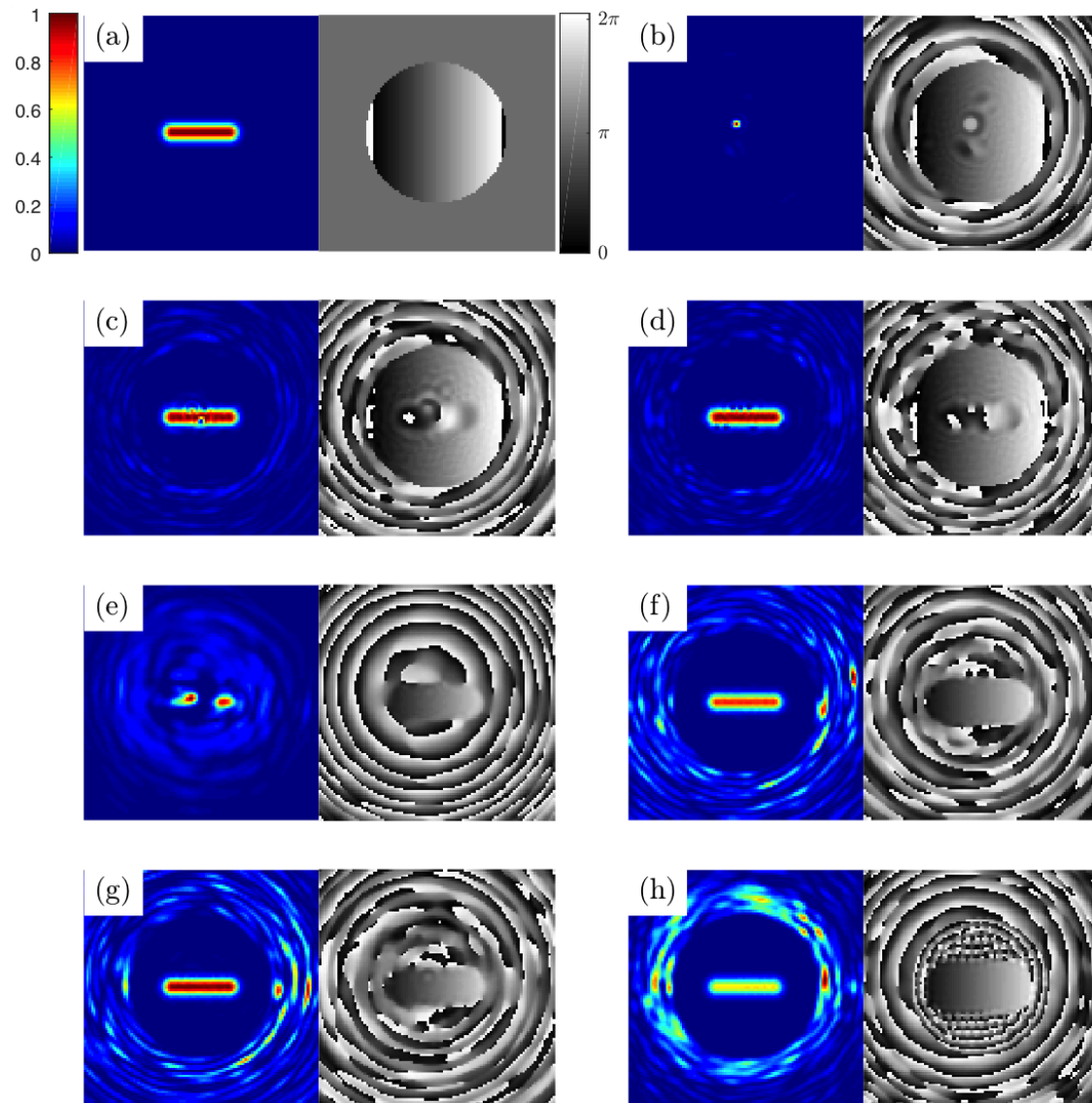


Figure 4.15: The output plane intensity and phase results for the cost function investigation; a) Target intensity profile and target phase profile. The predicted intensity and phase profiles for b) CF1a, c) CF1b, d) CF1c, e) CF2a, f) CF2b, g) CF2c and h) CF3 are shown alongside.

A selection of high fidelity light patterns in both amplitude and phase, aimed at showcasing the versatility of this technique, are shown in Figure 4.16 with particular applications to cold atom trapping in mind. All patterns were programmed to have the same diagonal

offset from the centre of the output plane in order to avoid the undiffracted light, which necessarily fixes two of the guess phase parameters ( $D$  and  $\mu$ ). The first pattern resembles a Laguerre-Gaussian (LG) mode - such a pattern has a broad range of uses [139] and is useful for inducing circulation states in trapped atoms [140] - the ring-shaped amplitude profile is accompanied by a phase winding from 0 to  $2\pi$ . A discrete, 12-spot ring lattice with a similar phase winding is also shown, which has potential applications simulating magnetic flux in a solid state system [141]. A discrete square lattice with a similar phase winding is also shown. On the right, a graphene quantum simulator [142] consisting of ultracold atoms trapped in a honeycomb type lattice with alternating phase values between nearest neighbours can be realised using the intensity and phase profiles shown. Below, a flat top intensity profile combined with an inverse square power-law phase profile has been suggested for investigating sonic horizons and artificial black holes [143]. A Gaussian line intensity profile, meanwhile, can be used to trap particles like for optical tweezers, while the linear phase gradient across the line could cause them to flow [144]. Finally, as a display of the flexibility of the method, we show a profile with uncorrelated intensity and phase distributions - that of a chicken (intensity) and eggs (phase). A summary of the associated parameters for each of these patterns is shown in Table 4.2.

Pattern	$\sigma$ (mm)	$R$ (mrad px <sup>-2</sup> )	1-F	$\eta$ %	$\epsilon_\Phi$ %	$\epsilon_{nu}$ %
Laguerre-Gauss	1.0	4.5	$3.0 \times 10^{-6}$	41.5	0.0003	0.005
Graphene	1.4	2.7	$4.4 \times 10^{-4}$	13.1	0.0003	0.01
Ring Lattice	1.2	3.9	$1.5 \times 10^{-6}$	24.6	0.00006	0.001
Flat Top	1.0	4.5	$1.8 \times 10^{-4}$	11.3	0.2	0.007
Square Lattice	1.2	4.5	$1.6 \times 10^{-5}$	10.6	0.0009	0.02
Gaussian Line	1.4	2.9	$1.4 \times 10^{-5}$	20.4	0.001	0.002
Chicken and Egg	1.6	4.5	$7.1 \times 10^{-2}$	2.0	1.3	-

Table 4.2: Table summarising error values and optimisation parameters for the patterns shown in Figure 4.16.

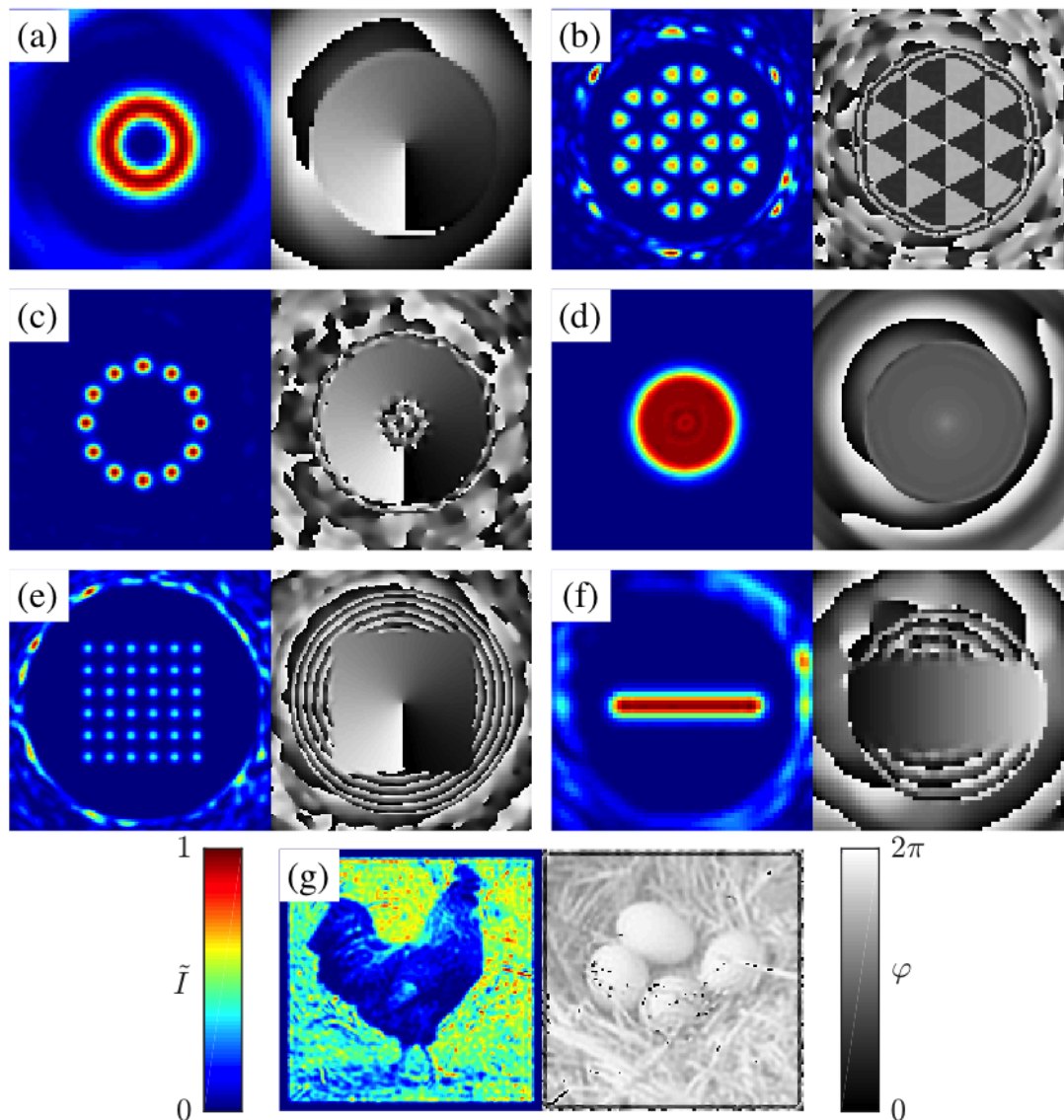


Figure 4.16: Normalised intensity  $\tilde{I}$  (in colour) and phase  $\varphi$  (in grey) results for various target patterns using the conjugate gradient minimisation and the cost function  $C_3$ . Error metrics for each pattern are shown in Table 4.2. Figure taken from [131].

The experimental setup for verification of the calculated holograms is shown in Figure 4.17. The output from a 1070nm laser is expanded to a  $1/e^2$  waist of 3.0mm and split using a half waveplate and PBS combination. The reflection is phase-modulated by an SLM (BNS P1920) and focused using an  $f=150$ mm achromatic doublet onto a CCD camera (Thorlabs

DCU200 Series). The other path provides a reference beam that is used to obtain the phase of the modulated light after interference with the modulated beam. The extracted intensity and phase profiles for a Gaussian line phase profile with a linear phase gradient (Figure 4.17b), a Gaussian ring with a phase winding (Figure 4.17c) and a honeycomb lattice with alternating phase between nearest neighbours (Figure 4.17d) are shown below. More details again can be found in [115].

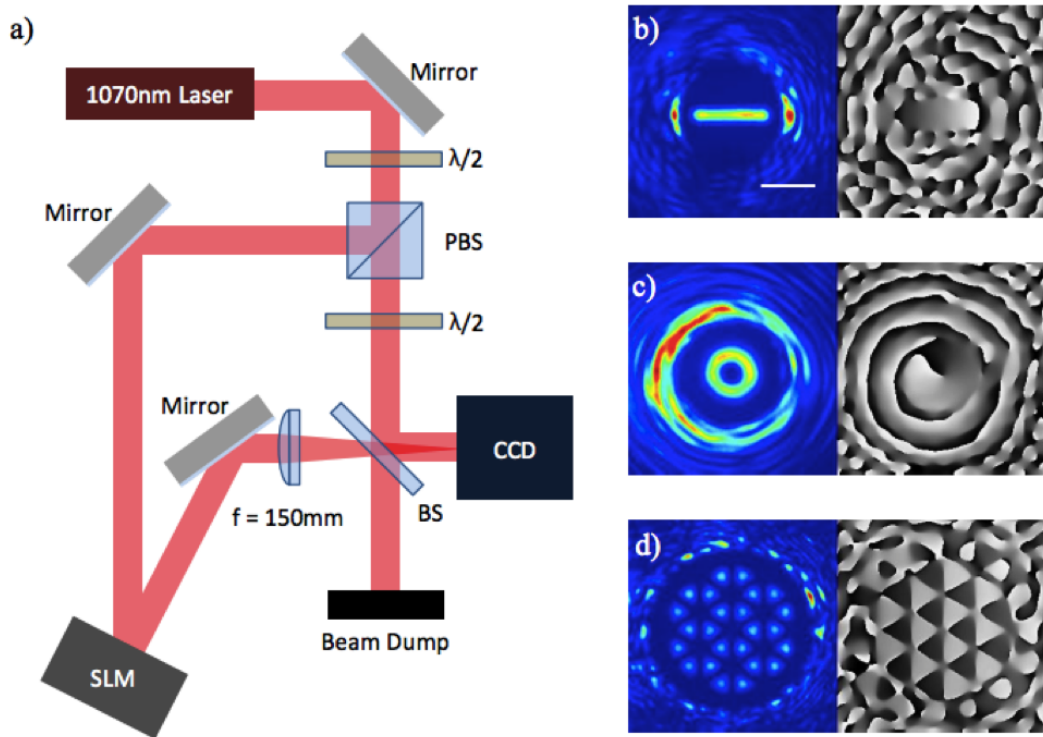


Figure 4.17: a) Setup for experimental verification of the calculated holograms. The first  $\lambda/2$  waveplate varies the power between the reference beam and the SLM beam, and the second waveplate fixes the polarisation of the reference beam for interference with the SLM beam; b-d) Measured intensity (left) and phase (right), with the white scalebar denoting  $300\mu\text{m}$  and being common to all images. The colour scaling is the same as Figure 4.16. Taken from [131].

## 4.5 SLM Experimental Implementation

Having discussed the main results achieved with the MRAF and CG codes computationally, we can now discuss the next steps achieved experimentally. After the BEC evidence was

seen, the aim was to successfully trap atoms in arbitrary trap geometries, specifically traps aimed at applications involving quantum simulation and atomtronics.

### 4.5.1 Setting Up the Vertical Trapping Path

At the beginning of the optical evaporation sequence from chapter 3, roughly  $1.0 \times 10^7$  atoms were trapped in the horizontal ODT at a temperature of  $8.8 \mu\text{K}$ . A motorised rotatable waveplate is used to lower the intensity of the horizontal ODT to perform the optical evaporation. Now, the power that is removed from the horizontal ODT may be used for the light sheet and holographic optical trap that will allow the trapping of cold atoms in different geometries.

A diagram of the vertical trapping path is shown in Figure 4.18. After the reflection off the PBS that is placed after the motorised waveplate, the light passes through a Crystal Technologies AOM (model 3110-197) in a simple single pass configuration, able to achieve a diffraction efficiency in the first order of 90%. Trapping is performed using the first order light so that the AOM can be used a fast switch if needed - the zeroth order light is blocked using beam blocks. The light is then split again using another waveplate-PBS combination - one path to be used for the SLM and the other path to be used for the light sheet. The priority will first be placed on the SLM path, before the light sheet implementation is discussed in section 4.7. The reflection off the PBS is then expanded (to ensure the incoming light fills the entire array of the SLM) - this is achieved using a confocal telescope in a 1:4 setup, also ensuring that more power can be used for the input beam by increasing the area. Initial alignment of the vertical trapping path was performed by simply using a mirror in place of the SLM - after rough alignment was achieved, irises can be inserted along the path, the mirror replaced with the SLM, and the beam re-aligned through the irises. After the SLM, a 40mm focal length lens is used to produce the target intensity pattern, and this pattern is then imaged onto the atoms using the 40mm 1:1 confocal telescope seen in the figure, placed after the dichroic mirror. Additionally, the target patterns can be imaged onto a Thorlabs DCU224M CCD camera by using a flip-mirror placed after the SLM (this path has been omitted from the figure for clarity), useful for diagnosing experimental target patterns before attempting to trap using the desired pattern.

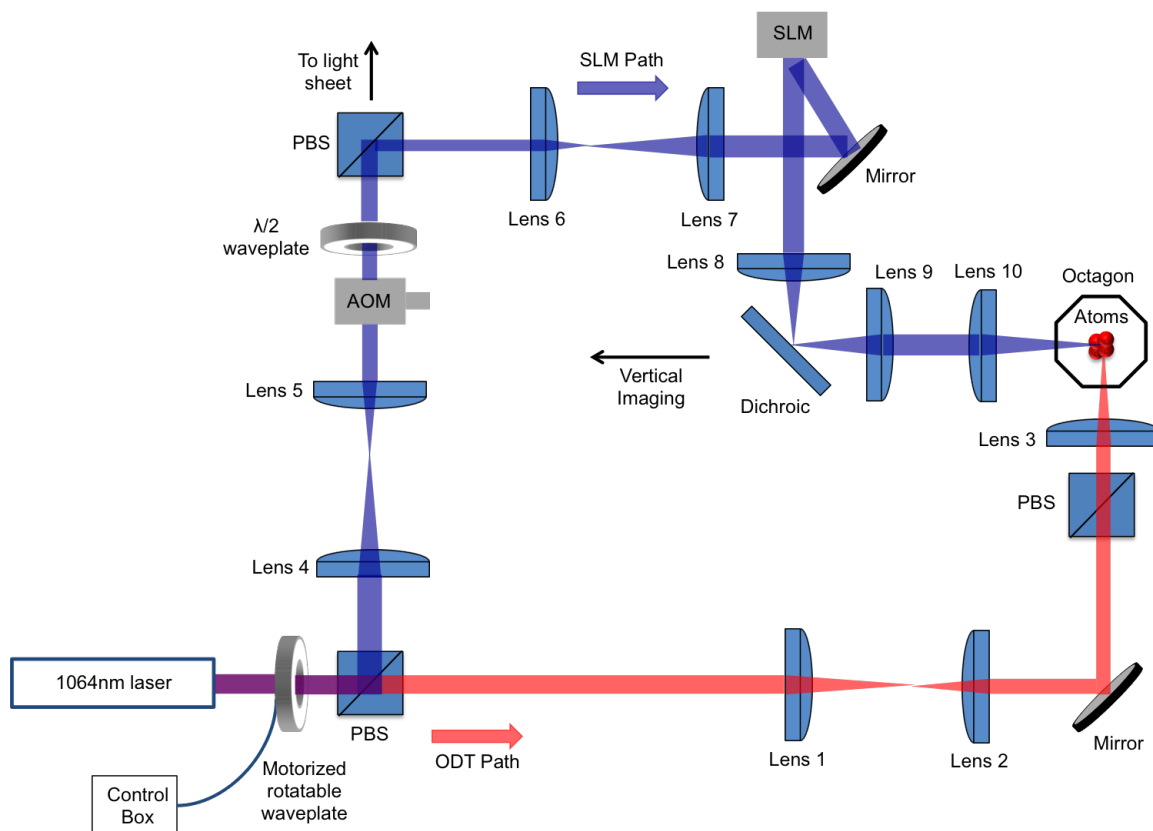


Figure 4.18: Diagram of the optical path for the 1064nm laser light for setting up the vertical trapping path. Focal length of lenses: Lens 1 = 150mm, Lens 2 = 60mm, Lens 3 = 60mm, Lens 4 = 100mm, Lens 5 = 50mm, Lens 6 = 50mm, Lens 7 = 200mm, Lens 8 = 40mm, Lens 9 = 40mm, Lens 10 = 40mm. A mirror is used instead of the SLM for initial vertical beam alignment. The light sheet path is discussed in section 4.7.

To set up trapping of atoms along the vertical direction initially, we place a flip-mirror in front of the SLM in Figure 4.18. We start off using a large beam and use the horizontal and vertical imaging to look for atoms trapped in the vertical ODT as well as the horizontal ODT. The telescope consisting of lenses 6 and 7 in Figure 4.17 was originally set up differently; lens 7 had a focal length of 100mm, resulting in a 1:2 telescope and creating a beam with a  $1/e^2$  half width of roughly 1mm incident on the 40mm focal length lens 8. This results in a focus of about  $13.5\mu\text{m}$   $1/e^2$  half width. Due to the high power being used, the optical traps in the horizontal and vertical direction were capable of trapping atoms straight after the RF evaporation. With about 800mW of power in both axes, we estimate the trap depth of the vertical ODT to be about  $470\mu\text{K}$ , compared to the  $120\mu\text{K}$  of the horizontal ODT which has a comparatively larger waist. The resulting Rayleigh range

of the vertical ODT is also much shorter (about 0.54mm for the vertical ODT, compared to 7.4mm for the horizontal ODT), providing some confinement along the propagation direction if enough power is provided. This allows the vertical ODT to trap some atoms without being fully overlapped with the horizontal ODT. Performing imaging along the horizontal would then lead to diagnosis between the foci of the two traps.

A short TOF (0.5ms) was used when taking absorption images along the horizontal as some back-reflected light from the ODT was picked up by the camera if an in-situ shot was attempted. Initial diagnosis using the vertical imaging is shown in Figure 4.19a, which is an in-situ shot after aligning the vertical ODT onto the horizontal ODT along the horizontal. Switching to horizontal imaging, the same run in Figure 4.19a indicates that there is a large difference in alignment along the vertical in Figure 4.19b - the faint cloud near the bottom is a result of atoms trapped in the vertical ODT. Figure 4.19c shows the result of overlapping the vertical ODT focus onto the horizontal ODT, after a 2s hold time. We trap roughly  $1.4 \times 10^5$  atoms in Figure 4.19c.

For a more accurate characterisation of this crossed-dipole trap setup, we performed a quick temperature run to see if the temperature measured corresponds to roughly 10% of the combined trap depth for both ODTs (as a rough rule-of-thumb). A standard experimental sequence was run, and now as the horizontal ODT power is lowered it is transferred to the vertical ODT. After a 1s hold in the cross-dipole configuration the temperature was estimated to be  $5\mu\text{K}$ , which is quite a rough approximation given that long TOF measurements were difficult given the small number of atoms and the quick expansion (measurements up to 2.5ms TOF only).

The powers for the horizontal ODT and vertical ODT in this case were 140mW and 70mW respectively, giving trap depths of about  $4.8\mu\text{K}$  and  $41\mu\text{K}$  respectively for a total trap depth of  $45.8\mu\text{K}$  (orthogonal polarisation for the two beams means that no interference occurs). The extracted temperature for the cloud is therefore in good agreement with the theorised combined trap depth.

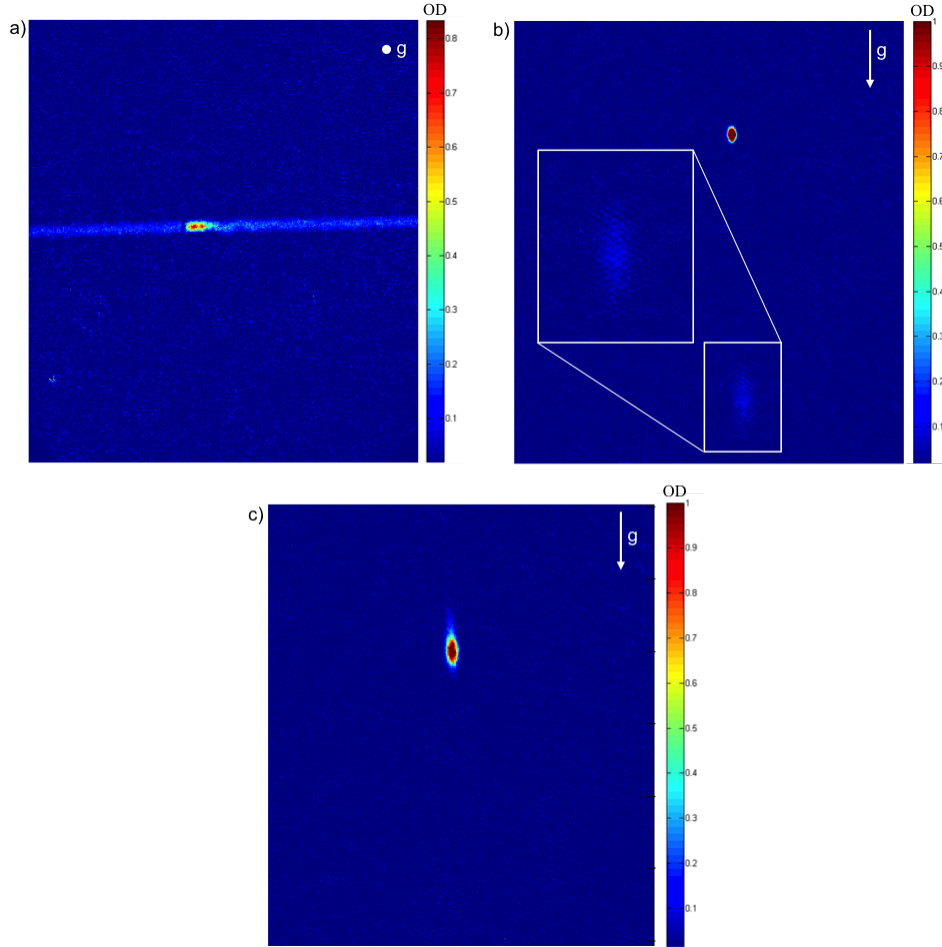


Figure 4.19: Absorption image examples taken when performing the initial alignment of the vertical 1064nm beam; a) Absorption image taken with the vertical imaging setup, in-situ, showing overlap of the vertical ODT with the horizontal ODT, with 800mW of power in each beam; b) Absorption image taken with the horizontal imaging, after 0.5ms TOF, of the same run from the first image, showing that the focus of the vertical ODT (inset) needs to be shifted vertically towards the horizontal ODT focus; c) Another horizontal imaging shot, after 0.5ms TOF, but now with the vertical focus shifted to overlap with the horizontal one. The vertical beam has 200mW, while the horizontal beam has 800mW.

#### 4.5.2 Setting Up the SLM Alignment

After completing the initial vertical beam alignment, the mirror can be replaced with the SLM and the first order of diffraction aligned onto the atoms for simple patterns. We now

wish to expand the beam size for overfilling of the SLM - instead of the 1:2 telescope before the SLM, we replace the  $f=100\text{mm}$  lens with a  $f=200\text{mm}$  lens to give a 1:4 telescope and increase the  $1/e^2$  half-width of the beam to  $2.2\text{mm}$ . A larger beam incident on the  $f=40$  focusing lens gives a tighter focus at the position of the atoms (in this case about  $6\mu\text{m}$ ). From a safety point of view, we must be careful not to direct too much power onto the SLM, as this SLM has a damage threshold of  $5\text{ W/cm}^2$ . Considering the peak intensity ( $2P/\pi w^2$ ) of the beam incident on the SLM (with the  $1/e^2$  half width of  $2.2\text{mm}$ ), the absolute maximum power that could be directed onto the SLM would be  $380\text{mW}$ . To be safe, we decide to work at just above half this maximum rating, by limiting the maximum power to the SLM to be  $200\text{mW}$  (using the PBS and half-waveplate combination after the AOM).

For trapping and alignment of the first order of diffraction, we note that our SLM diffracts 35% of the total light into the first order. From the initial  $200\text{mW}$  available, this would mean a total of  $70\text{mW}$  in the first order before taking into account the efficiency of the calculated light patterns. For a calculated spot size of  $6\mu\text{m}$  as mentioned above, the resulting trap depth for just  $70\text{mW}$  of power is about  $167\mu\text{K}$ , which should be sufficiently deep enough to trap atoms even from just after the RF evaporation stage, which is useful for initial alignment. For the more complex trap geometries which have a very low light efficiency, the resulting trap depth should still be capable of trapping atoms after the total evaporation sequence is completed. For the alignment, we use the MRAF algorithm to create a pair of diffraction limited spots (Figure 4.20). In the MRAF code, the two spots were created with a separation of 30 pixels, aligned along the direction of propagation of the horizontal ODT. When testing this pattern offline using the flip-mirror and  $f=40\text{mm}$  lens combination next to the SLM, the separation of the spots was measured to be  $93\mu\text{m}$  as detected by the CCD camera, such that each pixel in the MRAF calculation corresponds to  $3.1\mu\text{m}$ . The mixing parameter used was 0.65, and the input  $1/e^2$  beam waist was  $2.5\text{mm}$  (it was found that  $2.5\text{mm}$  gave smoother patterns on the camera for diffraction limited spots compared to the real beam waist of  $2.2\text{mm}$ ). The pattern was also shifted by (128,128) pixels from the centre to avoid the undiffracted light, and this offset was maintained for future patterns to ensure good alignment when changing target patterns. Finally, the efficiency for this double spot pattern was 71.6% - taking this efficiency into account with the diffraction efficiency into the first order results in a trap depth of just above  $50\mu\text{K}$  for each individual spot in the pattern.

An absorption image of atoms trapped in the double spot pattern is shown in Figure 4.20. With the trap depth mentioned above, these images are obtained after relaxation of the magnetic field gradient directly after the RF evaporation concluded, with  $200\text{mW}$  incident on the SLM as mentioned before. The atoms were held for a  $200\text{ms}$  wait time before  $0.5\text{ms}$  TOF expansion. A total of  $2.6 \times 10^5$  atoms were trapped in the below image. Also shown alongside are the associated images for the target pattern, the predicted intensity output, and the intensity as seen on the CCD camera when applying the phase pattern to the SLM.

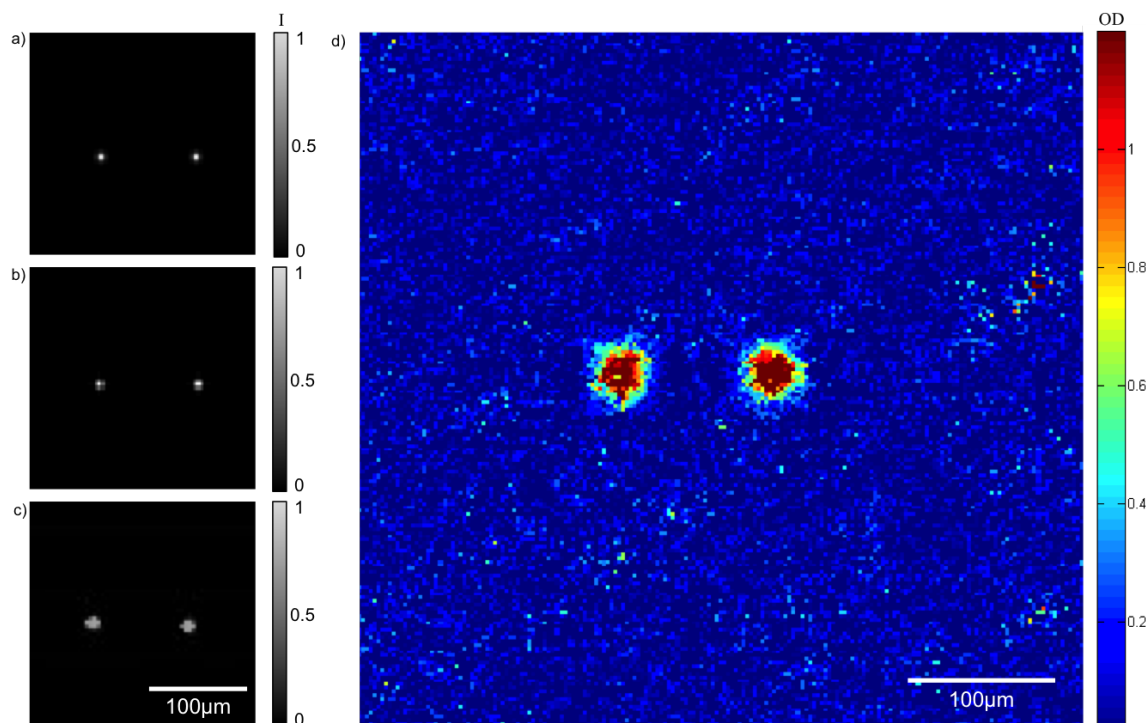


Figure 4.20: a) Target pattern for the MRAF calculation; b) The predicted intensity pattern after 200 iterations with a mixing parameter of  $m=0.65$ , with efficiency 0.716; c) An image taken of the pattern when applying the resulting phase hologram to the SLM; d) Vertical absorption image of atoms trapped in the double spot pattern, taken at 0.5ms TOF, with roughly  $2.6 \times 10^5$  atoms trapped in total.

## 4.6 Cold Atoms in Holographic Traps

At this point, we wanted to demonstrate the flexibility of our holographic traps by trapping atoms in more geometries, both discrete and continuous. These results are shown in Figure 4.21 below. The first pattern is an extension of the double spot pattern to a sequence of 4 spots, again generated using the MRAF algorithm for better light efficiency compared to the CG method. The separation of the spots was kept at 30 pixels like for the double spot pattern, spaced along the propagation axis of the horizontal ODT. With a mixing parameter of  $m=0.65$  the light efficiency for the predicted pattern was 71.5%. For the initial power of 200mW incident on the SLM, with 35% of light in the first order, the overall power in each spot is calculated to be 12.5mW, giving an estimated trap depth of  $29.8\mu\text{K}$ . The total number of atoms in the quad spot was about  $2.6 \times 10^5$  after a 0.5ms TOF.

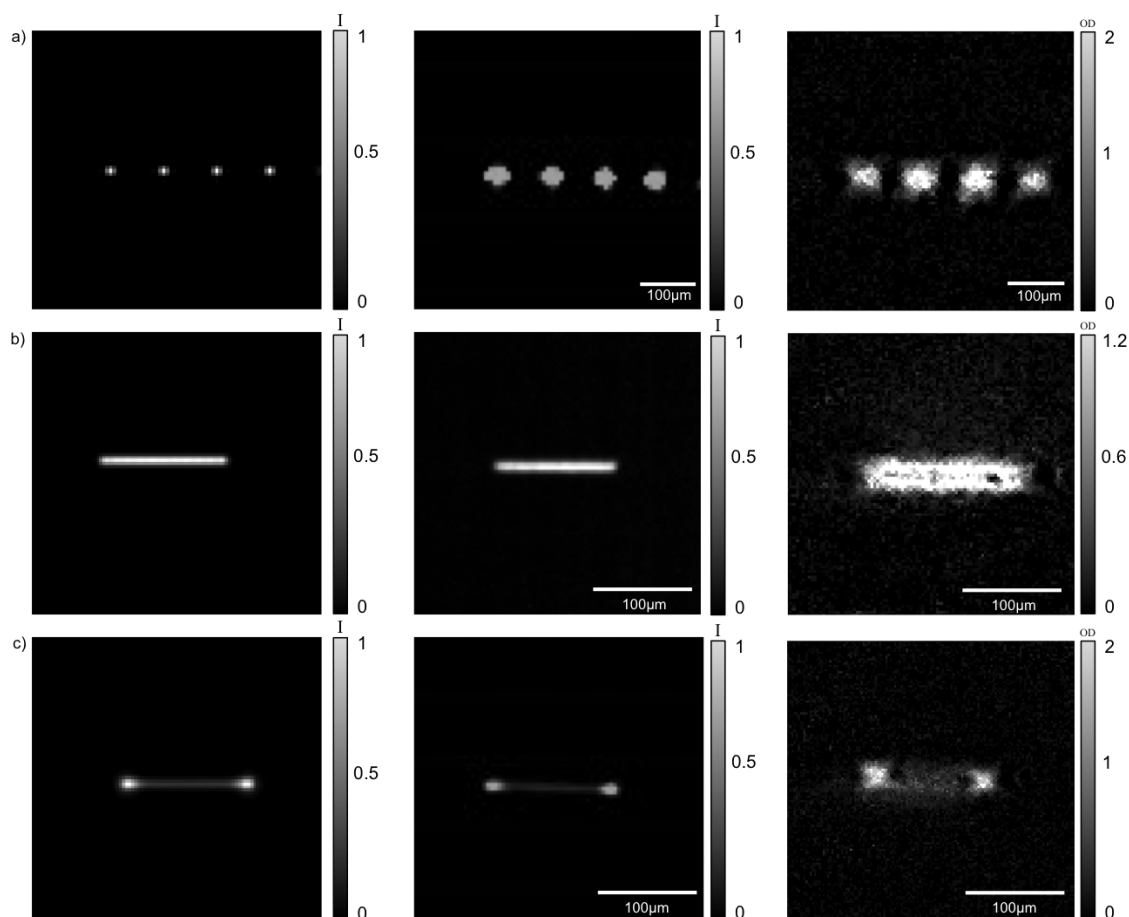


Figure 4.21: Selection of 1D trapping potentials used to trap cold atoms. The left column shows the predicted intensity patterns at the conclusion of the algorithm, the middle column shows images taken with the CCD camera showing the real experimental pattern after applying the hologram to the SLM, and the right column are short TOF absorption images of the trapped atoms; a) A sequence of four spots in a line, calculated using MRAF and trapping a total of  $2.6 \times 10^5$  atoms; b) A Gaussian line pattern, calculated using CG with a flat phase at the output, and trapping a total of  $1.6 \times 10^5$  atoms; c) A dumbbell pattern, calculated with CG with a flat phase at the output, and trapping a total of  $1.1 \times 10^5$  atoms.

An example of a continuous pattern generated using the CG algorithm is that of a Gaussian line in Figure 4.21b. The Gaussian line pattern was programmed to have a length of 40 pixels and a width of 2 pixels, which corresponds to a length of  $124 \mu\text{m}$  and a  $1/e^2$  half width of  $6.2 \mu\text{m}$ . The pattern was programmed along the axis of the ODT once again, and used the same offset as before to minimise misalignment from changing patterns.

The resulting light efficiency for the Gaussian line pattern was 9.8%, while the fidelity had a value of 0.99886. For 200mW incident on the SLM with the 35% first order diffraction efficiency, the total power available for the atoms was about 6.85mW, which gives a trap depth of  $0.8\mu\text{K}$ . The ODT was ramped down to 2% of the initial 3.5W, resulting in 70mW of the ODT light still present and a 2% trap depth of  $2.4\mu\text{K}$ . Combined, the total trap depth is roughly  $3.19\mu\text{K}$ . For obtaining the absorption image a 0.5ms TOF was used and the total atom number trapped was  $1.6 \times 10^5$ .

The third example of SLM trapped atoms along the propagation axis of the ODT is one combining the discrete spots and continuous line features - a “dumbbell” shape consisting of two Gaussian spot reservoirs connected by a narrow channel. This structure has applications for studies of transport of cold atoms between the two reservoirs. The two Gaussian spots were programmed to have a  $1/e^2$  half width of 4 pixels, with the channel having a width of 2 pixels and a length of 40 pixels (the same as the Gaussian line above). The peak intensity of the channel was 25% of the peak intensity of the individual reservoirs. Experimentally this results in a  $124\mu\text{m}$  length Gaussian line, width  $6.2\mu\text{m}$ , with two Gaussian spots on the end of width  $12.4\mu\text{m}$ . The CG code was used for this pattern, and again a flat phase was kept at the output plane, with the same programmed offset. The efficiency for the dumbbell pattern was 11.51%, giving a total power of about 8.1mW at the position of the atoms and a trap depth at the reservoir of  $4.5\mu\text{K}$ . The ODT was again evaporated down to 2% power, leaving 70mW for a trap depth of  $2.4\mu\text{K}$  due to the ODT and giving a combined trap depth of  $6.9\mu\text{K}$ . The fidelity of the dumbbell pattern was 0.9995. A 0.5ms TOF was undertaken before the absorption image in Figure 4.21c, where a total of  $1.1 \times 10^5$  atoms were trapped.

## 4.7 Light Sheet Setup

After managing to trap atoms in simple 1D geometries using just the SLM beam and a low amount of ODT power, attention turned to setting up the light sheet path to act as a canvas on which more complicated optical patterns that require the extra confinement can be attempted. Patterns, such as the ring trap, that extend beyond the width of the horizontal ODT require additional confinement, which will be provided by the light sheet.

The light sheet power is provided by the transmission output of the PBS in Figure 4.18. As mentioned before, the reflection path continues to the SLM and provides the holographic trap; now, we remove the beam block originally placed in the way of the light sheet path in order to re-use that power as the motorized waveplate rotates.

To simplify the initial alignment of the light sheet, we first aim to trap atoms in a focused ODT originating from the light sheet path without the cylindrical lens in place - the aim is to overlap the light sheet beam with the horizontal ODT beam using the PBS shown in Figure 4.23. For the horizontal ODT beam, at maximum power (about 3.5W on the atoms) an estimated trap depth of  $120\mu\text{K}$  is created at the position of the

atoms for a beam with a  $1/e^2$  waist of  $50\mu\text{m}$ . For the light sheet path, the beam size is initially reduced using a 2:1 telescope to give a  $1/e^2$  half width of  $0.55\text{mm}$  for passage through the AOM. The resulting beam is slightly diverging over a reasonably long path length - to obtain an estimate of the beam waist of this focused ODT we obtain an image of the focused spot offline by directing the light along the same path length and using an available  $f=50\text{mm}$  lens (instead of the  $f=60\text{mm}$  lens in the recess) to image the spot onto a Thorlabs DCU224M CCD camera (Figure 4.22a). We can then extract the data and fit a Gaussian (Figure 4.22b), which gives the  $1/e^2$  waist to be about  $12.4\mu\text{m}$ . Since the waist is proportional to the focal length of the lens, we can estimate that the spot of this ODT at the position of the atoms after the  $f=60\text{mm}$  lens in the recess is about  $15\mu\text{m}$ .

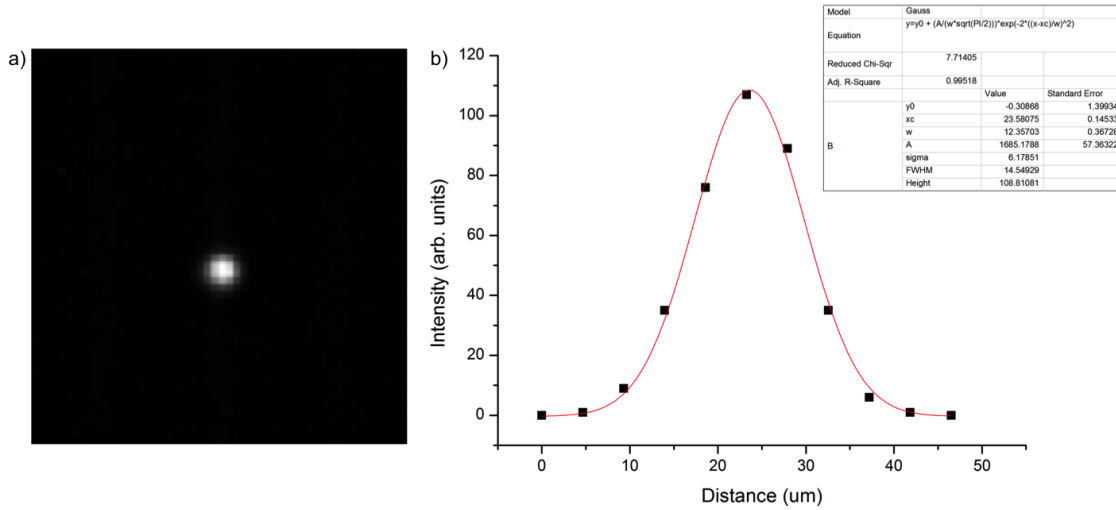


Figure 4.22: a) Camera image of the focused spot created with an  $f=50\text{mm}$  focal length lens for the beam on the light sheet path; b) Gaussian fit for this spot gives the beam waist estimate (inset).

Without any further lenses, we direct this beam through the viewport and through the  $60\text{mm}$  lens in the recess, creating a focused ODT with a waist of roughly  $15\mu\text{m}$  at the position of the atoms. For the initial trapping of atoms in the focus of this ODT, we send all available power that we had for the horizontal ODT into this light sheet path ODT (about  $3.5\text{W}$ ). The tighter waist resulting from the larger initial beam size results in a deeper optical trap (about  $1.35\text{mK}$ , sufficient to trap the atoms in after the RF evaporation has finished (similar to what is done for the regular horizontal ODT).

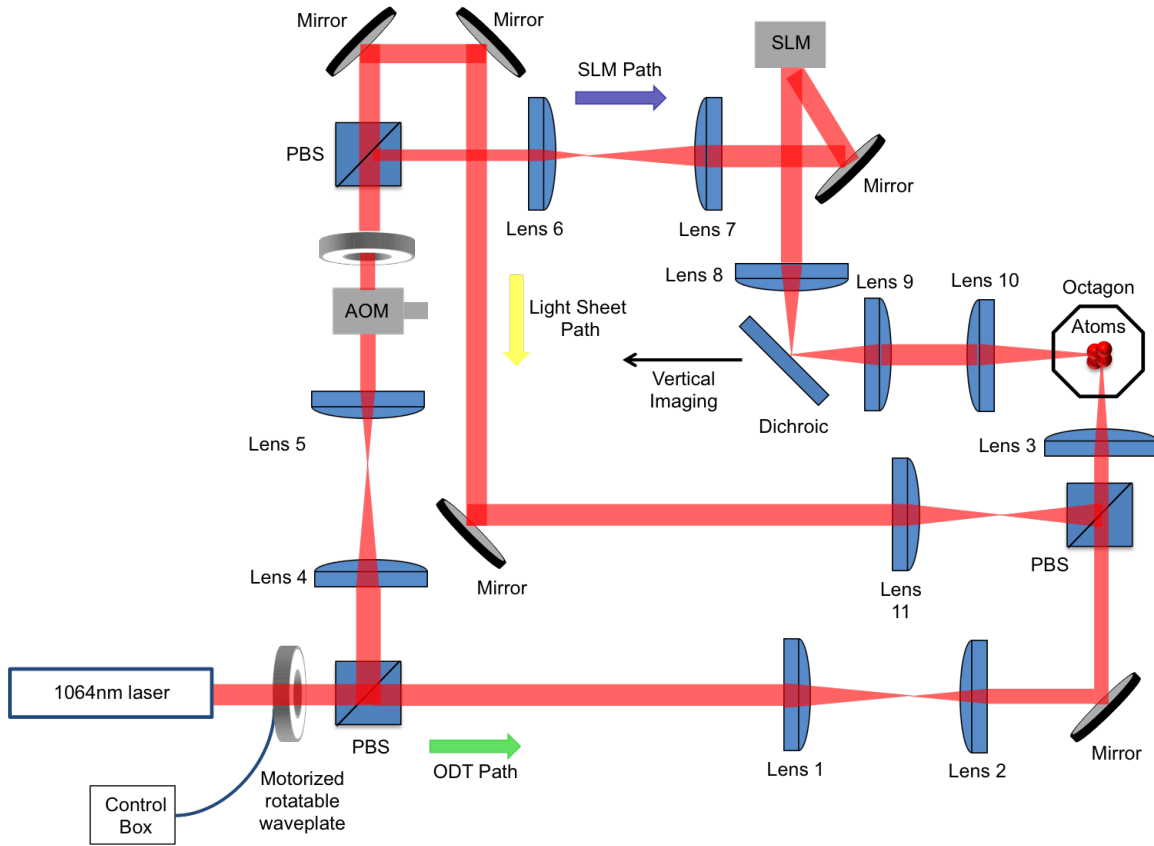


Figure 4.23: Diagram of the full optical path for the 1064nm laser light, comprising ODT path, SLM path and light sheet path. Focal length of lenses: Lens 1 = 150mm, Lens 2 = 60mm, Lens 3 = 60mm, Lens 4 = 100mm, Lens 5 = 50mm, Lens 6 = 50mm, Lens 7 = 200mm, Lens 8 = 40mm, Lens 9 = 40mm, Lens 10 = 40mm, Lens 11 = 150mm (cylindrical).

This procedure was carried out until we managed to trap atoms in the ODT on this path (see Figure 4.24). Figure 4.24a) shows an example absorption image of atoms in the usual horizontal ODT for a short (0.5ms) TOF, for comparison. Figure 4.24b) is an example image of atoms trapped using just the ODT along the light sheet path for the same TOF. After optimising the position to ensure good overlap with the horizontal ODT using both the horizontal and vertical imaging, we then set up the light sheet.

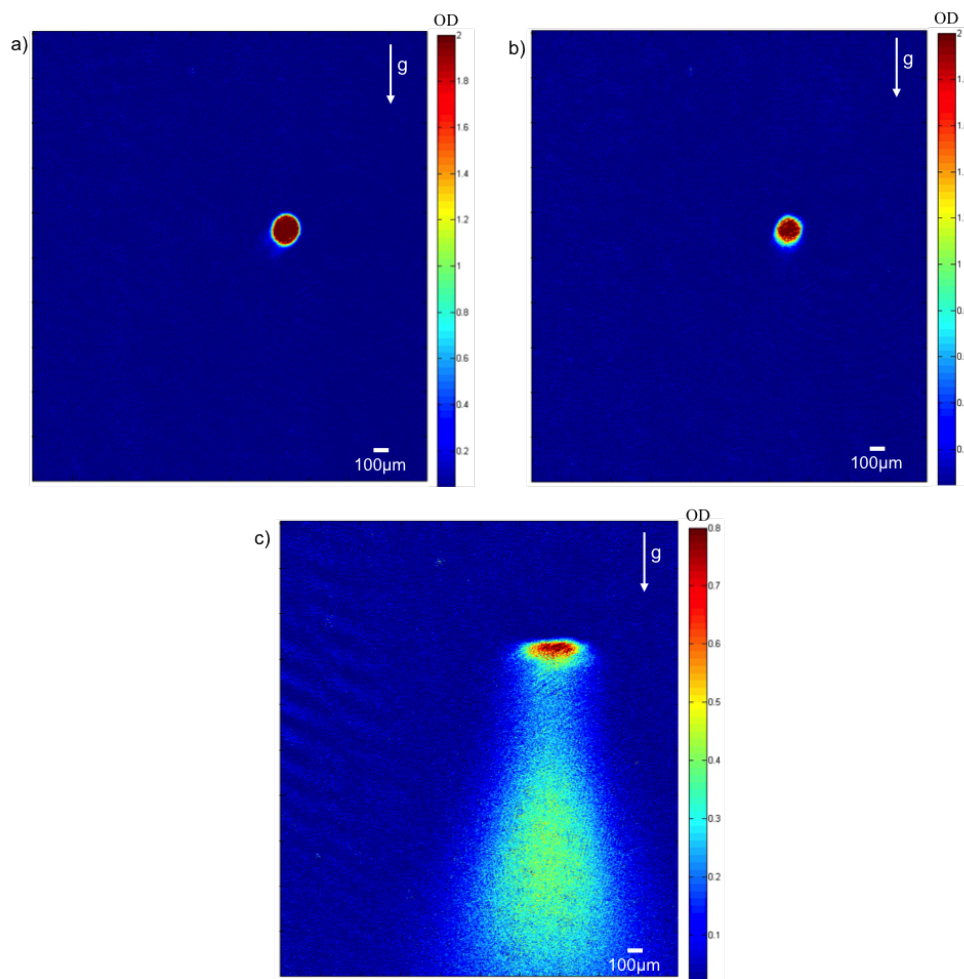


Figure 4.24: a) Absorption image of atoms trapped in the usual horizontal ODT; b) Absorption image of atoms trapped in the focused ODT created along the light sheet path; c) Absorption image of atoms in the light sheet potential just after the magnetic field gradient has been relaxed. All images taken after a 0.5ms TOF.

For our experiment, we use a  $f=150\text{mm}$  focal length cylindrical lens to create the light sheet - the combination of the  $f=150\text{mm}$  cylindrical lens and the  $f=60\text{mm}$  spherical lens in the recess results in a beam of  $1/e^2$  waist  $(543 \times 15)\mu\text{m}$  being created, which is comparable to other light sheets used in similar experiments [57]. The resulting trap depth of just the light sheet is roughly  $37\mu\text{K}$ . An image of atoms trapped in this light sheet configuration is seen in Figure 4.24c) - due to the reduced trap depth, the experimental sequence does not have the 100ms wait time after the magnetic field expansion down to  $14\text{G/cm}$ ; as can be

seen the atoms fall out of the trap.

After performing the alignment of the light sheet onto the ODT, the next step was to ensure good overlap for the light sheet and SLM beams. Horizontal imaging can again be used to diagnose the two beams as there should already be reasonable alignment from performing the previous experiments with simple SLM traps. Indeed, Figure 4.25a) below shows the absorption image resulting from the light sheet with a single spot SLM pattern (elongated due to the relatively weak focusing along the propagation axis). Alignment could be optimised further still using a simple double spot pattern, but this time orientated in the orthogonal direction to the horizontal ODT propagation axis. Without the light sheet present (achieved using a beam block), the number of atoms trapped in the double spot pattern is relatively low (about  $6.4 \times 10^4$ ), with an uneven distribution also present (Figure 4.25b). Without then changing the alignment and using the light sheet, we achieve a comparatively larger number of trapped atoms (about  $2.5 \times 10^5$ ), with a more even distribution as well (Figure 4.25c).

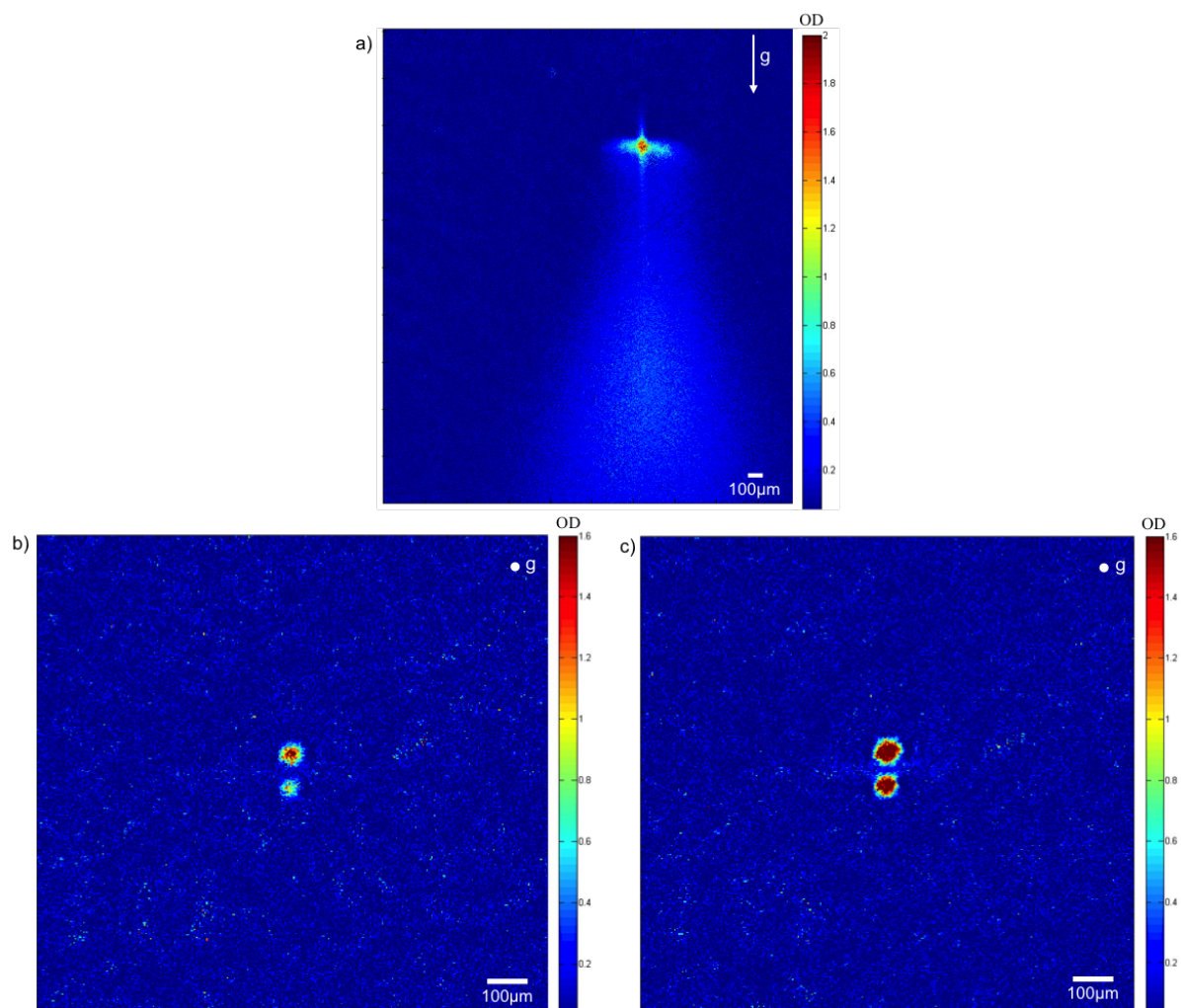


Figure 4.25: a) Horizontal absorption image taken with both the SLM and light sheet paths present to ensure overlap in the vertical direction; b) Vertical absorption image of a double spot pattern created orthogonal to the ODT propagation axis without the light sheet present, trapping a total of  $6.4 \times 10^4$  atoms; c) Vertical absorption image of the same double spot pattern but now with the light sheet path unblocked, resulting in a greater number of atoms trapped (a total of  $2.5 \times 10^5$  atoms). All images taken after 0.5ms TOF.

## 4.8 Additional Trap Configurations

With the light sheet in place, more complex patterns can be attempted. The main additional light patterns of interest in our group are ring traps for atomtronics and a star-shape

geometry for investigations of the topological Kondo effect - more background on these applications can be found in section 1.2 of Chapter 1.

The ring trap and Kondo patterns were created using the CG minimisation routine. The ring was programmed to have a diameter of 16 pixels (corresponding to a diameter of about  $50\mu\text{m}$ ), and a  $1/e^2$  half width of  $6.2\mu\text{m}$ . The resulting predicted intensity profile had a fidelity of 0.99988, with a light efficiency of 12.6%. This results in roughly 8.8mW total power for the ring trap at the position of the atoms. The horizontal ODT is now ramped all the way to 0% in the experimental setup now that the light sheet is present, almost extinguishing it completely (a measured power of 1.2mW is detected through the PBS, giving a trap depth of about  $0.04\mu\text{K}$ ). The light sheet, on the other hand, has about half of the full optical power available (measured to be about 1.5W) - we found we had to reduce the light sheet power as it would end up dominating the overall potential. The ring trap depth alone is roughly 225nK, while the light sheet trap depth is  $15.8\mu\text{K}$ . A total of  $9.3 \times 10^5$  atoms are trapped in the ring trap (Figure 4.26). The estimated critical temperature for condensation to occur in the described ring trap plus light sheet geometry is  $T_C \sim 358\text{nK}$ .

The cross pattern was programmed to have a set of four Gaussian lines, of length  $60\mu\text{m}$  each and the centres of two Gaussian lines along one axis set to be  $90\mu\text{m}$  apart to ensure a sufficient gap in the centre. Each Gaussian line has a width of  $6\mu\text{m}$ . The resulting intensity profile has a fidelity of 0.99939 with a light efficiency of 10.7%. This results in a total of 7.5mW for the cross pattern at the position of the atoms. The horizontal ODT is again ramped to 0% and the light sheet has the same potential as for the ring pattern. Each individual Gaussian line trap has a depth of roughly 445nK, while the light sheet trap depth is again  $15.8\mu\text{K}$ . A total of  $4.7 \times 10^5$  atoms were trapped in the cross pattern (Figure 4.26). For an estimation of the critical temperature in a single Gaussian line plus light sheet potential, assuming an even distribution of atoms in each line, the critical temperature is estimated as  $T_C \sim 356\text{nK}$ .

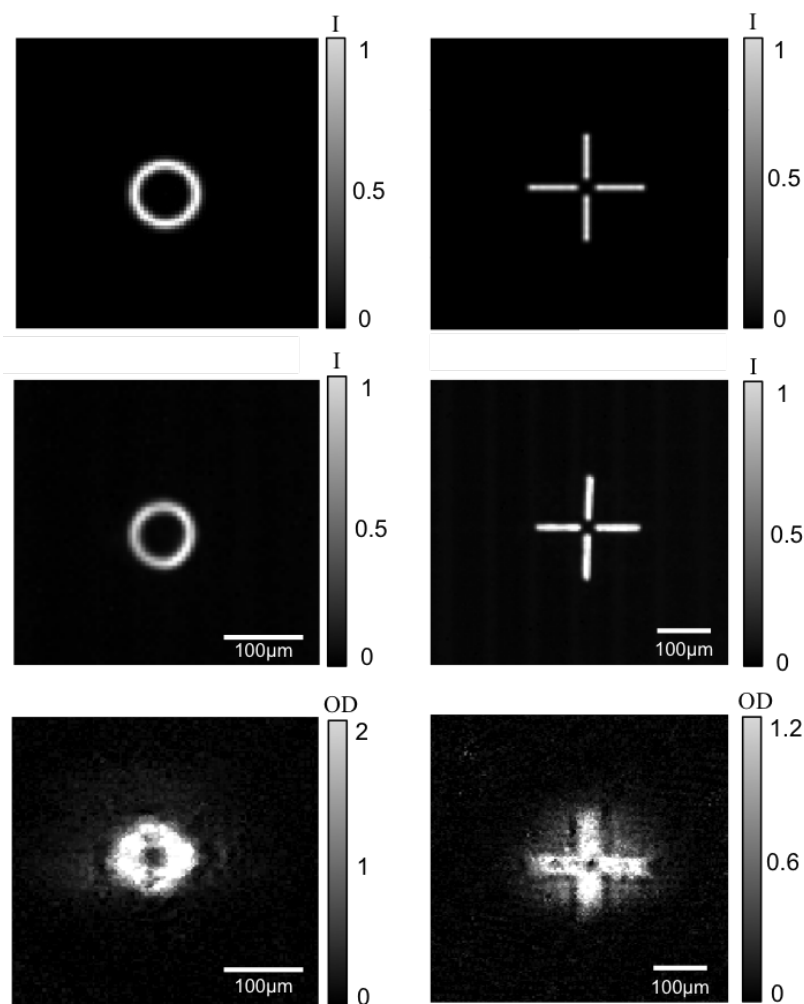


Figure 4.26: Images of atoms trapped in a ring trap (left) and a Kondo cross pattern (right). The top row of images shows the predicted intensity profile at the conclusion of the CG algorithm, the middle row shows the camera images of the light pattern after the phase has been loaded onto the SLM, and the lower row are short TOF (0.5ms) absorption images. A total of  $9.3 \times 10^5$  atoms are trapped in the ring trap and about  $4.7 \times 10^5$  atoms are trapped in the cross pattern.

The attraction of using red-detuned light to trap atoms as opposed to blue-detuned light is that it opens up the possibility of using the phase of the light at the position of the atoms to further manipulate the atomic cloud. A simple example of this is, instead of using a flat phase profile in the output plane for the target patterns above, we instead attempt to manufacture a phase slip in the output plane such that the destructive interference can

engineer a very narrow barrier. To accomplish this, we create two target patterns of a single Gaussian line - one pattern has a continuous, flat phase profile across the line while the other has a sharp  $\pi$  phase change halfway across the line. In the resulting intensity profiles (Figure 4.27), the resulting destructive interference at the output plane produces a slip in the intensity profile, and so programming phase jumps into the output plane light can result in thin barriers being generated. This brief example of output plane phase control opens up the avenue of using discrete phase jumps to engineer barriers that are close to the diffraction limit for e.g. the junction in the cross pattern shown above.

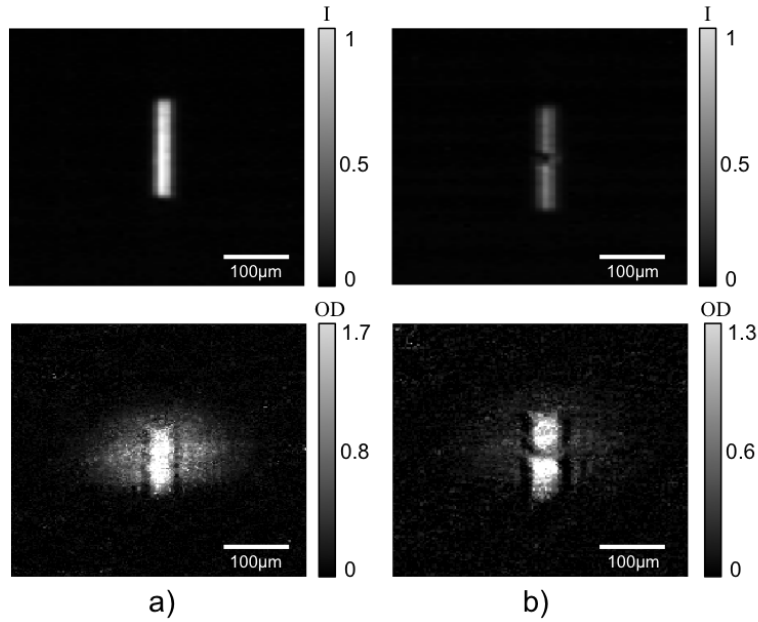


Figure 4.27: Top row of images show the resulting intensity profiles obtained from the CCD camera, while bottom row shows short (0.5ms) TOF images of atoms trapped in a) Gaussian line target profile with a flat phase and b) the same Gaussian line target profile but with a phase slip of  $\pi$  halfway along the line.

## 4.9 Summary

We have successfully achieved the trapping of cold atoms in multiple spatial geometries using phase manipulation of red-detuned light with a single SLM displaying an appropriate phase pattern generated using computational techniques developed over the course of this project. Illumination of a single SLM with overlapped light of different wavelengths allows a composite optical pattern to be generated for experiments with limited optical access, while conjugate gradient minimisation provides light patterns with a high degree of fidelity and

---

accuracy, important for successful trapping of low temperature atoms. These techniques further the amount of control over both the amplitude and phase of the optical field for atomic manipulation, with a selection of light patterns provided that highlight the versatile nature of phase-only spatial light modulators.

Our experimental apparatus recycles the laser power that is removed from the optical dipole trap during evaporative cooling, transferring it to an illumination beam to be phase-modulated by the SLM plus a light sheet canvas onto which the holographic traps are generated. Specifically, the focus of this project was the trapping of cold atoms in ring traps and in narrow waveguides for applications to atomtronics and quantum simulation.

# Chapter 5

## Conclusions

### 5.1 Summary

In conclusion, the variety of techniques and devices available for the trapping and manipulation of ultracold atoms continues to offer excellent possibilities for furthering our understanding of fundamental quantum questions and condensed matter systems towards the goal of quantum sensors and metrology instrumentation.

In the context of this thesis, one focus has been the creation of a compact MOT apparatus for teaching and outreach purposes. The motivating factor behind developing this setup is the modern drive within the cold atoms community for transferring the bulky lab-based quantum sensing and measurement equipment into scaled down systems that have real-world applications. Our apparatus is not intended to perform as a fully integrated device; instead, our aim is to provide an accessible and robust cold atoms demonstration that is intuitive for both an undergraduate laboratory setting and as an outreach exhibit for the general public. By setting up the dichroic atomic vapour laser lock (DAVLL) as well as the sidebands electronics, the portable MOT has been established as an undergraduate laboratory experiment whereby we have given examples of a couple of measurements that are at the appropriate level for an undergraduate honours lab student. Comparable setups were showcased at public engagement events in collaboration with the University of Strathclyde in 2015; the apparatus at the outreach events made use of the grating chip to generate the necessary cooling beams and provide a significant simplification to the whole setup when the experiment was taken outside the lab.

The second goal of the project was the integration of a phase-only SLM into our main experimental setup after producing the first BECs seen at St Andrews. The double vacuum chamber apparatus was designed and built after realising that the use of light induced atomic desorption (LIAD) to regulate the background pressure within a single chamber apparatus would provide neither a large enough MOT nor a sufficient lifetime for the atomic cloud to progress towards quantum degeneracy. The choice of 2D MOT as a loading mech-

anism for the 3D MOT was chosen to provide fast MOT loading with a high atomic flux, while the pressure difference between loading and experiment chambers is maintained with a custom-made differential pumping tube. After optimisation of the MOT parameters to ensure roughly  $10^9$  atoms are captured into the purely magnetic trap, the computer control of the experiment was developed to ensure full Labview control of the experimental sequence. To incorporate a figure of merit for the performance of our system, we compared our phase space density (PSD) results during the evaporation sequence with those in [20] where the authors employ a similar hybrid evaporative cooling scheme to quantum degeneracy. We find that we obtain comparable PSD numbers, with our pure condensate atom number ( $1.95 \times 10^5$ ) lower by one order of magnitude than the number reported in [20] ( $2 \times 10^6$ ).

The final part of this project focused on loading the ensemble of cold atoms into holographic optical traps generated using a single phase-only SLM. The multi-wavelength and high fidelity phase and amplitude control techniques (using the MRAF and CG algorithms respectively) furthers the amount of control and flexibility offered by the SLM, both computationally and experimentally. The multi-wavelength technique, implemented in Matlab, is designed as a method that allows light of different wavelengths to be overlapped onto a single SLM and form a composite optical structure for atom manipulation. Specifically, the versatility of such a setup is ideal when optical access for light of multiple wavelengths is limited, and additional wavelengths can be added by overlapping the light onto the existing optical path. For the high fidelity light patterns using conjugate gradient minimisation, we define a figure of merit for the performance of our algorithm by comparing our results with those of [138] using the non-uniformity error defined in equation 4.25. The authors of [138] developed full amplitude and phase control of the output plane light using an IFTA, which they compare to a previous regionally-constrained algorithm in [145] - they found that the regionally-constrained algorithm was more accurate at the expense of light efficiency. For the far-field holograms of lines of continuous intensity with a phase gradient, the regional algorithm gives  $\epsilon_{nu} = 0.04\%$ ,  $\epsilon_{\Phi} = 1.63\%$  and  $\eta = 3.48\%$ . The full-plane IFTA, on the other hand, was less accurate with  $\epsilon_{nu} = 3.48\%$  and  $\epsilon_{\Phi} = 3.77\%$  but with a much higher efficiency  $\eta = 77.84\%$ . In our case, the comparable continuous patterns are smoother and more accurate -  $\epsilon_{nu}$  is lower by more than a factor of 6 and  $\epsilon_{\Phi}$  is lower by one to two orders of magnitude compared to the regional IFTA. Additionally, our light efficiency for the conjugate gradient patterns is more than a factor 3 higher than the regional IFTA (although still less than the full-plane IFTA). Experimentally, we note that our images of cold atoms trapped in continuous geometries compare well to those seen in Figure 1.1(h) and Figure 1.1(j). Additionally, by trapping with red-detuned light in our case as opposed to blue detuned light, we show that sufficiently smooth optical patterns can be generated whereby atoms are trapped in the highest intensity portions of the beam, compared to trapping in the dark with blue-detuned light. Finally, trapping with red-detuned light also opens up the avenue of using the phase of the light at the position of the atoms in order to further manipulate the atoms.

## 5.2 Future Plans

In the near future there are a number of immediate additions to be made to the portable MOT setup. The most pressing of these would be to swap out the current AD590 temperature sensor that has been part of the outreach MOT setup since the beginning of the project for a thermistor, which we have tested to ensure there is no adverse effect on it from turning on the microwave generation electronics. Proper temperature stabilisation of the laser diode will then drastically improve the DAVLL that we have integrated into the setup, ensuring frequency stabilisation over long periods for both teaching and outreach. While the DAVLL lock is capable of maintaining the laser frequency for the teaching lab measurements of the atom number and the pressure at the position of the MOT, the temperature stabilisation of the diode is necessary for the outreach applications where the apparatus is more susceptible to perturbations.

The addition of the grating chip technology, provided by the University of Strathclyde, is also of high priority when it comes to public engagement, significantly simplifying the optical alignment compared to the three pairs of retro-reflected MOT beams currently. The alignment requirements of the six-beam MOT, while a useful tool for the undergraduate lab that gives practice at overlapping the various cooling beams, would be impractical if the portable MOT is to be transported for outreach. The grating chip, using just a single input beam to form the optical molasses, would provide a much more robust system and allow faster setup at the venue. Additional shim coils for the compensation of stray magnetic fields may also be necessary in order to successfully integrate the grating chip, which are currently not in place for the standard six-beam MOT.

As well as the quantitative data acquisition currently set up for the compact MOT (measuring the number of atoms in the MOT and estimating the pressure at the region of the MOT), another task would be to obtain an estimate of the temperature of the cloud by observing the expansion of the cloud during a molasses phase with the laser light still present. A CCD camera is used to acquire images of the cloud at regular intervals during this slow expansion when the coils are turned off. The temperature can then be extracted from the rate of expansion of the atomic cloud, which provides an intuitive insight into how cold the atoms really are. The ability to obtain an estimate of the temperature of the cloud without the need for switching the laser beams off (by having to use, for example, mechanical shutters) would be an important step for both teaching and outreach.

For the holographic trapping of cold atoms, the combination of the light sheet potential plus the potentials generated from the SLM using the high fidelity CG minimisation routine has resulted in the successful trapping of atoms in both ring and cross pattern geometries. The addition of blue-detuned light could lead to smaller diffraction-limited features, and therefore tighter trapping potentials and narrower barriers. Tighter trapping potentials would aid reaching the Tonks-Girardeau regime, while narrow barriers results in better tunneling between the guides. For the red-detuned light currently in use, further manipulation with the phase of the light at the output plane allows relatively straight-

forward barriers to be engineered in the Kondo pattern, as opposed to keeping the phase flat and manufacturing a gap using the amplitude of light alone. Additionally, dynamic manipulation of the light profile is required for the investigations of rotation when using ring traps.

Now that the initial trapping of atoms in red-detuned traps has been achieved, an important milestone for this experiment would be probing methods by which the atomic gas can be made as cold as possible by deforming, or expanding, the trapping potential dynamically. Achieving extremely low temperatures is important for both the rotation sensing and quantum simulation applications, and as such it is crucial that we probe the capability of our SLM traps for achieving this. Such a demonstration of dynamic trap manipulation is also necessary for imparting rotation to an ultracold gas contained within a ring trap. For the investigations of the topological Kondo effect, an improvement on the diffraction limit of our system is also likely needed - the diffraction limit for our current setup is  $\sim 6\mu\text{m}$ . To reach the Tonks-Girardeau regime, the waist of the narrow waveguides would need to be around  $1\mu\text{m}$ . Blue-detuned light can provide narrower guides than red-detuned light, but it will also be necessary to improve the diffraction limit of our optical system further. Our current choice of atomic species ( $^{87}\text{Rb}$ ) also makes reaching the Tonks-Girardeau regime more challenging due to the difficulty of using Feshbach resonances to tune the scattering length. An alternative atomic species is caesium ( $^{133}\text{Cs}$ ) - Feshbach resonances using  $^{133}\text{Cs}$  can greatly increase the scattering length and consequently aid reaching a true one-dimensional Tonks gas.

# Bibliography

- [1] M. H. Anderson, J. R. Ensher, M. R. Matthews, C. E. Wieman, and E. A. Cornell, “Observation of Bose-Einstein condensation in a dilute atomic vapor”, *Science*, vol. 269, p. 5221, 1995.
- [2] K. B. Davis, M. -O. Mewes, M. R. Andrews, N. J. van Druten, D. S. Durfee, D. M. Kurn, and W. Ketterle, “Bose-Einstein Condensation in a Gas of Sodium Atoms”, *Phys. Rev. Lett.*, vol. 75, p. 3969, 1995.
- [3] C. C. Bradley, C. A. Sackett, and R. G. Hulet, “Bose-Einstein Condensation of Lithium: Observation of Limited Condensate Number”, *Phys. Rev. Lett.*, vol. 78, p. 985, 1997.
- [4] D. G. Fried, T. C. Killian, L. Willmann, D. Landhuis, S. C. Moss, D. Kleppner, and T. J. Greytak, “Bose-Einstein Condensation of Atomic Hydrogen”, *Phys. Rev. Lett.*, vol. 81, p. 3811, 1998.
- [5] H. Deng, G. Weihs, C. Santori, J. Bloch, and Y. Yamamoto, “Condensation of Semiconductor Microcavity Exciton Polaritons”, *Science*, vol. 298, p. 199, 2002.
- [6] S. O. Demokritov, V. E. Demidov, O. Dzyapko, G. A. Melkov, A. A. Serga, B. Hillebrands, and A. N. Slavin, “Bose-Einstein condensation of quasi-equilibrium magnons at room temperature under pumping”, *Nature*, vol. 443, p. 430, 2006.
- [7] J. Klaers, J. Schmitt, F. Vewinger, and M. Weitz, “Bose-Einstein condensation of photons in an optical microcavity”, *Nature*, vol. 468, p. 545, 2010.
- [8] A. Einstein, “Quantentheorie des einatomigen idealen Gases”, *Königliche Preußische Akademie der Wissenschaften. Sitzungsberichte*, p. 261, 1924.
- [9] A. Einstein, “Quantentheorie des einatomigen idealen Gases. Zweite Abhandlung”, *Sitzungsberichte der Preußischen Akademie der Wissenschaften (Berlin), Physikalisch-mathematische Klasse*, p. 3, 1925.
- [10] A. Einstein, “Zur Quantentheorie des idealen Gases”, *Sitzungsberichte der Preußischen Akademie der Wissenschaften (Berlin), Physikalisch-mathematische Klasse*, p. 18, 1925.

- [11] S. N. Bose, “Plancks gesetz und lichtquantenhypothese”, *Zeitschrift für Physik*, vol. 26, p. 178, 1924.
- [12] W. Ketterle, D. S. Durfee, and D. M. Stamper-Kurn, *Making, probing and understanding Bose-Einstein condensates. In Bose-Einstein condensation in atomic gases, Proceedings of the International School of Physics “Enrico Fermi”, Course CXL*. Amsterdam: IOS Press, 1999.
- [13] E. L. Raab, M. Prentiss, A. Cable, S. Chu, and D. E. Pritchard, “Trapping of Neutral Sodium Atoms with Radiation Pressure”, *Phys. Rev. Lett.*, vol. 59, p. 2631, 1987.
- [14] H. J. Metcalf and P. van der Straten, *Laser Cooling and Trapping*. Springer, 1999.
- [15] K. B. Davis, M. -O. Mewes, M. A. Joffe, and W. Ketterle, in “Fourteenth International Conference on Atomic Physics, Boulder, Colorado, 1994, Book of Abstracts, 1-M3” (University of Colorado, Boulder, Colorado), 1994.
- [16] W. Petrich, M. H. Anderson, J. R. Ensher, and E. A. Cornell, in “Fourteenth International Conference on Atomic Physics, Boulder, Colorado, 1994, Book of Abstracts, 1M-7” (University of Colorado, Boulder, Colorado), 1994.
- [17] S. Stellmer, B. Pasquiou, R. Grimm, and F. Schreck, “Laser Cooling to Quantum Degeneracy”, *Phys. Rev. Lett.*, vol. 110, p. 263003, 2013.
- [18] J. Hu, A. Urvoy, Z. Vendeiro, V. Crépel, W. Chen, and V. Vuletić, “Creation of a Bose-condensed gas of  $^{87}\text{Rb}$  by laser cooling”, *Science*, vol. 358, p. 1078, 2017.
- [19] M. D. Barrett, J. A. Sauer, and M. S. Chapman, “All-Optical Formation of an Atomic Bose-Einstein Condensate”, *Phys. Rev. Lett.*, vol. 87, p. 010404, 2001.
- [20] Y.-J. Lin, A. R. Perry, R. L. Compton, I. B. Spielman, and J. V. Porto, “Rapid production of  $^{87}\text{Rb}$  Bose-Einstein condensates in a combined magnetic and optical potential”, *Phys. Rev. A*, vol. 79, p. 063631, 2009.
- [21] M. R. Andrews, C. G. Townsend, H.-J. Miesner, D. S. Durfee, D. M. Kurn, and W. Ketterle, “Observation of Interference Between Two Bose Condensates”, *Science*, vol. 275, p. 637, 1997.
- [22] M. Greiner, O. Mandel, T. Esslinger, T. W. Hänsch, and I. Bloch, “Quantum phase transition from a superfluid to a Mott insulator in a gas of ultracold atoms”, *Nature*, vol. 415, p. 39, 2002.
- [23] M. R. Andrews, D. M. Kurn, H.-J. Miesner, D. S. Durfee, C. G. Townsend, S. Inouye, and W. Ketterle, “Propagation of Sound in a Bose-Einstein Condensate”, *Phys. Rev. Lett.*, vol. 79, p. 553, 1997.

- [24] M. R. Matthews, B. P. Anderson, P. C. Haljan, D. S. Hall, C. E. Wieman, and E. A. Cornell, “Vortices in a Bose-Einstein Condensate”, *Phys. Rev. Lett.*, vol. 83, p. 2498, 1999.
- [25] K. W. Madison, F. Chevy, W. Wohlleben, and J. Dalibard, “Vortex Formation in a Stirred Bose-Einstein Condensate”, *Phys. Rev. Lett.*, vol. 84, p. 806, 2000.
- [26] W. Petrich, M. H. Anderson, J. R. Ensher, and E. A. Cornell, “Stable, Tightly Confining Magnetic Trap for Evaporative Cooling of Neutral Atoms”, *Phys. Rev. Lett.*, vol. 74, p. 3352, 1995.
- [27] T. Bergeman, G. Erez, and H. Metcalf, “Magnetostatic trapping fields for neutral atoms”, *Phys. Rev. A*, vol. 35, p. 1535, 1987.
- [28] U. Ernst, A. Marte, F. Schreck, J. Schuster, and G. Rempe, “Bose-Einstein condensation in a pure Ioffe-Pritchard field configuration”, *Europhys. Lett.*, vol. 41, p. 1, 1998.
- [29] M. Gildemeister, E. Nugent, B. E. Sherlock, M. Kubasik, B. T. Sheard, and C. J. Foot, “Trapping ultracold atoms in a time-averaged adiabatic potential”, *Phys. Rev. A*, vol. 81, p. 031402(R), 2010.
- [30] O. Morizot, Y. Colombe, V. Lorent, H. Perrin, and B. M. Garraway, “Ring trap for ultracold atoms”, *Phys. Rev. A*, vol. 74, p. 023617, (2006).
- [31] B. E. Sherlock, M. Gildemeister, E. Owen, E. Nugent, and C. J. Foot, “Time-averaged adiabatic ring potential for ultracold atoms”, *Phys. Rev. A*, vol. 83, p. 043408, 2011.
- [32] M. Gildemeister, B. E. Sherlock, and C. J. Foot, “Techniques to cool and rotate Bose-Einstein condensates in time-averaged adiabatic potentials”, *Phys. Rev. A*, vol. 85, p. 053401, 2012.
- [33] M. Keil, O. Amit, S. Zhou, D. Groswasser, Y. Japha, and R. Folman, “Fifteen years of Cold Matter on the Atom Chip: Promise, Realizations and Prospects”, *Journal of Modern Optics*, vol. 63, p. 1840, 2016.
- [34] J. Reichel, W. Hänsel, and T. W. Hänsch, “Atomic Micromanipulation with Magnetic Surface Traps”, *Phys. Rev. Lett.*, vol. 83, p. 3398, 1999.
- [35] R. Folman, P. Krüger, D. Cassettari, B. Hessmo, T. Maier, and J. Schmiedmayer, “Controlling Cold Atoms using Nanofabricated Surfaces: Atom Chips”, *Phys. Rev. Lett.*, vol. 84, p. 4749, 2000.
- [36] N. H. Dekker, C. S. Lee, V. V. Lorent, J. H. Thywissen, S. P. Smith, M. Drndić, R. M. Westervelt, and M. Prentiss, “Guiding Neutral Atoms on a Chip”, *Phys. Rev. Lett.*, vol. 84, p. 1124, 2000.

- [37] H. Ott, J. Fortagh, G. Schlotterbeck, A. Grossmann, and C. Zimmermann, “Bose-Einstein Condensation in a Surface Microtrap”, *Phys. Rev. Lett.*, vol. 87, p. 230401, 2001.
- [38] W. Hänsel, P. Hommelhoff, T. W. Hänsch, and J. Reichel, “Bose-Einstein condensation on a microelectric chip”, *Nature*, vol. 413, p. 498, 2001.
- [39] T. C. Li, H. Kelkar, D. Medellin, and M. G. Raizen, “Real-time control of the periodicity of a standing wave: an optical accordion”, *Opt. Express*, vol. 16, p. 5465, 2008.
- [40] G. Wirth, M. Ölschläger, and A. Hemmerich, “Evidence for orbital superfluidity in the P-band of a bipartite optical square lattice”, *Nature Physics*, vol. 7, p. 147, 2011.
- [41] P. Soltan-Panahi, J. Struck, P. Hauke, A. Bick, W. Plenkers, G. Meineke, C. Becker, P. Windpassinger, M. Lewenstein, and K. Sengstock, “Multi-Component Quantum Gases in Spin-Dependent Hexagonal Lattices”, *Nature Physics*, vol. 7, p. 434, 2011.
- [42] D. Jaksch, C. Bruder, J. I. Cirac, C. W. Gardiner, and P. Zoller, “Cold bosonic atoms in optical lattices”, *Phys. Rev. Lett.*, vol. 81, p. 3108, 1998.
- [43] M. Köhl, H. Moritz, T. Stöferle, K. Günter, and T. Esslinger, “Fermionic Atoms in a Three Dimensional Optical Lattice: Observing Fermi Surfaces, Dynamics, and Interactions”, *Phys. Rev. Lett.*, vol. 94, p. 080403, 2005.
- [44] R. Jördens, N. Strohmaier, K. Günter, H. Moritz, and T. Esslinger, “A Mott insulator of fermionic atoms in an optical lattice”, *Nature*, vol. 455, p. 204, 2008.
- [45] U. Schneider, L. Hackermüller, S. Will, T. Best, I. Bloch, T. A. Costi, R. W. Helmes, D. Rasch, and A. Rosch, “Metallic and Insulating Phases of Repulsively Interacting Fermions in a 3D Optical Lattice”, *Science*, vol. 322, p. 1520, 2008.
- [46] W. S. Bakr, J. I. Gillen, A. Peng, S. Fölling, and M. Greiner, “A quantum gas microscope for detecting single atoms in a Hubbard-regime optical lattice”, *Nature*, vol. 462, p. 74, 2009.
- [47] J. F. Sherson, C. Weitenberg, M. Endres, M. Cheneau, I. Bloch, and S. Kuhr, “Single-atom resolved fluorescence imaging of an atomic Mott insulator”, *Nature*, vol. 467, p. 68, 2010.
- [48] W. S. Bakr, A. Peng, M. E. Tai, R. Ma, J. Simon, J. I. Gillen, S. Fölling, L. Pollet, and M. Greiner, “Probing the Superfluid-to-Mott Insulator Transition at the Single-Atom Level”, *Science*, vol. 329, p. 547, 2010.
- [49] M. Endres, M. Cheneau, T. Fukuhara, C. Weitenberg, P. Schauß, C. Gross, L. Mazza, M. C. Bañuls, L. Pollet, I. Bloch, and S. Kuhr, “Observation of Correlated Particle-Hole

- Pairs and String Order in Low-Dimensional Mott Insulators”, *Science*, vol. 334, p. 200, 2011.
- [50] M. Miranda, R. Inoue, Y. Okuyama, A. Nakamoto, and M. Kozuma, “Site-resolved imaging of ytterbium atoms in a two-dimensional optical lattice”, *Phys. Rev. A*, vol. 91, p. 063414, 2015.
- [51] R. Yamamoto, J. Kobayashi, T. Kuno, K. Kato, and Y. Takahashi, “An ytterbium quantum gas microscope with narrow-line laser cooling”, *New J. Phys.*, vol. 18, p. 023016, 2016.
- [52] L. W. Cheuk, M. A. Nichols, M. Okan, T. Gersdorf, V. V. Ramasesh, W. S. Bakr, T. Lompe, and M. W. Zwierlein, “A Quantum Gas Microscope for Fermionic Atoms”, *Phys. Rev. Lett.*, vol. 114, p. 193001, 2015.
- [53] E. Haller, J. Hudson, A. Kelly, D. A. Cotta, B. Peaudecerf, G. D. Bruce, and S. Kuhr, “Single-atom imaging of fermions in a quantum-gas microscope”, *Nature Physics*, vol. 11, p. 738, 2015.
- [54] M. F. Parsons, F. Huber, A. Mazurenko, C. S. Chiu, W. Setiawan, K. Wooley-Brown, S. Blatt, and M. Greiner, “Site-resolved Imaging of Fermionic Lithium-6 in an Optical Lattice”, *Phys. Rev. Lett.*, vol. 114, p. 213002, 2015.
- [55] A. Omran, M. Boll, T. Hilker, K. Kleinlein, G. Salomon, I. Bloch, and C. Gross, “Microscopic Observation of Pauli Blocking in Degenerate Fermionic Lattice Gases”, *Phys. Rev. Lett.*, vol. 115, p. 263001, 2015.
- [56] G. J. A. Edge, R. Anderson, D. Jervis, D. C. McKay, R. Day, S. Trotzky, and J. H. Thywissen, “Imaging and addressing of individual fermionic atoms in an optical lattice”, *Phys. Rev. A*, vol. 92, p. 063406, 2015.
- [57] K. Henderson, C. Ryu, C. MacCormick, and M. G. Boshier, “Experimental demonstration of painting arbitrary and dynamic potentials for Bose-Einstein condensates”, *New J. Phys.*, vol. 11, p. 043030, 2009.
- [58] T. A. Bell, J. A. P. Glidden, L. Humbert, M. W. J. Bromley, S. A. Haine, M. J. Davis, T. W. Neely, M. A. Baker, and H. Rubinsztein-Dunlop, “Bose-Einstein condensation in large time-averaged optical ring potentials”, *New J. Phys.*, vol. 18, p. 035003, 2016.
- [59] C. Ryu, A. A. Blinova, P. W. Blackburn, and M. G. Boshier, “Experimental realization of Josephson junctions for an Atom SQUID”, *Phys. Rev. Lett.*, vol. 111, p. 205301, 2013.
- [60] J. Liang, R. N. Kohn, M. F. Becker, and D. J. Heinzen, “High-precision laser beam shaping using a binary-amplitude spatial light modulator”, *Appl. Opt.*, vol. 49, p. 1323, 2010.

- [61] G. Gauthier, I. Lenton, N. M. Parry, M. Baker, M. J. Davis, H. Rubinsztein-Dunlop, and T. W. Neely, “Direct imaging of a digital-micromirror device for configurable microscopic optical potentials”, *Optica*, vol. 3, p. 1136, 2016.
- [62] C. Muldoon, L. Brandt, J. Dong, D. Stuart, E. Brainis, M. Himsforth, and A. Kuhn, “Control and Manipulation of Cold Atoms in Optical Tweezers”, *New J. Phys.*, vol. 14, p. 073051, 2012.
- [63] T. A. Haase, D. H. White, D. J. Brown, I. Herrera, and M. D. Hoogerland, “A versatile apparatus for two-dimensional atomtronic quantum simulation”, *Rev. Sci. Instrum.*, vol. 88, p. 113102, 2017.
- [64] V. Boyer, R. M. Godun, G. Smirne, D. Cassettari, C. M. Chandrashekar, A. B. Deb, Z. J. Laczik, and C. J. Foot, “Dynamic manipulation of Bose-Einstein condensates with a spatial light modulator”, *Phys. Rev. A*, vol. 73, p. 031402(R), 2006.
- [65] S. Bergamini, B. Darquié, M. Jones, L. Jacubowicz, A. Browaeys, and P. Grangier, “Holographic generation of microtrap arrays for single atoms by use of a programmable phase modulator”, *Journal of the Optical Society of America B*, vol. 21, p. 1889, 2004.
- [66] F. Nogrette, H. Labuhn, S. Ravets, D. Barredo, L. Béguin, A. Vernier, T. Lahaye, and A. Browaeys, “Single-Atom Trapping in Holographic 2D Arrays of Microtraps with Arbitrary Geometries”, *Phys. Rev. X*, vol. 4, p. 021034, 2014.
- [67] S. Franke-Arnold, J. Leach, M. J. Padgett, V. E. Lembessis, D. Ellinas, A. J. Wright, J. M. Girkin, P. Öhberg, and A. S. Arnold, “Optical ferris wheel for ultracold atoms”, *Optics Express*, vol. 15, p. 8619, 2007.
- [68] G. D. Bruce, J. Mayoh, G. Smirne, L. Torralbo-Campo, and D. Cassettari, “Smooth, holographically generated ring trap for the investigation of superfluidity in ultracold atoms”, *Physica Scripta*, vol. T143, p. 014008, 2011.
- [69] G. D. Bruce, S. L. Bromley, G. Smirne, L. Torralbo-Campo, and D. Cassettari, “Holographic power-law traps for the efficient production of Bose-Einstein condensates”, *Phys. Rev. A*, vol. 84, p. 053410, 2011.
- [70] G. D. Bruce, M. Y. H. Johnson, E. Cormack, D. A. W. Richards, J. Mayoh, and D. Cassettari, “Feedback-enhanced algorithm for aberration correction of holographic atom traps”, *Journal of Physics B: Atomic, Molecular and Optical Physics*, vol. 48, p. 115303, 2015.
- [71] P. W. H. Pinkse, A. Mosk, M. Weidemüller, M. W. Reynolds, T. W. Hijmans, and J. T. M. Walraven, “Adiabatically Changing the Phase-Space Density of a Trapped Bose Gas”, *Phys. Rev. Lett.*, vol. 78, p. 990, 1997.

- [72] F. Buccheri, G. D. Bruce, A. Trombettoni, D. Cassetari, H. Babujian, V. E. Korepin, and P. Sodano, “Holographic optical traps for atom-based topological Kondo devices”, *New J. Phys.*, vol. 18, p. 075012, 2016.
- [73] P. Laurent, P. Lemonde, E. Simon, G. Santarelli, A. Clairon, N. Dimarcq, P. Petit, C. Audoin, and C. Salomon, “A cold atom clock in absence of gravity”, *European Physical Journal D - Atomic, Molecular, Optical and Plasma Physics*, vol. 3, p. 201, 1998.
- [74] S. Kulas, C. Vogt, A. Resch, J. Hartwig, S. Ganske, J. Matthias, D. Schlippert, T. Wendrich, W. Ertmer, E. Rasel, M. Damjanic, P. Weßels, A. Kohfeldt, E. Luvsandamdin, M. Schiemangk, C. Grzeschik, M. Krutzik, A. Wicht, A. Peters, S. Herrmann, and C. Lämmerzahl, “Miniaturized lab system for future cold atom experiments in microgravity”, *Microgravity Science and Technology*, vol. 29, p. 37, 2017.
- [75] P. R. Berman, *Atom Interferometry*. Academic Press, 1997.
- [76] K. Bongs, W. Brinkmann, H. Dittus, W. Ertmer, E. Göklü, G. Johannsen, E. Kajari, T. Könemann, C. Lämmerzahl, W. Lewoczko-Adamczyk, G. Nandi, A. Peters, E. M. Rasel, W. P. Schleich, M. Schiemangk, K. Sengstock, A. Vogel, R. Walser, S. Wildfang, and T. van Zoest, “Realization of a magneto-optical trap in microgravity”, *J. Mod. Opt.*, vol. 54, p. 2513, 2007.
- [77] T. van Zoest, N. Gaaloul, Y. Singh, H. Ahlers, W. Herr, S. T. Seidel, W. Ertmer, E. M. Rasel, M. Eckart, E. Kajari, S. Arnold, G. Nandi, W. P. Schleich, R. Walser, A. Vogel, K. Sengstock, K. Bongs, W. Lewoczko-Adamczyk, M. Schiemangk, T. Schuldt, A. Peters, T. Könemann, H. Müntinga, C. Lämmerzahl, H. Dittus, T. Steinmetz, T. W. Hänsch, and J. Reichel, “Bose-Einstein Condensation in Microgravity”, *Science*, vol. 328, p. 1540, 2010.
- [78] J. Rudolph, W. Herr, C. Grzeschik, T. Sternke, A. Grote, M. Popp, D. Becker, H. Müntinga, H. Ahlers, A. Peters, C. Lämmerzahl, K. Sengstock, N. Gaaloul, W. Ertmer, and E. M. Rasel, “A high-flux BEC source for mobile atom interferometers”, *New J. Phys.*, vol. 17, p. 065001, 2015.
- [79] J. Rudolph, N. Gaaloul, Y. Singh, H. Ahlers, W. Herr, T. A. Schulze, S. T. Seidel, C. Rode, V. Schkolnik, W. Ertmer, E. M. Rasel, H. Müntinga, T. Könemann, A. Resch, S. Herrmann, C. Lämmerzahl, T. van Zoest, H. Dittus, A. Vogel, A. Wenzlawski, K. Sengstock, N. Meyer, K. Bongs, M. Krutzik, W. Lewoczko-Adamczyk, M. Schiemangk, A. Peters, M. Eckart, E. Kajari, S. Arnold, G. Nandi, W. P. Schleich, R. Walser, T. Steinmetz, T. W. Hänsch, and J. Reichel, “Degenerate Quantum Gases in Microgravity”, *Microgravity Sci. Technol.*, vol. 23, p. 287, 2010.
- [80] T. Schuldt, C. Schubert, M. Krutzik, L. G. Bote, N. Gaaloul, J. Hartwig, H. Ahlers, W. Herr, K. Posso-Trujillo, J. Rudolph, S. Seidel, T. Wendrich, W. Ertmer, S. Hermann,

- A. Kubleka-Lange, A. Milke, B. Rievers, E. Rocco, A. Hinton, K. Bongs, M. Oswald, M. Franz, M. Hauth, A. Peters, A. Bawamia, A. Wicht, B. Battelier, A. Bertoldi, P. Bouyer, A. Landragin, D. Massonnet, T. Lévèque, A. Wenzlawski, O. Hellmig, P. Windpassinger, K. Sengstock, W. von Klitzing, C. Chaloner, D. Summers, P. Ireland, I. Mateos, C. F. Sopena, F. Sorrentino, G. M. Tino, M. Williams, C. Trenkel, D. Gerardi, M. Chwalla, J. Burkhardt, U. Johann, A. Heske, E. Wille, M. Gehler, L. Cacciapuoti, N. Gürlebeck, C. Braxmaier, and E. Rasel, “Design of a dual species atom interferometer for space”, *Exp. Astron.*, vol. 39, p. 167, 2015.
- [81] J. A. Rushton, M. Aldous, and M. D. Himsworth, “Contributed review: The feasibility of a fully miniaturized magneto-optical trap for portable ultracold quantum technology”, *Rev. Sci. Instrum.*, vol. 85, p. 121501, 2014.
- [82] K. I. Lee, J. A. Kim, H. R. Noh, and W. Jhe, “Single-beam atom trap in a pyramidal and conical hollow mirror”, *Optics Letters*, vol. 21, p. 1177, 1996.
- [83] J. J. Arlt, O. Maragò, S. Webster, S. Hopkins, and C. J. Foot, “A pyramidal magneto-optical trap as a source of slow atoms”, *Optics Comms.*, vol. 157, p. 303, 1998.
- [84] S. Pollock, J. P. Cotter, A. Laliotis, and E. A. Hinds, “Integrated magneto-optical traps on a chip using silicon pyramid structures”, *Optics Express*, vol. 17, p. 14109, 2009.
- [85] R. S. Williamson III, P. A. Voytas, R. T. Newell, and T. Walker, “A magneto-optical trap loaded from a pyramidal funnel”, *Optics Express*, vol. 3, p. 111, 1998.
- [86] S. Pollock, J. P. Cotter, A. Laliotis, F. Ramirez-Martinez, and E. A. Hinds, “Characteristics of integrated magneto-optical traps for atom chips”, *New. J. Phys.*, vol. 13, p. 043029, 2011.
- [87] M. Vangelyn, P. F. Griffin, E. Riis, and A. S. Arnold, “Single-laser, one beam, tetrahedral magneto-optical trap”, *Optics Express*, vol. 17, p. 13601, 2009.
- [88] C. C. Nshii, M. Vangelyn, J. P. Cotter, P. F. Griffin, E. A. Hinds, C. N. Ironside, P. See, A. G. Sinclair, E. Riis, and A. S. Arnold, “A surface-patterned chip as a strong source of ultracold atoms for quantum technologies”, *Nature Nanotechnology*, vol. 8, p. 321, 2013.
- [89] J. P. McGilligan, P. F. Griffin, E. Riis, and A. S. Arnold, “Diffraction grating characterization for cold-atom experiments”, *J. Opt. Soc. Am. B*, vol. 33, p. 1271, 2016.
- [90] J. P. McGilligan, P. F. Griffin, E. Riis, and A. S. Arnold, “Phase-space properties of magneto-optical traps utilising micro-fabricated gratings”, *Optics Express*, vol. 23, p. 8948, 2015.

- [91] J. P. Cotter, J. P. McGilligan, P. F. Griffin, I. M. Rabey, K. Docherty, E. Riis, A. S. Arnold, and E. A. Hinds, “Design and fabrication of diffractive atom chips for laser cooling and trapping”, *Appl. Phys. B*, vol. 122, p. 172, 2016.
- [92] J. P. McGilligan, P. F. Griffin, R. Elvin, S. J. Ingleby, E. Riis, and A. S. Arnold, “Grating chips for quantum technologies”, *Scientific Reports*, vol. 7, p. 834, 2017.
- [93] C. J. Myatt, N. R. Newbury, and C. E. Wieman, “Simplified atom trap by using direct microwave modulation of a diode laser”, *Optics Letters*, vol. 18, p. 649, 1993.
- [94] P. Feng and T. Walker, “Inexpensive diode laser microwave modulation for atom trapping”, *Am. J. Phys.*, vol. 63, p. 905, 1995.
- [95] E. W. Streed, A. P. Chikkatur, T. L. Gustavson, M. Boyd, Y. Torii, D. Schneble, G. K. Campbell, D. E. Pritchard, and W. Ketterle, “Large atom number Bose-Einstein Condensate machines”, *Rev. Sci. Instrum.*, vol. 77, p. 023106, 2006.
- [96] W. Süptitz, G. Wokurka, F. Strauch, P. Kohns, and W. Ertmer, “Simultaneous cooling and trapping of  $^{85}\text{Rb}$  and  $^{87}\text{Rb}$  in a magneto-optical trap”, *Optics Letters*, vol. 19, p. 1571, 1994.
- [97] K. L. Corwin, Z.-T. Lu, C. F. Hand, R. J. Epstein, and C. E. Wieman, “Frequency-stabilized diode laser with the Zeeman shift in an atomic vapor”, *Applied Optics*, vol. 37, p. 3295, 1998.
- [98] A. Millet-Sikking, I. G. Hughes, P. Tierney, and S. L. Cornish, “DAVLL lineshapes in atomic rubidium”, *J. Phys. B: At. Mol. Opt. Phys.*, vol. 40, p. 187, 2007.
- [99] D. J. McCarron, I. G. Hughes, P. Tierney, and S. L. Cornish, “A heated vapor cell unit for dichroic atomic vapor laser lock in atomic rubidium”, *Rev. Sci. Instrum.*, vol. 78, p. 093106, 2007.
- [100] G. C. Bjorklund, “Frequency-modulation spectroscopy: a new method for measuring weak absorptions and dispersions”, *Optics Letters*, vol. 5, p. 15, 1980.
- [101] J. H. Shirley, “Modulation transfer processes in optical heterodyne saturation spectroscopy”, *Optics Letters*, vol. 7, p. 537, 1982.
- [102] J. Zhang, D. Wei, C. Xie, and K. Peng, “Characteristics of absorption and dispersion for rubidium D2 lines with the modulation transfer spectrum”, *Optics Express*, vol. 11, p. 1338, 2003.
- [103] J.-B. Long, S.-J. Yang, S. Chen, and J.-W. Pan, “Magnetic-enhanced modulation transfer spectroscopy and laser locking for  $^{87}\text{Rb}$  repump transition”, *Optics Express*, vol. 26, p. 27773, 2018.

- [104] N. K. Metzger, R. Spesyvtsev, G. D. Bruce, B. Miller, G. T. Maker, G. Malcolm, M. Mazilu, and K. Dholakia, “Harnessing speckle for a sub-femtometre resolved broadband wavemeter and laser stabilization”, *Nature Communications*, vol. 8, p. 15610, 2017.
- [105] R. W. G. Moore, L. A. Lee, E. A. Findlay, L. Torralbo-Campo, G. D. Bruce, and D. Cassetari, “Measurement of Vacuum Pressure with a Magneto-Optical Trap: a Pressure-Rise Method”, *Rev. Sci. Instrum.*, vol. 86, p. 093108, 2015.
- [106] T. Arpornthip, C. A. Sackett, and K. J. Hughes, “Vacuum-pressure measurement using a magneto-optical trap”, *Phys. Rev. A*, vol. 85, p. 033420, 2012.
- [107] T. W. Hodapp, C. Gerz, C. Furtlehner, C. I. Westbrook, W. D. Phillips, and J. Dalibard, “Three-dimensional spatial diffusion in optical molasses”, *Appl. Phys. B*, vol. 60, p. 135, 1995.
- [108] C. J. Pethick and H. Smith, *Bose-Einstein Condensation In Dilute Gases*. Cambridge University Press, 2nd ed., 2008.
- [109] J. R. Anglin and W. Ketterle, “Bose-Einstein condensation of atomic gases”, *Nature*, vol. 416, p. 211, 2002.
- [110] C. J. Foot, *Atomic Physics*. Oxford University Press, 2005.
- [111] K. Dieckmann, R. Spreeuw, M. Weidemüller, and J. Walraven, “Two-dimensional magneto-optical trap as a source of slow atoms”, *Phys. Rev. A*, vol. 58, p. 3891, 1998.
- [112] J. Schoser, A. Batär, R. Löw, V. Schweikhard, A. Grabowski, Y. Ovchinnikov, and T. Pfau, “Intense source of cold Rb atoms from a pure two-dimensional magneto-optical trap”, *Phys. Rev. A*, vol. 66, p. 23410, 2002.
- [113] W. Wohlleben, F. Chevy, K. Madison, and J. Dalibard, “An atom faucet”, *The European Physical Journal D - Atomic, Molecular, Optical and Plasma Physics*, vol. 15, p. 237, 2001.
- [114] P. V. GmbH, *Vacuum Technology Book Volume II, Part 2 - Know-how Book*. Pfeiffer Vacuum GmbH, 2013.
- [115] D. Bowman, “Ultracold Atoms in Flexible Holographic Traps”, PhD Thesis, University of St Andrews, 2018.
- [116] J. Dalibard and C. Cohen-Tannoudji, “Laser cooling below the Doppler limit by polarization gradients: simple theoretical models”, *Journal of the Optical Society of America B*, vol. 6, p. 2023, 1989.
- [117] D. A. Steck, “Rubidium 87 D line data”, available online at <http://steck.us/alkalidata> (revision 2.1.5, 13 January 2015).

- [118] Y. Castin and R. Dum, “Bose-Einstein condensates in time dependent traps”, *Phys. Rev. Lett.*, vol. 77, p. 5315, 1996.
- [119] R. W. Gerchberg and W. O. Saxton, “A practical algorithm for the determination of phase from image and diffraction plane pictures”, *Optik*, vol. 35, p. 237, 1972.
- [120] M. Pasienski and B. DeMarco, “A high-accuracy algorithm for designing arbitrary holographic atom traps”, *Optics Express*, vol. 16, p. 2176, 2008.
- [121] M. Clark and R. Smith, “A direct-search method for the computer design of holograms”, *Optics Communications*, vol. 124, p. 150, 1996.
- [122] M. Mitchell, *An Introduction to Genetic Algorithms*. MIT Press, 1998.
- [123] C. MacArthur, “Algorithmic optimisation of holographic optical traps”, Masters Thesis, University of St Andrews, 2015.
- [124] T. Harte, “A conjugate gradient minimisation approach to generating holographic traps for ultracold atoms”, Masters Thesis, University of St Andrews, 2012.
- [125] T. Harte, G. D. Bruce, J. keeping, and D. Cassetari, “Conjugate gradient minimisation approach to generating holographic traps for ultracold atoms”, *Optics Express*, vol. 22, p. 26548, 2014.
- [126] J. R. Shewchuk, “An introduction to the conjugate gradient method without the agonizing pain”, <https://www.cs.cmu.edu/quake-papers/painless-conjugate-gradient.pdf>, 1994.
- [127] H. Pang, J. Wang, A. Cao, and Q. Deng, “High-accuracy method for holographic image projection with suppressed speckle noise”, *Optics Express*, vol. 24, p. 22766, 2016.
- [128] T. Shimobaba and T. Ito, “Random phase-free computer-generated hologram”, *Optics Express*, vol. 23, p. 9549, 2015.
- [129] A. L. Gaunt and Z. Hadzibabic, “Robust digital holography for ultracold atom trapping”, *Scientific Reports*, vol. 2, p. 271, 2012.
- [130] D. Bowman, P. Ireland, G. D. Bruce, and D. Cassetari, “Multi-wavelength holography with a single spatial light modulator for ultracold atom experiments”, *Optics Express*, vol. 23, p. 8365, 2015.
- [131] D. Bowman, T. L. Harte, V. Chardonnet, C. D. Groot, S. J. Denny, G. L. Goc, M. Anderson, P. Ireland, D. Cassetari, and G. D. Bruce, “High-fidelity phase and amplitude control of phase-only computer generated holograms using conjugate gradient minimisation”, *Optics Express*, vol. 25, p. 11692, 2017.

- [132] C. Becker, S. Stellmer, P. Soltan-Panahi, S. Dörscher, M. Baumert, E. Richter, J. Kronjäger, K. Bongs, and K. Sengstock, “Oscillations and interactions of dark and dark-bright solitons in Bose-Einstein condensates”, *Nature Physics*, vol. 4, p. 496, 2008.
- [133] J. L. Helm, S. J. Rooney, C. Weiss, and S. A. Gardiner, “Splitting bright matter-wave solitons on narrow potential barriers: Quantum to classical transition and applications to interferometry”, *Phys. Rev. A*, vol. 89, p. 033610, 2014.
- [134] D. Simpson, D. Gangardt, I. Lerner, and P. Krüger, “One-dimensional transport of bosons between weakly linked reservoirs”, *Phys. Rev. Lett.*, vol. 112, p. 100601, 2014.
- [135] R. R. Sakhel, A. R. Sakhel, and H. B. Ghassib, “Nonequilibrium dynamics of a Bose-Einstein condensate excited by a red laser inside a power-law trap with hard walls”, *Journal of Low Temperature Physics*, vol. 173, p. 177, 2013.
- [136] T. D. Team, “Theano: A python framework for fast computation of mathematical expressions”, *arXiv:1605.02688*, 2016.
- [137] D. Bowman, T. L. Harte, V. Chardonnet, C. D. Groot, S. J. Denny, G. L. Goc, M. Anderson, P. Ireland, D. Cassettari, and G. D. Bruce, “University of St Andrews research data: Data underpinning high-fidelity phase and amplitude control of phase-only computer generated holograms using conjugate gradient minimisation”, *doi:10.17630/f30dd10e-9708-4cbf-8fcb-4b91869a1415*, 2017.
- [138] L. Wu, S. Cheng, and S. Tao, “Simultaneous shaping of amplitude and phase of light in the entire output plane with a phase-only hologram”, *Scientific Reports*, vol. 5, p. 15426, 2015.
- [139] A. M. Yao and M. J. Padgett, “Orbital angular momentum: origins, behaviour and applications”, *Advances in Optics and Photonics*, vol. 3, p. 161, 2011.
- [140] A. Ramanathan, K. C. Wright, S. R. Muniz, M. Zelan, W. T. Hill, C. J. Lobb, K. Helmerson, W. D. Phillips, and G. K. Campbell, “Superflow in a toroidal Bose-Einstein condensate: An Atom circuit with a tunable-weak link”, *Phys. Rev. Lett.*, vol. 106, p. 130401, 2011.
- [141] M. Huo, W. Nie, D. A. W. Hutchinson, and L. C. Kwek, “A solenoidal synthetic field and the non-abelian aharonov-Bohm effects in neutral atoms”, *Scientific Reports*, vol. 4, p. 5992, 2014.
- [142] V. E. Lembessis, J. Courtial, N. Radwell, A. Selyem, S. Franke-Arnold, O. M. Aldosary, and M. Babiker, “Graphene-like optical light field and its interaction with two-level atoms”, *Phys. Rev. A*, vol. 92, p. 063833, 2015.

- [143] S. Butera, N. Westerberg, D. Faccio, and P. Öhberg, “Nonlinear synthetic gauge potentials and sonic horizons in Bose-Einstein condensates”, *rxiv:1605.05556v2*.
- [144] Y. Roichman, B. Sun, Y. Roichman, J. Amato-Grill, and D. G. Grier, “Optical forces arising from phase gradients”, *Phys. Rev. Lett.*, vol. 100, p. 013602, 2008.
- [145] S. Tao and W. Yu, “Beam shaping of complex amplitude with separate constraints on the output beam”, *Optics Express*, vol. 23, p. 1052, 2015.